Growth, Diffusion, and Loss of Subsurface Ice on Mars: Experiments and Models

Thesis by

Troy Lee Hudson

In Partial Fulfillment of the Requirements

for the Degree of

Doctor of Philosophy

California Institute of Technology

Pasadena, California

2008

(Defended April 29, 2008)

For Thomas.

I love you, Boo.

"The subtlety of nature is greater many times over than the subtlety of the senses and understanding; so that all those specious meditations, speculations, and glosses in which men indulge are quite from the purpose, only there is no one by to observe it."

– Francis Bacon, *Novum Organum, 1620*

"I swear, by my life and my love of it, that I will never live for the sake of another man, nor ask another man to live for mine."

– Ayn Rand, *Atlas Shrugged, 1957*

"In theory, theory and practice are the same.
In practice, they're not."

– Lawrence Peter Berra

Acknowledgments

The work presented herein would not have been possible without the assistance, known or unknown, of many persons.

The first few years of this work were conducted at the Jet Propulsion Laboratory and I received much help, physical and intellectual, from Greg Peters, Nathan Bridges, Jackie Green, and Steve Fuersteneau during my time at the Extraterrestrial Materials Simulation Laboratory. Much fruitful collaboration came from the involvement of Barney Farmer, whose visits and conversations were always welcome. Also well met during that time was Mike Hecht, who has been, and continues to be, a supporter of my work, a champion of my post-graduate career, a strong source of encouragement for the completion of this thesis, and a role-model for my future as a scientist.

My advisor, Oded Aharonson, deserves a tremendous amount of credit for this work and for my professional development. He has frequently acknowledged my skills as an experimentalist and has helped develop my abilities as a theorist and modeler. I believe that our complimentary strengths enabled us to produce worthwhile scientific discoveries that would not have been possible individually. I have appreciated his simultaneously cheerful and serious attitude, and am glad to have developed a rapport with him that I hope will continue.

My only regret regarding Norbert Schorghofer is that a more involved working relationship with him did not develop before the end of his tenure as a post-doc at Caltech. Nevertheless, we have had much fruitful collaboration and, as with Oded, it has proved most educational. I thank him for his assistance, remote or in person, and am inexpressibly grateful for his helpful responses to my frequent inquiries. I can only hope I have been able to help him as much as he has helped me.

More than any other professor from whom I have taken classes in my years of education, am I grateful that I was able to both learn and to teach under the guidance of George Rossman. My greatest unfulfilled wish for my time at Caltech is that I was not able to collaborate with him more thoroughly. I hope the future will provide that opportunity. I hope, too, that the friendship which I feel has developed between us can be maintained and built upon.

I also must thank: Alex Hayes, my office mate, confidant, and gym partner. May our dreams of bridging the scientist–engineer schism be fulfilled. Matt Siegler, a font of tireless enthusiasm and assistance. Best of luck with your experimental endeavors in the Ice Lab. Bruce Murray, my first

contact at Caltech. Though without verification of this belief, I feel that his impressions of my potential were a contributing factor to my acceptance to the GPS graduate program. I hope my progress, efforts, and future work will please him. And Hermann Engelhardt, a master of all things ice. I have enjoyed working alongside him in the Ice Lab and am thankful that we were able to revitalize that facility together.

Technical and scientific support, as well as much friendly advice, has come my way from Mike Black, Scott Dungan, Ma Chi, and Mike Garcia. A special and heartfelt thank you. Hello! Thank you. to Chris Baumgartner: a brilliant source of help in all things electrical, and an occasional very welcome relief from the stress of the day. Thank you, hello! My profound thanks to the fine ladies who staff the Planetary Science and the GPS Division offices. Irma Black, Nora Oshima, Leticia Calderon, Sarah DeFusco, Jean Grinols, Marcia Hudson, and the ever-cheerful Tess Puig. Also, my thanks to and fond memories of Mrs. Donna Sackett. I also wish to thank the individuals of the various stockrooms about campus, whose advice and assistance in obtaining much-needed and last-minute items for the laboratory helped prevent frustration and delays.

Beyond the Caltech community, I thank my mother, my father, and my stepfather for everything they have done to make me the man I am. For instilling and encouraging my love of learning. For supporting *many* years of education. For teaching me how to think. And for understanding and loving me for who I am.

Most important to my personal growth, sanity, and enjoyment of these wonderful years of my life has been the love, support, and unflagging encouragement of my friends and soul mates in Los Angeles, throughout the US, and across the world. To list all of you here would take many, many pages. But if you've given me one word of encouragement, one fun evening, one laugh, or one moment of relief from my own delusions of adequacy, you are on that list. Thank you.

Abstract

Innovative experiments and models are used to explore the behavior of subsurface ice on Mars. Through communication with the atmosphere, the porous regolith of Mars hosts significant quantities of ice which grow, evolve, and are lost in response to climate changes. As a controlling property of rate of ice response to a changing equilibrium state, the diffusive properties of several regolith simulants are measured in Mars-like environments. Ice loss through a variety of particle sizes, particle size distributions, packing densities, and salt contents are examined and reveal that many unconsolidated media exhibit diffusion coefficients in the range of 2–6 $cm^2\ s^{-1}$, indicating a response time on the order of several thousand years for ice within the upper meter of the regolith. Only high salt contents or mechanically packed micron-sized dust are observed to exhibit substantially lower coefficients, suggesting that strong diffusive barriers may not form as readily as previously invoked.

The growth of ice directly from vapor under diffusive control is reproduced for Mars-like environmental conditions in the absence of the liquid phase. As predicted, ice deposits preferentially at grain contact points and the ice table interface is sharp and strongly controlled by near-surface temperature perturbations. The quantity of ice deposited as a function of depth and time accords well with new numerical models of vapor diffusion and ice deposition, though constriction of the pore space reduces the diffusion coefficient faster than originally expected.

A numerical model incorporating a fast solution to subsurface ice growth predicts near-surface ice contents for the last 300,000 years of Mars' history at high latitude locations, including specifically the Phoenix landing site. Several parameterizations of constriction developed from laboratory observations of ice growth are employed and compared. The thickness of the ice-free layer above the ice table has the strongest effect on the quantity of ice accumulated, though subsurface massive ice sheets and ice-free porosities also affect the ice profile. If predicted ice loss events have emptied the upper 0.5–1.0 m of regolith prior to 300,000 years ago, pore ice formed through diffusive processes will have been unable to fill the most rapidly accumulating depths with ice in this time unless ice-saturated regolith exists within $\sim$0.5 m of the surface. Predictions of these experiments and models will be tested by the imminent arrival of the Phoenix Mars Lander and future Mars missions.

Contents

Chapter 1

Subsurface Ice on Mars

Water has played a central role in the evolution of surface materials (*e.g., Banin et al.*, 1992), geomorphology (*e.g., Baker et al.*, 1992; *Baker*, 2001), and in potentially habitable environments on Mars (*e.g., McKay et al.*, 1992; *Cabrol et al.*, 2007). Areas of ancient Mars experienced massive floods capable of sculpting large channels, fluvial valleys, and dendritic networks (*e.g., Sharp and Malin*, 1975; *Carr*, 1981; *Baker*, 1982; *Baker et al.*, 1992; *Carr*, 1996; *Masson et al.*, 2001; *Komatsu and Baker*, 2007). Formerly wet environments have produced characteristic local and regional morphologies (*e.g., Banin et al.*, 1992), and various mineral assemblages including iron oxides (*e.g., Christensen et al.*, 2000), sulfate deposits (*e.g., Squyres and Knoll*, 2005), and diagenetic alteration products (*e.g., Squyres et al.*, 2004b). Though not as active in forming surface features today as in the past, water continues to modify the planetary surface through its role in the formation of the polar caps, gullies, and possibly slope-streaks (*e.g., Jakosky and Haberle*, 1992; *Carr*, 1996; *Malin and Edgett*, 2000; *Mellon and Phillips*, 2001; *Ferris et al.*, 2002; *Schorghofer et al.*, 2002).

The water cycle on Mars includes a number of reservoirs which may exchange with each other on various timescales. The atmosphere, polar caps, and near-surface regolith may interact through convective transport, condensation/sublimation, and adsorption (*e.g., Farmer and Doms*, 1979; *Jakosky*, 1983; *Clifford*, 1993; *Smith*, 2002). Perhaps the most voluminous reservoir, however, is the porous regolith (*Rossbacher and Judson*, 1981), which presently communicates with the atmosphere through the physical process of diffusion. The timescales involved in this exchange range from diurnal breathing to multi-million year climate variation. The rate of water vapor diffusion through the regolith determines how long ice can survive in the subsurface when exposed to a drier atmosphere (*e.g., Smoluchowski*, 1968; *Farmer and Doms*, 1979; *Paige*, 1992; *Mellon and Jakosky*, 1993; *Mellon et al.*, 2004; *Schorghofer and Aharonson*, 2005). Diffusion also determines how fast the regolith can be recharged with atmospherically derived vapor (*Mellon and Jakosky*, 1995; *Hudson et al.*, 2008) subject to the conditions of vapor supply and vapor gradients. Predicting present and past reservoir locations and volumes, constraining exchange rates between them, and understanding the dynamics of subsurface ice evolution motivate the study of the diffusion of water vapor in the subsurface of

Mars.

Extensive subsurface ice on present-day Mars has been observed within a meter of the surface at latitudes polewards of approximately 60° (*Boynton et al.*, 2002; *Feldman et al.*, 2002). Past epochs on Mars no doubt also harbored buried ice, though its distribution may have been significantly different (*Squyres et al.*, 1992; *Mellon and Jakosky*, 1995; *Carr*, 1996). A number of investigations have examined the equilibrium behavior of subsurface ice under the present climate (*e.g., Mellon and Jakosky*, 1993; *Mellon et al.*, 2004; *Schorghofer and Aharonson*, 2005), and under various climate conditions as modulated by orbital and axial parameters (*e.g., Mellon and Jakosky*, 1995; *Mellon et al.*, 1997; *Levrard et al.*, 2005; *Schorghofer*, 2007). The ice, though protected from extremes of temperature by the overlying regolith, diffusively exchanges with the atmosphere and feels the effects of atmospheric vapor content and subsurface temperature. While unrelated to the equilibrium position of the ice table, the diffusive properties of the porous media overlying ice exert a first-order control on the rate of response of the ice table's position to changing conditions.

Sub-freezing (*i.e.,* bulk liquid-free) vapor diffusion in soils finds further application in the evolution of subsurface ice on Earth. The longevity of ice in cold, arid locations such as the Dry Valleys of Antarctica constrains timescales of terrestrial climate change (*Sugden et al.*, 1995; *Hindmarsh et al.*, 1998). Many sites in the McMurdo Dry Valleys have dry permafrost within the upper meter of the glacial till comprising the valley floor (*Bockheim*, 2002). The depth and extent of this ice may be controlled in part by vapor diffusion processes, particularly where precipitation and mean annual temperatures are low and liquid water is largely absent (*Hindmarsh et al.*, 1998; *McKay et al.*, 1998; *Schorghofer*, 2005). While the studies in this work are motivated by Mars, they are also be relevant for such localities on Earth.

1.1 The Ice Table

When diffusive processes govern the distribution of ground ice, the interacting driving forces of temperature and vapor density control its distribution. The vapor concentration gradients exist between the ice and the atmosphere, and also within the ice itself if porous. In a steady-state environment, the interface between a perennially ice-free regolith and a perennially ice-bearing regolith defines the physical ice table. The temporal qualifier allows the regolith above the ice table to experience periodic ice deposition and loss in response to daily and seasonal changes of atmospheric humidity and subsurface temperature. Beneath such regions that harbor no annually stable ice, the balance of driving forces creates a finite depth of equilibrium: the depth where the mean annual vapor density of the atmosphere matches the equilibrium vapor density over ice. When the physical ice table is not coincident with this equilibrium depth it evolve toward it by gaining or losing mass.

1.1.1 Observational data

Recent measurements by the Gamma Ray Spectrometer on the Mars Odyssey spacecraft have been used to identify significant quantities of subsurface hydrogen in the upper meter of the martian regolith (*Boynton et al.*, 2002; *Feldman et al.*, 2002). In equatorial regions, the hydrogen-rich areas are usually less than 10% H by mass, which may be due to hydrated minerals or adsorbed water (*Feldman et al.*, 2002; *Feldman et al.*, 2004a; *Jakosky et al.*, 2005). However, mid- to high-latitude regions exhibit quantities of hydrogen which cannot be accomodated by any known mineral but one: water ice. Observed hydrogen abundances converted to water-equivalent units reveal quantities up to 50% water by mass (70% water ice by volume) in certain areas. The black contours in Figure 1.1 show the polar distribution of these measured water contents in units of mass percent. Some of this ice may fill the pore spaces of a particulate medium, while some may exist as layers of relatively debris-free ice; the existing data are insufficient to determine an unambiguous depth distribution. Different regions may prove to harbor different patterns of ice density with depth and may also be heterogeneous in ice content over small spatial scales.

1.1.2 Equilibrium models

Surface water was abundant in Mars' ancient past and produced numerous large features on the surface such as chaotic terrain, outflow channels, and drainage networks (*Carr*, 1996). In more recent geological times, most of the remaining water has retreated into the subsurface as ice (*Squyres*, 1984), and some has formed the permanent ice caps and polar layered terrain. Early models of the evolution of subsurface ice investigated the retreat rates and present depths of buried ice sheets which had been sublimating into a dry atmosphere for billions of years (*Smoluchowski*, 1968; *Soderblom and Wenner*, 1978). Theoretical understanding of astronomically induced changes to Mars' climate have brought forth the modern paradigm that significant fluctuations of insolation distribution and atmospheric water content have taken place on timescales of millions of years, or even faster (*Ward*, 1974; *Toon et al.*, 1980; *Carr*, 1996). This has led to a suite of models which predict the current equilibrium position of the ice table given knowledge of the present day atmospheric water content, insolation, and surface thermal properties. The degree to which such models accord with presently available or future observations may be explained in part by the rate at which exchange between this reservoir and the atmosphere can occur.

Mellon and Jakosky (1993) were the first to employ a complete vapor diffusion model to determine the global equilibrium positions of the ice table. Improved measurements of soil thermal properties and the effect of pore-ice on regolith thermal conductivity were incorporated into a later implementation of this model (*Mellon et al.*, 2004). *Schorghofer and Aharonson* (2005) have employed a similar model to create maps of subsurface ice stability which include regions of seasonally

stable and permanent ice. Figure 1.1 shows the results of their model, compared to the data from the Mars Odyssey spectrometers.

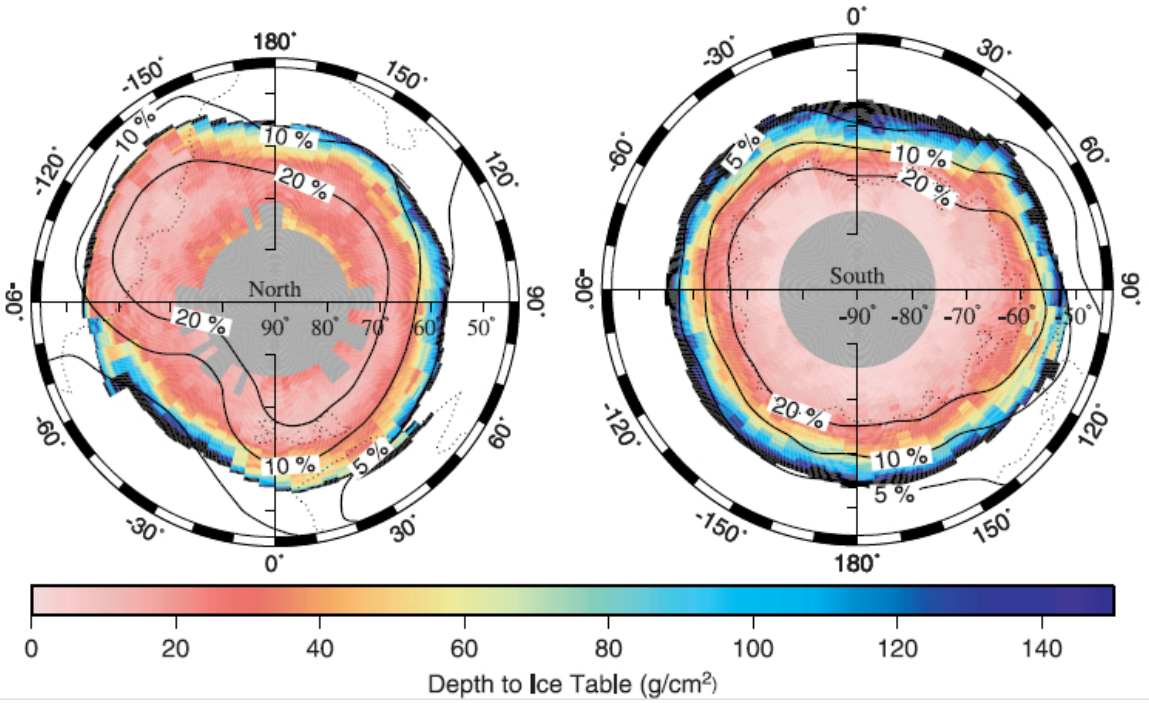

Figure 1.1: Polar maps of predicted ice table burial depths in gm cm^{-2} (color scale), and mass percent of water-equivalent hydrogen derived from Mars Odyssey measurements (solid black contours) *Feldman et al.* (2003). Ground ice is unstable in the white areas, and missing data are shown in gray. The assumed volumetric ice fraction is 40%. Dashed lines are 200 J m^{-2} K^{-1} s$^{-1/2}$ contours of thermal inertia. Figure reproduced from *Schorghofer and Aharonson* (2005).

Models of modern subsurface ice equilibrium and observations of real subsurface ice match quite well, strongly suggesting that much subsurface ice resides at or close to its equilibrium position. This further implies either a climate which has been relatively stable for some time, a fast response time of subsurface ice distribution, or perhaps both.

Several effects may be responsible for deviations of the observations from model predictions of ice position and quantity. Shallow regolith thermal properties may be probed with diurnal temperature measurements to derive near-surface thermal inertias; however, the thermal structure for much of Mars beneath a few centimeters remains hidden. Just as the thermal properties of the near-surface regolith varies significantly across the surface of Mars (*Mellon et al.*, 2000), so may the deeper subsurface. An explanation for the mismatch central to the theme of this work is the moderation by overlying ice-free regolith of the response time of the ice to a changing equilibrium. As with its thermal properties, the martian regolith is no doubt heterogeneous in its geometric structure as well; barriers in different regions will possess differing resistances. Ice in one location may be able to respond quickly to a large shift in equilibrium position, while a more shielded spot would respond

sluggishly. Such heterogeneities may exist over local scales, while large regions of similar geologic character may exhibit broadly similar rates of response.

1.2 Regolith Breathing

The position of the equilibrium ice table depends only on the temperature of the subsurface ice and the vapor content of the atmosphere. As diurnal, annual, and obliquity-scale temperature waves propagate into the subsurface, and as the atmospheric moisture content changes, they alter the regions of ice stability. Rather than affecting this equilibrium, the physical process of diffusion governs the *rate* at which vapor exchange occurs. Thus the 'breathing' of the regolith, particularly on timescales longer than annual, is subject to first-order control by the process of molecular diffusion, parameterized by the diffusion coefficient.

1.2.1 The diffusion coefficient

The magnitude of mass flux driven by a concentration gradient is proportional to that gradient, a relationship called Fick's First Law of Diffusion. The diffusion coefficient, with units of length squared per time, is the proportionality constant relating the gradient and the flux. The value of this quantity for two different gases in unconstrained space depends on interactions between molecules and is understood in terms of kinetic theory (*Chapman and Cowling*, 1970). When a porous medium occupies some of the volume through which diffusion occurs, interactions between molecules and the material reduce this free-gas diffusivity by an amount which depends on the geometry of the space available to gas transport.

Figure 1.2 schematically shows the vapor exchange interaction between a ground ice and the atmosphere, moderated by an intervening layer of porous ice-free regolith. The schematic ignores the effects of adsorbed water, which are unimportant on timescales of one year or longer (see Section 3.6.1 and *Schorghofer and Aharonson*, 2005). The net flux of vapor moving either in or out of the regolith (but never both at once) is indicated by the wavy arrows. The gradient of water vapor concentration in the host gas (CO_2 on Mars) drives this transport. This gradient exists between the the atmosphere and the shallowest ice. But diffusion-driving gradients can also exist amongst various depths within the ground ice if it is porous. Beneath the deepest ground ice, vapor can diffuse into the regolith against the geothermal gradient if it remains below the saturation density. If ice deposits in this region, the vapor pressure of deeper, warmer ice will be greater than the shallower ice above, and the mass flux through ice-bearing layers will always be toward the atmosphere.

Large diffusion coefficients reduce mass flux relative to that of free-gas diffusion only slightly; a low diffusivity reduces the flux and will impede all vapor transport if the diffusion coefficient is identically zero. Values of the diffusion coefficient for the martian regolith have been used by a

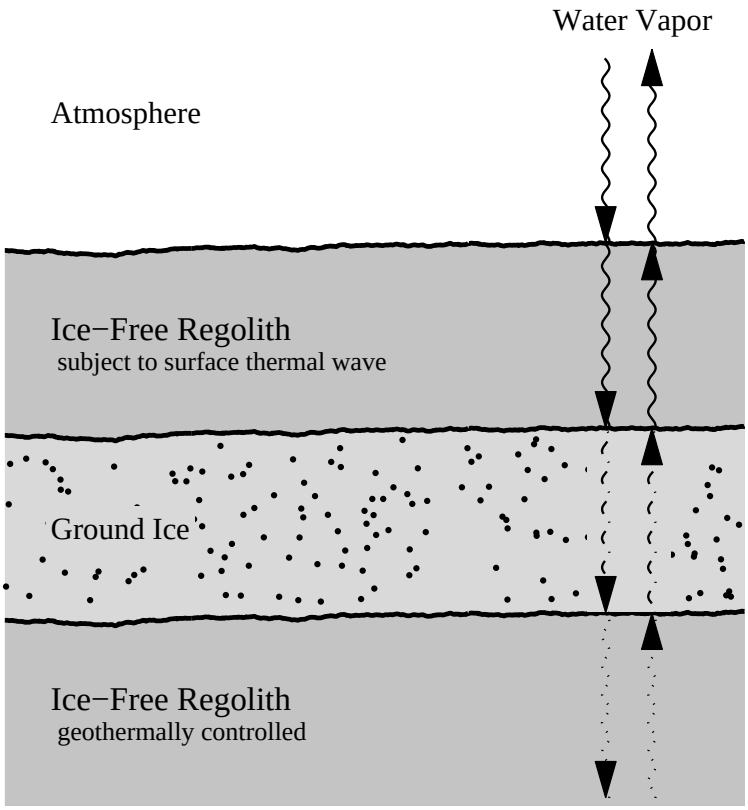

Figure 1.2: Schematic of various diffusion regions in an ice-bearing regolith. The mean annual vapor density gradient may be directed into or out of the upper layers of the regolith and the next flux may be directed inward or outward, though never both at once. Ground ice may fall on a continuum which includes pure slab ice, pore-filling ice, and ice partially filling pore spaces. Only if the ice-bearing medium is porous will diffusion occur in this layer. In the bottom layer, where temperatures are dominated by the geothermal gradient, the flux of water may still occur in either direction if unsaturated, but will always be directed toward the atmosphere in a saturated (*i.e.,* ice-bearing) region. Note that both the upper and lower boundaries of the ground ice are not static.

number of previous investigators as a parameter in models of subsurface vapor communication with the atmosphere. These values are based both on predictions of theoretical work and extrapolations of experimental diffusion data to Mars surface conditions. No samples of the martian regolith, much less undisturbed samples with their natural pore structures intact, are available and *in-situ* measurements on Mars thus far have not addressed soil diffusivities directly.

1.2.2 Previous investigations

Many of the papers described in this section calculate diffusion coefficients from the kinetic theory of gases as applied to porous media. All such methods require additional input parameters describing the geometry of the pore space. Porosity, or void volume, may be estimated from particle size distributions and shapes or measured directly for real samples. Another parameter, tortuosity,

which describes the degree of interconnectivity and convolution of the void space, is not amenable to direct measurement. Even for mathematically simulated pore spaces, the value of this dimensionless number depends on the physical model used and proves intractable to calculate in all but the most simple cases. No robust relationship between porosity and tortuosity exists that holds for a wide variety of particle shapes and sizes. Thus, the value of tortuosity is usually obtained from experiment by measuring porosity and diffusivity. The ratio of porosity to tortuosity parameterizes the change in diffusion coefficient from free-gas to porous-media conditions and is often called the obstruction factor.

In a seminal paper, *Smoluchowski* (1968) calculates diffusion coefficients for a range of particle sizes and porosities using the kinetic theory of gases as presented by *Kennard* (1938) and *Evans et al.* (1961). He presents a range of values between 4×10^{-4} and 12 cm^2 s^{-1}. The lower end of this range applies to porosities of 1–10% and particle diameters less than 10 μm. Such values may be appropriate for deep, compacted regoliths or for porous rock such as sandstone. For more typical near-surface, unconsolidated soil properties, *i.e.,* porosities of 50–80% and 10–200 μm particle diameters, he obtains diffusivities between 0.7 and 11 cm^2 s^{-1}. Smoluchowski cites no reference for tortuosity, but presents values of 1, 5, and 10, for 80%, 50%, and lower porosities, respectively.

Rather than strictly calculating from theory, *Flasar and Goody* (1976) directly reference experimental measurements of gas diffusion in porous media. The works cited therein include *Currie* (1960), who performed experiments on diffusion through dry granular materials of hydrogen in air at STP, and also *Papendick and Runkles* (1965), whose work considered oxygen diffusion in porous media at STP. Both of these earlier works present factors relating free-gas and porous media diffusion coefficients for a variety of materials. Flasar and Goody use these to determine a range of porous-media diffusion coefficients of 0.4–13.6 cm^2 s^{-1} for the surface of Mars at 610 Pa and 210 K. The upper limit they give is the temperature- and pressure-extrapolated value of free-gas diffusion given by Boyton and Brattain in *Washburn et al.* (2003) (but see Section 2.3). A real porous medium will have an obstruction factor less than unity, hence the diffusion coefficient would necessarily all below this limit.

Farmer (1976) cites both Smoluchowski and Evans *et al.,* and quotes Smoluchowski's values directly. Farmer shows that his model, with a regolith diffusivity of 1.0 cm^2 s^{-1}, matches the observed amplitude of martian seasonal variation in atmospheric water content at 25°N latitude, and presents a range of 1.0–3.0 cm^2 s^{-1} as appropriate for Mars. *Jakosky* (1983) references Flasar and Goody but gives a slightly modified range of 0.3–10 cm^2 s^{-1}.

Clifford and Hillel (1983) examine the mechanics of diffusion on Mars in great detail; they also cite measurements of diffusion in porous media, all performed at 25–30°C. Most involve the diffusion of H_2 or He, and many were performed at pressures of 1 atmosphere or higher. Their derivation from kinetic theory computes values for diffusivity given only a pore size distribution and a value

for tortuosity.

Fanale et al. (1986) and *Zent et al.* (1986), in tandem papers, perform their own calculations to derive diffusivity from gas kinetics and reference Smoluchowski for values of tortuosity. They use a porosity of 50% for all cases and a tortuosity of 5. For a pressure of 610 Pa and a temperature of 210 K, their expression gives a free-gas diffusivity of 13.2 cm^2 s^{-1} and a porous medium diffusivity of 0.44 cm^2 s^{-1}. These values are essentially the same as the limits given by *Flasar and Goody* (1976).

A later paper by *Clifford and Hillel* (1986) focuses on Knudsen diffusion in the Mars regolith (*i.e.,* diffusion through small pore spaces in the limit of molecule–wall collisions). *Fanale et al.* (1986) estimate a diffusion coefficient of 0.02–0.22 cm^2 s^{-1} for pore radii from 1 to 10 μm.

Mellon and Jakosky (1993) present a diffusive model for the regolith. This work includes a detailed derivation of the porous media diffusion coefficient similar to *Clifford and Hillel* (1983), but uses collision integrals to calculate free-gas diffusion coefficients, while Clifford and Hillel cite *Wallace and Sagan* (1979). For a pressure of 600 Pa, a temperature of 200 K, and a pore radius of 1–10 μm, the expression of Mellon and Jakosky gives a porous medium diffusion coefficient of 2–10 cm^2 s^{-1}.

The experiments performed or referenced in the above mentioned investigations were conducted above the freezing point of water and at high (relative to present-day Mars) pressures. Few measurements have focused on the diffusion of water vapor, a substance condensible in the temperature range of interest and highly adsorptive on most natural materials. The measurements of free-gas diffusion of H_2O in CO_2 at conditions other than those appropriate to Mars' surface have been extrapolated in temperature and pressure. Only recently have direct measurements of the diffusion of gases in porous media at conditions of low temperature and Mars surface pressures begun to appear in the literature (*Chittenden et al.*, 2006; *Bryson et al.*, 2007). The experiments described in Chapters 3 and 4 measure the diffusion coefficient of a variety of porous materials. The physical configuration of these experiments are chosen to mimic the temperatures, pressures, humidities, and diffusing gas species occurring on the surface of present-day Mars.

1.3 Barriers to Diffusion

Most experiments providing data on granular media diffusivities have been conducted with particles of uniform size, a circumstance which limits their applicability to natural particle assemblages. As demonstrated by all landed Mars missions, the surface of Mars exhibits a wide variety of soil types with different particle sizes, morphologies, and compositions (*Yen et al.*, 2005), and small regions exhibit heterogeneous distribution of these types. This suggests that the diffusive properties of the martian regolith may vary over small length scales.

On Earth, the mobilization of chemical species by liquid water may produce horizons of mineralization which have significantly reduced porosities and permeabilities relative to the host rock. Such barriers impede the movement of pore water and can form perched water tables and aquacludes. Though perhaps not mobile in the present climate, high concentrations of subsurface salts detected by the MER spacecraft (*Vaniman et al.*, 2004; *Yen et al.*, 2005), and the common occurrence of surface duricrusts (*Landis et al.*, 2004; *Wang et al.*, 2006), admits the possibility that liquid water has redistributed and redeposited such soluble minerals within regolith pore spaces. If the crystallization of these salts tended toward a pore-filling habit, rather than forcing the grains apart, the reduction of pore space would be coincident with a reduction in diffusivity and reduced water vapor flux. Barriers may persist indefinitely in subsequent drier conditions and impede the flow of water vapor, even if the salt minerals responsible for pore closure are water soluble.

Considering physical rather than chemical processes, the regolith of Mars exhibits a wide variety of particle sizes, from milimeter-sized and larger grains to aeolian sediment to dust fine enough for atmospherically suspended (*Kahn et al.*, 1992; *Squyres et al.*, 2004a). Aeolian processes can sort grain sizes such that a near-surface regolith could exhibit an particle assemblage of uniform size and shape (*Sullivan et al.*, 2005). Yet many processes also exist which can mix sediments, giving rise to soils with a broad particle size distribution. Fine particles deposited from atmospheric suspension may fill in the pores of a coarser matrix, reducing the diffusivity of the bulk material (*Farmer*, 1976). Alternatively, dust may also coat larger grains and prevent close packing, 'fluffing' the regolith, increasing the overall porosity and thereby increasing the diffusion coefficient.

Dust alone may comprise some near-surface regolith in various regions of Mars. Such dust, with particle sizes on the order of a few microns or less, can exhibit either a high or low diffusivity. If physically compacted or dispersed in a lubricating medium such as water, fine dust can achieve close-packed arrangements which may have pore sizes comparable to the particle diameters. A broad-scale overburden will encourage mechanical compaction of dust also producing small pores and thus diffusivities. Processes involved in the generation of polar layered terrain may produce low diffusivity dust layers in the following manner: Dust-bearing ice is deposited during one season or climate regime and then lost during the other half of the cycle. During the phase of net loss, as the ice sublimates, the remaining dust forms a lag. While this lag may initially have a high diffusivity, subsequent deposition of ice above would compact in, increasing its ability to preserve the ice beneath during future periods of loss (*Levrard et al.*, 2005).

A number of factors act to prevent dust derived from airfall (in the absence of snow) from packing closely. The low mass of dust particles (implying low kinetic energies) and the inefficiency of chemical weathering processes on Mars permit jagged edges to persist. The irregular dust grains will interlock more readily than smooth particles, and resist falling into compact arrangements. Electrostatic charging of dust should be efficient on Mars (*Merrison et al.*, 2004), and airborne

particles may flocculate into aggregates which retain their low density upon deposition (*Abrahamson and Marshall*, 2002). These effects may act alone or in concert to produce a larger diffusivity than highly compacted dust with micron-scale pores.

This work includes diffusion coefficient measurements for media of known dust fraction, salt content, or state of compaction. The results assist understanding of how the diffusivity of a given natural porous medium on Mars may be modified by these factors.

1.4 Growth of Subsurface Ice

In the present climate, ice exists in the shallow subsurface at latitudes poleward of about 60 degrees as predicted by models (*e.g., Leighton and Murray*, 1966; *Mellon and Jakosky*, 1993; *Schorghofer and Aharonson*, 2005) and confirmed by observations (*e.g., Boynton et al.*, 2002). *Litvak et al.* (2006), show that the ice content of the ice-rich layer depends on latitude, and the ice content they derive is consistent with the existence of interstitial ice in some latitude range. During previous epochs, the stability regions were hypothesized to occupy higher latitudes when Mars' obliquity was low, and may have been global during high obliquity periods (*Mellon and Jakosky*, 1995; *Head et al.*, 2003). While some of the presently observed ice may have been emplaced by precipitation and subsequent burial, much of the shallow ground ice has been derived directly from atmospheric water vapor (*Mellon and Jakosky*, 1993; *Schorghofer*, 2007).

Ice accumulates in a permeable medium if a humidity gradient supplies water molecules to locations where the gas-phase vapor density exceeds saturation. On Mars, such a gradient can exist between a warm and humid but unsaturated atmosphere and a cold and therefore saturated location in the subsurface; the flux being directed toward the already saturated cold spot. This infilling phenomenon was first modeled numerically by *Mellon and Jakosky* (1993) and these models indicate that, for latitudes where stability criteria permit subsurface ice, it will accumulate in pore spaces beneath an ice-free layer.

Theoretical treatment of the equilibrium ice table suggests that the interface will be sharp, transitioning from an ice-rich regolith to an ice-free one over short distances (*Schorghofer and Aharonson*, 2005). The boundary for a given atmospheric water content will follow subsurface isotherms and will therefore be subject to perturbations from inhomogeneities in surface albedo and the presence of masses of relatively higher or lower thermal inertia (*Sizemore and Mellon*, 2006).

The growth of ice in a porous medium been treated theoretically (*Hobbs and Mason*, 1964; *Hobbs*, 1974). From surface energy arguments, ice is expected to form first at grain contact points, *i.e.,* areas of high negative curvature. However, the phenomenon of diffusive ice growth in a porous medium has not been previously demonstrated experimentally. The distribution of accumulating ice feeds back into the geometry of the pore spaces and also the thermal conductivity of the bulk medium.

The formation of subsurface ice reduces a porous medium's diffusivity via constriction of the pore space. As ice accumulates, it reduces the available volume for vapor transport and thereby diminishes the mass flux. A regolith with an initially large pore diameter will transition from Fickian-dominated to Knudsen-dominated diffusion as the open pores become smaller. Subsurface ice grows most rapidly near the equilibrium depth (*Mellon and Jakosky*, 1995; *Schorghofer and Aharonson*, 2005), so constriction will be most efficient at this point, strongly inhibiting diffusion and reducing deposition rates when filling fractions are high.

Laboratory experiments described herein produce for the first time the phenomenon of diffusive transport and ice deposition in a porous medium at Mars conditions. The resulting ice content profiles reveal the presence and sharpness of the developed ice table and its depth relative to the predicted equilibrium position. A variety of atmospheric humidity regimes and experiment durations are employed to provide information about the rate at which the pores fill; long-duration experiments allow the ice-filled state to be approached. A numerical model of ice deposition, run with experimental temperatures, humidities, and ice-free diffusivity as inputs, incorporates parameterizations of pore-space reduction. Comparisons between the model and experimental data allow these schema to be evaluated.

1.5 Subsurface Ice Evolution

Much of the predictive work concerning subsurface Mars ice has focused on the ice table and its equilibrium position given the current Mars climate (*Leighton and Murray*, 1966; *Farmer and Doms*, 1979; *Fanale et al.*, 1986; *Paige*, 1992; *Mellon and Jakosky*, 1993, 1995; *Mellon et al.*, 2004; *Schorghofer and Aharonson*, 2005). There are only a few investigations of the behavior of subsurface ground ice on Mars beneath the ice table. Bounded above by this interface, the region termed the cryosphere experiences perennial ground ice, analogous to permafrost on Earth. The quantity, depth, and distribution of ice beneath the ice table affects estimations of total Mars water inventories, the the interpretation of observations by planned and future missions, and our understanding of the present and past state of water on Mars.

Clifford (1993) extensively discusses the subsurface hydrology of Mars under the assumption that a cryosphere of varying thickness overlies an active hydrosphere which can supply water from deep underground to shallower depths. This recharge allows ground ice to exist in the warm and otherwise dry equatorial regions without invoking climate change or extreme preservation mechanisms. *Mellon et al.* (1997) consider the evolution of a subsurface ice sheet which initially saturates 200 m of regolith pore space. Because of the depth range covered, only the geothermal gradient drives diffusive flux through this model and, as in *Clifford* (1993), the effect of the annual thermal wave on ice evolution in the shallow regolith is not considered. Such shallow depths, however, are a region of the cryosphere

easily observable by landed missions and therefore invites particular consideration.

The Mars Odyssey detection of high-latitude subsurface hydrogen, interpreted as ice, is limited to the upper meter of the regolith column. Direct investigations by the Phoenix Mars Lander, and perhaps future landed missions as well, will probe the shallow non-polar subsurface. Models which track the evolution of ice and predict its subsurface distribution in this depth range will help direct future measurements and will aid the interpretation of observations.

In *Mellon and Jakosky* (1995), the authors explore the distribution of ice derived from atmospheric water vapor in the upper few meters of the regolith at various latitudes for 2.5 Myr of Mars' orbital history. For latitudes equatorward of 60–70 degrees, their model shows that shallow regolith desiccation could occur to a depth of 1 to 2 meters. This is consistent with the work of *Schorghofer* (2007), who models the evolution of a massive ice sheet for 5 million years, incorporating the formation of a diffusive lag and ice redeposition in pore spaces. The simulation by *Schorghofer* that includes variable atmospheric humidity reveals three significant loss events between 300–600 thousand years ago. This implies that the subsurface ice targeted by Phoenix and much of the high-latitude ice sensed by Mars Odyssey has formed as a pore-filling substance since that time.

The amount of ice able to accumulate since the last major loss event will depend on feedbacks of deposited ice on the regolith diffusion coefficient and subsurface thermal conductivity, in addition to the availability of water. The shallowest ice-bearing regions (*i.e.,* the ice table) accumulate ice most rapidly and therefore exhibit greater reduction of flux than deeper, less ice-rich levels. Investigations by *Hudson et al.* (2008) (Chapter 5) indicate that constriction deviates from a linear function in filling fraction, enhancing this effect and resulting in a reduced quantity of deposited ice for similar temperature histories.

Ice within a particulate regolith also modifies the thermal conductivity of the bulk material (*Paige*, 1992), altering the amplitude and penetration depth of the thermal wave. Both the ice which deposits in pore spaces from atmospheric vapor and deep relic ice left behind after the last climatically induced loss event will contribute greater conduction of heat to depth. The effect of large-amplitude temperature variations on ice temperature will be strongest for ice within a few diurnal skin depths of the surface. Many regions with subsurface ice today exhibit a layer of ice-free regolith which protects shallow subsurface ice from these extremes, yet at some locations (*e.g.,* the Phoenix landing site) the thinness of the barrier may allow attenuated diurnal fluctuations to penetrate to the stable ice.

The feedback of these mechanisms and Mars' complex insolation history preclude analytical solutions to ice distributions over long timescales. Forward numerical modeling under assumptions of identical insolation and atmospheric humidity history will permit the effects discussed above to be examined independently. The present-day ice content predicted by the models will differ depending on the position of deep ice, the thickness of shallow ice-free layers, and the degree of non-linearity

involved in constriction. The magnitude and direction of the effects can thus be assessed and this understanding will assist interpretations of shallow ice content profiles observed on Mars in the future.

1.6 Implications for Future Investigations

Future studies will employ experimental data such as those reported here to produce more accurate models, and will use the results of these laboratory investigations and simulations of ice growth and loss processes to inform interpretations of observational data. These possibilities have motivated this study of porous media diffusivities and of the evolution of subsurface ice at Mars surface conditions.

1.6.1 Global climate models

The water cycle of Mars has been an object of investigation using sophisticated general circulation models (GCMs) incorporating a variety of physical processes (*Forget et al.*, 1999; *Richardson and Wilson*, 2002; *Haberle et al.*, 2003). The latest generation of these models now include vapor diffusion processes and permit the subsurface to be both a source and sink of water vapor. While the amount of water potentially evolved from any given reservoir in one year's time under the present climate is ∼10–100 precipitable microns (*Zent et al.*, 1993; *Schorghofer and Aharonson*, 2005), this quantity represents a significant fraction of the present atmospheric water abundance. Regions with high dust contents may also incorporate large volumes of adsorbed water which can be gained and lost on diurnal and annual timescales. The ability of regions with high storage capacities to saturate in a given time, and the rate at which they remove water from or add water to the atmosphere, will depend on the diffusion coefficient of the soil. The presence of such large or active subsurface reservoirs will affect the accuracy of models of the Mars water cycle.

GCMs also investigate the water cycle during past climate epochs when surface ice was stable at locations different from those that currently harbor seasonal frosts (*Mellon and Jakosky*, 1993; *Chamberlain and Boynton*, 2007) and when precipitation may have been an active process. (*Haberle et al.*, 2003; *Mischna and Richardson*, 2005). The necessity of incorporating the exchange of subsurface ice, and the changing positions and volumes of stable reservoirs, grows in importance as the time span covered by these models becomes comparable to or exceeds subsurface–atmosphere communication timescales. Employing both the high-fidelity tracking of atmospheric conditions provided by GCMs and the evolution of subsurface reservoirs on long timescales would be limited by the computation speed of the GCM system. One solution employs the GCM to compute a steady climate state (requiring approximately 10 model years) and uses these steady-state values as constraints on physically simpler yet much faster evolution models of water reservoirs such as the polar caps, subsurface ice, and surface ice deposits. These models would be run in series, passing termi-

nal conditions to subsequent stages as input parameters. A coupled model such as this would lead to a better understanding of Mars' long-term water cycle, of regions of surface and subsurface ice stability, of the variation of atmospheric water content over millions of years, and possibly of the formation of climate-controlled terrain such as the polar layered deposits.

Both long- and short-duration models would be improved by the incorporation of spatially varying regolith diffusion coefficients. The demonstrably heterogeneous nature of the martian regolith, as observed by landers and from orbit, implies that the diffusion coefficients of various regions will be different. Even given the result that many loose-particle materials exhibit similar diffusion coefficients (see Chapters 3 and 4 and *Hudson et al.*, 2007; *Hudson and Aharonson*, 2008), the effect of minor variations could accumulate when considered over large spatial or temporal scales. By relating pore size to particle size, and determining the global variation of the latter using measurements obtained from orbit, a rough global map of diffusivity may be constructed. One step of this process, relating observable surface properties to particle size, has been performed for martian fines using reflectance spectra (*Ruff and Christensen*, 2002), and for a broader range of particle sizes using thermal inertia (*Kieffer*, 1976; *Jakoksy and Christensen*, 1986; *Mellon et al.*, 2000). In *Mellon and Phillips* (2001), distinct thermal inertia and albedo units were defined from Thermal Emission Spectrometer measurements. Spatial variations in diffusivity may be assigned based on such surface units if the particle size derived from thermal inertia measurments correlates, even broadly, with diffusivity. Using such a map as a set of input parameters for GCMs, the effect of spatially varying diffusion coefficients on the water cycle could be assessed. Caution must be exercised in relating observable surface properties to pore size, or even in relating particle size to pore size, since the correlations depend on many factors, some of which are still poorly constrained.

1.6.2 Phoenix Scout lander

The Phoenix Scout mission is the first robotic exploration of Mars deliberately targeted at a site expected to possess water in the form of subsurface ice. Landing site selection has been based in part on Mars Odyssey measurements, but also on theoretical predictions of ice table equilibrium depth at high latitudes (*Arvidson et al.*, 2008). These investigations indicate the presence of ice at the landing site within a few decimeters of the surface (*Boynton et al.*, 2006; *Mellon et al.*, 2008).

The Robot Arm on Phoenix will be used to excavate up to half a meter into the surface, exposing and potentially sampling the ice. Analyses of soil thermal conductivity and surface albedo will help further refine subsurface thermal models and predictions of ice table equilibrium. The depth of the observed ice table, if different from the predictions, may be used to refine both the history of the atmospheric vapor content at the site and the diffusion coefficient of the soil. This latter endeavor will also be assisted by observations of soil particle sizes with the Optical Microscope.

By examining the ice table itself, the habit of the subsurface ice, whether it exists as a pore-

filling substance or as a massive, regolith-poor layer, will be revealed. This observation directly tests the ice age model of *Schorghofer* (2007) and the models of Chapter 6, which predict massive ice retreat followed by diffusive replenishment, giving a present-day configuration of unsaturated pore-ice near the equilibrium depth. If the filling fraction can be estimated through qualitative measurements of ice mass and regolith porosity, or perhaps correlated with the mechanical strength of the ice-bearing layer, further models of ice growth rates can be assessed. Future missions may glean further information about water in Mars' past by examining subsurface ice distributions with ground-penetrating radar or coring into ice-rich ground; they may also extract isotopes and trapped gases from subsurface ice or polar ice sheets, which are expected to hold a record of the planetary climate, as do ice sheets on Earth (*Murray et al.*, 1972; *Cutts and Lewis*, 1982; *Laskar et al.*, 2002).

1.7 This Work

In Chapter 2, the theory of gaseous diffusion is reviewed, with particular emphasis on diffusion in porous media and the conditions and processes which prevail on the surface of Mars. Chapter 3 covers the materials, methods, results, and interpretations of experiments which simulate buried ice loss into a dry martian atmosphere. The content of these chapters was previously published in *Hudson et al.* (2007).

Chapter 4 extends the investigations of Chapter 3, using the same experimental procedure, to examine enhanced diffusion barriers in the form of salt-encrusted soils, mixtures of sand and dust particles, and fine dust—both compacted and uncompacted. The content of this chapter is published in *Hudson and Aharonson* (2008).

In Chapter 5, the converse process to the ice loss in Chapters 3 and 4 is investigated. Atmospherically derived water vapor is driven down a static, thermally induced vapor density gradient to fill the pore spaces of an initially dry regolith. This represents the first experimental investigation of diffusively derived pore ice under any conditions. The measured ice content profiles are compared to numerical models of vapor diffusion and deposition. The phenomenon of pore space constriction is emphasized, since the experiments indicate that the effect of deposited ice on the diffusion coefficient may not be linear, as assumed in previous models (*Mellon and Jakosky*, 1995). The content of this chapter has been submitted for publication as *Hudson et al.* (2008).

Numerical models investigating the evolution of cryospheric ice over several obliquity cycles are the subject of Chapter 6. These models use Mars' history of orbital parameters and insolation variation to determine how and to what extent parameters such as deep ice content, ice-free surface-layer thickness, and constriction non-linearity affect the distribution of pore-filling ice, which has accumulated since predicted loss events of 300–600 thousand years ago.

Chapter 2

Diffusion Theory

2.1 Chapter Summary

The evolution of ice in diffusive contact with a planet's atmosphere through a barrier of porous material is affected by the thermal and geometric properties of the regolith. The former controls the propagation of diurnal, annual, and long-term thermal waves into the subsurface and thereby modulates the temperatures experienced at depth. The latter set of properties, including porosity, pore size and shape, and tortuosity, influence the rate at which gas molecules migrate in response to chemical potential gradients. Temperature, through its effect on the saturation vapor density of air and the vapor pressure of ice, determines the concentration of water molecules in the subsurface. Changing temperatures may create a positive, negative, or identically zero concentration gradient with respect to the vapor density in the atmosphere. If a gradient of concentration exists, there will be a net flux of water molecules down the gradient, resulting in a net growth or depletion of the subsurface ice with time, even under isobaric conditions. The magnitude of this flux depends both on the magnitude of the concentration gradient and on the diffusive properties of the soil, as represented by the diffusion coefficient, D.

Here expressions are developed for vapor transport in a sublimation environment where temperature and pressure can change with time and space. Gas-kinetic models for determining diffusion coefficients are presented, as well as some summarized empirical observations. The distinction between two primary types of diffusion, Fickian and Knudsen, are described, as are methods for handling the transition between the two regimes. Tortuosity is discussed and several methods for extracting this dimensionless geometric property of a porous medium are presented. Effects other than concentration diffusion that may operate in experimental apparatus as well as in natural environments are examined. Finally, the governing equation for ice deposition via diffusion is given.

Throughout this work, subscript 1 refers to H_2O and subscript 2 to the carrier gas, usually CO_2. For example, p_1 is the partial pressure of H_2O and ρ_1 the density of water vapor. The total pressure is denoted by $p_0 = p_1 + p_2$ and the total mass density by $\rho_0 = \rho_1 + \rho_2$. A script $\mathcal{D}$ refers to free-gas

diffusion coefficients while roman italic D refers to diffusion in a porous medium.

2.2 Vapor Transport

Diffusion of mass is due to differences in concentration, temperature, and pressure (*Reid et al.*, 1987). The general expression for diffusive flux of one dilute gas (species 1) in another (species 2) at low velocities is (*Landau and Lifshitz*, 1987, §57, §58)

$$J_{\text{Diff}} = -\rho_0 \left[\mathcal{D}_{12} \frac{\partial}{\partial z} \frac{\rho_1}{\rho_0} + \frac{\mathcal{D}_T}{T} \frac{\partial T}{\partial z} + \frac{\mathcal{D}_p}{p_0} \frac{\partial p_0}{\partial z} \right], \tag{2.1}$$

where J_{Diff} is the diffusive mass flux of gas 1, $\mathcal{D}_{12}$ the mutual diffusion coefficient, $\mathcal{D}_T$ the coefficient for "thermodiffusion", T the temperature, and $\mathcal{D}_p$ the coefficient of "barodiffusion". Thermodiffusion and barodiffusion are usually small compared with concentration diffusion (see sections 2.6.2 and 2.6.3).

Equation (2.1) holds in a reference frame where the center of mass velocity of the gas mixture is zero. In an environment where temperature and total pressure change little, and the vapor concentration is low, the concentration diffusion J_{Diff} would be simply described by

$$J_{\text{Diff}} = -\mathcal{D}_{12} \frac{\partial \rho_1}{\partial z}. \tag{2.2}$$

For a detailed discussion of reference frames and non-isothermal diffusion laws, see *Cunningham and Williams* (1980).

The porosity, ϕ, of a porous medium restricts the cross-sectional area available for transport. A second factor called tortuosity, τ, accounts for the increase in path length which the molecules must follow. The diffusion coefficient in a porous medium in the Fickian diffusion regime, D_{F}, can be written as (*Mason and Malinauskas*, 1983)

$$D_{\text{F}} = \frac{\phi}{\tau} \mathcal{D}_{12}. \tag{2.3}$$

The ratio ϕ/τ is also called the "obstruction factor". In principle, this reduction in diffusivity can be obtained theoretically from the void space geometry. In practice, the void space geometry is seldom known, even for soils in a laboratory environment.

In a porous medium, equation (2.2) is replaced by

$$J_{\text{Diff}} = -D \frac{\partial \rho_1}{\partial z}, \tag{2.4}$$

where J_{Diff} is the flux due to concentration diffusion. The effective diffusion coefficient, D, subsumes all effects of gas molecule collisions with pore walls and other gas molecules, and the geometry of

the pore spaces through which gas travels.

2.3 Diffusion Coefficient

The coefficient of diffusion is the product of mean velocity and mean free path, with a prefactor that can be temperature dependent. The mean velocity depends only on temperature; the mean free path is inversely proportional to the density of the gas. Thus, a thinner atmosphere has a higher diffusivity. The diffusivity of an unconfined gas at rest, in which molecules diffuse through an interstitial gas, forms the basis for understanding the diffusivity of a porous regolith.

Theoretical expressions can be obtained for the diffusion coefficient, $\mathcal{D}_{12}$, in a dilute gas at rest consisting of vapor species 1 and 2. The coefficient of self-diffusion, $\mathcal{D}_{11}$, is not measured in these experiments.

The coefficient of diffusion in a binary mixture of rigid elastic spherical molecules is, to first order in the density of the diffusing species, (*Chapman and Cowling*, 1970)

$$\mathcal{D}_{12} = \frac{3}{8 n_0 \sigma_{12}^2} \sqrt{\frac{k_B T}{2\pi} \left(\frac{1}{m_1} + \frac{1}{m_2} \right)}. \tag{2.5}$$

The number density n_0 is obtained from the ideal gas law, $n_0 = p_0/k_B T$, $\pi\sigma_{12}^2$ is the scattering cross section, k_B is the Boltzmann constant, and m_1 and m_2 are the molecular masses.

The parameter σ_{12} is computed by averaging the molecular radii of each species, $\sigma_{12} = (\sigma_1 + \sigma_2)/2$. The cross section for individual molecules can be determined from viscosity measurements of pure gases. *Chapman and Cowling* (1970) report molecular radii for CO_2 and N_2. *Schwertz and Brow* (1951) calculate a molecular radius for H_2O from the molecular volume of the liquid. The values are listed in Table 2.1.

For intermolecular forces other than a model of rigid elastic spheres, a temperature-dependent prefactor is introduced via the collision integral $\Omega_{12}(T)$ (*Mason and Malinauskas*, 1983; *Reid et al.*,

Parameter	Value	Reference
σ^{hes} (CO_2, N_2)	4.63, 3.76 Å	*Chapman and Cowling* (1970)
σ^{hes} (H_2O)	2.7 Å	*Schwertz and Brow* (1951)
σ^{LJ} (H_2O, CO_2, N_2)	2.641, 3.941, 3.798 Å	*Reid et al.* (1987)
ϵ/k (H_2O, CO_2, N_2)	809.1, 195.2, 71.4 K	*Reid et al.* (1987)

Table 2.1: Model parameters for the mutual diffusion coefficient. σ^{hes} = molecular radius of hard elastic spheres, σ^{LJ} and ϵ/k are parameters of the Lennard-Jones potential. The collision integral for the Lennard-Jones potential can be expressed as $\Omega_{12} = A(T^*)^{-B} + Ce^{-DT^*} + Ee^{-FT^*} + Ge^{-HT^*}$. Values for the constants A, B, C, D, E, F, G, H are given in *Neufeld et al.* (1972) and *Reid et al.* (1987). The dimensionless temperature T^* is given by $T^* = k_B T/\epsilon_{12}$ and the molecule specific parameter ϵ is computed for a gas pair by $\epsilon_{12} = \sqrt{\epsilon_1 \epsilon_2}$.

1987),

$$\mathcal{D}_{12} = \frac{3}{8 n_0 \sigma_{12}^2} \sqrt{\frac{k_B T}{2\pi} \left(\frac{1}{m_1} + \frac{1}{m_2} \right)} \frac{1}{\Omega_{12}(T)}. \tag{2.6}$$

The length parameter σ_{12} now depends on the intermolecular force law and its value is not the same as for the rigid elastic spherical molecules. For a Lennard-Jones potential, the function $\Omega_{12}(T)$ and parameters for H_2O, CO_2, and N_2 are given in Table 2.1.

For an ideal gas of hard elastic spheres, the diffusion coefficient depends on temperature as $T^{3/2}$, as can be seen from equation (2.5). For other intermolecular potentials, the temperature dependence is described by equation (2.6), and can be shown to have an exponent between 0 and 2. The free-gas diffusion coefficient is inversely proportional to pressure for any intermolecular potential.

Equation (2.6) is a first-order expansion derived from Chapman-Enskog theory. To lowest order, the diffusion coefficient does not depend on the relative concentration of the two gases, n_1/n_2, but only on the total number density, $n_0 = n_1 + n_2$, and on the temperature. Hence the diffusion coefficient is symmetric, $\mathcal{D}_{12} = \mathcal{D}_{21}$.

The second-order approximation of the diffusion coefficient introduces a dependence on n_1/n_2 (*Chapman and Cowling*, 1970). For a hard sphere model and low concentrations of species 1 ($n_1 \ll n_2$), the diffusion coefficient is increased by a factor of

$$\frac{1}{1 - m_1^2/(13m_1^2 + 30m_2^2 + 16m_1 m_2)}.$$

For low H_2O concentration in a CO_2 or N_2 atmosphere, this correction is <1%. The maximum correction for any mixing ratio for H_2O–CO_2 is 4%, and for H_2O–N_2 it is 2%, both occurring as $n_2 \to 0$. Hence the dependence of the diffusion coefficient on the proportions of the mixture can be neglected in comparison to other uncertainties.

Holman (1997) gives a semiempirical equation by *Gilliland et al.* (1974)

$$\mathcal{D}_{12} = 435.7 \mathrm{cm^2 s^{-1}} \frac{T^{3/2}}{p_0 (V_1^{1/3} + V_2^{1/3})^2} \sqrt{\frac{1}{M_1} + \frac{1}{M_2}},$$

where T is in Kelvin, p is in pascals, V_1 and V_2 are molecular volumes of gases 1 and 2, and M_1 and M_2 are their molar weights. Holman cautions that this expression is useful for various mixtures, but should not be used in place of experimental values of $\mathcal{D}_{12}$ when available.

The coefficient of mutual diffusion $\mathcal{D}_{12}$ has been directly measured from evaporation rates of water into pure gases. Measurements for H_2O–CO_2 are reported or compiled by *Guglielmo* (1882), *Winkelmann* (1884a,b, 1889), *Trautz and Müller* (1935a,b), *Schwertz and Brow* (1951), *Rossie* (1953), and *Crider* (1956) in the temperature range 291–373 K at atmospheric pressure. *Nagata and Hasegawa* (1970) use gas chromatography to determine the diffusivity at 394 K and higher temperatures. The International Critical Tables (*Washburn et al.*, 2003) list $\mathcal{D}_{\mathrm{H_2O \cdot CO_2}} =$

$(0.1387\ \mathrm{cm^2 s^{-1}})(T/T_0)^2(p_{\mathrm{ref}}/p)$, citing experiments by Guglielmo and Winkelmann. A comprehensive review of gaseous diffusion coefficients by *Marrero and Mason* (1972) recommends $\mathcal{D}_{\mathrm{H_2O\cdot CO_2}} = (9.24\times10^{-5}\ \mathrm{cm^2 s^{-1}})T^{3/2}\exp(-307.9/T)(p_{\mathrm{ref}}/p)$ for T in the range 296–1640 K. A diffusivity scaling often cited in the context of Mars studies is from *Wallace and Sagan* (1979), who use a prefactor determined from *Schwertz and Brow* (1951) to write $\mathcal{D}_{\mathrm{H_2O\cdot CO_2}} = (0.1654\mathrm{cm^2 s^{-1}})(T/T_0)^{3/2}(p_{\mathrm{ref}}/p_0)$. In all cases, $p_{\mathrm{ref}} = 1013$ mbar and $T_0 = 273.15$ K.

Measurements for H_2O–N_2 are available from *Hippenmeyer* (1949), *Schwertz and Brow* (1951), *Bose and Chakraborty* (1955–56), *Crider* (1956), *Nelson* (1956), and *O'Connell et al.* (1969) in the range 273–373 K. *Marrero and Mason* (1972) recommend $\mathcal{D}_{\mathrm{H_2O\cdot N_2}} = (1.87\times10^{-6}\ \mathrm{cm^2 s^{-1}})\times T^{2.072}(p_{\mathrm{ref}}/p_0)$ in the temperature range 282–373 K.

Figure 2.1 shows theoretical and experimental values of the mutual diffusion coefficient as a function of temperature. The empirical fits from *Marrero and Mason* (1972) and the International Critical Tables are based on measurements at high temperature and may not provide accurate results when extrapolated below 273 K. The empirical fits, the theoretical formula for a Lennard-Jones potential, and the theoretical formula for hard elastic spherical molecules predict slightly different temperature dependences. Measurement errors and uncertainties in cross sections introduce additional deviations that limit the accuracy to which diffusion coefficients can be computed for a free gas.

The Martian atmosphere consists of 95% CO_2, the next most abundant gases being nitrogen and argon. The fraction of gases other than CO_2 is small enough to be ignored and we consider a pure CO_2 atmosphere. According to the elastic hard sphere model, equation (2.5), the diffusion coefficient in CO_2 is smaller than in N_2 at the same pressure and temperature by a factor of

$$\frac{\mathcal{D}_{\mathrm{H_2O\cdot CO_2}}}{\mathcal{D}_{\mathrm{H_2O\cdot N_2}}} = \frac{\sigma^2_{\mathrm{H_2O\cdot N_2}}}{\sigma^2_{\mathrm{H_2O\cdot CO_2}}}\frac{\sqrt{1/18+1/44}}{\sqrt{1/18+1/28}} \approx 0.72. \tag{2.7}$$

Assuming a Lennard-Jones potential, this ratio would be 0.68–0.69 in the temperature range 150–293 K.

2.4 Mean Free Path and Knudsen Diffusion

The mean free path for species 1, diffusing in a gas composed of species 1 and 2, is (*Chapman and Cowling*, 1970)

$$\lambda_1 = \frac{1}{n_1\pi\sigma_{11}^2\sqrt{2} + n_2\pi\sigma_{12}^2\sqrt{1+m_1/m_2}}. \tag{2.8}$$

When only one gas is present, the familiar formula $\lambda_1 = 1/(\sqrt{2}n\pi\sigma^2)$ is recovered. When $n_1 \ll n_2$, the first term in the denominator, resulting from like-molecule collisions, is negligible. With this expression, the mean free path of H_2O in a dry CO_2 atmosphere at 600 Pa and 200 K is $\lambda_1 \approx 9$ μm.

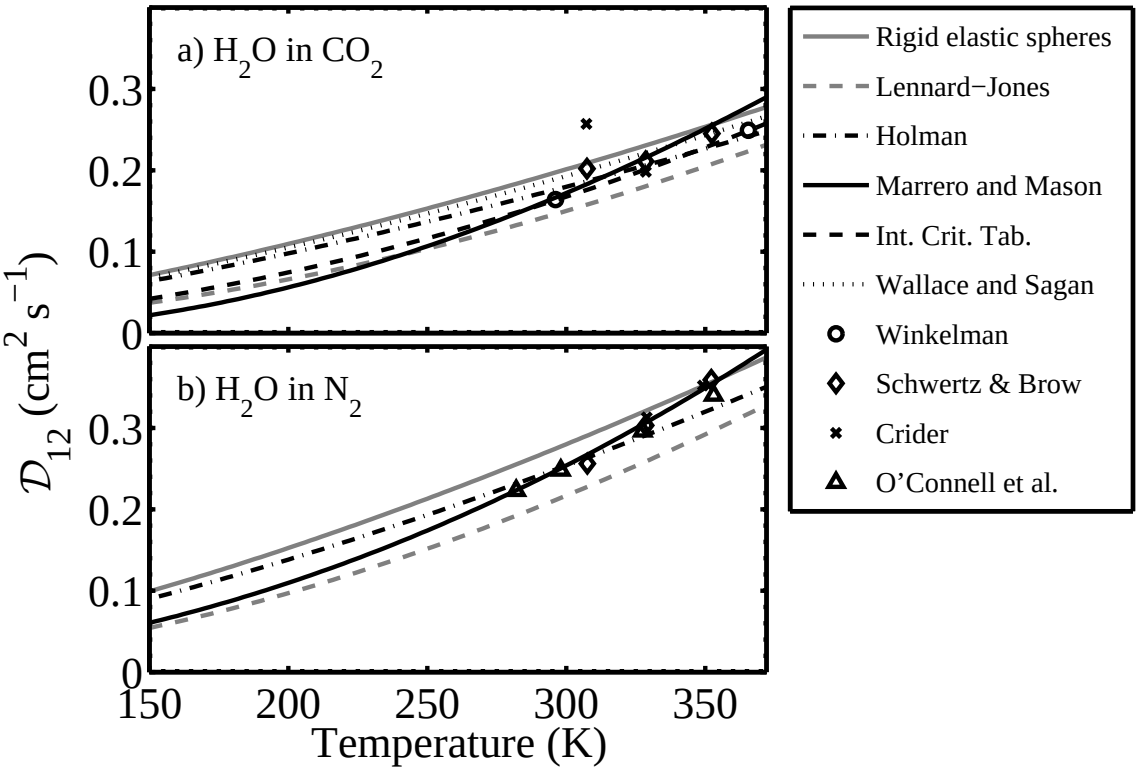

Figure 2.1: Theoretical and measured diffusion coefficients for H_2O in a) CO_2 and b) N_2 as a function of temperature at 1013 mbar. Grey lines are theoretical formulae with model parameters, black lines indicate fits to measured values, and individual markers indicate specific measured values.

The mean free path of H_2O in a dry N_2 atmosphere is longer than in a dry CO_2 atmosphere at the same pressure and temperature by a factor of 1.2.

In a porous solid with interconnected pathways, a gas molecule may collide with another molecule or with the pore walls. When the gas pressure is high, molecule-molecule collisions dominate and the system is said to be in the normal or Fickian regime.

At low pressure, collisions are dominantly between molecules and the walls, and the free path is restricted by the geometry of the void space. In this regime, termed Knudsen diffusion, the presence of other gases no longer affects the transport, and the flux depends only on the density gradient of the species of interest (water in this study) and can be written as (*Mason and Malinauskas*, 1983)

$$J_1 = -D_K \frac{\partial \rho_1}{\partial z}. \tag{2.9}$$

As for Fickian diffusion, the Knudsen diffusion coefficient D_K is proportional to the mean velocity. For example, in a long, straight, circular capillary of radius $r \ll \lambda_1$, the diffusion coefficient at low

pressure is

$$D_{\mathrm{K}} = (2/3)\bar{\nu}_1 r, \tag{2.10}$$

where the mean velocity is $\bar{\nu}_1 = \sqrt{8k_B T/\pi m_1}$ (*Mason and Malinauskas*, 1983; *Clifford and Hillel*, 1986).

Evans et al. (1961) give an expression for D_{K} in materials with interconnected, convoluted pore spaces

$$D_{\mathrm{K}} = \frac{4}{3}\bar{\nu}_1 K_0, \tag{2.11}$$

where K_0 is a structural parameter (with dimensions of length) accounting for both pore geometry and the scattering of the diffusing molecules off the pore walls. They give an expression for K_0

$$\frac{1}{K_0} = \frac{128}{9} n_d \frac{\tau}{\phi} r^2 \left(1 + \frac{1}{8}\pi a_1\right), \tag{2.12}$$

where n_d is the number density of "dust" particles (meaning the porous medium). Here, r is the particle size in the dusty gas model (which may be an average of a particle size distribution), and a_1 is the fraction of molecules that are both scattered diffusely and have their speeds thermalized to a Maxwellian distribution. *Evans et al.* (1961) suggest that a_1 is 1 for most gases. In the case of spherical particles with an average radius $\bar{r}$, n_d can be estimated as $(3/4)(1-\phi)/\pi\bar{r}^3$, giving

$$D_{\mathrm{K}} = \frac{\pi}{8+\pi}\frac{\phi}{1-\phi}\frac{\bar{\nu}_1 \bar{r}}{\tau}. \tag{2.13}$$

These expressions show that D_K is independent of pressure and changes as $T^{1/2}$ with temperature.

Experiments by *Sizemore and Mellon* (2007) have shown that the pore size distributions in disaggregated particles of small size, even pure dust of micron-scale dimensions, tend toward rather large pores, up to 100 microns in diameter or more. Work by Clifford and Hillel has shown that the overwhelming majority of flux in such bimodal or skewed distributions is carried through the largest pores (*Clifford and Hillel*, 1983). Thus, even though a porous regolith may contain particles on the order of 1 micron, the larger size of pores may put diffusion at $p_0 = 6$ mbar largely in the Fickian diffusion regime, with only a minor Knudsen contribution.

At intermediate pressures, collisions with pore walls and with other molecules occur with significant frequency. This "transition region" is defined by the ratio of pore size to mean free path r/λ_1. In the Knudsen regime r/λ_1 is much smaller than 1 and in the Fickian regime r/λ_1 is much greater than 1. Equations (2.2) and (2.9) can be combined by summing their contributions to $\partial\rho_1/\partial z$. Neglecting advection in (2.2) we obtain

$$\frac{\partial \rho_1}{\partial z} = -J_1 \left(\frac{1}{\mathcal{D}_{12}} + \frac{1}{D_K}\right). \tag{2.14}$$

Thus the combined or effective diffusion coefficient may be written

$$D^{-1} = \mathcal{D}_{12}^{-1} + D_{\mathrm{K}}^{-1}. \tag{2.15}$$

This is known as the Bosanquet relation and was discussed by *Pollard and Present* (1948) and more recently described in *Mason and Malinauskas* (1983) in the context of gas diffusion through porous media.

2.5 Tortuosity

Porosity quantifies the reduction in cross-sectional area available for gaseous transport, while tortuosity, τ, is a quantity which characterizes the convoluted nature of the porous pathways followed by diffusing species. The theoretical determination of tortuosity is model dependent and extremely cumbersome for all but the most simple geometries. It is most often the case that the other parameters in equation (2.3), D_{F}, ϕ, and $\mathcal{D}_{12}$, are determined from experiment and τ is calculated from these.

In Chapter 3, experiments are performed at a range of pressures to extract independent Knudsen and Fickian diffusion coefficients. Having thus obtained the purely Fickian diffusion coefficient, equation (2.3) is used with the Fickian diffusion coefficient to determine τ. For the experiments in Chapter 4, variable pressure measurements are not performed. Instead, the method of *Zalc et al.* (2004) is employed, wherein a strictly geometric tortuosity factor, independent of diffusion regime, is derived. Knowledge of the pore space geometries obtained from mercury porosimetry measurements are used to calculate a Knudsen diffusion coefficient. Employing the Bosanquet relation (equation 2.15), D_K and $\mathcal{D}_{12}$ are used with measured values for the effective diffusion coefficient, D, to compute the obstruction factor, and from this determine τ as per equation (2.3).

The free gas diffusivity for either the method employing variable pressures or that using pore geometries may be calculated using one of the formulas in Section 2.3. The experimental procedures described below do not measure $\mathcal{D}_{12}$, and no such measurement of water in CO_2 at Mars surface conditions yet exists in the literature. Care must be taken when using extrapolated values of free-gas diffusivity since there is considerable variation among the expressions available, limiting the accuracy of any calculation involving $\mathcal{D}_{12}$. In the analyses of Chapter 3 and Chapter 4, the extrapolation method of *Wallace and Sagan* (1979) is used to maintain consistency with previous investigators of diffusion on Mars. With different methods, the value of $\mathcal{D}_{12}$ at 250 K and 600 Pa varies between 17.5 and 32.0 $\mathrm{cm^2 s^{-1}}$.

Computation of the Knudsen diffusion coefficient, required for the method described in *Zalc et al.*

(2004), is still more cumbersome. In that work, D_K is written as

$$D_K = \frac{1}{3}\langle l_p \rangle \langle \nu \rangle \left[\frac{\langle l_p^2 \rangle}{2\langle l_p \rangle^2} - \beta \right], \tag{2.16}$$

where ν is the mean molecular velocity ($\nu = \sqrt{8k_BT/\pi m_1}$), $\langle l_p \rangle$ is the first moment of the chord length distribution (*Levitz*, 1993), and β is a series sum of cosine angles between sequential trajectory segments separated by wall collisions. The term outside brackets is the same, within a factor of two, of the simple kinetic expression for the Knudsen diffusion coefficient in straight capillaries defined in equation (2.10). The term in brackets takes into account deviations from exponential path length distributions and Knudsen cosine-law scattering from pore walls, as opposed to random scattering which occurs among gas molecules. Note that in both equations, D_{K} is independent of pressure.

Chords are defined as successive ballistic molecular paths with both ends terminated by a pore wall; they may therefore be smaller or larger than any individual pore. In *Zalc et al.* (2004), the model pore structures used result in nearly exponential chord distributions such that the first term in brackets is near unity. But many real soils may have different distributions and this quantity can vary significantly. *Gille et al.* (2002, 2001) describe a method for determining $\langle l_p \rangle$ from pore diameter distributions determined from mercury porosimetry. The β term, however, depends only on the model selected to describe molecular collisions with pore walls (*Levitz*, 1993). For the frequently used Knudsen cosine law, this gives $\beta = 4/13 = 0.3077$, for porosities up 42% (*Zalc et al.*, 2004) and greater (E. Iglesia, personal communication, 2008), a porosity range which covers all simulants considered in this study except the salt crusts.

The bulk porosity for porous media in these laboratory analyses is determined through a gravimetric method detailed in Section 3.3, and the porosities for various simulants are summarized in Table 3.1. Quantitative measurements of the pore size distribution were made for selected simulant materials at a commercial analytical facility; the analysis results are given in Section 4.3.2.

2.6 Effects Other than Concentration Diffusion

2.6.1 Advection

Mass transfer of a gas results not only from diffusion, which describes the relative motion of gases, but also from advection, where a difference in pressure causes bulk motion of the gas.

The vertical velocity of gas w is given by Darcy's law,

$$w = -\frac{\kappa}{\mu}\frac{\partial p_0}{\partial z}, \tag{2.17}$$

where κ is the intrinsic permeability of the porous medium and μ the dynamic viscosity of the gas.

The total mass flux is the sum of diffusive and advective transport,

$$J_1 = J_{\rm Diff} + J_{\rm Adv} = J_{\rm Diff} + w\rho_1, \tag{2.18}$$

where $J_{\rm Adv} = w\rho_1$.

Most of our experiments take place at a total chamber pressure of ∼600 Pa. At the ice surface, there is a pressure contribution both from the CO_2 in the chamber and the saturation pressure of H_2O. Assuming the pressure difference across the sample equals the saturation vapor pressure, we can set a lower bound on permeability. From equations (2.17), (2.18), and (2.22),

$$J_1 \Delta z = -\rho_0 \frac{\kappa}{\mu} \Delta p_0. \tag{2.19}$$

The viscosity of CO_2 and N_2 at 200 K and 1 bar pressure are 1.00×10^{-5} Pa s and 1.29×10^{-5} Pa s, respectively (*Lide*, 2003). Using measured values of $J_1 \approx 10^{-5}$ kg m^{-2} s^{-1}, $\Delta z = 0.05$ m, and $\rho_0 \approx 0.01$ kg m^{-3} from one of our experiments on 50–80 μm glass beads, the minimum permeability is $\kappa = 3 \times 10^{-12}$ m^2 or 3 darcy. This is similar to permeability values measured for grains tens of microns in size, where $\kappa \sim 10^{-12}$ m^2 (*Freeze and Cheng*, 1979; *deWiest*, 1969).

For sublimation from an impermeable ice layer, the lower boundary condition is $J_2 = 0$. The total mass flux, however, is not zero because the ice is a source of vapor, $J_1 \neq 0$. Mass conservation for species 1 and 2 requires (*Landau and Lifshitz*, 1987)

$$J_1 = -\mathcal{D}_{12}\rho_0 \frac{\partial}{\partial z}\frac{\rho_1}{\rho_0} + w\rho_1 \tag{2.20}$$

$$J_2 = -\mathcal{D}_{12}\rho_0 \frac{\partial}{\partial z}\frac{\rho_2}{\rho_0} + w\rho_2 = 0. \tag{2.21}$$

The ratio of advective to diffusive flux can be obtained by dividing the second term of the first equation by the first term. Solving the second equation for w and substituting, we obtain

$$\frac{J_{\rm Adv}}{J_{\rm Diff}} = \frac{c(z)}{1 - c(z)}. \tag{2.22}$$

The mass concentration of H_2O is denoted by $c = \rho_1/\rho_0$. The total flux is given by

$$J_1 = -\mathcal{D}_{12}\rho_0 \frac{1}{1-c}\frac{\partial c}{\partial z}. \tag{2.23}$$

When the CO_2 column is at rest and H_2O vapor moves outward, the gas mixture as a whole effectively moves outward, and there must always be a pressure difference Δp_0 across the sample that drives this advective flow. On the other hand, the pressure difference can never exceed the saturation vapor pressure over ice. The factor of $1/(1-c)$ is an approximate estimate of the error

due to advective flux being counted as diffusive.

The saturated vapor pressure over ice at 260 K is 195.8 Pa. In 600 Pa of CO_2, this gives a large advective correction factor, $1/(1-c)$, of 1.32. However, at the upper sample surface the partial pressure of water is significantly lower and the correction factor here is found to be 1.01–1.07 in our experiments. The error thus introduced by the average value of c is on the order of 10%. It will be shown that this error is of the same order as the systematic scatter in our experimental determinations of D.

For small c, the advective contribution disappears, $J_1 = J_{\mathrm{Diff}}$, and the pressure difference also becomes negligible. The concentration of water vapor is limited when saturation vapor pressures are low. A practical compromise is reached for experiments between low temperature conditions with small advection contributions and higher temperature conditions which allow faster experimental runs.

On Mars, pressure differences, and therefore advection, can result from winds or thermal expansion. A temperature increase by 30% leads to a thermal expansion by 30% over a thermal skin depth, which is on the order of 1 m for the annual cycle and 3 cm for the diurnal cycle. The expansion thus corresponds to an airflow of 30 cm per year for the annual cycle and 1 cm per sol diurnally. The velocity of water vapor due to concentration differences is estimated as the diffusion coefficient divided by depth such that for $D = 10$ cm^2 s^{-1} and a burial depth of 100 cm, the diffusive flux is 0.01 cm s^{-1} or 9 m per sol, many orders of magnitude faster than thermal expansion.

2.6.2 Thermodiffusion

In a system without concentration gradients, vapor still diffuses due to differences in temperature (*Grew and Ibbs*, 1952). This is known as "thermal diffusion" or "thermodiffusion". The inverse effect, where the diffusion of one gas in another results in the establishment of a transient temperature gradient is known as the "diffusion thermoeffect". The liquid analog to gaseous thermodiffusion is known as the "Soret effect" (*Grew and Ibbs*, 1952). *Chapman and Cowling* (1970) provide a first-order expression for the thermodiffusion ratio $k_T = \mathcal{D}_{\mathrm{T}}/\mathcal{D}_{12}$:

$$k_T = \frac{\mathcal{D}_T}{\mathcal{D}_{12}} = 5(C-1)\frac{s_1\frac{n_1}{n_1+n_2} - s_2\frac{n_2}{n_1+n_2}}{Q_1\frac{n_1}{n_2} + Q_2\frac{n_2}{n_1} + Q_{12}}, \tag{2.24}$$

where

$$\begin{aligned} s_1 &= m_1^2 E_1 - 3m_2(m_2-m_1) + 4m_1m_2A \\ Q_1 &= \frac{m_1}{m_1+m_2}E_1\left[6m_2^2 + (5-4B)m_1^2 + 8m_1m_2A\right] \\ Q_{12} &= 3(m_1^2-m_2^2) + 4m_1m_2A(11-4B) + 2m_1m_2E_1E_2. \end{aligned}$$

Analogous expressions hold for s_2 and Q_2, with interchanged indices. The thermodiffusion coefficient can be positive or negative and vanishes for low concentrations. The parameters A, B, C, E_1, and E_2 depend on the intermolecular forces. For a model of rigid elastic spherical molecules, $A = 2/5$, $B = 3/5$, $C = 6/5$, and $E_1 = (2/5m_1)\sqrt{2/m_2}(m_1 + m_2)^{3/2}\sigma_{11}^2/\sigma_{12}^2$. In the elastic hard sphere model, k_T is independent of temperature and pressure, but it does depend on the proportions of the mixture n_1/n_2 (*Chapman and Cowling*, 1970).

It is conventional to introduce the thermal diffusion factor $\alpha_T = k_T n_0^2/(n_1 n_2)$, which no longer vanishes for low concentrations. Using the formulae above, this factor is at most $\alpha_T \approx 0.8$ for H_2O–CO_2. For H_2O–N_2, the maximum α_T is less than 0.4. The theoretical value of the thermodiffusion ratio is thought to be larger for elastic spheres than for other models of intermolecular forces (*Chapman and Cowling*, 1970). From equation (2.1), we see that thermodiffusion is reduced relative to concentration diffusion by a factor $k_T(\Delta T/T)/\Delta(\rho_1/\rho_0)$. Assuming $n_1 \ll n_2$ and $\Delta n_2/n_2 \ll \Delta n_1/n_1$, this factor is approximately $\alpha_T(m_2/m_1)(\Delta T/T)p_1/\Delta p_1$.

For a typical experiment involving ice loss (Chapters 3 and 4) $\Delta T/T \lesssim 0.01$ and $\Delta p_1/p_1 \approx 0.5$, and thermodiffusion is smaller than concentration diffusion by a factor of $0.4 \times 0.01 \times 0.5 \times 44/18 = 0.005$ or less and is therefore negligible. On Mars, a diurnal temperature amplitude of 30 K around a mean temperature of 210 K has $\Delta T/T \sim 0.14$. It is conceivable that thermodiffusion contributes noticeably to vapor transport on Mars, but concentration diffusion still dominates.

2.6.3 Barodiffusion

"Pressure diffusion" or "barodiffusion" is the relative diffusion of molecular species due to gradients in total pressure. *Landau and Lifshitz* (1987) and *Cunningham and Williams* (1980) provide an expression for the barodiffusion coefficient in a mixture of two ideal gases:

$$k_p = \frac{\mathcal{D}_p}{\mathcal{D}_{12}} = (m_2 - m_1)c(1-c)\left(\frac{1-c}{m_2} + \frac{c}{m_1}\right). \tag{2.25}$$

In a single fluid there is no barodiffusion phenomenon and the coefficient vanishes. For a mixture, the coefficient can be positive or negative, though heavier molecules tend to go to regions of higher pressure. According to equation (2.1), barodiffusion is smaller than concentration diffusion by a factor of $k_p(\Delta p_0/p_0)/\Delta c$. If we assume that $\Delta c \approx c \ll 1$ and use equation (2.25), this factor is about $0.4\Delta p_0/p_0$ in an N_2 atmosphere and $0.6\Delta p_0/p_0$ in a CO_2 atmosphere. Barodiffusion is negligible when $\Delta p_0/p_0 \ll 1$.

Sublimative ice loss experiments in Chapters 3 and 4 take place at a total chamber pressure of ∼600 Pa. At the ice surface, there is a pressure contribution both from the CO_2 in the chamber and the saturation pressure of H_2O, which is at most ∼200 Pa at 260 K. Assuming the pressure difference across the sample equals the saturation vapor pressure, $p_0 = 800$ Pa. This overly pessimistic pressure

difference leads to a barodiffusion contribution of less than 15% of the size of the concentration diffusion.

None of the coefficients $\mathcal{D}_{12}$, $\mathcal{D}_T$, or $\mathcal{D}_p$ depend on gravity, nor does the advective contribution. The potential energy $m_1 g \Delta z$ required to move molecules through the diffusive barrier, or through meters of regolith, is negligible compared with their kinetic energy $(3/2)k_B T$.

Adsorption can significantly effect the transport of water in a non-steady-state environment by attenuating local vapor density gradients and acting as either a source or a sink for water vapor. Adsorption effects will be further discussed in Section 3.6.1 where it will be shown that they are not important on the time scales considered.

2.7 Diffusive Ice Growth

Conservation of mass leads to an expression for the accumulation of ice in pore spaces as a function of time:

$$\frac{\partial \sigma}{\partial t} = -\frac{\partial J_1}{\partial z} = \frac{\partial}{\partial z}\left(D\frac{\partial \rho_1}{\partial z}\right), \tag{2.26}$$

where σ is the density of ice relative to total volume. Hence, ice accumulates in a permeable medium as a humidity gradient supplies water molecules. The presence of ice changes the thermal properties of the regolith by increasing the thermal conductivity of an unconsolidated porous medium. But the formation of subsurface ice is also expected to reduce the diffusivity, and hence the rate of infilling, due to constriction of the pore space. As the pore space is reduced, a regolith with an initially large pore diameter will transition from Fickian diffusion, where molecule-molecule collisions dominate, to Knudsen diffusion wherein most collisions are between molecules and the pore walls. It has been suggested (*Mellon and Jakosky*, 1995) that ice deposited from the vapor phase may completely choke off vapor transport paths. Since subsurface ice has been shown to grow most rapidly near its equilibrium depth (*Mellon and Jakosky*, 1995; *Schorghofer and Aharonson*, 2005), choking would occur first at this level and inhibit diffusion to greater depths. Further discussion of the constriction phenomenon is found in Chapter 5.

Chapter 3

Ice Loss Experiments

3.1 Chapter Summary

This chapter describes a set of experiments to measure diffusion coefficients, D, in unconsolidated porous materials at Mars-like conditions. The materials chosen are simple proxies for real Mars soils, of which no samples or small-scale data currently exist. The experiments were designed to closely reproduce the conditions under which sublimative ice loss to a relatively dry atmosphere occurs on Mars. Thus, solid ice acted as the source for the diffusing species, gaseous H_2O. The diffusion host gas was CO_2 at ∼600 Pa pressure and the whole environment was maintained below the freezing point of water.

Four materials were used to simulate the martian regolith with varying degrees of fidelity or with a particular focus. Despite the differences between these simulants, the range of diffusion coefficients measured (including micron-sized dust) fell between approximately 2.8–5.4 $cm^2\ s^{-1}$, though for mechanically packed dust lower values of $0.38 \pm 0.26\ cm^2\ s^{-1}$ were observed.

The survival of shallow subsurface ice on Mars and the providence of diffusion barriers are considered in light of these measurements.

3.2 Experimental

The experiments were conducted at the Mars Simulation and Ice Laboratory at Caltech. Custom built stainless-steel vacuum chambers contained within walk-in freezers were used to achieve Mars-like conditions of temperature, pressure, and low humidity.

These experiments simulate the evolution of near-surface ice on present-day Mars inasmuch as the atmosphere is very dry with a frost point well below the temperature of the ice. Thus the ice is driven to sublimate into the atmosphere resulting in a loss of mass of the regolith-ice-container system. Although the conditions may not replicate any particular location on Mars (being too warm, in general, for regions expected to possess subsurface ice today) they do emulate the geometry and

fundamentally important physics for the investigation of vapor diffusion.

The source of water vapor in these diffusion experiments is a block of ice made from purified water. The ice is frozen in the presence of both a heat source to retard surface freezing and a bubbler to provide mechanical agitation. This procedure allows most gases exsolved upon freezing to escape through the top surface, resulting in a cylinder of largely bubble-free ice.

Ice samples are cut from the cylinder in 1-cm-thick slices and frozen with a small amount of additional water into plastic caddies ∼7 cm in diameter. The caddy heights, being 2, 3, 6, and 11 cm, permit sample thicknesses over the ice of 1, 2, 5, and 10 cm, respectively. See Figure 3.2 a) for an example of a 2 cm caddy with ice and thermocouple in place.

3.2.1 Chamber setup

A custom built stainless-steel vacuum chamber from LACO Technologies was used to perform these ice-loss experiments. In basic design the chamber is a vertical cylinder with a removable lid, silicone O-ring seals, and multiple electrical and fluid feedthroughs. A schematic of the chamber with sample and measurement apparatus is shown in Figure 3.1. The volume of the chamber is 2.3×10^{-2} m^3.

During an experiment, an Alcatel rotary vacuum pump continuously evacuates the chamber at an effective pumping speed of 0.34 m^3 hr^{-1}. The pressure is monitored with a Baratron capacitance manometer with a full-scale range of 10 torr. Evacuation is compensated by input of dry CO_2 regulated with an MKS PDR 2000 gauge controller connected to either 1) a normally-open solenoid valve (earlier experiments) or 2) an active PID closed-loop control using an STEC-4400 mass flow controller (MFC). The setpoint of the MFC is controlled via an output channel on a USB-1408FS datalogger from Measurement Computing Corporation. The PID algorithm and datalogger are run through the LabView development environment. The total pressure is maintained at ∼600 Pa in the case of the solenoid valve control, and at a more uniform 586 ± 0.1 Pa in the case of the MFC. The continuous replacement of chamber gas in either case results in a very dry atmosphere above the samples (see Figure 3.2 b).

Decompression of the dry CO_2 from its holding cylinder and passage through gas loops in the freezers produces a stable chamber air temperature approximately equal to the ambient freezer temperature. The walk-in freezers are on a 12-hour defrost cycle which results in twice-daily temperature spikes of approximately 0.5 K. These perturbations to the environment decayed in about 60 minutes prior to a compressor upgrade in April of 2007. Following the upgrade, the perturbations were much smaller and lasted less than 30 minutes. Fiberglass and Styrofoam insulation around the chamber minimizes these fluctuations.

Water content in the chamber atmosphere is monitored using capacitive relative humidity (RH) chips from Honeywell (HIH-3602-C). These integrated-circuit sensors contain both an RH proportional voltage output and a 1000 ohm platinum resistance temperature device (RTD) which is

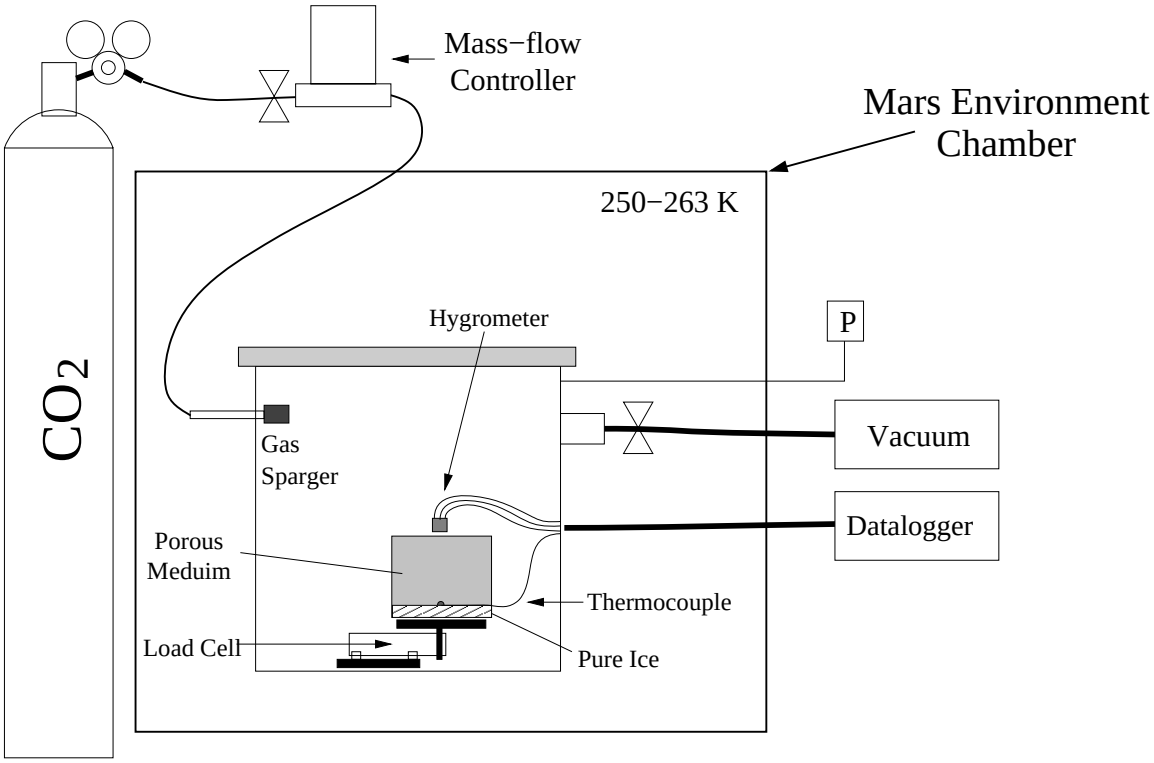

Figure 3.1: Schematic of the diffusive ice-loss experimental setup. The main environmental chamber is housed within a walk-in freezer with temperatures of 250–263 K. The CO_2 atmosphere is constantly exchanged and maintained at 600 Pa total pressure. Gas entering the chamber is passed through a diffusing sparger to minimize directed air currents. Temperature, humidity, mass, and pressure data are recorded by a datalogger which resides outside the cold room.

measured in a 3-wire half-bridge configuration. The RH chips are reported by the manufacturer to be accurate down to temperatures of 233 K and 0% relative humidity. The combined RH and temperature measurements allow the partial pressure of water at the sensors to be calculated. The sensors are positioned at the center of the sample tops within 1 cm of the surface (see Figure 3.2 c).

Sample mass is continuously monitored with Omega Engineering LCEB-5 strain gauge load cells (maximum capacity 5 lbs) in a wheatstone bridge configuration with an excitation of 5 V and an output of 2.0 mV/V. This instrument has a noise level of 0.2% of reading and a 0.03% full scale linearity. Mass-loss rates are calculated by monitoring the sample mass and drawing a linear regression through the values obtained over many hours.

The data from an experiment are recorded with a Campbell Scientific CR1000 data logger and saved to computer via the LoggerNet software package. The system is able to run two simultaneous experiments in a single vacuum chamber with identical ambient conditions by using dual load cells, thermocouples, and RH/RTD chips.

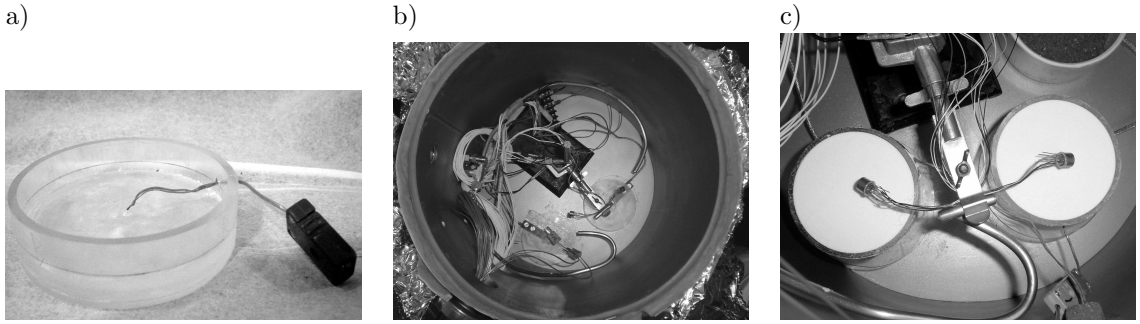

Figure 3.2: a) Closeup of thermocouple positioning in a caddy designed to accommodate 1 cm of ice and a 1 cm sample. The caddies are ∼7 cm in diameter. b) Down-looking view into the vacuum chamber (30 cm diameter) showing two load cells, gas and electrical feedthroughs, and RH/RTD chips attached to a ring-stand for positioning. c) A closeup of two glass bead samples in place with RH/RTD chips positioned 1 cm above sample surfaces

3.2.2 Experimental method

The mass of the ice-free caddy plus its thermocouple wire and connector is measured with a precision balance. After the 1 cm bubble-free ice disks are frozen into place, the combined system is weighed again. The total mass of ice and thereby its volume and thickness in the caddy can be determined. The media are poured into the caddies from their holding containers and planed off with a straight edge to match the height of the caddy. Most samples are not actively compressed, but may be subject to self-compaction. In most cases where self-compaction occurs, the sample surfaces remain within 1 mm of the caddy top. Some samples with very high dust fractions exhibit some settling as the container is moved from the preparation station to the vacuum chamber. This is at most 12% of the 5 cm sample depth. The reduced thickness is measured and included in subsequent calculations; additional material is not added.

The total mass of the entire sample assembly is measured, giving the total mass of simulant. The sample assembly is connected to the thermocouple feedthrough, placed on the load cell within the chamber, and the RH/RTD sensor is positioned above the sample. The chamber is sealed and pumped down to 600 Pa at a rate of ∼100 Pa per second. This slow pump-down prevents disturbance of the sample as any interstitial gases escape.

All steps described above are performed in a walk-in freezer at 263 K. The relative humidity of the freezer interior is quite high, usually around 80%, but the absolute humidity is low. Surface-melting, capillarity, and their effects on the initially dry simulant are thus minimized. Exposure of the samples to freezer air for the brief period between the storage vessel and the start of an experiment does not allow significant amounts of water to adsorb or freeze onto the simulant (as confirmed by water content measurements). Any minor amounts of water which adsorbs onto the sample is rapidly removed once introduced to the sublimation environment of the experiments.

Once the samples are in place and the chamber has reached Mars pressures, the experiment is

left to run for at least 12 hours. Transients due to adsorption of water in the sample or temperature disequilibrium decay after approximately two hours. The faster the mass-loss rate from the sample, the less time needed to obtain a sufficient number of points to ensure linearity and draw a regression line. For samples with a high impedance to gas flow, or for experiments run at lower temperatures, up to three days may be needed to achieve a high degree of confidence in the measurements.

Following the completion of an experimental run, the chamber is slowly purged to room-pressure; the slow back-fill prevents air currents from disturbing the sample. The sample material is dumped into a metal or glass vessel which is immediately weighed, then placed into an oven at 383 K. After 24 to 48 hours the sample is completely dry with respect to non-structural water and is weighed again. The sample is now dry and may be recycled for future experiments. Clumping of some materials containing smaller particles occasionally requires mechanical sieving to break up the aggregates.

Consolidated media such as glass fritted disks (described below) are epoxied in place inside glass rings with the same diameter as the ice caddies. During an experiment, these are placed over a 1 cm deep ice-filled caddy and secured in place with water-resistant vacuum grease. Following an experiment, the ice surface is examined to determine if any leaks occurred between the ice caddies and the glass rings. The low-pressure, low-temperature environment gives rise to distinct ice surface morphologies if the vapor escapes in a rapid or asymmetric way. Any experiments showing such leaks are discarded.

3.2.3 Measured quantities

All data for calculating diffusion coefficients is taken from the stable interval following initial transients. Additional small perturbations in temperature due to defrost cycling of the freezer compressor have no apparent effect on the mass loss curve and have a very small contribution to the average temperature value calculated for a 12+ hour experiment.

The mass loss rate is derived from a least-squares fit to the post-transient mass data versus time (see Figure 3.3). The temperature of the load cell fluctuates less than 1 K; there is no sensible temperature effect on the values reported. Residuals to the linear fit of mass loss are less than 1% in all experiments. Given the area of the sample surface (39.8 cm^2) and the density of ice, retreat rates in mm hr^{-1} and total H_2O flux are calculated.

A T-type thermocouple wire passes through the wall of each caddy 1 cm from the bottom and extends to the center of the cylinder. This wire is positioned on the surface of the ice disk and frozen into place, allowing the tip to remain in contact with the ice during the first 2–4 mm of retreat. See Figure 3.2 a) for a close-up of thermocouple positioning. The wire is 36-gauge and has a negligible spring force to affect the load-cell reading. It is assumed that the vapor at the surface of the ice is saturated with respect to water vapor. The temperature thus measured gives the saturation vapor pressure at the surface of the ice via the ITS-90 formulation for vapor pressure

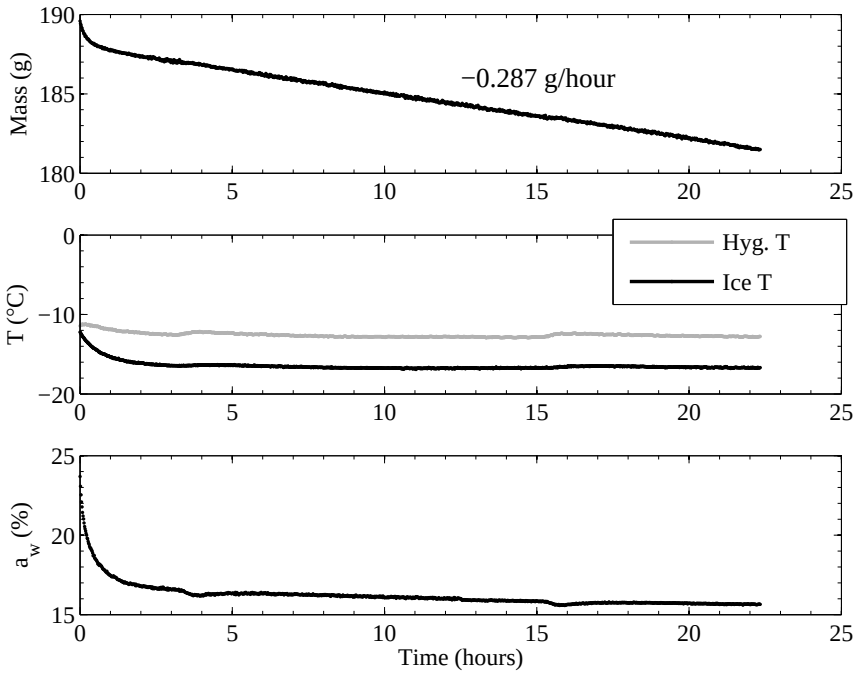

Figure 3.3: Data for a single sample: February 17, 2006. Conditions: 40 μm glass beads, 2 cm thick, T $\approx$ 263 K. The mass loss rate displayed in the top axis is determined from a linear regression to post-transient data.

(*Hardy*, 1998). Figure 3.3 shows ice surface temperature as a function of time for one experiment.

The RH/RTD sensors simultaneously report water activity, a_w, and ambient temperature at the sensor. Figure 3.2 c) shows examples of placement and Figure 3.3 shows the data as reported. Capacitive sensors such as the HIH-3602 are responsive to water activity rather than to relative humidity (*Anderson*, 1995; *Koop*, 2002). The difference is that water activity is the ratio of vapor content of the atmosphere p_1 to the saturation vapor pressure over liquid water, $p_{\rm sv}^{\rm liq}$, rather than over ice:

$$a_w = p_1/p_{\rm sv}^{\rm liq}. \tag{3.1}$$

Thus the true relative humidity is given by:

$$RH = p_1/p_{\rm sv}^{\rm ice} = a_w p_{\rm sv}^{\rm liq}/p_{\rm sv}^{\rm ice}. \tag{3.2}$$

The equation for $p_{\rm sv}^{\rm liq}$ is determined from data on supercooled water taken from *Hare and Sorensen* (1987). The ITS-90 formulation is used for $p_{\rm sv}^{\rm ice}$ to determine RH, and then used again to convert the relative humidity calculated above the sample into a partial pressure of water via the ideal gas law.

3.3 Materials

The martian regolith is a complex substance. Early lander-based measurements of elemental composition show close similarity among widely spaced sites (*Arvidson et al.*, 1989). Despite discoveries by both Viking and the MER mission that reveal significant chemical and physical differences among the non-rocky components of the surface (*Moore et al.*, 1979), they are very similar in absolute terms over planetary-scale distances. Various investigators have used the JSC Mars–1 palagonite ash from Mauna Kea to simulate Mars regolith in a variety of experiments (*Gilmore et al.*, 2004; *Cooper and Mustard*, 2002; *Gross et al.*, 2001). Martian soils no doubt come in a variety of grain size distributions, grain shapes, porosities, compositions, and degrees of compaction and cementation. With respect to the demonstrably heterogeneous Martian regolith, the Mars–1 soil is not assumed to match a particular locality on Mars, but rather is a complex, natural soil material which may represent a general class of Mars regolith. A thorough description of JSC Mars–1 can be found in *Allen et al.* (1997, 1998).

JSC Mars–1 contains a variety of minerals which exhibit different patterns of fracture, cleavage, and surficial chemical structure making this a very complex regolith simulant. The JSC Mars–1 simulant can be easily characterized, but the parameter space to be explored is vast. Working with fine-grained granular media presents many challenges, particularly with regards to repeatability. To eliminate some of the complexities involved in studying a chemically and physically heterogeneous disaggregated mineral assemblage, some simpler and more easily handled proxies for porous regolith materials are used.

50–80 μm beads: An easily characterized and handled material used frequently in these experiments. Obtained from AGSCO Corporation, this material is composed of spherical soda lime glass (specific gravity: 2.50) beads with a narrow particle size distribution.

"Coarse" Frits: The only consolidated media used in this study, these are disks composed of sintered borosilicate glass beads (specific gravity: 2.53). These porous filter disks were obtained from ChemGlass Inc., whose catalog states that the nominal pore size for the "coarse" category of frits are between 50 and 80 μm.

1–3 μm dust: These smaller particles act as a proxy for Mars airborne dust. Obtained from Powder Technology, Inc., under the trade name "Arizona Test Dust", this is a natural silicate mineral with a specific gravity of 2.65. It exhibits a narrow particle size range of equant yet angular particles.

JSC Mars–1: Weathered palagonitic ash from Pu'u Nene cinder cone, Hawai'i. This natural basaltic mineral assemblage has a wide particle size distribution from 1 mm down to < 1 μm,

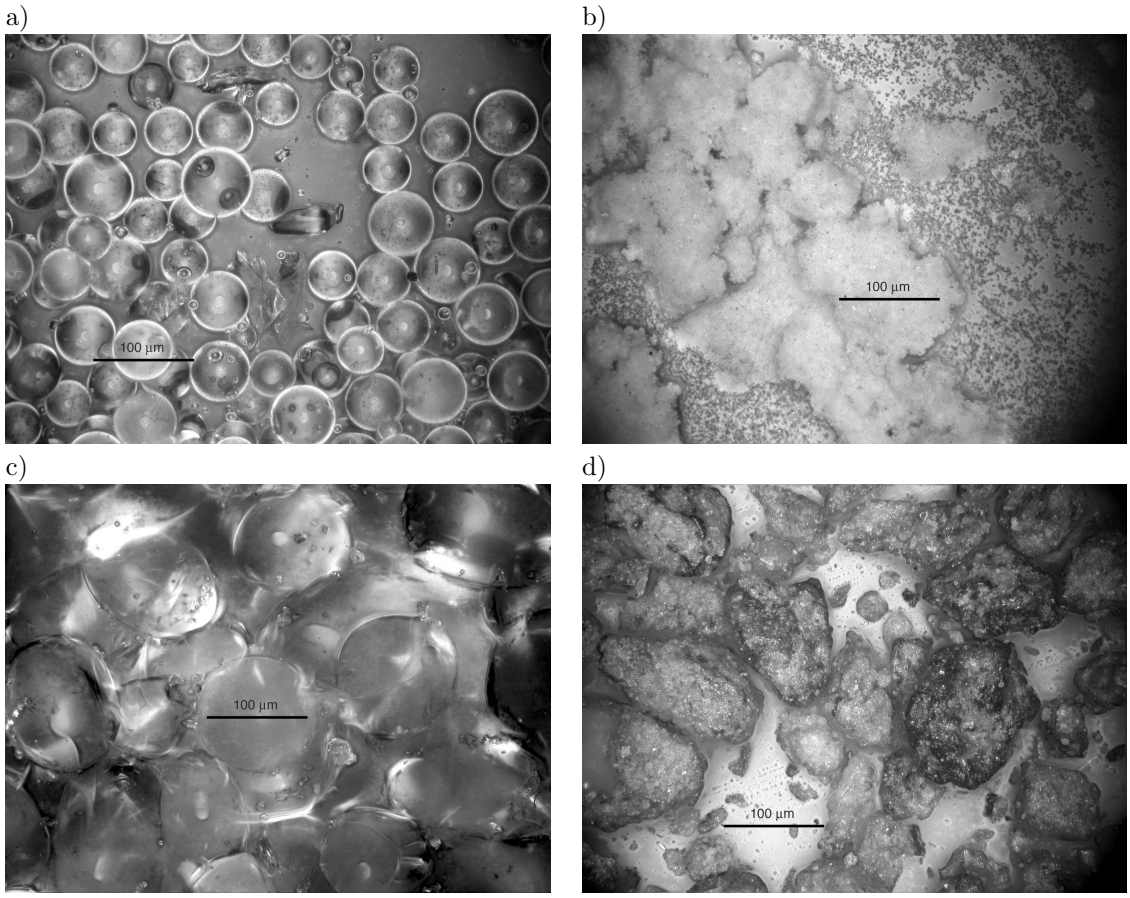

Figure 3.4: Optical micrographs of regolith simulants: a) 50–80 μm beads, b) 1–3 μm Arizona Test Dust (note the presence of aggregates), c) "Coarse" fritted disks, pore size 50–80 μm, and d) raw JSC Mars–1

and a complex overall mineralogy. The washed and sifted supply of this simulant was obtained through the Johnson Space Center Curator.

Wind-blown sand particles on Mars were proxied by the glass beads, whose size range is similar to that observed in Mars wind-tunnel experiments and at MER landing sites (see Section 3.3.1). The Arizona Test Dust approximates size characteristics of dust on Mars. The porous frits were chosen to illustrate experimental repeatability given a medium with an unchanging geometry. JSC Mars–1 was selected because it has been frequently used in other investigations of Mars analogue materials.

See Figure 3.4 for optical micrographs of these simulants at the same scale. Prior to use, all samples are dried in an oven at 383 K and then stored in air-tight containers.

Geometric porosities of the separate materials were determined by weighing a known volume of bulk sample to determine a bulk density, ρ_{bulk}, and ratioing this against the known specific gravity of the individual particles ($\phi = 1 - \rho_{\mathrm{bulk}}/\rho_{\mathrm{true}}$). The results are given in Table 3.1.

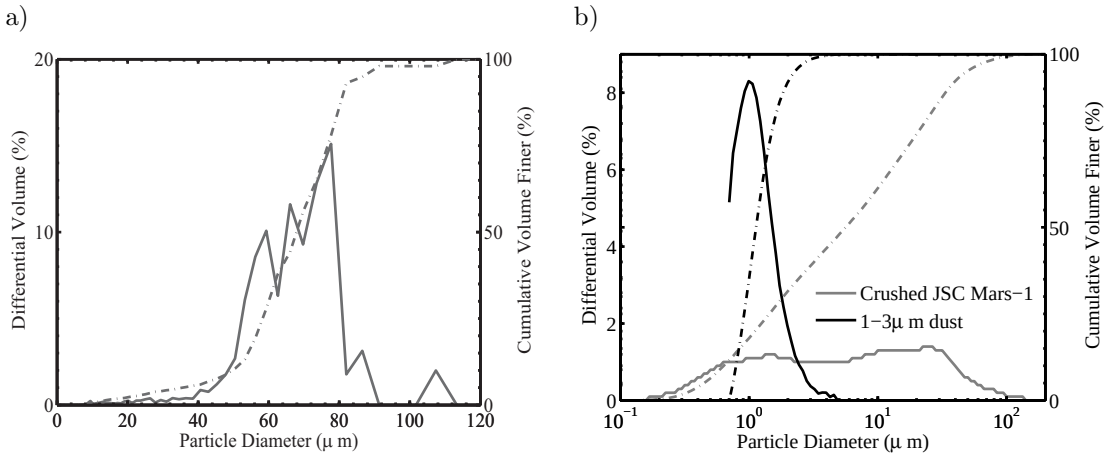

Figure 3.5: Particle-size histogram (solid) and cumulative finer (dash-dot) plots for a) 50–80 μm glass beads and b) crushed JSC Mars-1 and 1–3 μm dust

3.3.1 Glass beads

The spherical beads of soda lime glass exhibit a narrow particle size distribution between 50 and 80 microns, equivalent to the sedimentological category of "fine sand". As seen in the optical micrograph image in Figure 3.4a, the bead particles are all nearly perfect spheres. The sample was analyzed by Particle Sizing Systems using a model 780 AccuSizer with light obscuration and light scattering techniques. Ninety percent of the particles are larger than 48 μm and only 10% are larger than 80 μm. The volume-weighted mean particle size is 64.4 μm, with a median of 66.1 μm and a mode of 77.7 μm, reflecting a slight skew towards the larger diameters. The results of the analysis are shown graphically in Figure 3.5 a). At least 70% of the beads fall within the size range given, with no more than 10% being larger, no more than 20% being smaller, and no more than 3% being broken or angular in shape.

Within a factor of two in friction threshold velocity, these are similar to the 100 μm size of the most easily lofted particles under martian conditions (*Greeley et al.*, 1980). Terrestrial analogs and wind-tunnel experiments suggest that suspended dust is usually not incorporated into sand dunes, and Spirit Microscopic Imager pictures indicate that sand sheets in Gusev crater are largely composed of fine to medium sand-sized particles.

Pore sizes may be estimated from particle size. Between three coplanar spherical particles of

Simulant	ϕ, %	ρ_{bulk}, g cm^{-3}	ρ_{true}, g cm^{-3}
50–80 μm Glass Beads	42±1.0	1.46±0.5	2.50
Crushed JSC Mars-1	64±1.0	1.09±0.5	3.07
Loose 1–3 μm dust	86±0.2	0.25±0.03	2.65
Packed 1–3 μm dust	75±0.8	0.66±0.03	2.65

Table 3.1: Porosities, true densities, and bulk densities for simulant materials

the same radius, the theoretical minimum pore size is $r_{\min} = r_{\text{particles}}(3\sqrt{3}/4 - 1)$. The largest dimension between kissing points in a cubic packing of spheres is the diameter d. Between such wide openings the pore space constricts to only $d(\sqrt{2} - 1)$ when passing between one cubic unit cell to the next. Thus for a mixture of beads with 50–80 μm close-packed particles, the minimum pore size is 11.96 μm and the maximum is 80 μm. With a mean free path of $\sim$12 μm under experimental conditions, this gives a ratio of r/λ_1 from 1.0 to > 2.4, well within the transition regime between Fickian and Knudsen diffusion. Nevertheless, close-packing of spheres may not obtain throughout the sample and larger irregular pores are likely. Given the tendency for the majority of diffusive flux to be accommodated in the largest pores (*Clifford and Hillel*, 1983), it may be expected that diffusion will be dominated by Fickian processes, but that Knudsen interactions with the pore walls will also play a role.

3.3.2 Crushed JSC Mars-1 dust

JSC Mars-1 is a weathered palagonitic ash from the Pu'u Nene cinder cone on Mauna Kea, Hawai'i and has been used in a variety of Mars surface simulation experiments beyond its originally intended use as a spectral analog (*Gilmore et al.*, 2004; *Cooper and Mustard*, 2002; *Gross et al.*, 2001). The raw JSC Mars-1 was obtained through the Johnson Space Center Curator. A thorough description of JSC Mars–1 can be found in *Allen et al.* (1997, 1998).

Raw JSC Mars-1 particles were crushed to smaller sizes in a planetary ball mill. Batches of 250 mL of oven-dried raw material were run with 50 hardened steel milling balls at 590 RPM for two 10 minute cycles. The resulting particle size distribution was analyzed by Micromeritics Instrument Corporation on a Saturn DigiSizer 5200 using the laser light scattering technique. Particles were dispersed in a 0.3% Daxad 23 / 40% sucrose / water solution in an ultrasonic bath for 1–2 min. The measured median particle size is 5.46 μm. The whole distribution is bimodal with peaks at 1.5 and 25.2 μm; nearly 70% of the volume is larger than 2 μm. The volume percent and cumulative finer distributions for this simulant are shown as grey lines in Figure 3.5 b).

An average specific gravity of 1.91 for raw JSC Mars–1 as given by *Allen et al.* (1998) was quoted in *Hudson et al.* (2007). Recent analysis of the crushed sample with He gas-displacement in an AccuPyc 1330 Pycnometer at Micromeritics Instrument Corporation yielded an average particle density of 3.07 g cm^{-1}. This value is used in subsequent calculations in this paper.

3.3.3 1–3 micron dust

A fine dust with a very narrow particle size distribution, called "Arizona Test Dust" was obtained from Powder Technology Inc. The dust consists of a natural silicate material with a specific gravity of 2.65. The dust is composed of equant yet angular particles which easily form weak mm- to cm-

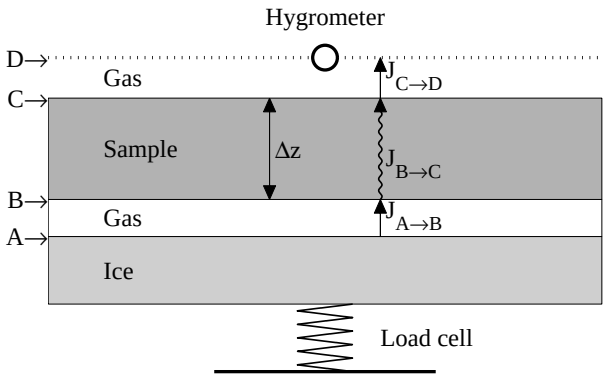

Figure 3.6: Generalized schematic of experimental setup showing gas gaps separating both the ice surface and hygrometer (RTD/RH chip) from the sample. By continuity, the vapor flux through the sample is the same as that through the gaps.

sized aggregates. Sieving breaks up these aggregates, but they easily reform under agitation or self compaction. Loose, aggregated dust alone has a calculated geometric porosity of $88 \pm 1\%$, while compressional packing results in a reduced porosity of $76 \pm 2\%$.

The particle size data for this sample, measured on a Coulter Multisizer, were provided by the manufacturer. The mean particle size is 1.19 ± 0.49 μm. The median is 1.132 μm, with less than 1.5 % of the volume in particles larger than 3 μm. The volume percent and cumulative finer distributions for this simulant are shown as black lines in Figure 3.5 b).

3.4 Analysis

This section details the procedure for reducing data from each experiment into diffusion coefficients. Figure 3.6 is a schematic drawing of the experimental setup with different levels in the sample column labeled A through D. Although unconsolidated samples always rest directly on the ice, the schematic is generalized to allow for a gap between positions A and B. A formalism to determine a correction term to account for gas gaps, sublimation effects, and true sample thickness is described below. An analysis method for the diffusion regime and pressure dependence of the diffusion coefficient is also presented.

3.4.1 Determining the diffusion coefficient

Equation (2.4) is valid in the limit where the mass concentration of H_2O, c, and therefore advection, is small, and it is used to extract the diffusion coefficient from measurements above (position "D" in Figure 3.6) and below (position "A" in Figure 3.6) the soil sample:

$$J_1 = D' \frac{\rho_{1\mathrm{A}} - \rho_{1\mathrm{D}}}{\Delta z}, \tag{3.3}$$

where D' is the "raw" diffusion coefficient. The vapor density above the sample $\rho_{1\mathrm{D}}$ is determined from measurements of temperature and humidity in the air which gives a partial pressure of water vapor $p_{1\mathrm{D}}$, and thereby $\rho_{1\mathrm{D}} = p_{1\mathrm{D}} M_1 / RT_{\mathrm{D}}$. Vapor density at the ice surface is calculated from the saturation vapor pressure determined from the measured ice temperature, $\rho_{1\mathrm{A}} = p_{sv}^{\mathrm{ice}} M_1 / RT_{\mathrm{A}}$.

3.4.2 Correcting the diffusion coefficient

When vapor is not diffusing through a porous medium it may still encounter resistance. To undergo gas-phase transport, H_2O molecules must first sublime from the ice surface into vapor. This vapor must then diffuse through a boundary layer and any intervening gas between the ice and sample surfaces. After passing through the sample, this vapor must pass from the sample surface to the hygrometer. These gas layers may not be well mixed, resulting in an underestimated diffusion coefficient. Additionally, the measured thickness of the samples is only from B to C, not from A to D. The diffusion coefficient defined in equation (3.3) is therefore referred to as the raw diffusion coefficient. A correction to the raw diffusion coefficient for the effects of sample thickness, sublimation effects, and gas gaps may be performed given sufficient data.

By conservation of mass, the flux of vapor is the same through all three barriers $J_{\mathrm{A}\to\mathrm{B}} = J_{\mathrm{B}\to\mathrm{C}} = J_{\mathrm{C}\to\mathrm{D}} \equiv J_1$ (see Figure 3.6). Assuming that the fluxes between A and B and between C and D are still proportional to the density gradient, $J_1 = J_{\mathrm{A}\to\mathrm{B}}$ can be used to determine $\rho_{1\mathrm{B}}$ and $J_1 = J_{\mathrm{C}\to\mathrm{D}}$ can be used to determine $\rho_{1\mathrm{C}}$, while $\rho_{1\mathrm{A}}$ and $\rho_{1\mathrm{D}}$ are measured. Substituting these into an expression analogous to equation (3.3) and simplifying, the resulting corrected expression for the diffusion coefficient in the sample is

$$J_1 = D\frac{\rho_{1\mathrm{B}} - \rho_{1\mathrm{C}}}{\Delta z} = D\frac{\rho_{1\mathrm{A}} - \rho_{1\mathrm{D}}}{\Delta z + z_{\mathrm{corr}}}. \tag{3.4}$$

The quantity z_{corr} has units of length and accounts for effects other than diffusion through the porous medium including gas-gas diffusion in gaps above and below the sample and any sublimation limitation.

The correction term z_{corr} can be determined if several measurements of identical samples with different thicknesses are available. By recasting the corrected expression, equation (3.4), as linear in terms of sample thickness, Δz,

$$\frac{\Delta\rho_1}{J_1} = -\frac{\Delta z}{D} - \frac{z_{\mathrm{corr}}}{D}, \tag{3.5}$$

a linear fit can be performed and the constants z_{corr}/D and $1/D$ determined by the intercept and slope, respectively. The same correction term should apply to all experiments with the same temperature, pressure, and sample type. The term z_{corr} may now be used with the right-hand-side of equation (3.4) to solve for corrected individual values of D. Since the total vapor density gradient

is smaller for thinner samples, the relative contribution of the gas gap is larger and the necessary correction $1/(\Delta z + z_{\mathrm{corr}})$ will likewise be larger. At some thickness, the ratio of gas layer resistance to porous medium resistance will be comparable to the systematic errors in the experimental method. For example, it was found that for glass beads, the effect of the correction term became negligible for samples greater than either 2 or 5 cm thick.

3.4.3 Diffusion regime

At intermediate pressures when both collisions with other molecules and with the pore walls are important, the diffusion is said to be in transition between the Fickian and Knudsen regimes. The Bosanquet interpolation derived in equation (2.15) says that the effective diffusion coefficient D is made up of contributions from both a pressure-dependent Fickian diffusion term and a Knudsen term:

$$\frac{1}{D(p_0)} = \frac{p_0}{p_{\mathrm{ref}} D_{\mathrm{F}}(p_{\mathrm{ref}})} + \frac{1}{D_{\mathrm{K}}}, \tag{3.6}$$

where we have explicitly written the pressure dependence of the Fickian term in terms of the value of D_{F} at a particular reference pressure, p_{ref}. Substituting equation (3.6) into (3.3) produces the complete expression for flux in terms of pressure and two diffusion coefficients:

$$J_1 = \frac{1}{\frac{p_0}{p_{\mathrm{ref}} D_{\mathrm{F}}(p_{\mathrm{ref}})} + \frac{1}{D_{\mathrm{K}}}} \frac{\rho_{1\mathrm{A}} - \rho_{1\mathrm{D}}}{\Delta z}. \tag{3.7}$$

If data is taken at a number of different pressures, the parameters $D_{\mathrm{F}}(p_{\mathrm{ref}})$ and D_{K} may be fit to the flux data.

3.5 Results

Presented here are the first diffusion coefficients measured for unconsolidated porous media under simultaneous conditions of low pressure and temperature appropriate to Mars surface and shallow-subsurface studies. Four simulant materials are considered, with the largest data set being for 50–80 μm beads. Limited investigations were also performed on three other simulant materials: porous glass filter disks (frits), JSC Mars–1, and 1–3 μm dust.

3.5.1 50–80 μm glass beads at 260 K

Experiments were run for several thicknesses and a regression was calculated to determine the correction term, z_{corr}, as described in Section 3.4.2. The correction term is found to be 0.58 ± 0.07 cm. The raw and corrected diffusion coefficients are plotted in Figure 3.7. The uncorrected diffusion coefficient is moderately correlated with sample thickness (R = 0.57). Applying the correction term

$z_{\rm corr}$ to the calculation of D nearly eliminates the correlation (R = -0.02).

The weighted mean of the corrected diffusion coefficients is 4.49 cm^2 s^{-1}, with a weighted standard deviation of 0.69 cm^2 s^{-1}. Raw values from 5 and 10 cm samples are indistinguishable from this range. If the dependence of diffusion coefficient on temperature of $T^{3/2}$ as appropriate for a hard elastic sphere model of Fickian diffusion is used, the value of D at a typical Mars temperature of 200 K is 3.06 ± 0.47 cm^2 s^{-1}.

For the diffusion coefficient of a free gas scaled to the the appropriate temperatures and pressures, the formula given by *Wallace and Sagan* (1979) is used, with a 6% error to account for differences between this and other calculations of $\mathcal{D}_{12}$. For conditions of 600 Pa and 260 K, the calculated $\mathcal{D}_{12}$ is 26.4 ± 0.7 cm^2 s^{-1}.

Experiments were conducted on columns of loose glass beads with thicknesses of 1 and 10 cm under an N_2 rather than CO_2 atmosphere. A correction term of 0.70 ± 0.14 cm was calculated and applied to these samples. The corrected diffusion coefficient determined under a CO_2 atmosphere is 4.62 cm^2 s^{-1} for 10 cm columns, while the same quantity for N_2 is 5.25 cm^2 s^{-1}. According to equation (2.7) the diffusion coefficient in N_2 should be larger than in CO_2 by a factor of approximately 1.4, *i.e.,* the ratio of $\mathcal{D}_{12}$ for H_2O in the two gases as determined using the expression of Holman in Section 2.3. The difference observed is a factor of 1.14. Though somewhat smaller than expected, the change in diffusion coefficients is of the right magnitude and direction. The agreement between obstruction factors in glass beads under different host gases but similar conditions of temperature and pressure validates the data analysis method.

3.5.1.1 *Errors and scatter*

Formal errors in the diffusion coefficient are calculated by taking partial derivatives of equation (3.4) with respect to five measurable quantities: z, $z_{\rm corr}$, J_1, $\rho_{1\rm A}$, and $\rho_{1\rm D}$. Each contributing partial is then sum-squared to give the total error in D. Flux error derives from mass loss errors, which are the standard deviations of all post-transient data points with respect to the linear regression. Error in sample thickness is estimated as a ± 1 mm measurement error in all cases.

Though ideally constant throughout a particular experiment, humidities, total pressures, and temperatures do exhibit some degree of time variation. Errors in $\rho_{1\rm D}$ and $\rho_{1\rm A}$ are taken from contributing errors in $T_{\rm ice}$, $T_{\rm air}$, RH, and p_0. Experiments with multiple thermocouples show variations in $T_{\rm ice}$ on the order of 0.4 K from the sample edge to its center. The error, $\mathrm{d}T_{\rm ice}$, is the greater of the standard deviation of the measurement of $T_{\rm ice}$ and 0.4 K. The error is no greater than 0.46 K for any experiment. The error in saturation vapor pressure at the ice surface is the difference between the saturation vapor pressures calculated at $T_{\rm ice} + \mathrm{dT_{ice}}$ and $T_{\rm ice} - \mathrm{dT_{ice}}$, making the error in p_{H_2O} at the ice surface a conservative overestimate. Errors in the quantities $T_{\rm air}$, RH, and p_0 are taken as the standard deviation of logged data points.

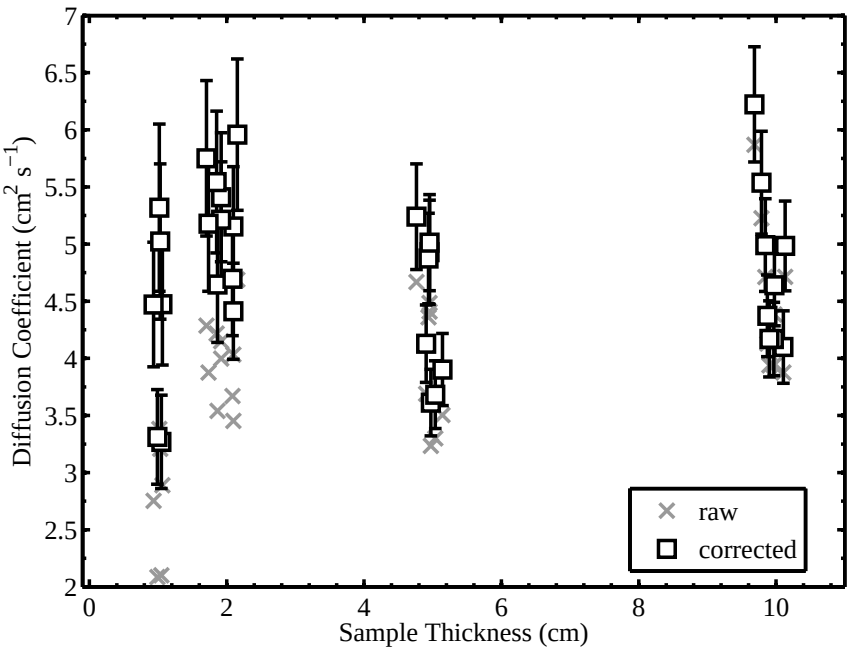

Figure 3.7: Measured and corrected diffusion coefficients for 50–80 μm glass beads at 263 K and 600 Pa. The influence of boundary layer diffusion decreases as the sample thickness (*i.e.,* resistance) increases. The correlations between D' (raw data) and thickness are 0.57, but only -0.02 between D (corrected data) and thickness.

Less than 2% of the error in the value of D for each experiment comes from z_{corr}, J_1, and $\rho_{1\mathrm{D}}$. The dominant errors are those in z and $\rho_{1\mathrm{A}}$, which range from 1–8% of the value of D. For all experiments the combined error is less than the value of D by a factor of ten or more.

The greatest uncertainty in D comes from systematic variation between experimental runs. Variations in input parameters to the diffusion coefficient such as thickness, relative humidity, temperature, pressure, and flux should be accounted for by the calculations since the expressions for D explicitly or implicitly include these parameters. Scatter may therefore arise for two reasons.

First, effects arising from advection, gas composition, and barodiffusion could contribute to each experimental run a flux unaccounted for in the described methodology. As stated above, the maximum contribution of any of these individual effects is expected to be no greater than 10%. Barodiffusion could contribute to each experimental run a flux unaccounted for in the described methodology. As stated above, the maximum contribution of any of these individual effects is expected to be no greater than 10%.

Second, there may be errors arising from changes in the experimental setup itself. The largest variation in measured quantities among samples of a given thickness is in relative humidity, which may vary by between 25–48% among individual experiments. Repositioning or substituting sample vessels may affect the flow of gases in the overturning chamber atmosphere. Water vapor densities at the surface of the sample may not be uniform in the horizontal or vertical directions and the

relative humidity measured by the hygrometer may not reflect the average environment across the the sample surface.

Numerous experiments have been run in many identical conditions, allowing confident bounds on measured diffusion coefficients to be given, though in some cases apparent outliers still have a discernible effect on the averages.

3.5.1.2 *Variable pressure experiments*

Experiments were performed at 300, 600, 1200, 3000, and 6000 Pa using a 5 cm column of 50–80 μm beads. Measurements at many thicknesses for each pressure are unavailable, so a correction term is not applied to the variable pressure data. It is not assumed that the correction term for glass beads is the same at all pressures, but it is assumed that 5 cm is enough thickness to make the correction contribution small at all pressures measured. Pressures less than $\sim$250 Pa were not used; at these lower pressures the vapor pressure of the ice becomes a significant fraction of the total chamber pressure and the experiment is no longer in a predominantly diffusive mode. A non-linear least-squares fit calculated using the method in Section 3.4.3 is compared to calculated (uncorrected) diffusion coefficients in Figure 3.8.

The fit parameters thus determined are $D_F(p_0) = 6.5\ (600\ \mathrm{Pa}/p_0)\ \mathrm{cm}^2\ \mathrm{s}^{-1}$ and $D_K = 9.8\ \mathrm{cm}^2\ \mathrm{s}^{-1}$ and are shown as solid lines in Figure 3.8. The transition pressure, where $D_F(p_0) = D_K$ is found to be at 398 Pa. The transition pressure corresponds to a mean free path of 18 μm, which is near the smaller end of the estimated pore size distribution. Mars surface pressures fall between the extremes measured, and are quite close to the transition pressure, placing materials of similar porosity and tortuosity to the 50–80 μm simulant in the transition regime.

At the beginning of this subsection, experiments performed at 600 Pa, with a mean free path of $\sim$12 μm, were shown to be within the diffusion transition regime. If the pressure is increased to 1200 Pa, the mean free path is only 5.9 μm, placing the largest pores within the Fickian regime; further increase to 5700 Pa should guarantee Fickian diffusion. Conversely, diffusive transport at 50 Pa would bring the smallest pores into pure Knudsen flow, but the bulk of the sample would still be in transition.

3.5.1.3 *Porosity and tortuosity*

The measured sample masses and their volumes are ratioed to determine a bulk density. Dividing by the true density of the component materials (2.5 g cm^{-3} in the case of glass beads) results in a geometric porosity. The porosity calculated may be an overestimate if some pore spaces are unavailable for gas transport. The range of porosities calculated for the 50–80 μm beads is $44 \pm 2\%$.

The six high-pressure experiments with $p_0 = 5890$ Pa should fall within the Fickian diffusion regime. The theoretically calculated free-gas diffusion at this pressure is $2.67 \pm 0.2\ \mathrm{cm}^2\ \mathrm{s}^{-1}$. The fit

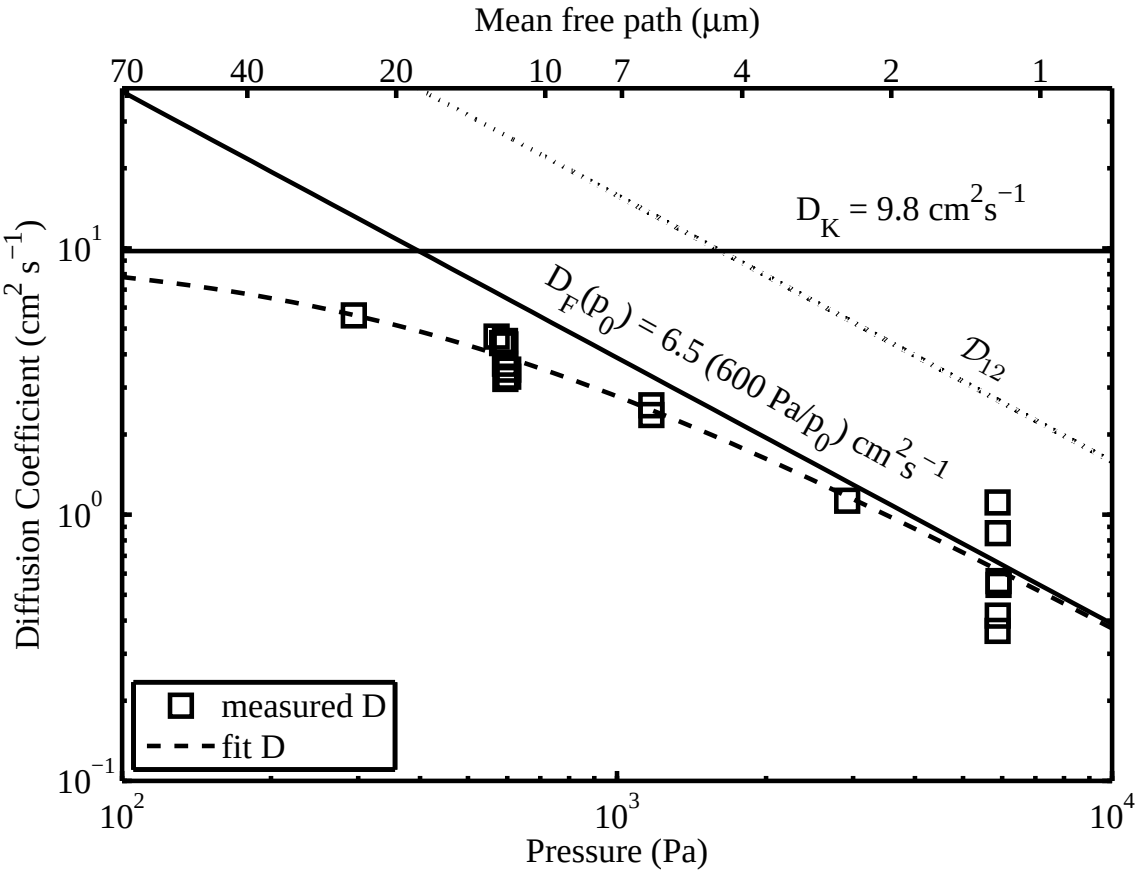

Figure 3.8: Diffusion coefficients versus pressure for 5 cm samples of 50–80 μm beads. Errors in D are smaller than the symbols. The diffusion coefficients obtained from equation (3.3) are plotted along with the fitted parameters $D_{\mathrm{F}}(p_0)$ and D_{K} (solid lines) and their interpolation D (dashed line). $\mathcal{D}_{12}$ is the free-gas diffusion coefficient as given by the expression of *Wallace and Sagan* (1979) (dotted line).

in Section 3.5.1.2 given a Fickian diffusion coefficient at 5890 Pa of 0.66 cm^2 s^{-1}. The obstruction factor is thus 0.25 ± 0.02. Using estimates for geometric porosity, equation (2.3) may be used to calculate a tortuosity $\tau = 1.7 \pm 0.6$. Using the raw data for each experiment instead of the fitted D_{F}, the weighted mean and standard deviation of the diffusion coefficient for the high-pressure experiments is 0.49 ± 0.18 cm^2 s^{-1}. With the same value of $\mathcal{D}_{12}$ given above, the obstruction factor $D/\mathcal{D}_{12} = \phi/\tau = 0.18 \pm 0.07$ and the tortuosity factor is $\tau = 1.5 \pm 0.6$.

Equation (2.3) is true for Fickian diffusion and is therefore appropriately applied to data taken at higher pressures. If this expression is used with values of D obtained at ~600 Pa, the value of the tortuosity obtained is $\tau = 2.4 \pm 0.3$. This is an overestimate of the tortuosity because the data are in the transition regime (see Figure 3.8) and include a component of Knudsen diffusion.

A distinction must be drawn between tortuosity and the tortuosity factor. As reviewed by *Epstein* (1989), "tortuosity" refers directly to the ratio of the pore path length L_e to the length of

the porous medium along the major flow or diffusion axis L. However in calculating the effective diffusion coefficient using a parallel-pore conceptual model, a second factor of L_e/L enters the expression because of the increase in capillary velocity over the axial velocity (along L) when there is no divergence of the flow. Thus the factor of τ presented herein is the "tortuosity factor", equal to $(L_e/L)^2$. The methods using either high-pressure data or (equivalently) the fitted Fickian diffusion coefficient give an increase in pore path length over sample length, L_e/L, of 1.3, while the overestimate made with individually determined values of D gives $L_e/L = 1.6$.

At lower pressures, as diffusion begins to transition into the Knudsen regime, D ceases to depend on pressure through $\mathcal{D}_{12}$ and the obstruction factor may be written with additional factors as shown in equations (2.11) and (2.12). In the formalism used by *Evans et al.* (1961), the τ in these equations is the same as the τ in equation (2.3). Equation (2.13) can be used to determine that the value of τ above will correspond to the fit value of $D_K = 9.8$ cm^{2}s^{-1} if the value of $\bar{r}$ for glass beads is 14.4 μm. This is only slightly larger than the theoretical minimum pore space of 11.96 μm, suggesting that the sample is near closest-packing and that few pathways much larger than $\sim$40 μm are available for diffusion. Calculated obstruction factors ($D/\mathcal{D}_{12}$) for glass beads range between 0.12 and 0.23 except for two outliers at 0.35 and 0.46 measured at high pressures. The majority are within the range of obstruction factors given by *Currie* (1960) for closest packing (0.13) to cubic packing (0.38) of spherical particles.

Mechanical packing (tamping, shaking, or pressing) of this sample does not measurably reduce porosity, and neither porosity, tortuosity nor their ratio correlate strongly with mass loss rate or the free-gas diffusion coefficient. There are no apparent correlations between quantities that should be independent, indicating that the above method of determining tortuosity is not systematically offset.

The data for water vapor fluxes show a greater spread in values for the thinner samples. A major factor which may contribute to the reduction in scatter with thickness is the averaging of pore geometry along the sample. The loose glass beads have a mean diameter of $\sim$55 μm. The measured obstruction factors suggest packing densities between hexagonally close-packed and cubic-packed, implying that there are between 180 and 230 layers of particles per centimeter. For thicker samples, the properties of the medium can average out and present smaller variations between experiments. Additionally, large voids occurring as a result of random packing will offer a very efficient path of vapor transport which could significantly impact the sample diffusivity. Such voids would be a smaller proportion of the total length for thicker samples, thus offering fewer wide, connected paths from the ice to the surface.

3.5.1.4 *Water contents*

Following each diffusion experiment, samples were weighed, baked in an oven at 383 K for >12 hours, and weighed again to gravimetrically determine water contents (per ASTM test method D2216). The weighing techniques employed allowed the determination of mass differences to within ±1 g. For 50–80 μm glass beads, the difference between pre- and post-bake masses was never more than this detection limit except for experiments with 10 cm samples. These large samples never exhibited more than 3 grams of difference, which corresponds to a maximum 6 mg g^{-1} of water content.

At the end of experiments involving 5 and 10 cm sample columns, the bottom 2 cm of sample exhibited mild cohesion while the upper portions of the sample showed none. This suggests that the water content would be relatively higher at the base of the sample if it were measured independently. Such a non-uniform distribution of adsorbed water could reflect the vapor gradient along the sample length. A higher partial pressure near the bottom would cause a larger degree of adsorption there and some threshold water content for cohesion may be reached.

The strongly linear behavior of the mass-loss curves following the initial thermal transients suggests that the absorptive capacity of the samples is filled in less than the transient time. This rate is much faster than would be obtained given only the ice retreat rates in the post-transient interval. It is likely that higher vapor pressures in thermal transient phase, vapor pumping from the ice during evacuation of the chamber, or absorption from the relatively moist freezer atmosphere acts to fill absorptive sites quickly. See the discussion of adsorption below (Section 3.6.1) for more detail on the steady-state nature of these experiments.

3.5.1.5 *Other effects*

If the transition rate from ice into vapor is comparable to the diffusive flux, this sublimation rate will limit the flux measured. For a given ice temperature, the total flux would be independent of the sample thickness if the flux were sublimation-rate limited. For such a constant flux, D would be observed to increase with sample thickness. This is observed in the uncorrected samples, though the effect may be due also to gas diffusion in the gaps above and below the porous medium. The correction term removes both effects simultaneously and since $z_{\mathrm{corr}} < z$, the sublimation limit correction is known to be small. Direct measurements of vapor density at the hygrometer, total flux, and the assumption of a saturated atmosphere below the sample produces valid data.

Sublimation carries away the latent heat of the subliming ice (2,845 kJ kg^{-1} at 273 K), cooling the sample surface. Multiple thermocouples embedded in the ice block during experiments both with and without a diffusive barrier show that temperature variations in the ice block are small. The maximum measured temperature difference across the 1 cm block (no cover, free ice) is no more than 0.8 K; the top surface near the caddy wall being the warmest spot. The ice (thermal conductivity:

2.2 W m^{-1} K^{-1}) therefore requires a heat input of approximately 180 W/m^2. Thermocouples near but not in contact with the a free ice surface record an atmospheric temperature of ∼255 K, which falls between that of the embedded thermocouples (∼250 K) and the RTD temperature element in the hygrometer (∼260 K). The apparent primary heat input to the ice is thus the warmer chamber atmosphere. When the ice is uncovered, this heat reaches it most effectively through convection. When a sample overlies the ice, heat is conducted through the diffusive barrier. Under a chamber atmosphere of 261 ± 0.6 K, the ice temperatures measured for 1, 5, and 10 cm are 256.1 K, 259.3 K, and 260.1 K, respectively. This shows that the thicker samples have heat inputs similar to the thin-sample cases, but their diffusive resistance allows less efficient cooling through sublimation.

3.5.2 50–80 μm glass beads at 253 K

Several experiments have been run on the 50–80 μm beads at reduced temperatures to take advantage of lower advective fluxes when saturation vapor pressures over ice are smaller (see equation (2.22)). A paucity of data points and a small spread of sample thicknesses prevent the calculation of a correction term; the data presented are the raw diffusion coefficients. The diffusion coefficient is found to be 4.21 ± 0.65 cm^2 s^{-1}, slightly lower than the value determined for samples run at 263 K, but indistinguishable within the range of systematic scatter. Extrapolation to 200 K results in $D = 3.03 \pm 0.47$ cm^2 s^{-1}, nearly identical to the extrapolation of the 263 K value of D. The free-gas diffusion coefficient at 253 K is ∼5% lower than $\mathcal{D}_{12}$ at 263 K. The calculated obstruction factor at 253 K is virtually identical to that determined at 263 K, and the tortuosity is likewise similar: $\tau = 2.4 \pm 0.4$.

3.5.3 Glass frits

To check the degree of systematic variation in the experimental setup, a series of experiments were performed with porous glass filter disks, or "frits". Stacks of frits with a nominal pore size of 80 μm were assembled with electrical tape into columns of 1–8 frits (∼0.5 to ∼5 cm) which were then fastened with tape onto caddies full of ice. The distance between the ice and the frits at the start of the experiments was less than 1 mm.

The calculated correction term z_{corr} was approximately zero and was therefore neglected. The diffusion coefficient determined, 2.80 ± 0.22 cm^2 s^{-1}, is about a factor of 1.6 lower than that measured for the unconsolidated 50–80 μm beads. As expected, the porous frits exhibit a lower degree of systematic scatter compared with that in the data for unconsolidated media. The uncertainty in the diffusion coefficients for the frits is ∼6%, while that for the glass beads is ∼16%.

The calculated porosity of the frits is $42 \pm 2\%$, indistinguishable from that of glass beads. Hence the lower diffusivity can be attributed to a more tortuous geometry of the sintered glass. The

calculated values of τ for the frits is 3.9 ± 0.4. This higher tortuosity may arise from the high temperatures and pressures of the sintering process; some of the large pore spaces which could occur in randomly packed and unconsolidated material are eliminated.

Though expected to be small (see the end of Section 2.6.3), the possible presence of gravity-dependent effects such as buoyancy were checked using an inverted experiment. Two sets of frits were run as usual for several hours. Then the chamber was opened and one set was inverted, with a gap allowing free gas flow at the sample surface above the load cell. The difference between the two runs of the inverted sample was 1.9%, while the difference between the two runs of the unaltered set was 3.1%, showing that systematic differences in the experiment exceed any measurable gravity effect on mass loss. The expected gravity-dependent effect is small as discussed in Section 2.6.3.

3.5.4 JSC Mars–1

JSC Mars–1 is the <1 mm fraction of weathered volcanic ash from the Pu'u Nene cinder cone, Hawai'i. The grains are composed of feldspar and Ti-magnetite, with minor olivine, pyroxene and glass. *Allen et al.* (1998) gives an average particle density of 1.91 ± 0.02 g cm^{-3}, but see Section 3.3.2. The uncompacted porosity is reported as 54%, decreaseable to 44% upon vibration(*Allen et al.*, 1997). Much of the mass of JSC Mars–1 is in particles larger than 149 μm, but there is a significant fraction of particles smaller than 5 μm. See the micrograph in Figure 3.4d for representative particle shapes for the raw (*i.e.,* uncrushed) material. Compared to the 50–80 μm glass beads, JSC Mars–1 has larger, more angular particles and a significant fraction of void-filling fines. However, the size and frequency of these fines is small and is not sufficient to block a significant fraction of the available pore space (*Allen et al.*, 1997).

The measured porosity is $58 \pm 2\%$, significantly larger than that determined for glass beads ($44 \pm 2\%$). This is due to the highly angular nature of the JSC Mars–1 particles; the interlocking jagged edges allow a more inflated structure to be stable against compaction. Thus, it is difficult to make estimations of the maximum and minimum pore sizes in the material. Pores larger than the largest particles would tend to form easily, but may just as often be filled with smaller material.

Unlike all other simulants, the JSC Mars–1 exhibits a pronounced decrease in raw diffusion coefficients with thickness. This is opposite the expected trend which would arise from the effects discussed in Section 3.4.2. It may be that the wide grain size distribution results in significant packing effects which give rise to smaller true diffusivities for thicker samples. The measured diffusion coefficient for JSC Mars–1 is 5.36 ± 0.72 cm^2 s^{-1}, slightly larger than the corrected value for glass beads, yet still within the range of uncertainties. The obstruction factor, 0.21 ± 0.03, is larger than the obstruction factor for glass beads, and the Fickian tortuosity $\tau = 2.6 \pm 0.4$ is slightly higher. Higher tortuosity may be a consequence of the wider particle size distribution and angular particle shapes which give rise to a more convoluted flow geometry.

A significant difference between the JSC Mars–1 and both glass beads and borosilicate frits is the amount of water retained during the course of an experiment. Approximately 10 g of water (69 mg g^{-1}) was retained at the end of an experiment with a 5 cm column of JSC Mars–1. Phyllosilicates, which could accommodate water in interlayer spaces, amount to less than 1% of the mass of the sample. More significant are small particles of weathered ash minerals including palagonite, glass, and nanophase ferric oxides which are abundant and contribute greatly to the specific surface area. The larger fraction of small particles in this simulant than in either of the other two presents a higher available surface capable of holding onto a larger amount of water.

3.5.5 1–3 micron dust

The mean particle size of the Arizona dust is 1.19 μm with a standard deviation of only 0.49 μm. The dust easily forms weak mm to cm sized aggregates that may be broken up by sieving, although they reform upon settling or mechanical agitation. Pore sizes in uncompacted samples emplaced by mechanical pouring are therefore expected to be bimodal, with a peak at small sizes ($\sim$2 μm) occurring within the aggregates, and a second, broad peak for inter-aggregate pores at sizes much larger than in any of the other simulants ($\sim$1 mm) (*Yu et al.*, 2003). Mechanical packing destroys the aggregates and closes up the largest pores. The loose, aggregated material has a calculated geometric porosity of $88 \pm 1\%$, while compressional packing results in a reduced porosity of $76 \pm 2\%$.

Data have not been taken at a sufficient spread of thicknesses to enable the calculation of a correction term for the 1–3 μm dust; the raw diffusion coefficients are reported. A significant difference is seen between loose and packed dust, the former being similar to the other simulants studied. The diffusion coefficient for the loose dust is 2.81 ± 1.32 cm^2 s^{-1}; the error bars are within the range of 50–80 μm beads and the glass frits. Packed dust exhibits a much lower diffusivity, with a mean D of 0.38 ± 0.26 cm^2 s^{-1}. One of the 2-cm-thick experiments exhibited a diffusion coefficient of 0.20 cm^2 s^{-1} while another gave a calculated D of 1.4 cm^2 s^{-1}. The small number of measurements on dust and the presence of outliers results in formal standard deviations in D and τ which are large. Further measurements are needed to refine these results and reduce the uncertainties (see Chapter 4).

A chamber pressure of 600 Pa places pores of micron size on the edge of the Knudsen regime, $r/\lambda_1 = 0.17$. The Knudsen obstruction factor may thus be defined with a quantity K_0, which depends on other factors in addition to ϕ and τ. Equations (2.11), (2.12), and (2.13) may be used to calculate a value of τ for the dust particles. Using this method, and estimating $\bar{r} = 2$ μm, the loose dust has $\tau = 5.0 \pm 1.7$, while the Fickian method (equation (2.3)) would give $\tau = 5.3 \pm 2.0$. This suggests that the loose dust behaves more like a coarser porous medium and is predominantly in the Fickian mode of diffusion. Packed dust, on the other hand, gives a tortuosity of 12.3 ± 5.1 with the Knudsen-appropriate equations, but $\tau = 23.5 \pm 10.9$ with equation (2.3). This estimate for τ depends on the

accuracy of the relationship between τ and D_K (equation (2.13)), and on the estimated average pore size. The very large values of τ seen here suggest that more quantitative methods (employing, for example, porosimetry measurements) are called for. While variable-pressure experiments were not performed on packed-dust to confirm that Knudsen diffusion was operating, the low values of diffusivity, differences between the two methods for calculating τ, and knowledge of particle size suggest that this is the appropriate regime. The small diffusivities and high tortuosities support the possibility that a thin layer of packed dust could dominate the diffusive resistance through a medium which is more open overall.

The small particles of the Arizona dust retain water well. About half as much water as the JSC Mars–1, around 34 mg g^{-1}, was retained at the end of the experiments. The dust is nearly pure silica and has no special mineralogical means of binding the water. The retained water is likely held in place through capillary action and the large surface area of the dust and dust aggregates.

3.5.6 Summary

Table 3.2 presents a summary of the data for each type of simulant.

Mass fluxes for all samples are plotted versus sample thickness in Figure 3.9. All simulants show decreasing flux at larger thicknesses. Experiments performed at 253 K, or experiments performed with packed dust, fall below the trend of other experiments. Figure 3.10 shows these fluxes as a function of temperature along with the evaporation rate curve for bare ice as given by *Ingersoll* (1970) for a dry atmosphere. Figure 3.10 also shows additional data obtained in later experiments than those described here; these will be discussed in Chapter 4.

Correction terms are applied as per Section 3.4.2 to experiments performed on glass beads at 263 K under CO_2 and N_2. The correction term determined for the glass frits is near zero and is neglected. Corrections are not applied to samples with an insufficient spread of thicknesses such as 1–3 μm dust and experiments on 50–80 μm glass beads at 253 K. A correction term is also not obtained for JSC Mars–1, which is a special case in which it is believed compaction effects result in different true diffusivities for different sample thickness.

Figure 3.11 displays the data for the simulants described in this chapter as a function of pressure; data at both temperatures ($\sim$260 K or $\sim$250 K) are included. The lines in this figure represent extrapolated free-gas diffusion coefficients using the expression of Wallace and Sagan. The trend of the variable pressure data (50–80 μm glass beads) follows this line with a constant obstruction factor of $\sim$0.18. Diffusivities for all simulants measured at 600 Pa except for packed dust fall within the range of 2.0–6.2 $cm^2\ s^{-1}$. The range of the mean values for different sample types and temperatures (but at 600 Pa only) is from 2.8 to 5.4 $cm^2\ s^{-1}$. Packed 1–3 μm dust has values of D between 0.2–1.4 $cm^2\ s^{-1}$, with a weighted mean value of 0.38 ± 0.26 $cm^2\ s^{-1}$. The obstruction factor for most simulants is between 0.09 and 0.23, while for packed dust it is 0.008–0.053. This suggests

Sample	T_{ice} [K]	D [cm^2 s^{-1}]	$D(200\ K) \propto T^{3/2}$ [cm^2 s^{-1}]	$D(200\ K) \propto T^{1/2}$ [cm^2 s^{-1}]	Porosity [%]	$\mathcal{D}_{12}$ [cm^2 s^{-1}]	$D/\mathcal{D}_{12}$	Tortuosity
50–80 μm beads	258.2 ± 1.7	4.49 ± 0.69[1]	3.06 ± 0.47	3.95 ± 0.61	44 ± 2	26.2±2.2	0.17 ± 0.03	2.4±0.3
50–80 μm beads, 6 kPa	261.2 ± 0.1	0.49 ± 0.18	0.33 ± 0.12	0.43 ± 0.16	42 ± 1	2.7±0.2	0.18 ± 0.07	1.5±0.6
50–80 μm beads, 253 K	249.4 ± 0.5	4.21 ± 0.65	3.03 ± 0.47	3.77 ± 0.58	44 ± 2	24.9±2.1	0.17 ± 0.03	2.4±0.4
50–80 μm beads, N_2	258.3 ± 1.9	5.33 ± 0.43[1]	3.63 ± 0.29	4.69 ± 0.38	43 ± 1	33.4±2.1	0.16 ± 0.01	2.6±0.2
"Coarse" glass frits	257.4 ± 1.5	2.80 ± 0.22	1.92 ± 0.15	2.47 ± 0.19	42 ± 2	26.4±2.3	0.11 ± 0.01	3.9±0.4
JSC Mars–1	257.3 ± 1.6	5.36 ± 0.72	3.67 ± 0.50	4.72 ± 0.64	58 ± 2	26.2±1.8	0.21 ± 0.03	2.6±0.4
1–3 μm dust—loose	256.2 ± 1.4	2.81 ± 1.32	1.94 ± 0.91	2.48 ± 1.17	88 ± 1	29.7±1.7	0.09 ± 0.04	5.3±1.9
1–3 μm dust—packed	260.6 ± 0.6	0.38 ± 0.26	0.25 ± 0.17	0.33 ± 0.23	76 ± 2	25.8±0.9	—	12.1±5.0[2]

Table 3.2: Summary of results for the experiments carried out at 263 K and 600 Pa in CO_2 unless otherwise noted. Weighted averages and standard deviations for T_{ice}, D, $\mathcal{D}_{12}$, $D/\mathcal{D}_{12}$, and Fickian tortuosity for all samples of a given type are listed. Diffusion coefficients are extrapolated to 200 K using $D \propto T^{3/2}$ and $D \propto T^{1/2}$ as appropriate for Fickian and Knudsen diffusion, respectively.

[1] Corrected D reported for samples for which correction data was available.

[2] Tortuosity estimated from the Knudsen diffusion coefficient and equation (2.13).

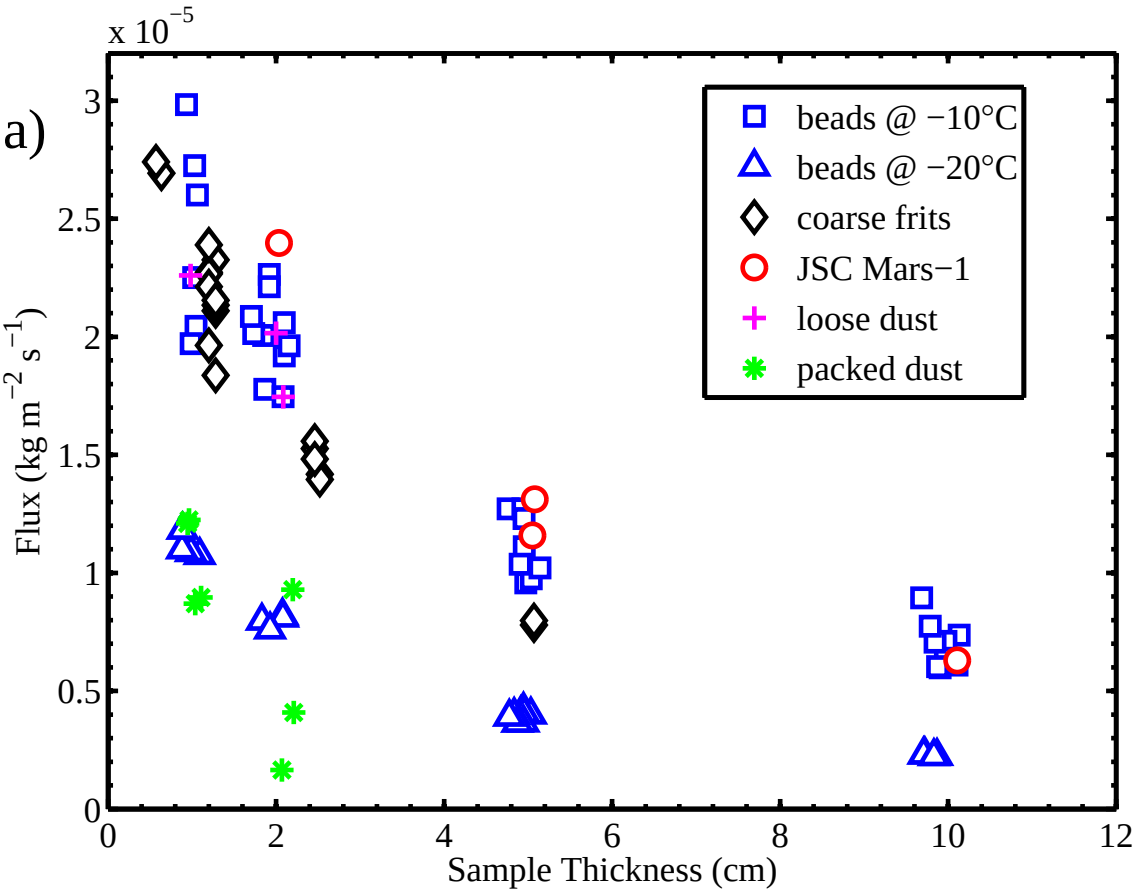

Figure 3.9: Flux versus sample thicknesses for each simulant as measured at 600 Pa and 263 K unless otherwise noted. Errors in flux are smaller than the symbols. The fluxes fall along the same curve for most experiments, notable exceptions being packed dust (asterisks) and 253 K experiments on glass beads (triangles).

that particle size and packing density, through their effect on the obstruction parameters ϕ and τ, are more important than particle shape (compare glass beads to frits), composition (compare glass simulants to JSC Mars–1), and size distribution (compare loose micron dust to other simulants).

When extrapolated to the Mars-appropriate temperature of 200 K, the diffusion coefficients obtained for samples other than packed dust fall in the range of 1.9–4.8 cm^2 s^{-1}. Both this and the 260 K values are at the low end of the range of 0.4–13.6 cm^2 s^{-1} given by *Flasar and Goody* (1976).

The tortuosity of the non-dust samples exhibits a range from 1.5 to 3.9. The tortuosity determined for high-pressure samples is closest to the true value, determinations made with equation (2.3) being overestimates when the diffusion regime is in transition. For the loose dust, calculations of τ with either equation (2.13) or equation (2.3) give similar results. Dust, whether loose or packed, exhibits a higher porosity. Given the results of *Clifford and Hillel* (1986), who show that larger pore spaces accommodate a majority of the flux, loose dust with large interstices between aggregates behaves as if it were in the Fickian regime with $r/\lambda_1 \approx 100/12 = 8.3$. A significant difference ($\sim 200\%$)

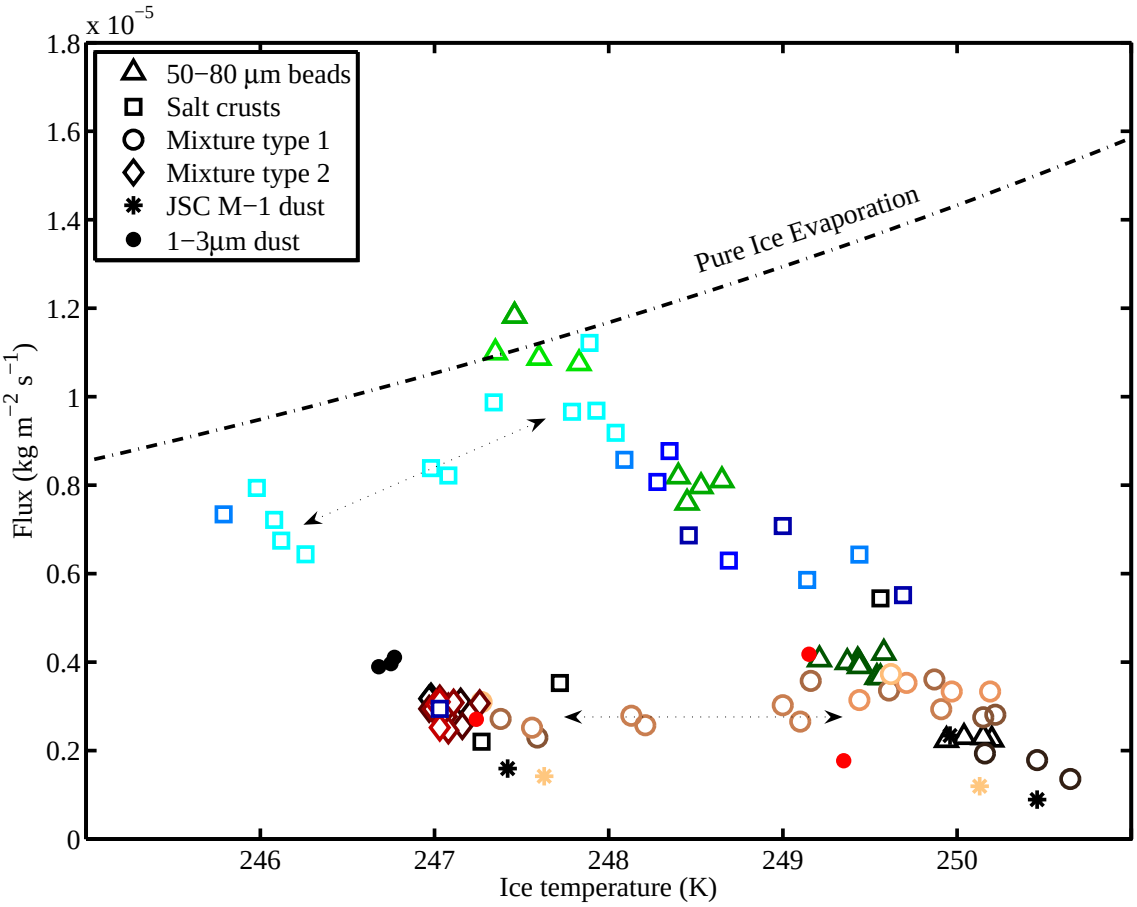

Figure 3.10: Flux versus ice temperature for each experiment; errors are smaller than the symbols. The dot-dashed line is the theoretical curve for evaporation of free ice into a dry atmosphere (*Ingersoll*, 1970). For a given sample, color trends from dark to light denotes decreasing resistance to diffusion (*e.g.*, lower thickness, dust content, or salt content). Arrows indicate trends within a single sample type as a function of temperature. See Section 4.2.1 for mixture type definitions.

results between the two calculation methods for τ when applied to the packed dust sample. Packed dust has only small pore spaces and its behavior is much closer to the Knudsen regime. Equation (2.13) may provide a more appropriate description in this case, though it still gives unusually high values of tortuosity: $\tau = 12.1 \pm 5.0$.

3.6 Discussion

The experimental setup simulates a static environment in which temperatures and humidities do not change significantly with time. A planetary subsurface is subjected to temperature and humidity variations on a variety of timescales, from diurnal to obliquity scale, which can affect the transport of water.

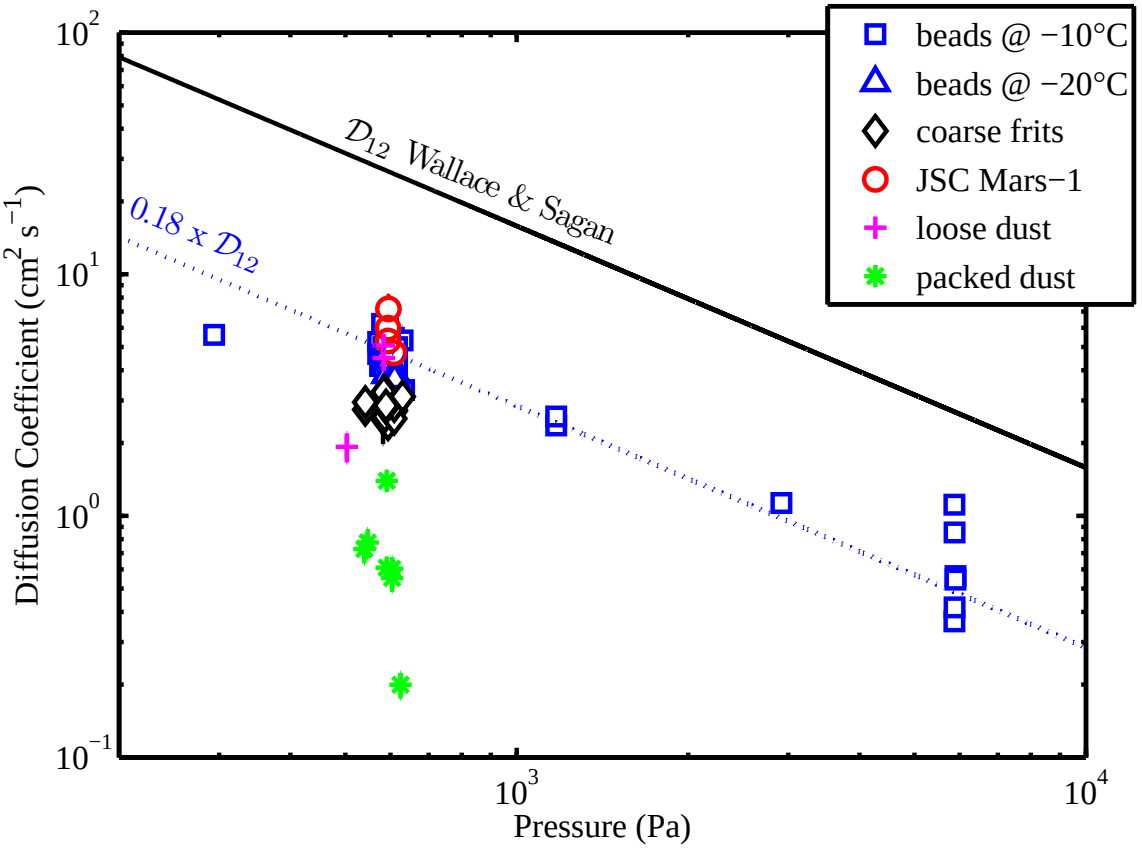

Figure 3.11: Diffusion coefficients versus pressure for all experiments. Errors in the diffusion coefficient are smaller than the symbols. The majority of experiments were run at 600 Pa. The solid line is the theoretically calculated value for the free-gas diffusion coefficient $\mathcal{D}_{12}$ as given by *Wallace and Sagan* (1979) for $T = 263$ K. The dotted line shows $\mathcal{D}_{12}$ scaled by an obstruction factor of 0.18. Packed dust falls below the trend of other experiments but 253 K experiments do not.

3.6.1 Adsorption

Rapid fluctuations in temperature arising from diurnal insolation changes could affect diffusion rates inasmuch as adsorption acts as a source or sink of water vapor. The non-equilibrium adsorption or desorption of water can have a significant effect on the instantaneous vapor density, and therefore on gradients in vapor density. Adsorption typically increases with partial pressure and therefore inhibits diffusion compared with a non-adsorbing environment by attenuating local vapor density gradients.

Adsorption results in a modification of the effective diffusion coefficient by a factor of $(1 + (1/\phi)\partial\alpha/\partial\rho_1)$, where ϕ is the porosity, α is the density of the adsorbed phase, and ρ_1 is the vapor density ((*Schorghofer and Aharonson*, 2005) and references therein). When $\partial\alpha/\partial\rho_1 = 0$, there is no adsorption. When $\partial\alpha/\partial\rho_1 = \infty$, there is complete adsorption of any additional water and $D = 0$. The term $\partial\alpha/\partial\rho_1$ for Mars temperatures is several orders of magnitude greater than unity according to *Zent and Quinn* (1995) and *Jakosky et al.* (1997).

This modification to the diffusion coefficient only applies when the system is out of equilibrium, when the adsorptive layer is undersaturated with respect to the local temperature and pressure and water adsorbs to the grain surfaces. If the temperature and local vapor density remain constant, the quantity of adsorbed water does not change with time; *i.e.,* no net exchange between the vapor and the adsorbate. Hence, in an environment that is temporally isothermal and isobaric, the diffusion remains unaffected by the adsorption after each local point in the regolith has reached an equilibrium with the vapor. Thus, the static experimental setup only experiences adsorptive effects in the initial moments of exposure of the ice to the soil, and they disappear by the time the thermal transients have passed (see Section 3.5.1.4 for a discussion of experimental absorptive saturation timescales).

The maximum temperature fluctuation experienced by the sample after initial transients occurs at its upper surface and will be no greater than the maximum air temperature fluctuations (± 0.45 K). With a specific surface area for glass beads between 0.015 and 0.03 $m^2\ g^{-1}$, such a change corresponds to a change in adsorbed mass of less than 1 $\mu g\ cm^{-3}$ (using the empirical isotherm presented by *Zent and Quinn* (1997) for the data of *Fanale and Cannon* (1971, 1974)). With these conditions the influence of adsorption cycles in these experiment is negligible.

On Mars, the scenario where adsorption has the greatest affect on the diffusion of vapor will be if adsorption proceeds from saturation to complete dessication and back over each cycle. The skin depth of adsorption and desorption is less than the thermal skin depth (*Jakosky*, 1983)

Adsorption on Mars greatly affects vapor density gradients on diurnal timescales, but long-term subsurface ice evolution depends on average gradients and adsorption has no accumulated effect (*Jakosky*, 1985; *Mellon and Jakosky*, 1993; *Schorghofer and Aharonson*, 2005). Thus these static experimental results are applicable to long-term near-surface ice evolution on Mars.

3.6.2 Temperature oscillations

The surface of Mars experiences large diurnal and seasonal temperature variations. The mean diffusive flux from a buried ice layer can be calculated using mean annual vapor densities (*Schorghofer and Aharonson*, 2005). The time-averaged density gradient in equation (2.2) is the same as the gradient of the time-averaged density, because the time integral and the spatial gradient can be interchanged. Neglecting the temperature dependence of the diffusion coefficient, one can then express the diffusive flux as $\langle J_1 \rangle = -D\langle \partial \rho_1 / \partial z \rangle = -D \partial \langle \rho_1 \rangle \partial z$. Angle brackets indicate a time average.

In the intervening layer between the ground ice and the atmosphere, frost and adsorbed water may form periodically. Unless stable throughout the year, this water will be lost again at a different time during the annual cycle and has no accumulated effect. In the long-term, it contributes nothing to the net vapor flux.

The mean vapor density gradient is simply $\partial \langle \rho_1 \rangle / \partial z \approx \Delta \langle \rho_1 \rangle / \Delta z$, where $\Delta \rho_1$ is the difference

between the vapor density at the surface and at the subsurface ice, and Δz is the spatial separation between these two points. For all but the most rapid timescales, mean annual values of vapor density control the evolution of subsurface ice. Since mean annual values govern the net transport, diffusion coefficients obtained from static experiments are applicable to the time-varying conditions on Mars.

3.6.3 Ice table evolution

Investigation by *Smoluchowski* (1968) of conditions which would permit long (>10 Gyr) survival times for buried ice was motivated by the assumption that Mars' climate may have allowed ice to be deposited at low latitudes very early in its history, but has remained essentially unchanged from its current conditions for the past ∼3.5 Gyr. To obtain such survival times in a completely dry atmosphere, his calculations assume extremely low porosities which lead to very low diffusion coefficients.

The water content of Mars' atmosphere is not zero; the current mean annual vapor pressure of water at the surface is ∼0.13 Pascals (*Farmer and Doms*, 1979; *Smith*, 2002). This small but non-zero quantity of atmospheric humidity introduces a frostpoint temperature of 198 K and thereby establishes an ice table equilibrium depth. The ice table will move until the mean annual vapor density above the ice is equal to the mean annual vapor density in the atmosphere and will thereafter be stationary until either its temperature changes or the atmosphere becomes more or less humid.

The equilibrium position of the ice table is not determined by regolith diffusivity, but solely by subsurface temperature and atmospheric water content. If ice is found (*e.g.,* through neutron spectroscopy, ground-penetrating radar, or trenching) to exist at a position away from the expected depth of equilibrium with respect to the current climate, it is possible that some transport-limiting process is slowing down the adjustment of the ice table.

Smoluchowski's work was based on the additional assumption that Mars' climate has been static for most of its history. More recent investigations (*Toon et al.* (1980) and many others since) have revealed that significant climatic variation occurs on more frequent timescales. Obliquity cycles of 125 kyr and 1.3 Myr and a longitude-of-perihelion precession with a 75 kyr period have dramatic effects on ice stability through the climatic variables of subsurface temperature and atmospheric water content (*Fanale et al.*, 1986; *Mellon and Jakosky*, 1995; *Zent and Quinn*, 1995). Assuming climate conditions on Mars were similar to their current state beyond several hundred thousand years in the past is therefore unrealistic.

The vapor transfer between the atmosphere and an ice-rich layer buried by a thickness, L, of porous medium is $J = D\Delta\langle\rho_1\rangle/L$. The rate at which the ice table evolves toward its equilibrium depth in response to a change in climate depends, therefore, on the value of D, and also on the vapor density difference between the saturated vapor above the ice and the atmosphere $\Delta\rho_1$, and the thickness of ice added or removed Z (positive downward). These terms are related by the

expression:

$$-\frac{d\mathrm{Z}}{dt} = -\frac{D\Delta\rho_1}{\rho_{\mathrm{ice}}}\frac{1}{\mathrm{Z}(t)} \tag{3.8}$$

where ρ_{ice} is the density of bulk ice. For a dry regolith of thickness L overlying pure ice, the loss of an ice layer of thickness, Z, in time, t, is given by

$$\mathrm{Z}(t) = \frac{D\Delta\rho_1}{\rho_{\mathrm{ice}}L}t. \tag{3.9}$$

Assuming that subsurface ice can be recharged during more favorable times, a conservative estimate for the maximum lifetime of a buried ice layer during a period of desiccating climate may be calculated by equation (3.9).

As an example, a 3% change in diffusivity at constant temperature would change the ice lost in one year by 3%. While diffusivity is a first-order control on the rate of subsurface ice evolution, its importance is dwarfed by the effects of subsurface ice temperature, particularly near the frostpoint. If the ice is near the frostpoint, a change by 5 degrees (less than 3%), from 200 to 205 K for example, will cause a 700% change in $\Delta\rho_1$. At higher temperature, a change of slightly less than 2%, from 260 to 265 K, will only change $\Delta\rho_1$ by 64%, but the absolute magnitude of the change will be much greater. In terms of ice loss, the former case means the difference between 3.6 and 24 millimeters of ice per year (a factor of $\sim$7), while the latter is the difference between 34 and 22 meters of ice per year ($\sim$50%).

Consider the evolution of a layer of near-surface ice for $\sim$38 kyr. This is one half-period of the shortest orbital climate variation (longitude-of-perihelion precession) and could represent the longest time during which the climate is in a single mode (*e.g.,* ice-loss) for some location on Mars. The depth of burial which would allow one meter of pure ice to retreat in this time by the method of equation (3.9) is presented in Figure 3.12 as a function of ice temperature.

If the ice fills interconnected pore spaces of a structural regolith matrix with low porosity ϕ, the removal of ice leaves behind a lag which increases in thickness. For a growing lag, L becomes $\mathrm{Z}(t)$ in (3.8) which makes t quadratic in Z. After integration,

$$\mathrm{Z}(t) = \left[\frac{2D\Delta\rho_1}{\rho_{\mathrm{ice}}}t + \mathrm{Z}^2(0)\right]^{\frac{1}{2}}. \tag{3.10}$$

The effect of the value of the diffusion coefficient on ice retreat depth versus time is shown in Figure 3.13 for ice at 200 K in a dry atmosphere for both "constant thickness" and "lag-forming" cases.

Relatively large diffusion coefficients of around 3 $\mathrm{cm}^2\ \mathrm{s}^{-1}$ allow ice to respond quickly to a climate change. Within one half-period of the 75 kyr climate cycle, a pure ice table buried by one meter of dry regolith could retreat to a depth of 19 cm. A pore-filling ice table initially retreats at about the

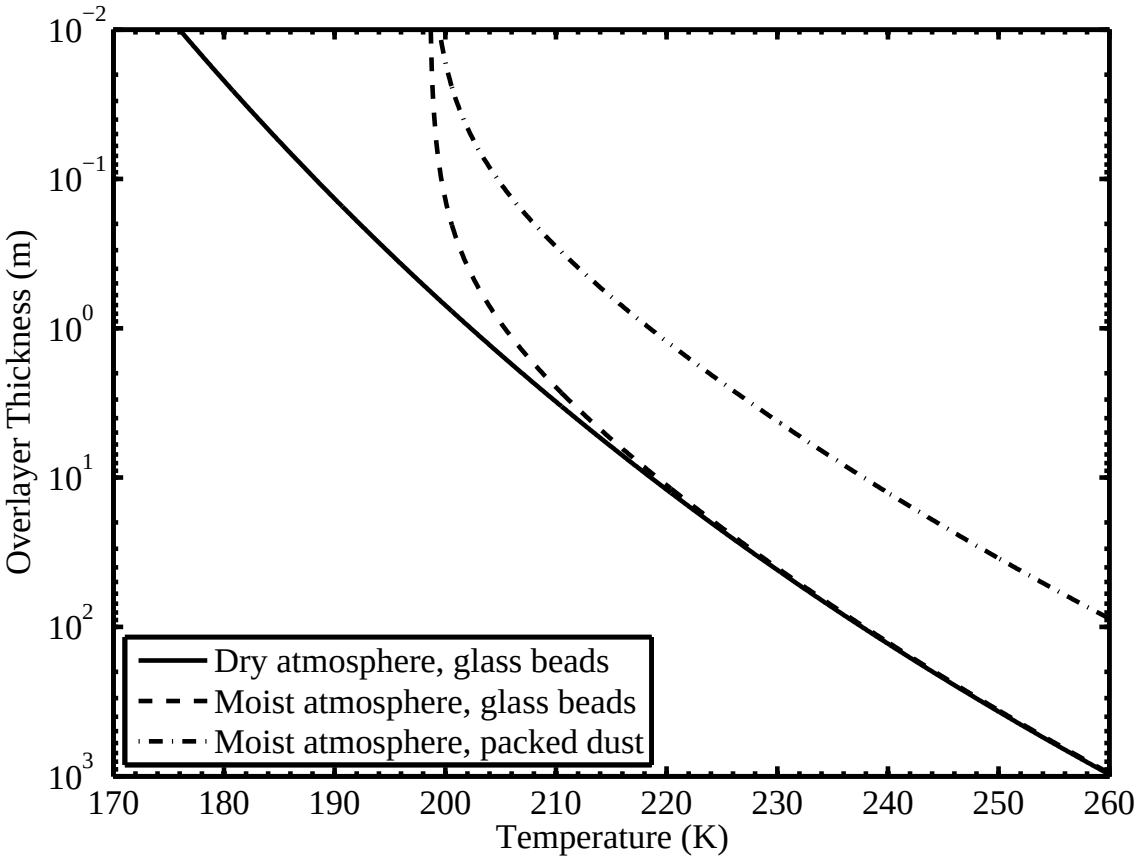

Figure 3.12: Regolith overlayer thickness required to allow one meter of ice retreat in ∼38 kyr (one-half of the 75 kyr climate cycle). The diffusion coefficients used are those extrapolated to 200 K via $D \propto T^{3/2}$ for glass beads and $D \propto T^{1/2}$ for packed dust, as appropriate for Fickian and Knudsen extrapolations, respectively. The values are in Table 3.2. The solid line represents zero atmospheric vapor density. The broken lines assume a present-day atmospheric vapor pressure of 0.13 Pa. With non-zero atmospheric humidity, ice is stable below the frostpoint and the overlayer thickness asymptotically approaches zero at this temperature (here, 198 K).

same rate because the area of ice exposed is reduced by the same factor ϕ as the volume density of ice, and would reach 60 cm in the same amount of time. A diffusion coefficient of 0.3 cm^2 s^{-1} causes the ice to respond more slowly and less than 1.9 cm of retreat is possible for a pure ice case in the same time. Warmer ice responds much more quickly: at 240 K, pure ice covered by one meter of regolith with $D = 0.3$ cm^2 s^{-1} would retreat by more than 700 cm in 38 kyr.

For the range of diffusivities measured in these experiments, the depth over which ice can respond to ∼100 kyr climate cycles is less than approximately one meter. This is similar to the difference in ice table equilibrium depths determined for a range of obliquities in the model of *Mellon and Jakosky* (1995). Whether or not present-day subsurface ice has responded to recent climate variations and is at its equilibrium depth with respect to the current climate will depend both on the ice temperature, the diffusivity of the overlying regolith, and whether the ice is a pore-filling substance or is a solid

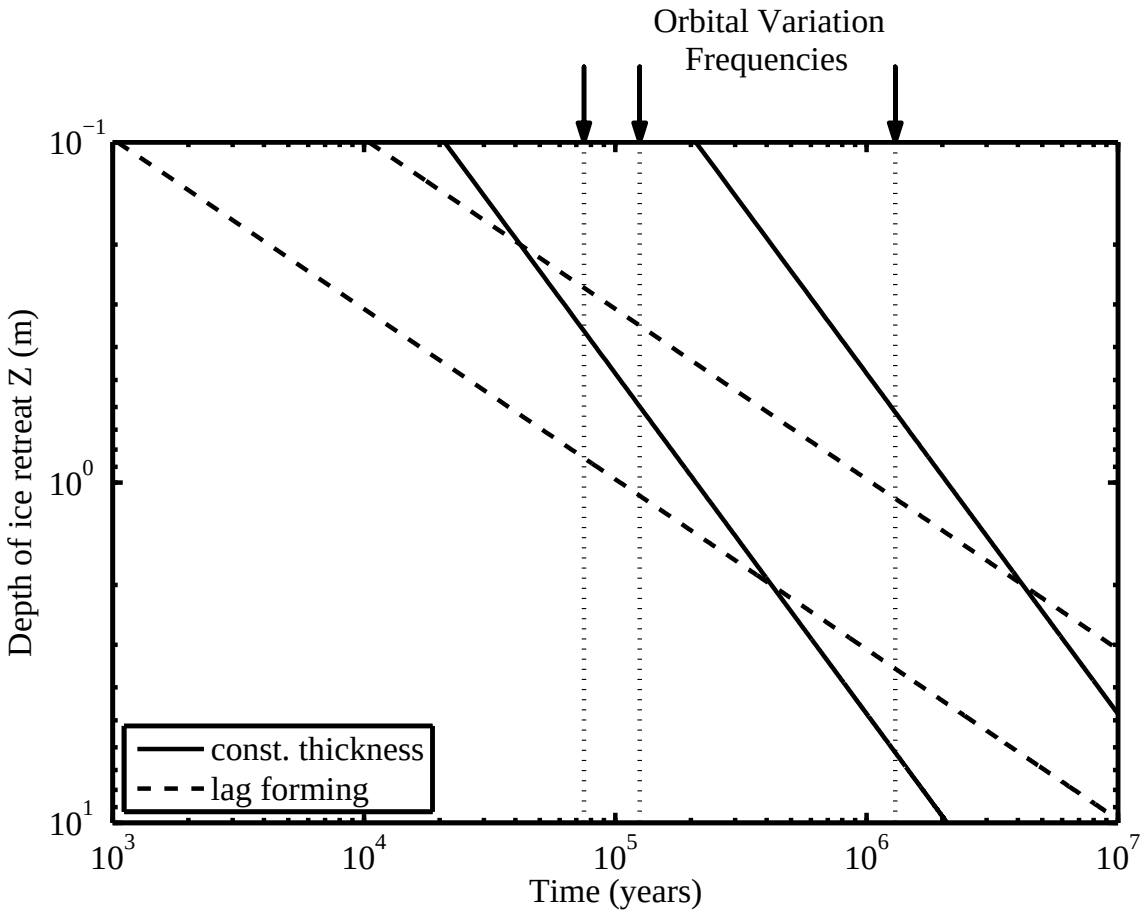

Figure 3.13: Retreat depth versus time for two values of the diffusion coefficient in a moist atmosphere. Solid lines show cases for pure ice under a regolith one meter thick. Dashed lines show lag-forming cases with an initial barrier of 1 mm. Values of D used are 3.0 cm^2 s^{-1} for the left lines, and 0.3 cm^2 s^{-1} for the right lines. $T_{\rm ice} = 200$ K. Vertical dotted lines are, from left to right, the frequencies of 75, 125, and 1300 kyr climate cycles.

slab of pure ice.

For cases with very high ice filled porosity, *e.g.,* polar layered deposits where the material is likely to be only a few percent dust, a lower porosity lag will still form as the ice sublimates.

This simple model is limited by the assumption of isothermal ice in equations (3.9) and (3.10) and Figure 3.13. As the ice front moves, its mean annual temperature will adjust to that specified by the soil thermal properties and the insolation at the surface. Soil thermal properties are very likely to be correlated with mass-transport diffusivity. Low density materials with a small amount of interconnectivity between individual grains (such as dust) are likely to have low thermal conductivities and hence low thermal inertias.

3.6.4 Diffusion in Mars surface processes

The degree to which the ice beneath a given regolith will be able to respond to variations of a particular frequency will depend on the value of the diffusion coefficient, lower values of D corresponding to a more sluggish response. Evidence for near-surface ice from Mars Odyssey (*Boynton et al.*, 2002; *Feldman et al.*, 2004b) is consistent with climate model predictions which imply that the present-day Mars ice tables are at or near their equilibrium positions with respect to the present climate (*Mellon and Jakosky*, 1993; *Mellon et al.*, 2004; *Schorghofer and Aharonson*, 2005). This suggests rapid communication between the subsurface ice and the atmosphere. *Schorghofer and Aharonson* (2005) estimate that a diffusivity of at least 1 $\mathrm{cm}^2\ \mathrm{s}^{-1}$ is required to achieve the observed balance between atmospheric water vapor and ground ice distribution within a single obliquity cycle. On timescales of years or decades, the coupling of atmospheric water circulation with the regolith will be strongest in soils with rapid diffusion. An upper limit on realistic soil diffusivities will set the maximum adjustment rate of subsurface ice to climate fluctuations.

Likewise, the lowest realistic soil diffusivity sets the minimum adjustment rate of subsurface ice to climate fluctuations. With $D = 1\ \mathrm{cm}^2\ \mathrm{s}^{-1}$ at 200 K and in a dry atmosphere, ice in the top meter can be sustained for at most 80 kyr. This result is obtained by inverting equation (3.10) for the time t it takes to retreat to depth Z, $t = (\mathrm{Z} - \mathrm{Z}_0)^2 \rho_{\mathrm{ice}} / (2D\Delta\rho_1) \leq \mathrm{Z}^2 \rho_{\mathrm{ice}} / (2D\Delta\rho_1)$.

The subsurface temperature cannot be expected to stay constant for longer than a few tens of thousands of years because of orbital variations in insolation. Variations on these longer timescales will be able to affect ice beneath porous regoliths with lower values of D. Additionally, during times of high atmospheric humidity the mean gradient in vapor density at particular latitudes may either vanish, resulting in stable subsurface ice, or reverse, resulting in ice accumulation.

Significant variability in the diffusive properties of the Martian regolith at different locations and depths is expected. The range of pore sizes and values of D given by the investigators mentioned in Section 1.2.2 reflects this uncertainty. In the absence of any global-scale data on regolith porosities or other quantities that would enable the calculation of D, most existing models incorporate spatially homogeneous diffusion coefficients.

These results are important in light of the frequent use of diffusivity of regoliths as inputs to models. Long-term models of the Mars water cycle will be affected by the distribution and extent of lower-diffusivity regoliths which act as sluggish sinks or sources of atmospheric water. In their work considering the recent history of the northern polar layered deposits, *Levrard et al.* (2005) present as a possibility the "common presumption" than dust-containing polar water ice could form a thick lag deposit upon sublimation which would protect deeper ice. They introduce a factor f which reduces the flux when covered by a growing lag. This factor is directly related to the obstruction factor ϕ/τ; values of ϕ/τ determined through these experiments can inform estimations of the factor f.

Skorov et al. (2001) claim that pore radii in Mars regoliths are between 0.1 and 10 microns

and therefore Knudsen conditions obtain. In the same sentence, however, they say that sand- and granule- sized "clodlets" are present. The experiments in this chapter with uncompacted dusts suggest that the presence of such clodlets (in particular, the void spaces between them) would enhance the proportion of Fickian diffusion.

In papers considering conditions which could give rise to transient liquid water on present-day Mars, *Hecht* (2002), *Clow* (1987), and *Farmer* (1976) point out that the presence of a snow or dust cover can significantly suppress evaporative cooling. This circumvents the limitation identified by *Ingersoll* (1970) that evaporative cooling exceeds the solar constant already at temperatures below melting. The reduced heat loss allows ice in favorable environments to reach the melting point. The possibility of transient liquid applies both to the formation of geomorphic features such as crater-wall gullies and sub-glacial drainage networks, and also to problems of water availability for possible Martian organisms.

Other investigators invoke low values of diffusivity as well. *Murray et al.* (2005) suggest that a near-surface barrier with a low diffusion coefficient could explain geomorphic features in Cerberus Fossae as persistent equatorial ice rafts that have remained since the last eruption of water from Cerberus. *Head et al.* (2005) invoke low diffusion coefficients to explain the possible existence of tropical glaciers on Mars. Appropriately for greater depths where porosity may be greatly reduced, *Krasnopolsky et al.* (2004) and *Weiss et al.* (2000) assume a small pore size of order microns when considering the diffusion of methane and other gases.

The experimental findings presented here show relatively high values of D for a range of unconsolidated regolith types. Lower values, such as would be required by the arguments of some of the investigations above, only appear in mechanically modified soils.

3.6.5 Mars regolith properties

The combined results of the experimental investigations and the calculations presented in this section are applicable to Mars only insofar as reasonable estimates of true regolith properties can be made. Dunes and other aeolian landforms indicate the widespread presence of particulate matter with sand-sized grains. Atmospheric scattering effects and observations by surface landers verify the global presence of very fine dust.

The Mars Exploration Rovers (MER) both see soils composed of rounded grains with a maximum size of 100 μm. Grain sizes extend down to the limit of resolution of the Microscopic Imager, but the size distribution down to micron-size dust is not known. The soil compositions are remarkably uniform across the five landing sites of Viking, Pathfinder, and MER, having more in common with each other than the analyzed rocks at those sites (*Yen et al.*, 2005). Since aeolian processes are efficient at sorting grain sizes, it is possible that areas exist on Mars where the regolith is composed of windblown sand particles of nearly homogeneous size. Other areas may be dust laden and better

represented by micron or sub-micron sized dust.

Putzig et al. (2005) have used Thermal Emission Spectrometer (TES) observations of Martian surface thermal properties to estimate global thermal inertia at 3 km resolution. Along with earlier work by *Kieffer et al.* (1973) and *Christensen* (1986), these observations show that Mars' surface has large regions with a significant fraction of unconsolidated dust ($\leq$ 40 μm). Such materials are characterized by low thermal inertias, while both sand-sized particles and indurated fines can give intermediate values between loose dust and solid rocks. At 600 Pa, dust particles with diameters $\leq$ 2 μm will exhibit primarily Knudsen diffusion if the pore sizes are comparable to the grain size. The results presented here suggest that this condition only obtains when the dust has been packed by some mechanism. Regardless of how the dust is compacted, its thermal inertia will be higher than loose air-fall dust. Moderate thermal inertia regions indicative of a high proportion of sand-sized particles (approximated by the 50–80 μm beads) would fall in the transition region between Fickian and Knudsen diffusion.

In their theoretical investigation of the effects of pore size distribution on subsurface ice survival, *Clifford and Hillel* (1983) calculated flux distributions through 12 model pore size distributions. Their results showed that in all cases of non-uniform pore size, the largest pores always accounted for the highest percentage of total flux. They thus concluded that the geometric factor which most significantly influences ground ice loss rates (other parameters like temperature and humidity being equal) is the porosity characterized by the larger ($\geq$ 1 μm in their simulants) pores. Real soils almost always have polydisperse grain sizes, and it is likely that aggregation operates on Mars as least as efficiently as it does on the Moon. If a soil has more than a few percent of its pore space accommodated by statistically larger pores, the diffusion will be dominated by these more open pathways. Despite the presence of small pore spaces, the whole soil could have a diffusivity comparable to a monodisperse soil with an average pores size equal to its largest pores to within about 10–15% (*Clifford and Hillel*, 1983).

3.6.6 Obtaining low diffusivity on Mars

The experiments described in this chapter indicate that, for a variety of simulants with a range of particle sizes, shapes, and pore-space geometries, diffusivities under Martian surface conditions will be on the order of 2.8–5.4 cm^2 s^{-1}, the obstruction factor being between 0.09–0.21. Mechanically packing well-sorted large grains does not significantly reduce the diffusivity, and neither gravitational nor near-surface compressive packing will result in a substantial change in pore geometry. Evidence of dust deposition at lander sites and low thermal inertia values observed from orbit suggest a range of physical properties consistent with most shallow Martian sediments being porous and allowing significant diffusion of vapor (*Jakosky*, 1983). The values of D given above are significantly higher than those invoked by some papers referenced in Section 3.6.4.

The shape of dust can affect its diffusive properties. Micron-size particles are not easily abraded and often exhibit angular forms whose irregular edges easily interlock and prevent more efficient packing arrangements. Even perfectly spherical particles may agglomerate because of electrostatic forces or by cohesion due to adsorption of water. Whether deposited as individual grains or as millimeter to sub-millimeter scale aggregates, the structure of air-fall dust deposits is likely to be much more open than the physical packing limit, and the obstruction factor may be near the value of 0.18 observed for loose dust samples.

The simple idea of having wind-blown dust of the smallest particle sizes settle into the pore spaces of coarser exposed surface material, thereby blocking the escape of water vapor molecules, may not in fact produce the expected small effective diffusion coefficient. The results obtained here suggest that, in the absence of mechanical packing, the diffusion coefficient of the micron-sized particles is not very different from that of the larger particles.

A few purely mechanical process could operate on Mars and provide the packing force required to produce a significant reduction in the observed D (as was necessary for the laboratory measurements). Processes which result in systematically closer packing of the very fine particles, such as sedimentation or cementation, to produce a less porous layer (or the in-filling of the larger voids) could plausibly produce more resistive vapor transport barriers than simple wind-blown redistribution of the dust.

Examples of processes which will produce low diffusivity barriers with micron-size dust are:

Caliche or duricrust: Indurated soils, often described as "duricrust", have been observed at Viking, Pathfinder, and MER landing sites. No conclusive observations of the chemistry of these crusts yet exist, but it is likely that cementation by mobile salts plays a role in their formation. Additionally, subsurface salts deposits have been observed at the MER landing sites (*Cabrol et al.*, 2006; *Yen et al.*, 2007; *Wang et al.*, 2007) and salt is known to be an important component of the martian regolith (*Clark and van Hart*, 1981; *Vaniman et al.*, 2004; *Yen et al.*, 2005). Under certain conditions these could form subsurface cemented layers, similar to terrestrial caliche, which could impede the flow of water vapor.

Settling in liquid water: Water can deflocculate dust aggregates, mitigate electrostatic repulsion, and lubricate the sliding of angular particles, all of which permit higher packing densities. In their paper where they consider Knudsen diffusion on Mars through mixtures of small ($\leq$10 μm) particles, *Clifford and Hillel* (1983) model their distributions after natural samples which have been sedimented in fluid and then dried. The MER rover Opportunity has discovered evidence for shallow standing water on Mars' surface at some point in the past (*Squyres et al.*, 2004a). Whether any dense layers of small particles formed at such times could have survived unbroken to the present is unknown, but seems unlikely. Additionally, dense layers formed in standing

water have a tendency to crack upon subaerial drying, as observed on playas in terrestrial deserts and mud flats.

Physical packing: This process, requiring a significant downward force, is unlikely to act over broad areas unless large-scale burial of a region compacts previously emplaced dust. This mechanism may operate in the formation and subsequent burial by fresh ice of polar layers. Exhumation processes may destroy whatever cohesive layers were formed, although still-buried dense layers of dust are possible. Additionally, mixtures of polydisperse grains which have less than a critical dust content (i.e. the quantity of fine dust required to fill the larger pore spaces) will not pack more tightly than is allowed by the larger grains under the moderate pressures experienced in the upper few meters of a regolith column.

There are few investigations into the porous geometry of martian air-fall dust in the literature. *Moore* (1987) discusses the density and probable particle size composing "drift material" at Viking lander sites. A number of criteria suggest that the drift material examined by Moore is from 0.1–10 μm in size. The observed density of 1.0–1.3 g cm^{-3} would, for basaltic material, correspond to a porosity of 44–66%. Such low porosities cannot be attained with the micron-sized dust used in these experiments without dispersal in water. The drift material may have been subject to some porosity-reducing surface process.

Further studies are needed on the processes of dust deposition under Mars surface conditions so that pore size distributions for dust can be estimated for a wide range of particle sizes and shapes. Based on the current understanding of Mars soils and these laboratory observations, it seems difficult to produce low diffusivity barriers, except perhaps by the action of liquid water, chemical deposition, or both.

Investigations on Mars processes that invoke low diffusivity materials should address the formation mechanism of such barriers. Porous media with moderate diffusivities ($\sim$2–5 cm^2 s^{-1}) are easily formed from a variety of regolith materials, but lower diffusivities are difficult to obtain even in the presence of micron-sized dust.

3.6.7 Conclusions

These experiments have measured diffusion coefficients in several regolith simulants under conditions of sublimation and at pressures appropriate to the surface of Mars. The experimental setup used mimics the geometry and environment of martian subsurface ice overlain by a porous material. Diffusion coefficients are obtained from mass loss, ice temperature, humidity, and sample thickness; simulant porosity and chamber pressure are also measured. The vapor transport theory of Chapter 2 is applicable not only to the experimental setup, but also to variable pressure and temperature environments as exist on Mars.

Previous considerations of diffusive processes on Mars have been primarily based on the kinetic theory of gases in porous media or on experiments at conditions significantly different from those on the martian surface. These studies suggest a wide range of possible values of the diffusion coefficient, from a high of 13.6 $cm^2\ s^{-1}$ to a low of 0.4 $cm^2\ s^{-1}$ for unconsolidated near-surface regoliths, with values on the order of 10^{-3} $cm^2\ s^{-1}$ for extremely low porosity materials.

Experiments with glass beads in the 50–80 μm size range are a proxy for aeolian sediments on Mars. Measured at a pressure of 600 Pa, the diffusivity is determined to be $D = 4.49 \pm 0.69$ $cm^2\ s^{-1}$. The obstruction factor is determined to be 0.17 ± 0.03 and measured porosity is $44 \pm 2\%$.

Data taken over a range of pressures and thicknesses provide a Fickian and a Knudsen diffusion coefficient for 50–80 μm glass beads. The pressure-dependent Fickian diffusivity is (600 Pa/p_0) $\times$ 6.5 $cm^2\ s^{-1}$ and the Knudsen diffusivity is 9.8 $cm^2\ s^{-1}$. The crossover pressure where dominance changes between one regime and the other is found to be about 398 Pa. This is consistent with the definition of the transition region as given by the ratio of mean pore size to mean free path (r/λ_1). The pressure-independent tortuosity in the Fick regime 1.7 ± 0.6, a value significantly smaller than the value of $\tau = 5$ given by Smoluchowski (and quoted by some subsequent investigators) for porosities around 50%.

The highest experimentally measured diffusivity is 7.2 $cm^2\ s^{-1}$ for a thin sample of JSC Mars–1, which exhibits an obstruction factor of 0.27 ± 0.03. A number of other simulants (porous fritted disks and loose 1–3 μm dust) have diffusivities similar to the glass beads. The range covered by these simulants is 2.8–5.4 $cm^2\ s^{-1}$ (see Table 3.2). The only observation of a significantly reduced diffusivity is with mechanically packed 1–3 μm dust which exhibits an average D of 0.38 ± 0.26 $cm^2\ s^{-1}$. Diffusion coefficients are slightly reduced when extrapolated to 200 K using either the Fickian ($T^{3/2}$) and Knudsen ($T^{1/2}$) temperature dependencies (also in Table 3.2).

The variation of D among experiments with the same simulant is 8 to 16% for non-dust samples. Gravity, adsorption, and other forms of diffusion have been shown to play no significant role in the experiments.

While the vapor density over ice as a function of temperature is a very strong determiner of the equilibrium position and evolution rate of subsurface ice, the diffusivity of the overlying regolith is also a first-order control on the rate of subsurface ice migration. In extreme cases, low diffusivity barriers could act to protect buried ice from being lost during periods of dry climate as suggested by *Smoluchowski* (1968).

There are few purely mechanical process on Mars which could produce a significant reduction in porosity for micron-sized air-fall dust, thereby obtaining a diffusivity similar to Smoluchowski's low values. Invoking significant reduction of D requires an explanation of which processes lead to the formation of the low diffusivity barrier and how those processes fit in context with other observations. There are a number of processes which may give rise to such barriers. The efficacy of such processes

and their prevalence on past and present-day Mars warrant further study. In Chapter 4, the efficacy of particle-size mixtures, salt-cemented sediments, and dusts to act as barriers to vapor diffusion are explored.

Chapter 4

Diffusion Barriers

4.1 Chapter Summary

The focus of the experiments described in this chapter is to address the effects on vapor transport of various physical barriers which are more complex than homogeneous porous media. The diffusion coefficient of water vapor is measured at conditions appropriate to the surface of Mars for a variety of particle size mixtures and soil compositions. The work of *Hudson et al.* (2007) (Chapter 3) on the diffusivity, D, of dusts (*i.e.,* particles with mean sizes < 10 μm) is extended. Mixtures of two dusts types with larger particles (50–80 μm glass beads) are studied and the effect of varying dust content on D is discussed. Chemically cemented duricrusts are simulated with magnesium sulfate encrusted glass beads, and a range of salt contents are examined.

The environmental chamber and instrumental setup are identical to that described in *Hudson et al.* (2007) and Section 3.2 in all but two respects. (1) The freezer temperature was reduced to give ambient chamber temperatures of ∼250 K rather than ∼263 K. (2) Pressure is now maintained more accurately with active PID control of an STEC-4400 mass flow controller via an USB-1408FS datalogger from Measurement Computing Corporation. A schematic of the experimental setup is in Figure 3.1. As before, data for calculating diffusion coefficients are taken from the stable interval following the decay of initial transients.

Most unconsolidated mixtures were not actively compressed, but may be subject to self-compression. In most cases, the sample surfaces remain within 1 mm of the caddy top despite sublimation of the ice on which they rest. Some samples with very high dust fractions exhibit some settling as the container is moved from the preparation station to the vacuum chamber. This amounts to about 12% of the 5 cm sample depth, at most. The reduced thickness is measured and included in subsequent calculations; additional material is not added.

It is found that the value of the diffusion coefficient can be reduced by up to a factor of 10 for heavily salt-encrusted soils, with the minimum observed D being 0.4 ± 0.04 cm^2 s^{-1}. Moderate amounts of salt only produce minor reductions in D. Mechanical packing of pure dusts can lower D

by a similar amount, while mixtures including a portion of sand-sized particles produce at most a factor of ∼4 reduction.

This work indicates that present-day processes of aeolian redistribution, moderate levels of salt encrustation, and volatile loss from dirty ice would be inefficient at producing soil deposits and lags on Mars that pose significant barriers to diffusion. Therefore, subsurface ice deposits that are thermally unstable would not be protected against sublimative loss by such materials.

4.2 Materials

A variety of materials have been used to explore the effects of particle size distribution and salt crust formation on diffusion coefficients in simulated Mars soils. Properties of glass beads, crushed JSC Mars-1 dust, and 1–3 micron dust are described in Section 3.3. Figure 3.4 shows optical micrographs of the simulants at the same scale. Further description of preparation methods used for mixtures and salt crusts are presented here. Prior to use, all samples are dried in an oven at 383 K and then stored in air-tight containers.

Geometric porosities of the separate materials were determined by weighing a known volume of bulk sample to determine a bulk density, ρ_{bulk}, and ratioing this against the known specific gravity of the individual particles ($\phi = 1 - \rho_{\mathrm{bulk}}/\rho_{\mathrm{true}}$). The results are given in Table 3.1.

4.2.1 Mixtures

Throughout this work, "Mixture Type 1" will refer to mixtures of crushed JSC Mars-1 material and 50–80 μm glass beads. "Mixture Type 2" will refer to mixtures of 1–3 μm silica dust and glass beads.

To study the effect of bimodal particle distributions, particularly the effect of included dust in a deposit of sand-sized particles, six mixtures (A through F) of silica-glass beads (nominal diameter 50–80 μm) and either crushed JSC Mars-1 or 1–3 μm dust were prepared. The mixtures, both in terms of mass fraction of fines ($X_f = M_f/(M_f + M_c)$ and mass ratio of fines to coarse material (M_f/M_c) are shown in Table 4.1. Volume fraction of dust is an indeterminate quantity since ϕ and ρ_{bulk} for the fine materials can vary over a large range depending on the degree of compaction in the mixture; it is therefore not used to describe the mixtures.

The porosity of the mixtures may be estimated by first calculating the fraction of the volume occupied by each component. Given a measurement of total mixture volume V_T and mixture mass M_T, the volume fraction of each are $v_f = (M_f/V_T)(1/\rho_{f,\mathrm{true}})$, and $v_c = (M_c/V_T)(1/\rho_{c,\mathrm{true}})$, where M_f and M_c are the masses of the fine and coarse components as calculated from $M_f = X_f M_T$ and $M_c = (1 - X_f)M_T$. The free volume is then the sum of these volume fractions subtracted from

	A	B	C	D	E	F
Mixture Type 1						
X_f(%)	43.1	27.4	15.9	11.4	7.06	3.29
M_f/M_c(%)	75.6	37.8	18.9	12.9	7.56	3.40
ρ_{mix}, (g cm^{-3})	2.72	2.63	2.58	2.55	2.53	2.52
Mixture Type 2						
X_f(%)	39.8	24.9	14.2	10.1	6.19	2.82
M_f/M_c(%)	66.0	33.1	16.6	11.2	6.60	2.90
ρ_{mix}, (g cm^{-3})	2.56	2.54	2.52	2.51	2.51	2.50

Table 4.1: Porosities of mixtures with glass beads

unity:

$$\phi_{\mathrm{mix}} = 1 - \frac{M_T}{V_T}\left[\frac{X_f}{\rho_{f,\mathrm{true}}} + \frac{(1-X_f)}{\rho_{c,\mathrm{true}}}\right]. \tag{4.1}$$

Here, ρ_{mix} is determined as proxy for the true density of the mixture if it were composed of a homogeneous granular component, thus: $\rho_{\mathrm{mix}}^{-1} = X_f/\rho_{f,\mathrm{true}} + (1-X_f)/\rho_{c,\mathrm{true}}$. These values are also given in Table 4.1. Individual porosities are determined for each simulant and are tabulated in the auxiliary material.

The amount of dust included in a mixture may, in addition to its mass fraction of the total, be thought of in terms of the proportion of pore spaces in the dust-free coarse sample which are filled. An attempt to produce a range of mixtures from dust-free up to the "critical mixture", where all pore spaces are filled, guided initial choices of dust mass fractions. The critical mixture concept is in fact a less useful definition in practice since the coarse component, in all but the most dust-free mixtures, will be pushed apart by intervening dust particles. Additionally, the dust within the pores may undergo some degree of compaction due to the weight of the overlying material. This effect will be enhanced if coarser (and therefore denser) material is included, as in a mixture. Thus the value for the bulk density of the fines (needed to calculate the critical mixture) may cover a significant range, even within a single sample.

Smooth variation of measured diffusion coefficient is expected as the mass fraction of dust is increased from pure glass beads to pure dust. These experiments exhibit that diffusion through pure unpacked dust can be several cm^2 s^{-1} higher than the value found for glass beads, while for mechanically compacted dust it can be much lower. As stated above, the weight of the dense glass beads should act, at small dust fractions, to compress the dust toward a packed configuration. Mechanical compaction is not applied to these samples.

4.2.2 Salt crusts

Magnesium sulfate was chosen to study the behavior of salt crusts as barrier-forming phenomena due to its availability, crystallization to a well-known phase (epsomite: $MgSO_4{\cdot}7H_2O$) under ambient conditions, and the known existence of sulfate salts on Mars (*Clark and van Hart*, 1981; *Vaniman*

et al., 2004; *Yen et al.*, 2005).

Distilled water is saturated with 250 g of anhydrous $MgSO_4$ per liter and then mixed with a given mass of 50–80 μm glass beads and excess distilled water to produce a slurry of dissolved salt and beads. A mold consisting of a plastic ring and support wires (see Figure 4.1a), is attached to a plastic base with water-resistant grease. The walls and base of this mold are coated with a thin layer of WD-40 lubricant to facilitate removal of the dried crust. Once poured into the mold, the slurry and mold were agitated to remove any trapped air and produce a flat upper surface; any excess was scraped off. Slurries were allowed to evaporatively dry in ambient lab conditions for approximately 6 hours. Internal cohesiveness then allowed them to be removed from the flat mold base and placed on a coarse wire mesh in a forced draft, thereby continuing to dry from both surfaces of the crust. After approximately 24 hours, when the crusts were completely dry, they were placed in a desiccator and moved into the freezer to thermally equilibrate with the environment prior to the start of an experiment.

Slurries were prepared with 0.5, 1.0, 2.5, 5.0, 7.5, and 10.0 wt% $MgSO_4$ (MW= 120.37 g mol^{-1}). When allowed to crystallize at ambient conditions, epsomite is produced (MW=246.37 g mol^{-1}) giving salt contents of 1.0, 2.0, 4.9, 9.7, 14.2, and 18.4% by weight epsomite.

To perform diffusion measurements, the 1 cm salt crusts are placed over an ice-filled 1 cm caddy and secured in place with water-resistant vacuum grease. Following an experiment, the ice surface is examined to determine if there were any leaks between the ice and salt caddies. The low-pressure, low-temperature environment gives rise to distinct ice surface morphologies if the vapor escapes in a rapid or asymmetric way. If any evidence for a leak is observed, the data and sample are discarded.

X-ray powder diffraction was performed on the sample crusts before and after exposure to experimental conditions. Most of the x-ray spectrum indicated the presence of an amorphous phase, *i.e.*, the glass beads. The peaks that did occur in the spectrum matched the intensity and location expected for epsomite. Samples of crust which incorporated greater proportions of material from the interior of the crust exhibited weaker peaks, indicating that the salt concentration decreased toward the caddy center. To examine the surface crusts more closely, the top and bottom surfaces of the crust were scraped following an experiment. The bottom surface of the crust (*i.e.*, the surface adjacent to the ice during the experiment) showed the same strong set of epsomite peaks as before exposure to experimental conditions. The upper surface scrapings (*i.e.*, from the surface exposed to the dry chamber atmosphere) exhibited a complete change of spectrum and revealed only the presence of hexahydrite, indicating a loss of the loosely bound seventh water molecule under desiccating low-pressure, low-temperature conditions. It is unknown how deeply into the sample this conversion penetrates.

For a 1-cm-thick crust of an initial composition of 14.2 wt% epsomite, the total amount of epsomite present is approximately 8.2 g. If it is assumed that one half of the crust converted

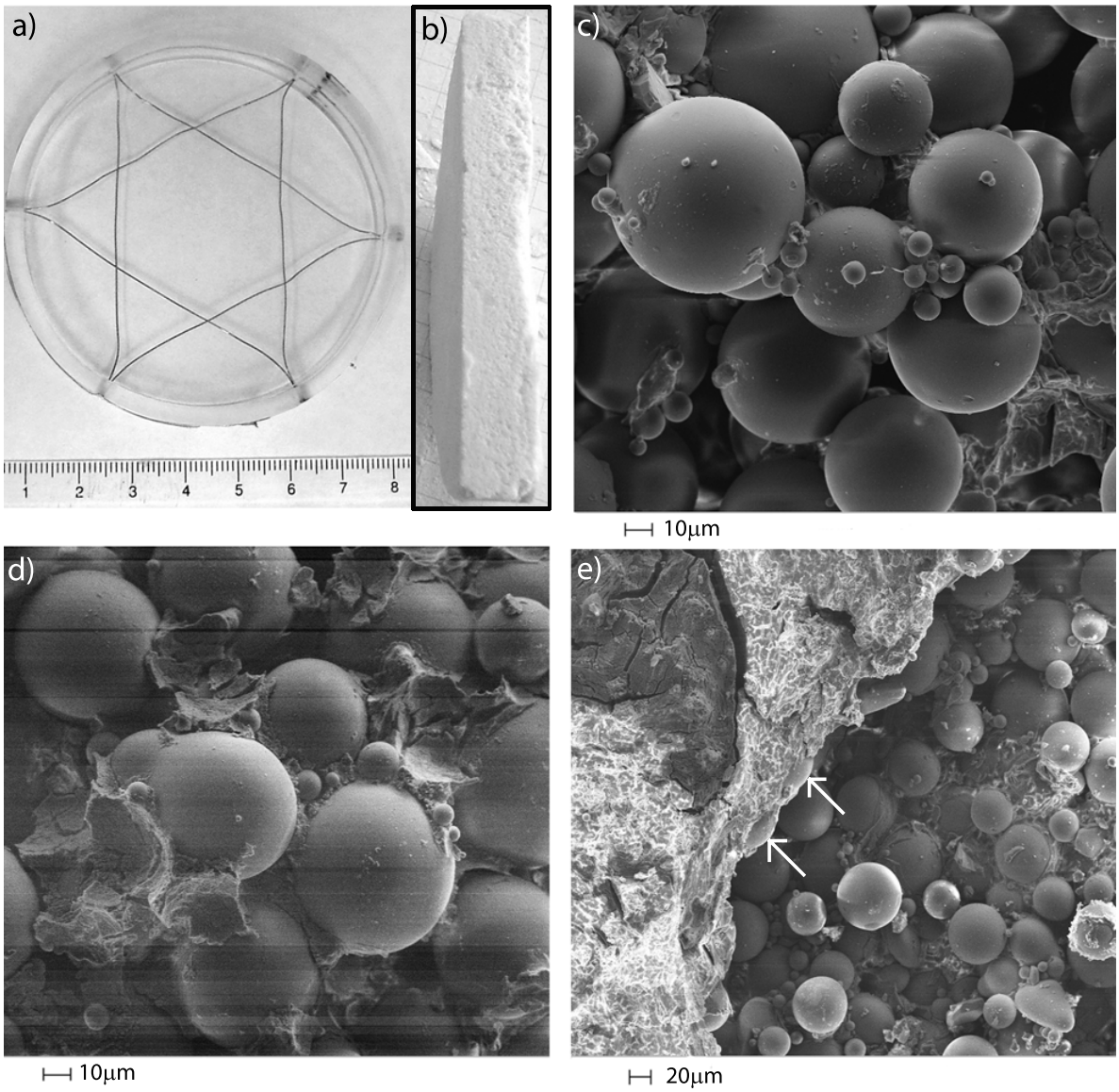

Figure 4.1: a) Empty salt crust caddy (1 cm depth) showing support wires. b) A cross section of a crust grown without wires. c)–e) SEM images of a 14.2 wt% epsomite salt crust after exposure to experimental conditions: c) Interior of crust: view of a cluster of beads held together by salt, beads much smaller than 50–80 μm are present in a significant number and frequently fill pore spaces between larger beads. d) Interior of crust: section of crust showing salt features filling void spaces between larger grains. Dehydration to hexahydrite is the presumed cause of the fracturing. e) Surface of crust: the left side of the image is dominated by an efflorescent crust of hexahydrite which embeds some beads (arrows) but is predominantly pure salt.

completely to hexahydrite, the mass of water lost would be 0.3 g. This is less that 4% of the total amount of mass lost through ice sublimation and contributes a negligible error to the measured flux.

The reconstructive transformation which takes place between epsomite and hexahydrite results in the destruction of large crystals in favor of much smaller crystallites. This micro-fracturing could increase the available vapor transport volume. The timescale of this transformation under these experimental conditions is not constrained, but linear mass loss rates are observed after initial transients, suggesting a diffusion coefficient which is largely constant in time. This implies two possibilities. First, transformation maybe rapid, occurring in the initial few hours of exposure to vacuum, and thus the diffusion coefficient measured is that of glass beads encrusted with fractured, dehydrated salts. The other possibility is that the transformation is gradual, occurring throughout the experimental duration, but has an effect on the diffusivity which is small compared to that arising from the overall salt content.

4.3 Analysis

4.3.1 Corrected diffusion coefficients

Unconsolidated samples rest directly on the ice while crusts have a discernible gap between the ice surface and the bottom of the sample. The vapor density difference across the sample is derived from measurements made at the ice surface and the position of the hygrometer. These may be different from the true lower and upper boundaries of the porous medium. By assuming that all fluxes are proportional to the density gradient across any given layer (whether free-gas or porous medium), and applying the conservation of mass requirement that all fluxes be equal in the absence of ice deposition or loss, a correction term is established which accounts for diffusion through the simulant-free portions of the column. The derivation of this correction is detailed in Section 3.4.2 and *Hudson et al.* (2007).

The necessary measurements of uncorrected diffusion coefficients at several sample thicknesses were done for 50–80 μm glass beads in the 250 K environment. The correction term was found to be at most 0.06 cm, or a 6% correction for a 1 cm thick sample. The shift in calculated diffusion coefficient is much less than the experimental error, even for the thinnest samples. For this reason, uncorrected measurements for salt crusts, though conducted on samples $\sim$1 cm thick, are accurate within the systematic errors. Mixtures were tested with sample columns 5 cm thick, a thickness which has a minimal correction contribution even at the warmer temperatures of *Hudson et al.* (2007).

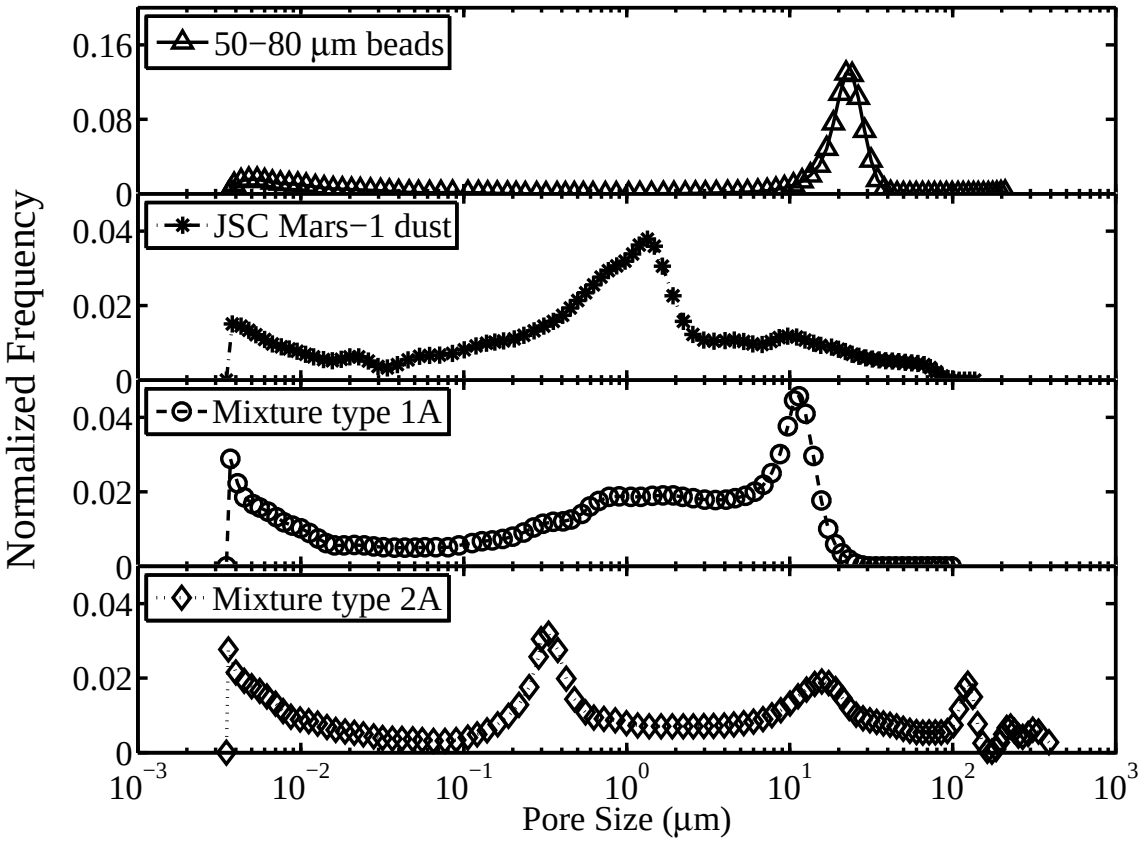

Figure 4.2: Normalized pore size distribution functions for four samples analyzed with mercury porosimetry

4.3.2 Pore structure

The porosity of the glass beads was determined with the basic method given in Section 3.3, while for mixtures it was estimated using equation (4.1). However, this latter method ignores the dust which may not only fill the interstices of the host sand but may also settle between the sand grains during agitation, thus pushing them apart and increasing the 'unfilled' volume. Salt crusts are even less amenable to simple interrogations or estimates of pore volume due to the unknown distribution of epsomite and sand grains following crystallization. Nevertheless, it is possible to determine the obstruction factor, the ratio of porosity to tortuosity, once the diffusion coefficient has been measured.

Four simulants were sent to Porous Materials, Inc. for analysis by mercury porosimetry. This technique reports pore size distributions, median pore diameter, pore volume and surface area. The simulants chosen for this analysis were pure 50–80 μm glass beads, pure crushed JSC Mars-1 dust, and the two most dust-rich varieties of Mixture Type 1 and Mixture Type 2 (Varieties "A" in Table 4.1). The pore-size distributions for these four materials are plotted in Figure 4.2.

Figure 4.2 reveals that the pore size for the 50–80 micron glass beads peaks sharply at ∼20–

25 microns. All distributions show significant tails at very small pore diameters, *i.e.*, 10 nanometers or less. These are likely to represent surface roughness, cracks, and other defects within individual grains in addition to very small passages between grains. While these passages do contribute marginally to the diffusible volume if interconnected, and to the tortuosity if blind, their contribution to the total flux will be negligible. As shown in *Clifford and Hillel* (1983), where pore sizes down to 1 nm are considered, pore distributions containing even a few percent porosity in larger (*i.e.,* micron-sized) pores experience most of their diffusive flux through these large spaces.

Examining the individual distributions reveals some interesting features. In crushed JSC Mars-1, the peak pore size, which is centered approximately on 1 micron, is much broader than for the more regular glass beads, and the pore distribution goes to zero almost nowhere below 100 μm. In the mixture containing both glass beads and JSC Mars-1 dust, the modal peak falls between the modal peaks of the two mixture components at about 10 microns. The pore diameter distribution in this material drops sharply to the right of this peak, being zero above 30 μm. This suggests that self-compaction and the availability of small grains acts to close off the largest pore spaces. Comparing the mixture of beads and JSC Mars-1 to the mixture composed of beads and 1–3 μm dust further underscores the effects of self-compaction. The micron-sized dust is much less dense than the crushed JSC Mars-1 and does not compress as readily under its own weight. The resulting multi-modal distribution has pore spaces indicative of close-packing of dust grains (*i.e.,* the peak at 0.3 μm), but also possesses a very significant fraction of pores greater than 100 microns across. In a material containing such large pores, which might be termed a 'fairy-castle' structure, these open spaces will accommodate the majority of the diffusive flux. However, these large pore spaces are unlikely to be connected as a high-diffusivity conduit throughout a thick porous medium; transport will be governed by the average resistive path experienced by a diffusing molecule which shall include segments of less open material. It should be cautioned that mercury porosimetry is a high-pressure intrusive technique and may result in a rearrangement of pores and particles; very fragile structures may be disrupted.

Of these four simulants, the one with the distribution which appears to have the lowest amount of large cross-section pore space available for transport is the 40% mass-fraction fines mixture of glass beads and crushed JSC Mars-1 dust. Effects that may be responsible for closing off large pores include altered bulk density, which enhances self compaction, and the availability of small particles to fill in the interstices. For further analyses of a broader selection of particle sizes and shapes, the reader is refered to the recent work of *Sizemore and Mellon* (2007). In Section 4.4.5 porosimetry measurements are used to estimate the tortuosity for these four samples.

4.4 Results

This section details the results of these investigations into the diffusive properties of glass beads, salt crusts, two types of bead and dust mixtures, and two types of pure dusts under Mars-like conditions. Figure 3.10 shows the vapor fluxes as a function of temperature for all simulants along with the evaporation rate curve for bare ice as given by *Ingersoll* (1970) for a dry atmosphere (data from the experiments of Chapter 3 are also included in that figure). Slightly different background temperatures used during the experiments result in the offset indicated by the arrows. The shift is nearly horizontal, indicating that flux is relatively insensitive to these small changes in absolute temperature.

4.4.1 50–80 μm glass beads at 250 K

Glass beads are the main component which comprises most of the more complex simulants used. Measurement of the compositionally and geometrically simple glass beads facilitates comparison with previous experiments (*Hudson et al.*, 2007). The beads are all nearly perfect spheres, 50–80 μm in diameter. Within a factor of two in friction threshold velocity, these are similar to the 100 μm size of the most easily lofted particles under martian conditions (*Greeley et al.*, 1980).

The dominant size of the beads is 50–80 μm, but the distribution has a significant tail down to smaller sizes as revealed in the particle size analysis in Figure 3.5 b); the smaller spheres can be seen in the SEM images in Figure 4.1c and 4.1d. For close-packed particles with such a size distribution, the minimum pore size is on the order of 10 μm and the maximum is $\sim$80 μm (see Section 3.3.1). At 600 Pa, the mean free path is $\sim$11.5 μm and diffusion should be dominated by Fickian processes of molecule-molecule collisions, but Knudsen interactions will contribute to an observable extent. The data for glass beads at 250 K in Chapter 3 are included in the data presented here. The weighted mean and standard deviations of the corrected diffusion coefficients is 3.69 ± 0.24 cm^2 s^{-1}. As mentioned in Section 4.3, the correction term for this simulant is $z_{\mathrm{corr}} \leq 0.6$ mm, and Figure 4.3 shows both the raw and corrected values. All raw values greater than 2 cm thicknesses fall within one standard deviation of the weighted mean.

If the Fickian dependence of diffusion coefficient on temperature and pressure, $T^{3/2}$ and P^{-1}, respectively, is used and typical Mars temperatures and pressures of 200 K and 600 Pa, respectively, are chosen, D(200 K) is determined to be 2.73 ± 0.28 cm^2 s^{-1}. The glass beads measured in these experiments have a mean geometric porosity of $44 \pm 2\%$, as determined from volume and mass measurements of the bulk sample and knoweledge of the true density of the particles.

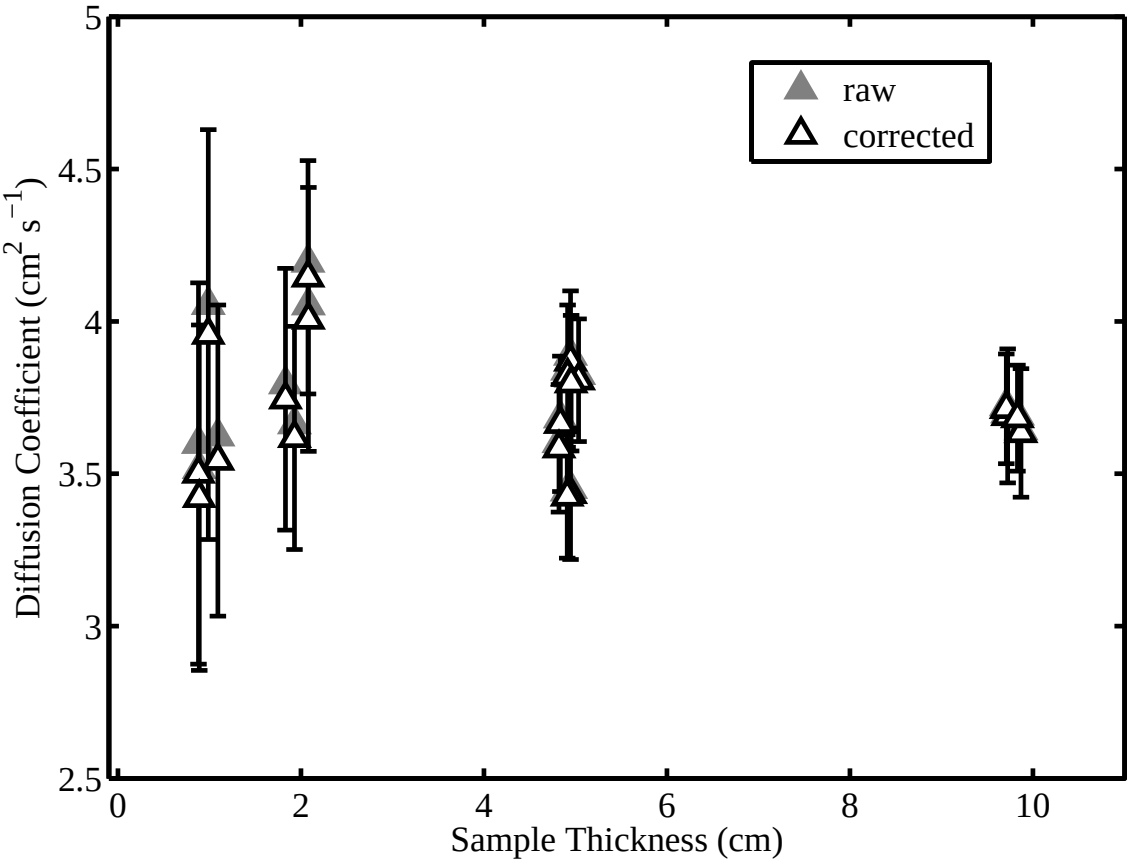

Figure 4.3: Raw and corrected diffusion coefficients for 50–80 μm glass beads at 250 K and 586 Pa. The correction term is only 0.06 cm; raw values are nearly indistinguishable from corrected values.

4.4.2 Epsomite salt crusts

The presence of sulfate salts on Mars, the frequency of observed duricrusts, and their potential for reducing soil porosity motivate their investigation. As convenient and consistent samples, glass beads cemented with magnesium sulfate salt are created in the laboratory and the diffusion coefficient is measured for a range of salt contents. Some inhomogeneities are observed within the salt crusts when they are broken following experiments. Outer layers of the crusts tend to be more cohesive than the center in samples with high salt contents. These layers may account for the majority of the diffusive resistance of the samples.

The diffusion coefficient data for the salt crusts is presented in Figure 4.4 which shows that the diffusion coefficient for crusts decreases with increasing salt content. The negative trend is expected, and a reduction in the diffusion coefficient by nearly a factor of 8 over that of pure glass beads occurs for salt concentrations of 18 wt% epsomite. Lacking measurements of the porosity, a tortuosity for the salt crusts cannot be calculated. Obstruction factors vary as the diffuson coefficient, and overall the factor is reduced from 0.14 to 0.02 between salt-free and the most salt-laden experiments.

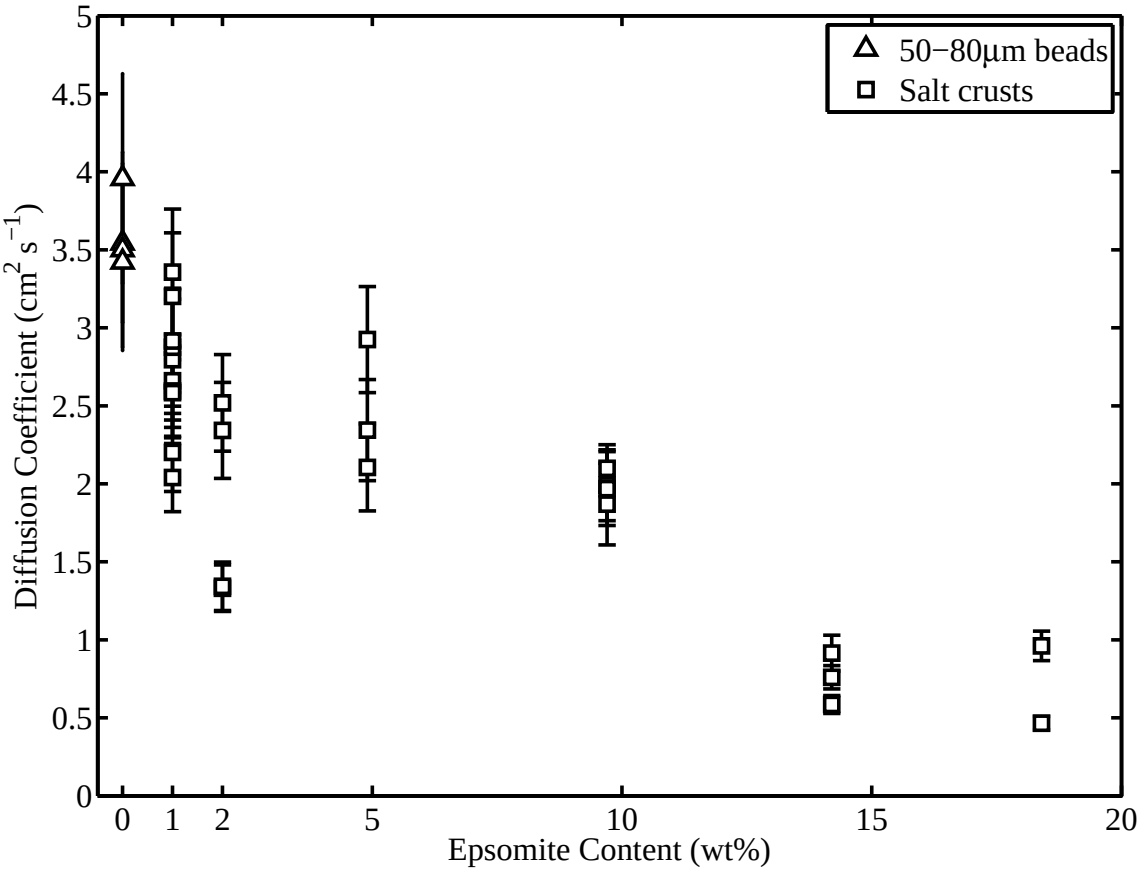

Figure 4.4: Diffusion coefficients for crusts of 50–80 μm glass beads and $MgSO_4 \cdot 7H_2O$ at 250 K and 586 Pa

4.4.3 Mixtures

The inclusion of small particles within a matrix of larger clasts can reduce the porosity available for vapor transport and has the potential to significantly change the diffusion coefficient (*Farmer*, 1976). The diffusion coefficient for mixtures of glass beads with both crushed JSC Mars-1 and 1–3 μm dust are plotted in Figure 4.5. For Mixture Type 1 (glass beads and crushed JSC Mars-1), the diffusion coefficient and obstruction factor decrease strongly with increasing dust mass fraction while measured porosity increases. However, for Mixture Type 2 (1–3 μm dust and glass beads), neither diffusion coefficient nor obstruction factor trend strongly with dust mass fraction, but an obvious positive correlation with porosity remains.

The calculated porosity for both types of mixtures are displayed in Figure 4.6. Also included is data for the measured porosity of packed samples of both pure crushed JSC Mars-1 and pure 1–3 μm dust. The trend for both types of mixtures as the mass fraction of dust increases is for the total porosity to increase and approach the values exhibited by pure dust. In the case of bead and 1–3 μm dust mixtures, this value seems to be reached at $X_f \approx 40\%$, the trend with beads plus crushed JSC

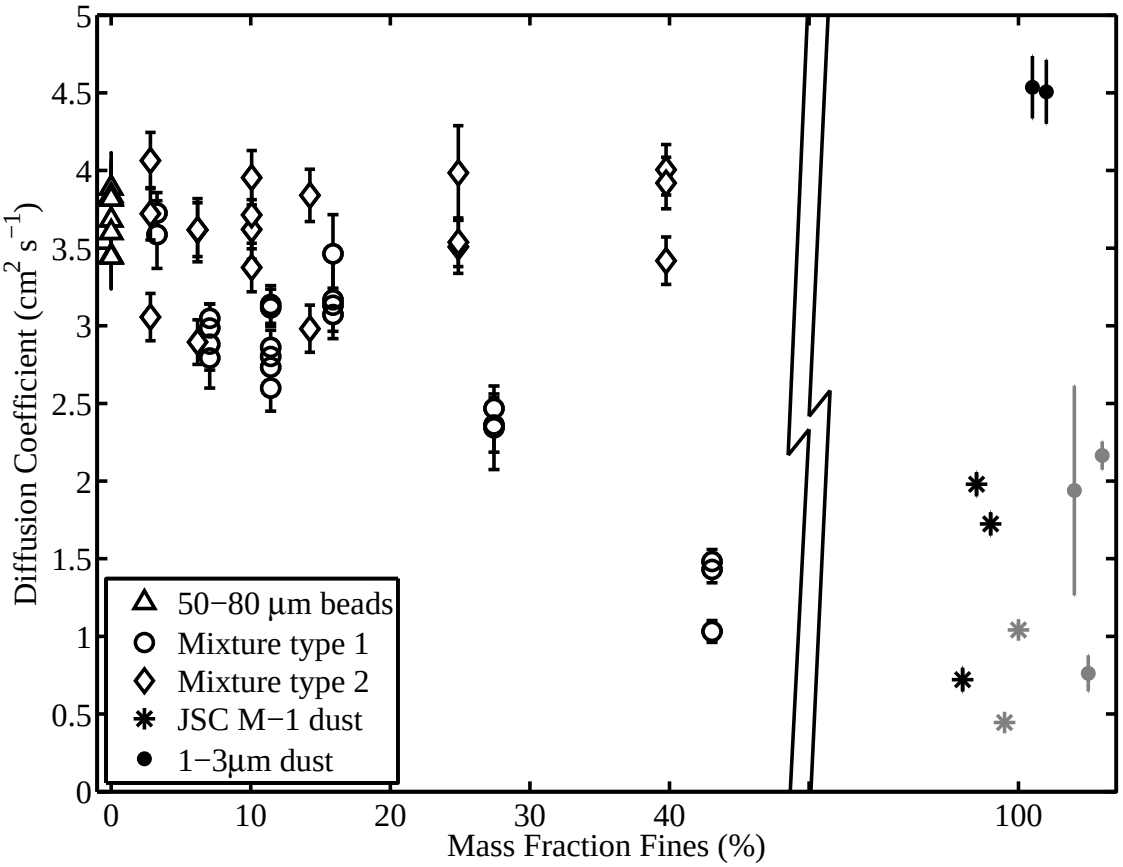

Figure 4.5: Diffusion coefficients for mixtures of 50–80 μm glass beads with crushed JSC Mars-1 (Mixture Type 1, circles), mixtures of glass beads with 1–3 μm dust (mixture type 2, diamonds), and diffusion coefficients for pure dusts (asterisks and filled circles). All data obtained at 250 K and 586 Pa. Mechanically compacted dust experiments are indicated in gray. All data to the right of the break are 100% dust by mass, but are separated for clarity.

Mars-1, if linear, would reach this point at approximately $X_f \approx$60%. The overall increase in porosity with dust content indicates that the included dust tends to coat the larger particles upon mixing and acts to keep them apart, thereby substantially increasing the total volume available. This is in contrast the case where dust might fill the available pore spaces of a coarse medium without increasing the spacing between larger particles.

The large increase in measured porosity for the micron-sized dust mixtures is counterbalanced by an apparent minor increase in the value of tortuosity, such that the obstruction factors ($D/\mathcal{D}_{12}$) hardly change with X_f. For mixtures containing beads and crushed JSC Mars-1, however, the increase in porosity is apparently superseded by a tortuosity which increases faster, leading to smaller obstruction factor with larger dust mass fraction. Since tortuosity should be constant with diffusion regime, all else being equal, it must be the case that high proportions of micron-scale dust give rise to very small pores, changing the overall structure and producing a greater tortuosity.

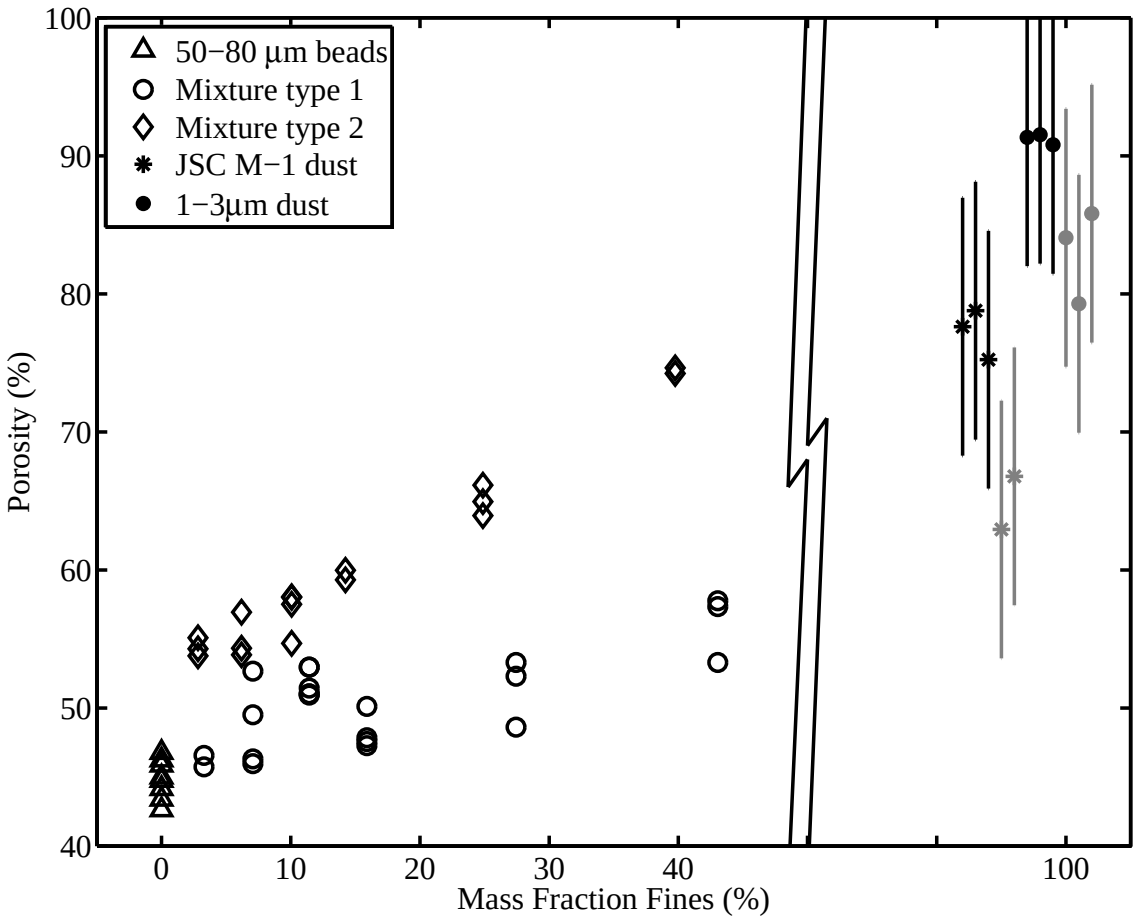

Figure 4.6: Porosities for pure glass beads (triangles), mixtures of beads and fine dusts (open circles and diamonds), and pure fine dusts (asterisks and closed circles). Mechanically packed dust samples are in gray. All data to the right of the break are 100% dust by mass, but are separated for clarity. Porosity of the mixtures of glass beads and crushed JSC Mars-1 (Mixture Type 1) increase slowly, while the less self-compacting mixures containing beads and micron-sized dust achieve much higher porosities.

4.4.4 Dusts

Pure samples of the 1–3 μm dust and crushed JSC Mars-1 were examined in both packed and unpacked configurations. Loose dust may be considered a crude approximation to airfall dust, while compaction simulates the effect of burial.

Loose dust was poured into the sample caddy and planed off to 5 cm thickness. The low-density 1–3 μm dust exhibited no observable self-compaction even in samples of this thickness. Both dust types were seen to deposit with visible sub-millimeter gaps between aggregates. Though aggregates of the size and density observed in this sample handling method are unlikely to be supportable by the thin martian atmosphere, airfall dust deposits on Mars will likely form low-density aggregates in response to electrostatic forces, resulting in deposits of even lower bulk density.

For compacted samples, the equivalent of between 5 and 8 cm of loose dust was pressed into the sample caddies with a flat circular plate. Air in the pore spaces was allowed to escape around the edges of the plate. Following compaction, the sample was weighed to determine a bulk density and total thickness.

The experiments show that packed and unpacked JSC Mars-1 has a range in diffusion coefficient from 0.45–1.98 cm^2 s^{-1}, with a weighted mean value of 0.77 ± 0.04 cm^2 s^{-1}. Data from both packed and unpacked samples are included in these values since their ranges overlap. The 1–3 μm dust exhibits a larger distinction between loose and compacted samples, with weighted mean values of 4.71 ± 0.22 and 1.64 ± 0.11 cm^2 s^{-1}, respectively.

4.4.5 Sample tortuosity

In Section 3.5.1.3 independent Fickian and Knudsen diffusion coefficients were determined and a tortuosity was calculated for 50–80 μm glass beads of 1.8 ± 0.6. This compares favorably with earlier measurements of tortuosity of glass spheres such as those by *Hoogschagen* (1955) who determined τ=1.3–1.5 and *Currie* (1960) who theoretically calculated values between 1.3 and 1.7 and experimentally found τ=1.4–2 for larger spheres (380 μm to 6 mm).

Here the method of *Zalc et al.* (2004), described in Section 2.5, is employed to estimate D_K and then the geometric (*i.e.*, independent of diffusion regime) tortuosity for the four selected samples of Section 4.3.2. This calculation takes as inputs the measured effective diffusion coefficient, porosity, free-gas diffusion coefficient, and the chord length distribution function, $p(l)$.

To retain consistency with earlier work (*Hudson et al.*, 2007) and with the work of a number of previous investigators, the method of *Wallace and Sagan* (1979) is used to determine the free-gas diffusion coefficient, $\mathcal{D}_{12}$, noting that other calculation methods produce values that are different from this by as much as a factor of 2, but are typically closer.

The chord length distribution is calculated from the pore size distribution, $V(x)$, (Section 4.3.2 and Figure 4.2 using the method described in *Gille et al.* (2002), which approximates the pore spaces as cylinders of varying lengths. Thus, $p(l)$ is given by

$$p(l) = \frac{\int_0^L x \cdot A_0(l,x) \cdot V(x) \mathrm{d}x}{\int_0^L x \cdot V(x) \mathrm{d}x}, \tag{4.2}$$

where l is random chord length within a pore, x is the pore diameter, L is a length parameter, and $A_0(l,x)$ is the chord length distribution of an infinitely long cylinder of diameter x. $A_0(l,x)$ is given

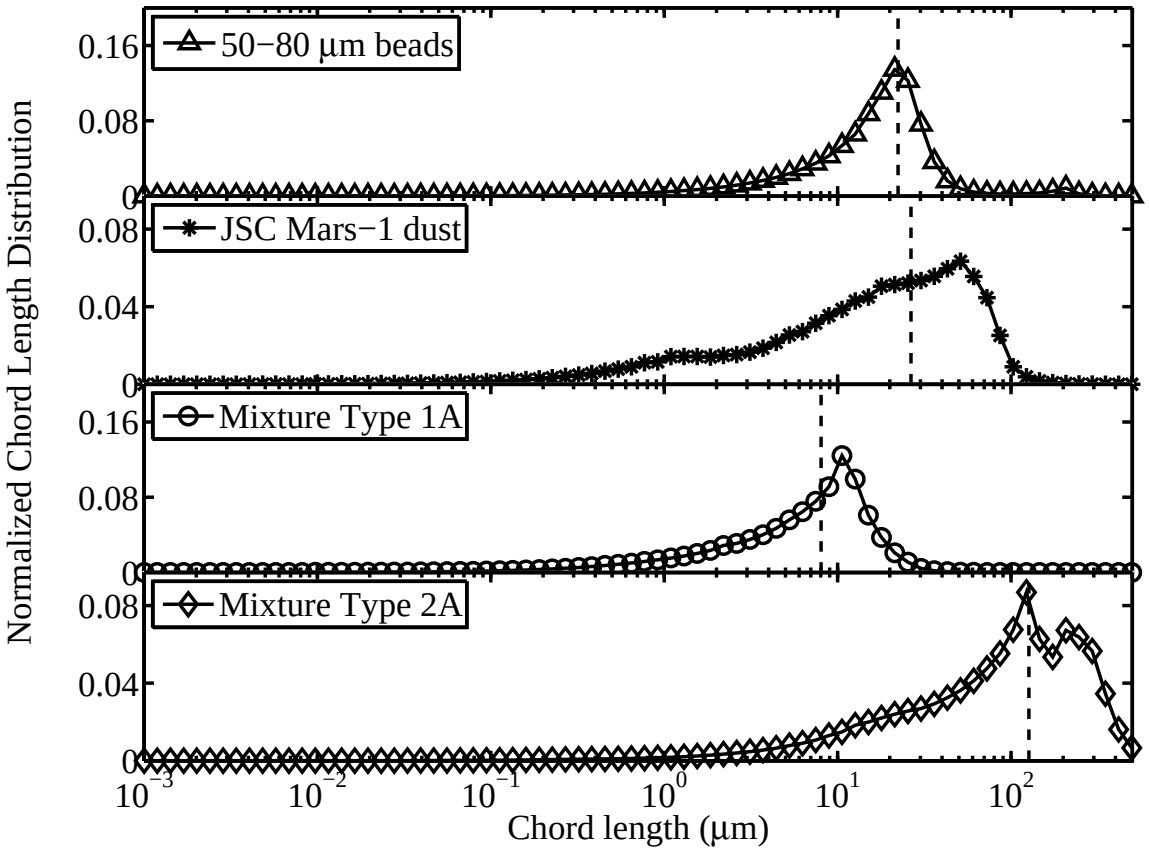

Figure 4.7: Normalized chord length distributions functions computed from pore size distributions. Vertical dashed lines are first moments of the chord length distributions, $\langle l_p \rangle$.

by *Gille et al.* (2001) as expressions involving Gauss' hypergeometric functions, ${}_2F_1$:

$$A(l,x) = \frac{3l}{4x^2} \cdot {}_2F_1\left(\frac{1}{2};\frac{5}{2};3;\frac{l^2}{x^2}\right),\ l < x \tag{4.3}$$

$$= \frac{3x^3}{4l^4} \cdot {}_2F_1\left(\frac{1}{2};\frac{5}{2};3;\frac{x^2}{l^2}\right),\ l > x. \tag{4.4}$$

The assumption of cylindrical pores may be violated in media with irregularly shaped grains.

The first and second moments, $\langle l_p \rangle$ and $\langle l_p^2 \rangle$, are computed in the standard way. Applying these techniques, chord length distributions and first moments are obtained, and these are displayed in Figure 4.7. Table 4.2 displays the mean diameter, $\bar{d}$, and first moment of the chord distribution, $\langle l_p \rangle$. Also computed and tabulated are the quotient $\langle l_p^2 \rangle / 2\langle l_p \rangle^2$, which describes the deviation of the chord length distribution function from an exponential distribution, and the calculated tortuosity, τ.

As Table 4.2 illustrates, the value of τ thus determined for glass beads is close to the expected values of $\sim$1.5. The other tortuosity values cover a range up to 6, which is high compared to

ranges used in early estimates of tortuosity (*e.g.*, 3–5 in *Smoluchowski* (1968))), and to more recent experimental studies (*Sizemore and Mellon*, 2007). Uncertainty in these numbers arises both from the variation in $\mathcal{D}_{12}$ and the possible violation of the cylindrical pore assumption. Taken together, these tortuosity estimates are not appreciably different from those used in previous diffusion studies, but their variation underscores the uncertainty of this quantity for many porous materials and highlights the importance of measuring the effective diffusivity directly, in the Fickian regime if possible. It would be useful to further explore the effects of particle size mixtures and salt content on pore structure and pore size distribution, and to determine the conditions which give rise to the greatest change in soil diffusive properties.

4.4.6 Summary

Table 4.3 presents a summary of the data for each type of simulant. For mixtures and salt crusts, the range of observed values of D, ϕ, and D/D_{12} are presented. Other simulants show weighted means and standard deviations.

Correction terms are applied to experiments performed on glass beads at 250 K under CO_2, though this correction ($z_{\mathrm{corr}} = 0.6$ mm) results in a comparable but smaller shift in the data than systematic scatter and formal errors. Corrections for salt crusts are determined to be unnecessary because the correction term for pure glass beads of the same thickness was found to be negligible at these temperatures. All other experiments are performed with 5 cm thick samples, which provides enough diffusive resistance to reduce the correction term below systematic errors; hence the values reported are unmodified.

Diffusivities for all simulants fall within the range of 0.47–4.7 cm^2 s^{-1}, as seen in Figure 4.8. Extrapolation to the Mars-appropriate conditions of 200 K and 600 Pa via the Fickian dependence of the diffusion coefficient on temperature and pressure yields the range 0.34–3.30 cm^2 s^{-1}. The obstruction factor for most simulants is between 0.02 and 0.20. Tortuosities calculated for four simulants cover a range of 1.5–6.

Simulant	ϕ, %	$\bar{d}$, μm	$\langle l_p \rangle$, μm	$\langle l_p^2 \rangle / 2\langle l_p \rangle^2$	τ
50–80 μm Beads	44	18.74	22.29	1.501	1.66
Crushed JSC Mars-1	77	5.35	26.46	1.002	6.01
Mixture Type 1A	56	4.42	8.03	0.794	1.68
Mixture Type 2A	75	32.7	126.65	0.903	3.82

Table 4.2: Porosities, average pore diameters, first moments of the chord length distributions $\langle l_p \rangle$, the exponential distribution deviation term, and tortuosities for four samples analyzed with mercury porosimetry.

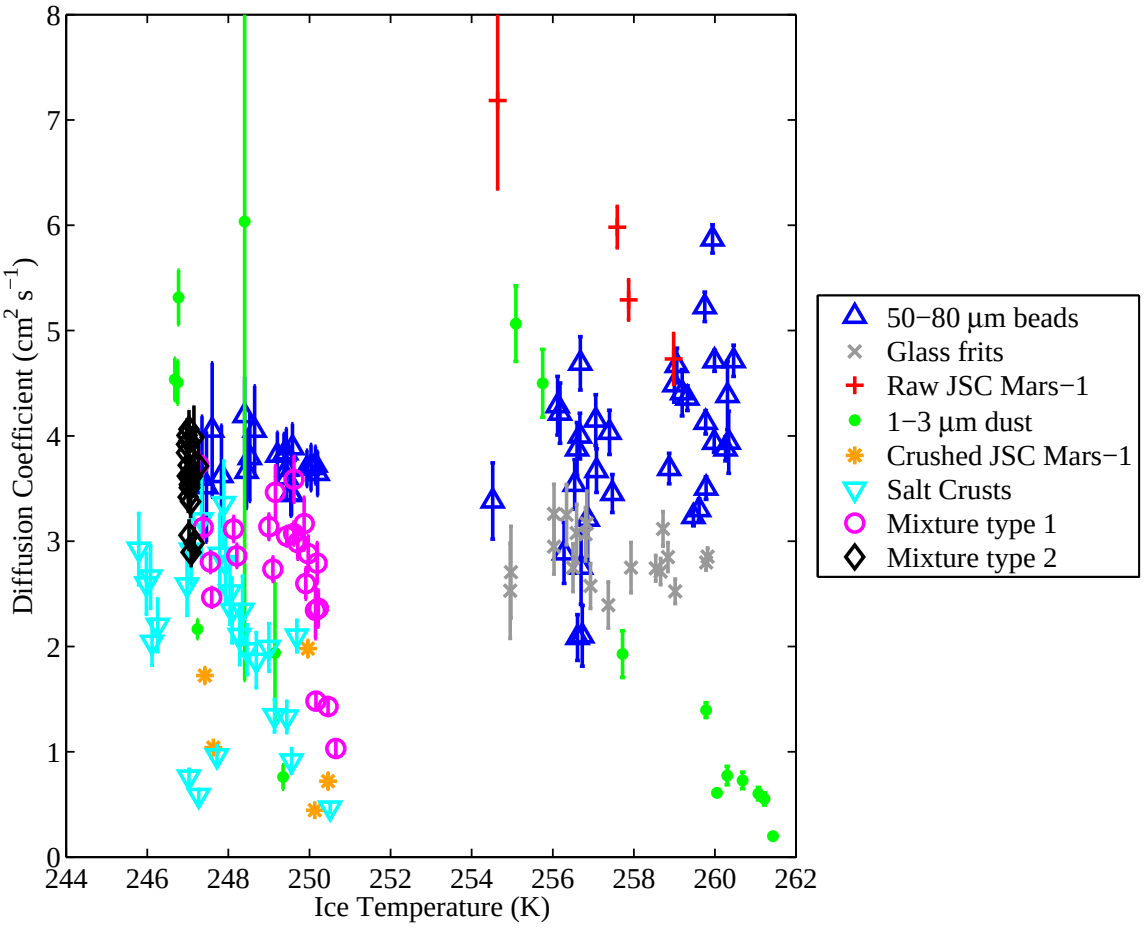

Figure 4.8: Diffusion coefficients for all simulants from Chapter 4 and Chapter 3.

Sample	T_{ice}, K	D, cm^2 s^{-1}	D^1, cm^2 s^{-1}	ϕ, %	$\mathcal{D}_{12}$, cm^2 s^{-1}	$D/\mathcal{D}_{12}$
50–80 μm beads	249.0 ± 0.4	3.69 ± 0.24	2.57 ± 0.16	44 ± 2	24.5 ± 3.0	0.150 ± 0.014
Beads + $MgSO_4 \cdot 7H_2O$	247.9 ± 0.4	0.47 – 3.36	0.34 – 2.34	N/A	24.8 ± 1.5	0.019 – 0.133
Beads + JSC Mars-1	249.4 ± 0.4	1.03 – 3.73	0.74 – 2.68	46 – 58	25.0 ± 1.6	0.041 – 0.150
Beads + 1–3 μm dust	247.1 ± 0.2	2.90 – 4.06	2.11 – 2.90	54 – 66	24.8 ± 1.5	0.117 – 0.160
JSC Mars-1, loose	246.7 ± 0.2	1.47 ± 0.08	1.03 ± 0.06	77 ± 9	24.7 ± 1.5	0.060 ± 0.006
JSC Mars-1, packed	247.5 ± 0.2	0.59 ± 0.03	0.42 ± 0.02	65 ± 9	25.9 ± 1.6	0.023 ± 0.002
1–3 μm dust, loose	248.9 ± 0.2	4.71 ± 0.22	3.36 ± 0.16	83 ± 9	24.9 ± 1.5	0.190 ± 0.015
1–3 μm dust, packed	248.6 ± 0.2	1.64 ± 0.11	1.16 ± 0.08	91 ± 9	25.1 ± 1.5	0.062 ± 0.006

Table 4.3: Summary of results for experiments carried out at 250 K and ~586 Pa in CO_2. Weighted averages and standard deviations are given when samples are approximately uniform. Minimum to maximum intervals are given where variation among samples is responsible for the range of observations. [1] Diffusion coefficients extrapolated to 200 K and 600 Pa using $D \propto T^{3/2}P^{-1}$, as appropriate for Fickian diffusion

4.5 Discussion

4.5.1 Experimental errors

See Section 3.5.1.1 for a discussion of systematic errors in the experimental setup. In brief, variations exist because gas mixing in the chamber atmosphere which is not necessarily the same among

different experiments, and because the localized measurement of humidity may not reflect the average environment across the sample surface. These issues are mitigated by multiple experiments which improve measurement statistics.

In Section 2.6.2 (*Hudson et al.*, 2007), it was shown that thermodiffusion is less than concentration diffusion by a factor of $0.8(m_2/m_1)(\Delta T/T)(p_1/\Delta p_1)$. The largest value of $\Delta T/T$ for any experiment is 0.015, while the average value is 0.009. For $(p_1/\Delta p_1)$, the extreme and average values are 1.8 and 1.2. Thus, the maximum expected contribution from thermodiffusion is 5% while more typical values are closer to 2%. In Section 2.6.3, an experssion for the ratio of barodiffusion to concentration diffusion was given as $0.6(\Delta p_0/p_0)$. The maximum possible Δp_0 is the saturation vapor pressure of water at 250 K (76 Pa), thus giving a maximum barodiffusion contribution of 7%. The value will be smaller for samples with higher permeability which therefore have smaller pressure gradients.

4.5.2 Advection

The corrected diffusion coefficient found for the glass beads in the experiments performed at 250 K is 3.69±0.24 cm^2 s^{-1}. By comparison, the value obtained in Section 3.5.2 for these same simulants at 263 K is 4.49 ± 0.69 cm^2 s^{-1}. Adjusted for the 12 K temperature difference using a $T^{3/2}$ dependence, and a P^{-1} correction for the overall 20 Pa pressure difference, this latter value would be 4.13±0.64 cm^2 s^{-1} at 250 K. The lower vapor pressures should result in a lower advective contribution in the colder chamber. Reducing the 263 K experiment value by a further 3% (as calculated in Section 2.6.1) gives 4.00±0.62 cm^2 s^{-1}, a value whose center is much closer to that measured in the 250 K chamber. However, since the error ranges of the two diffusion coefficients overlap, concluding that advection is responsible for the difference is not possible using this data.

4.5.3 Salts and salt crusts on Mars

The existence of salts on the surface of Mars is well established (*Clark and van Hart*, 1981; *Vaniman et al.*, 2004; *Yen et al.*, 2005), as is their association with surface crusts (*Landis et al.*, 2004; *Wang et al.*, 2006). *Chevrier and Mathé* (2007, and references therein) use lines of evidence from *in situ* and remote sensing observations to conclude that high sulfur abundances (compared to the surface of the Earth) are found over most of the known martian surface and that sulfur, particularly in the form of sulfate, is an important component in the evolution of the martian regolith.

The mobility of these salts and their observed ability to cement soil grains implies a potential for pore restriction or closure, and a concomitant reduction in the diffusivity of the salt-bearing soils and crusts. Recent observations by the Mars Exploration Rovers indicates the possibility of two populations of salt-bearing soils: lightly-cemented surface duricrusts containing a few percent of salt, and more loosely consolidated subsurface deposits of light-toned material which may be as

much as 50 wt% sulfate salt (*Cabrol et al.*, 2006; *Yen et al.*, 2007; *Wang et al.*, 2007).

Up to 50 wt% iron sulfate is inferred at the Paso Robles site observed by Spirit (*Cabrol et al.*, 2006). Many other sites present indications that magnesium sulfate is the dominant phase. Greater than 20 wt% in the wall of the trench named The Boroughs in Gusev crater was determined to be Mg and Ca bearing sulfate. The Mg/Ca ratio is high; approximately 5.

Analyses of sulfate stability fields under Mars surface conditions suggest that the most likely hydrated forms of magnesium sulfate are the monohydrate kieserite, or amorphous phases with from 1.2 to 2 molar units of water. Metastability may permit the persistence of more hydrated phases (*e.g.*, starkeyite, $MgSO_4{\cdot}4H_2O$) which may have originally formed under more favorable climate conditions. The existence of sulfate phases common on Earth (6-hydrate hexahydrite or 7-hydrate epsomite) in the shallow subsurface of Mars is unlikely at present (*Vaniman et al.*, 2004).

Regardless of their hydration state, salt crystals may form barriers to diffusion in Mars soils just as they do on Earth. Caliche, a calcium-bearing mineral cement, frequently occurs in terrestrial desert environments, forming layers are often sufficiently resistive that they completely impede the movement of water resulting in perched water tables or aquacludes, the disruption of which produces artesian springs. Such phenomena have been hypothesized to occur on Mars as part of gully formation mechanisms (*Malin and Edgett*, 2000). Though magnesium-bearing salts are rather water soluble (56.0g/100g water for $MgCl_2$, 35.7g/100g for $MgSO_4$ (*Lide*, 2003)) and would not form effective barriers to liquid water, they could impede or prevent the movement of vapor molecules.

In contrast to the sulfate-rich subsurface deposits observed by the rovers in isolated localities, indurated surface soils, called duricrust, have been observed at all Mars landing sites and are believed to be extensive (*Presley and Christiensen*, 1989). The physical properties of surface crusts at the Viking lander sites have been calculated and similar properties over much of Mars' surface are predicted (*Moore*, 1992). The cohesive strength of surface soils at Viking sites falls in the range of 1 to 11 kPa (the cohesion of dry clayey silts on Earth, such as dried mud flats, is between 10 and 30 kPa). Crusts at the edge of trenches carved by the Opportunity rover are shown in *Weitz et al.* (2006), and the cementation of soils at Gusev is discussed by *Cabrol et al.* (2006) and *Landis et al.* (2004). Conclusive observations of the exact mineral composition and physical structure of these crusts does not yet exist, but evidence supports that the cohesion of Viking crusts is related to the presence of SO_3 and Cl compounds (*Clark et al.*, 1977). Measurements by the MER instruments reveal large quantities of sulfates at numerous sites. Taken together, these data strongly suggest that salts, particularly sulfate salts, play a large role in duricrust formation. The laboratory-grown crusts have at most 10% by weight $MgSO_4$, a fraction smaller than that of the subsurface salts exemplified by the Paso Robles and Tyrone type soils.

In these experiments, a small amount of sulfate salt ($\sim$1%) produces a small reduction in the measured diffusion coefficient of 50–80 μm beads on the order of 1 $cm^2\ s^{-1}$. Further increases in

salt content have little apparent effect until >10 wt% epsomite, where reductions of D by a factor of 5 to 10 are observed.

As the water in the saturated slurry of the laboratory-grown crusts evaporates during formation, crystals preferentially form at points of low surface energy where nucleation is facilitated, such as grain contact points (see Figure 4.1 c). These crystals cement the grains of the material together once the water has evaporated, resulting in some reduction in porosity. Increasing the salt content may further reduce the porosity, but the majority of vapor transport pathways remain open. Beyond 5 wt% epsomite, the experimental scatter is reduced, which suggests that the overall change in pore geometry has become uniform among samples. As still more salt is added, the final porosity is substantially decreased, tortuosity rises, and D drops significantly. Laboratory salt crusts which completely block vapor diffusion have not been observed.

The protocol used for making laboratory crusts involves significant liquid water. This is not representative of any known present-day surface condition on Mars, yet geomorphic and geologic evidence, for example at Meridiani Planum, indicate that standing or subsurface water may have been a significant part of the geologic history in certain regions. The measurements here pertain to several studies invoking crust formation and solute transport processes that require small amounts of water. *Cabrol et al.* (2006) and *Landis et al.* (2004) discuss possible processes for the formation of salt crusts in the soils of Gusev crater. They suggest that humidity precipitated as frost during the cold Martian night, low thermal inertia of surface materials, and the presence of melting-point-lowering salts will result in a small transient liquid phase immediately following sunrise. Prior to evaporation, this liquid will dissolve salts which are then reprecipitated around the soil grains, resulting in crust formation. Such processes, they suggest, may only occur during particular seasons and possibly only during favorable years. *Wang et al.* (2006) conclude that the total amount of water activity necessary for the formation of Gusev crusts is likely to be low, as suggested by the limited quantity of evaporite deposition at the surface, the limited leaching of minerals by water, and the concentration of soluble elements. It may therefore be the case that the subsurface salt deposits and surface crusts are formed at different times, on different time scales, and with significantly different amounts of aqueous activity. The subsurface salts may be the source for a slow upward migration of chemical species which ultimately form the weak surface crusts. Taken together, the results of *Cabrol et al.* (2006); *Landis et al.* (2004); *Wang et al.* (2006) indicate formation mechanisms for salt crusts on Mars exist. Note, however, that they involve less water than the lab methods used here.

Intriguingly, the bright deposits revealed in rover wheel tracks have not yet been seen to outcrop anywhere in undisturbed regolith, leading to the hypothesis that their placement and vertical extent may be controlled by the surface-atmosphere interface through evaporation, set by the thermal wave penetration. The diffusion of oxidizing species from the atmosphere or surface layer of the regolith may also affect sulfate deposition. *Wang et al.* (2007) report long-term observations of two types

of light-toned soils (termed "yellowish" and "whiteish") at the Tyrone site during the Spirit winter campaign. The "yellowish" soils are observed to change spectral character after at least 175 sols exposure to martian surface conditions, becoming more like the "whiteish" soils. This indicates that the more deeply buried "yellowish" soils were not in equilibrium with the current environment and are undergoing some sort of chemical change, which *Wang et al.* suggest may be dehydration of $Fe_2(SO_4)_3 \cdot 7H_2O$.

These experimental results suggest that surface duricrusts which show weak degrees of cementation and likely have $< 10\%$ of soluble salt content will not present a substantial barrier to vapor transport, perhaps at most a factor of 2 reduction over uncemented soil. Higher salt content could lead to greater reductions in the diffusion coefficient, and soil salt contents of the appropriate concentrations have been observed. However, the deep sulfate salts which have thus far been uncovered by MER have appeared as loose subsurface powders with small particle sizes. If conditions elsewhere on Mars have permitted these subsurface salts to become mobilized and cemented, it is possible that the highest barriers to diffusion may be found beneath, rather than at, the surface.

4.5.4 Diffusion in Mars dusts

Dust is present everywhere on Mars and is a significant part of the present-day climate cycle. It forms an active surface layer which may be lofted and re-deposited by dust storms, and may also be incorporated deep into the regolith. Two types of dust with differing particle size distributions are examined in both mechanically packed and unpacked configurations.

The diffusivity values for packed and unpacked JSC Mars-1 dust samples overlap and cover a range from 0.4–2.0 $cm^2\ s^{-1}$, indicating that mechanical packing does little to alter the properties of this simulant, and that there is wide variation between successive simulants. The large particle size range for this dust allows larger grains to interlock and create a supporting matrix which retains large pore spaces even under externally applied compaction. Still, each sample is unique in its precise geometry, and variations among samples exist. The larger spread in diffusion coefficients at $X_f = 1$ than at lesser dust fractions (see below) indicates that the presence of larger particles at moderate dust fractions helps create a similar geometry from sample to sample through self-compaction, while the less massive pure dust samples are subject to greater variation. Mechanical packing has a significant effect on 1–3 μm dust, decreasing its diffusivity from 4.71 ± 0.22 to 1.64 ± 0.11 $cm^2\ s^{-1}$.

Thin surface airfall dust layers would not be subject to compaction forces but might instead be "fluffed" by electrostatic forces. Burial depths of greater than several decimeters could create increased packing of interstitial airfall dust over a wide areal extent. To affect near-surface vapor fluxes, soils compressed by deep burial would have to be subsequently exhumed. Widespread exhumation is possible, but the thermophysical and spectral properties of such deposits would be distinct from loose dust. Dispersal in water could also produce low-porosity, low-diffusivity deposits

composed of fine dust or coarse/fine mixtures, but the invocation of liquid water as a component in the diagenesis demands additional support from available geologic or geomorphic context data.

The possibility that diffusion coefficients in dust-bearing soils could be reduced by a factor of 2 or more as a function of depth may significantly affect models which include interaction with more than the surface regolith.

4.5.5 Sand and dust mixtures

Aeolian processes on Mars can produce well-sorted bedforms such as ripples (*Sullivan et al.*, 2005), and large-scale features such as dunes (*Greeley et al.*, 1992). The Microscopic Imagers on the MER spacecraft have observed soil grains down the limit of resolution (31 μm per pixel), and an observable particle size range of 50–200 μm has been determined (*Herkenhoff et al.*, 2004; *Jerolmack et al.*, 2006). Dust particles below the resolution limit are undoubtedly present at the rover sites and are likely to be present in significant quantities at dustier surface locales. The ubiquitous presence of dust on Mars' surface and observations of dust-rich, low thermal inertia regions suggest the strong possibility that mixtures of sand and dust-sized particles occur in some regions. Fluvial processes, volcanic processes, and impacts can agitate and mix surface regolith. If settling times after such disturbances are rapid, the unsorted or poorly-sorted character of the bulk material may be retained in the subsequent deposit. Agitation by shifting winds or long-term evolution through thermal expansion and contraction may mix initially separate particle size fractions at the surface in the absence of these more energetic processes.

Mixtures of two types have been produced and observed, using the 50–80 μm glass beads as the coarse fraction and two types of dust particles. These are not meant to be representative of any particular Mars soil, but instead show the behavior of regolith diffusivity as a function of dust content. These experiments support the expectation that even in the absence of mobilized and recrystallized salt acting as a pore-filling agent, the diffusive properties of loose surface soils are affected by the presence of pore-filling materials such as dust. Martian fines have a mean particle size of a few microns (*Greeley et al.* 2000, and references therein), similar to the 1–3 μm dust. Crushed JSC Mars-1 contains a range of particle sizes from sub-micron to 0.1 mm. These investigations have focused on homogeneous mixtures of sand and dust-sized particles, though *Farmer* (1976) suggests that thin dust mantles produced by airfall may fill the interstices of coarser material such that the diffusion coefficient is significantly reduced. The sample preparation method used includes initial mechanical agitation, but no subsequent compaction. The range of dust contents in the samples examined range from a clast-supported sediment with a very minor amount of included dust to a matrix-supported dust-rich deposit containing a minor proportion of separated, larger grains.

The difference in behavior between the two types of mixtures could be very significant for predictions of diffusive behavior of soils and sublimation lags on Mars. The trend seen in Figure 4.5

indicates that very small particles (1–3 μm dust) admixed with coarser grains do little to increase the diffusive resistance to vapor flux if the whole sample is not mechanically compacted. The diffusion coefficient is independent of the mixing fraction up to $X_f \approx 0.4$.

If the distribution of finer material includes a broad spectrum of particle sizes, *i.e.*, grains roughly equivalent in size to the coarser fraction in addition to fine particulates (as in crushed JSC Mars-1), then there is a marked reduction in diffusivity as the mass fraction of fines increases. This effect, for uncompacted mixtures, is a reduction in D to $\sim$2.5$\pm$0.3 cm^2 s^{-1} at $X_f = 0.4$.

The measured geometric porosity for both types of mixtures increases with X_f in a linear fashion as shown in Figure 4.6. The porosity of micron-sized dust and beads would reach a value equivalent to pure-dust samples at around $X_f = 0.6$. The trend with JSC Mars-1 mixtures is shallower, but the ultimate porosity for pure dust is also lower. As seen in Table 3.1, the porosity of dusty soils can be quite large in the absence of mechanical compaction. Even when compressed, the minimum porosity of pure-dust soils is never less than $\sim$ 80% in the case of 1–3 μm dust, and $\sim$ 60% in the case of crushed JSC Mars-1.

As expected for a constant experimental value of D_{12}, the behavior of the obstruction factor follows that of the diffusion coefficient. The increase in overall porosity toward pure dust demands that the degree of convolution of the pore geometry become larger to account for the decreasing diffusion coefficient. This is facilitated at lower dust contents in the case of crushed JSC Mars-1 by the broad particle size range. Dust composed only of micron-sized particles does not begin to have an appreciable effect on the pore geometry until its mass fraction is substantially higher. However, the implied increase in tortuosity may not occur for some micron-sized dust mixtures since it has been shown that the diffusion coefficient of uncompacted pure micron dust is *higher* than that of any observed mixture. The low bulk density of the dust, the roughly equivalent particle sizes, and the angular particle shapes prevents closer packing and greater degrees of obstruction. Only mechanical compression (or dispersal and settling in a dense lubricating medium such as water) would further reduce the observed diffusivity, thereby increasing tortuosity.

To determine a tortuosity for each of these simulants and track how their structures change with dust content, porosimetry measurements of additional samples would be needed. Increasing pressure so as to measure the diffusivity in a purely Fickian regime (and thus be able to use equation (2.3)) becomes difficult as the smallest pore sizes reach the scale of microns. The pore size distribution measurements have indicated that particle size mixtures can either reduce the availability of large pore spaces (*i.e.* Mixture Type 1–A) or greatly enhance the number and size of the largest pores (*i.e.* Mixture Type 2–A). For JSC Mars-1 and mixtures of glass beads with fines, the pore distributions measured were broad. According to the results of *Clifford and Hillel* (1983, 1986), who show that larger pore spaces accommodate a majority of the flux, even a high proportion of pore spaces experiencing significant numbers of molecule-wall collisions should be less significant to the

overall diffusion rate than the few large pathways which may be open in an uncompacted, dust-rich structure. Thus, a real soil may have many pore spaces which experience primarily Knudsen-type diffusion under Mars surface conditions, but a small proportion of large pores undergoing significantly Fickian diffusion may dominate the vapor flux.

Aeolian processes can be efficient at sorting particles, resulting in particle assemblages which consist mainly of grains of similar size. Wind ripples such as those in Meridiani Planum show a small scale variation in the size of surface particles, but the interiors of the ripples are composed of grains on the order of 50–200 μm (*Sullivan et al.*, 2005). Given the ubiquitous presence of micron-sized dust, and its tendency to adhere to solid surfaces, it is highly likely that some fraction of dust is incorporated into the soil. Dustier locales than Meridiani Planum may exhibit even higher concentrations of fines. However, the results presented here suggest that the diffusive properties of Mars soils will not be greatly affected by the presence of moderate amounts of micron-sized dust. Moreover, soils composed primarily of dust may exhibit the highest diffusivities. This conclusion, combined with the large specific surface areas for adsorption and expected large porosities of dusty deposits, supports the notion that dusty regions on Mars are significant components of past and present-day water cycles and are not isolated from the atmosphere.

The probability that an otherwise homogeneous layer of diffusive material will contain a crack or other efficient path to vapor transport will scale with the area considered. Such pathways may be caused by thermal cycling, micro-tectonic phenomena, slumping, or (in areas where possible) wetting and drying effects. The samples observed in this controlled laboratory environment are relatively small and are not generally subject to phenomena which cause cracking. However in certain cases where the material exhibited a moderate degree of cohesiveness (*e.g.*, pure dusts or mixtures incorporating crushed JSC Mars-1) cracking was initiated by slumping into the void left by sublimating ice. Sudden changes in mass loss rate, as would be expected if the crack extended from the surface to the ice, were not observed.

On Mars, such internal deformations of poorly to moderately cohesive regoliths may prevent cracking on the scale of millimeters from affecting the loss rate of ice which is several centimeters beneath the soil surface. If the material were highly cohesive a crack may penetrate deeply and remain unfilled, resulting in a locally depleted ice layer. The radius of influence of the crack will depend on the mechanical properties of the surrounding soil and whether the crack reaches the ice table.

4.5.6 Implications

The samples studied cover a wide range of particle size distributions, porosities, and salt contents. Yet in no case has more than an order of magnitude reduction in fluxes or simulant diffusivity been observed. At most, the diffusivity of the baseline soil simulant (50–80 μm glass beads) has been

reduced by a factor of about 8, with more common reductions being a factor of 2–3. Magnesium sulfate salt produces a moderate reduction at low salt concentrations, but has its greatest effect above 10 wt%. Mixtures of coarse and fine particles can produce a decreased diffusion coefficient (as for crushed JSC Mars-1) or no observable effect (as for 1–3 μm dust). Mechanical packing of pure dust samples results in a reduction in diffusivity by a factor of 4–8. Overall, regolith materials similar to the simulants studied should not be expected to reduce the transport of water vapor by much more than an order of magnitude. The mechanism of formation of a diffusive barrier is significant in determining the degree of restriction.

Dust and larger particles could be incorporated into ice-rich deposits in a variety of ways, and these dirty ices could then produce lags upon ice sublimation. Two examples of sublimation lags can be considered: mid-latitude glaciers and polar layered deposits. For mid-latitude glaciers to persist under climate conditions similar to the present for timescales comparable to obliquity variations, they would need to be buried beneath a lag of order tens of meters or more.

Polar layered terrain is composed of alternating bright and dark layers which are interpreted as relatively dust-poor and dust-rich deposits, respectively. The layering is believed to be tied to climate cycles and sequential eras of precipitation and sublimation. The dust in the layers may either be deposited contemporaneously with the ice, or could be emplaced as part of cyclical global dust storms. In both cases, the dust which collects to form the lag would not be subject to compaction forces until the next period of ice deposition. Sublimation during an ice-loss phase would build a lag of uncompressed micron-sized dust particles. If such a lag does not become thick enough to exhibit self-compaction (possibly on the order of a few decimeters), these experiments show that such an uncompressed material would not reduce surface fluxes of water vapor by more than an order of magnitude relative to unprotected ice at the same temperature (see Figure 3.10). Additionally, the amount of dust deposited with the ice would have to be significant to build up a monolayer of dust after the sublimation of meters of ice. Recent observations by subsurface radar sounding instruments estimate an impurity content ranging from 2–15% for the North and South Polar Layered Deposits (*Picardi et al.*, 2005; *Plaut et al.*, 2007), consistent with gravity and topography inversions for density (*Zuber et al.*, 2007).

The diffusivity of a given deposit can be estimated from remote observations as well as geologic and geomorphic contextual information. By considering the context as well as remote or *in situ* observables, three quantities which feed into porosity and tortuosity estimations: the dust content, degree of compaction, and grain size distribution, may be constrained. The results obtained may be used along with homogeneous media diffusion quantities in subsequent models of complex regoliths by adding the contributions of layers with relatively higher or lower dust contents in series.

All observations of salt-bearing and salt-encrusted soils on Mars have thus far been made at low-latitude sites where there is no buried ice. As yet there are no *in situ* observations of soil

mechanical and geometric properties from a site known to overly subsurface ice. The Phoenix lander could perform the first such observations. Trenching activities will also be reveal the presence of a cohesive surface layer if one exists. Chemical experiments performed by the MECA instrument's Wet Chemistry Lab will probe the type and amount of soluble salt component in the soil and the contribution of this salt to the diffusive barrier may be interpreted in light of the laboratory experiments presented.

Chapter 5

Ice Filling Experiments

5.1 Chapter Summary

These experiments demonstrate for the first time the deposition of subsurface ice directly from atmospheric water vapor under Mars surface conditions. Deposition occurs at pressures below the triple point of water, and therefore in the absence of a bulk liquid phase. Significant quantities of ice are observed to deposit in porous medium interstices; the maximum filling fraction observed in the experiments is ∼90%, but the evidence is consistent with ice density in pore spaces asymptotically approaching 100% filling. The micromorphology of the deposited ice reveals several noteworthy characteristics including preferential early deposition at grain contact points, complete pore filling between some grains, and captured atmospheric gas bubbles. The boundary between ice-bearing and ice-free soil, the "ice table", is a sharp interface, consistent with theoretical investigations of subsurface ice dynamics. Changes of surface albedo are shown to affect ice table morphology through their modulation of the local temperature profile. A variety of atmospheric humidity regimes and experiment durations are employed to provide information about the rate at which the pores fill. Accumulation of ice is shown to reduce the diffusive flux and thus hinder further ice deposition via constriction of available pore space. Numerical models of the experiments based on diffusion physics are able to reproduce experimental ice contents if the constriction parameterization has expected contributions in addition to reduced porosity. Several phenomena related to the evolution of subsurface ice are discussed in light of these results and interpretations are given for a range of potential observations to be made by the Phoenix Scout Lander.

5.2 Parameter Choices

The atmosphere of present-day Mars is dry, and the upper levels of the regolith are subject to ice-filling vapor density gradients on the order of 10^{-6} kg m^{-4}. Under these conditions, the maximum rate of ice deposition would fill a regolith with ∼40% porosity in approximately 10^5 years. Obviously,

such timescales are impractical for measurable ice contents to be developed in the laboratory. To enhance the deposition rate, a more humid atmosphere and a stronger vapor density gradient than found on Mars today are employed. This allows useful experiments to be run in hours or days rather than years. The way in which these choices affect the physics of diffusion (including an increased advection and thermodiffusion contribution) is discussed in Section 5.6.1.

The surface of Mars experiences substantial diurnal and annual variations in surface temperature. The mean annual vapor pressure experienced by ice within the top few thermal skin depths will be biased toward higher pressures at shallower depths due to the nonlinear dependence of vapor pressure on temperature. This gives rise to a gradient which will pump water vapor into the subsurface if the atmospheric vapor density is above that at equilibrium with ice at depth. Rather than employing a varying surface temperature to create a gradient, the laboratory setup instead uses a constant thermal gradient across the sample. The resulting large gradient in vapor density permits the rapid growth of ice.

A rough analytical approximation to the rate of ice growth may be obtained by assuming D is independent of depth, and thus $\partial\sigma/\partial t$ is proportional to $\partial^2\rho_1/\partial z^2$, according to Equation (2.26). Using the Clausius-Clapeyron expression for vapor pressure, the second derivative of the vapor density gradient may be approximated by

$$\frac{\partial^2}{\partial z^2}\left(\frac{p_{sv}}{T}\right) \approx \frac{p_{sv}}{T}\left[\left(\frac{H}{RT}\right)^2 - 4\frac{H}{RT} + 2\right]\left(\frac{1}{T}\frac{\Delta T}{\Delta z}\right)^2, \tag{5.1}$$

for a linear temperature gradient. Here, H is the enthalpy of sublimation and R the universal gas constant. This simple scheme assumes that D is also independent of time; hence it does not include pore constriction.

Converting Equation (5.1) to density using the ideal gas law, the time necessary to achieve significant accumulation of ice in a laboratory setup, $\sigma/\dot{\sigma}$, may be estimated. Since the temperature gradient enters quadratically in Equation (5.1), a strong temperature gradient is clearly desirable for experiments.

Figure 5.1 plots contours of the number of days required to achieve complete pore filling using $\Delta T/\Delta z = 13$ K cm^{-1} and an ice-free diffusivity of 4.7 cm^2 s^{-1}. The figure reveals a parameter window where significant ice volume accumulates within days. The pore filling times are underestimates for any given set of conditions since this model does not incorporate pore constriction, but it clearly shows the time advantage gained by operating at higher temperatures. Lower pressure accelerates the growth because of higher diffusion coefficients, but once the Knudsen regime is reached, the mean free path of molecules no longer increases with decreasing pressure. Overlying the contours are the conditions of mean annual temperature and pressure on Mars' surface today, the conditions in this experimental setup, and the conditions in the Dry Valleys of Antarctica.

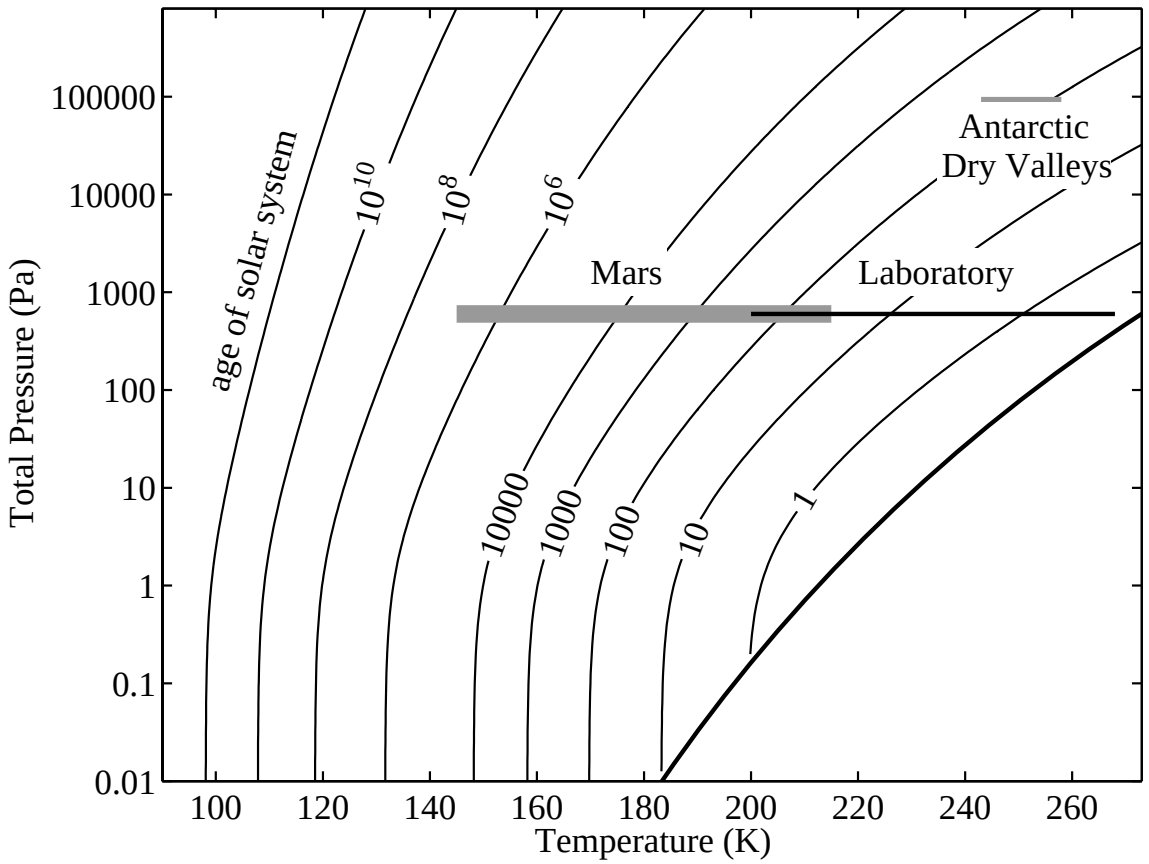

Figure 5.1: Contours of time in days to deposit a quantity of ice equivalent to 42% porosity for a temperature gradient of 13 K cm^{-1} using the simple model developed in Section 5.2 which assumes no constriction. The diffusivity of the simulant (500 μm glass beads) is extrapolated to appropriate temperatures and pressures using the Fickian formalism, which gives $D \propto p^{-1}T^{3/2}$. The heavy black curve is the saturation vapor line. The range of conditions on the surface of Mars, in the Dry Valleys of Antarctica (*Doran et al.*, 2002), and the experimental setup are indicated by horizontal bars. Note that the assumed temperature gradient for the laboratory experiments do not apply in these environments and that the growth rates would therefore be slower.

5.3 Experimental

5.3.1 Environmental control

Experiments were conducted at the Mars Simulation and Ice Laboratory at Caltech. A custom built stainless-steel vacuum chamber from LACO Technologies was used to achieve Mars-like pressures and a controlled humidity environment. The environmental chamber is a vertical cylinder with a removable lid, viton O-ring seals, and multiple electrical and fluid feedthroughs. The volume of the chamber is 2.3×10^{-2} m^3. Important environmental parameters which are controlled through the course of an experiment are the chamber pressure, atmospheric vapor density, and the top and bottom boundary temperatures of the sample column. These are maintained through 5 simultaneously operating PID control loops.

A schematic of the complete experimental setup is presented in Figure 5.2. Several interacting systems work to control the atmospheric vapor density and total pressure in the chamber. A vacuum pump continuously evacuates the chamber during an experiment and the pumping speed can be manually adjusted by a needle valve in the vacuum line. Evacuation is compensated by input of a controlled mixture of dry and humid CO_2. To create humid CO_2, dry CO_2 is passed through a mass flow controller (PID loop #1) and a sparger into a 5 L vessel of distilled, deionized water. The temperature of the water in this bubbler is maintained at 38° via PID control (loop #2) of a hemispherical heating mantle. The gas output of the bubbler leads to the main chamber. Pressure in the bubbler is forced down by the evacuation of the main chamber but is maintained at approximately 60 mbar by PID loop (#3) actuation of the dry gas input which feeds the bubbler. By maintaining a constant bubbler temperature and pressure, the vapor content of the head space gas in the bubbler is maintained to within about 10%. The bubbler pressure is kept slightly bellow the boiling point of water so that the head space gas has a high water content (typically ∼85–90% relative humidity at 30°C). This humid gas is fed into the main chamber through a mass flow controller optimized for regulating low-pressure flows. This MFC is also under PID control (loop #4) where a humidity sensor (described below) provides input to the loop by measuring the vapor density of water at the sample surface. A heating tape around the gas line from the bubbler prevents water from condensing before it reaches the chamber. A third mass flow controller regulates the input of dry gas into the main chamber (loop #5). The low-pressure MFC control loop (#4) first adjusts the input of humid gas to achieve the desired chamber vapor density. The dry gas loop (#5) then brings the total chamber pressure to 6 mbar. Pressure feedback between these two loops is rapid and settles within ∼5 minutes to a steady state which can be tuned so the controllers are far from saturation.

In this experiment, as much water as possible is removed before introducing sub-zero temperatures. Porous media simulant which has been kept dry in an oven at 400 K is cooled to approximately 320 K in a desiccator and then poured into place in the sample chamber. The chamber is then sealed and pumped down to 600 Pa and maintained with dry CO_2. The sample surface is maintained at 320 K by a halogen lamp until the measured vapor density drops below 0.1 g m^{-3}, usually several hours. Any water remaining in the chamber when the cold plate is activated is quickly gettered onto the lowest level of the soil. The low vapor densities measured in the cold, dry chamber suggest that any ice present when the chamber is opened to humid gas should only persist in the bottom 1–2 cm of the sample where the soil is $\lesssim$220 K, and it is later shown that this amount of ice is negligible.

The sample column is chilled from its base via a copper cold plate. A methanol recirculating chiller acts to keep the cold plate at 183±1 K. Thermal losses through silicone grease connecting the cold plate and the contact plate attached to the sample caddy results in a sample base temperature of approximately 193±2 K. The cold plate, cooling lines, and all other cold surfaces in the chamber are coated with polyurethane foam to slow heat conduction and prevent gettering of atmospheric

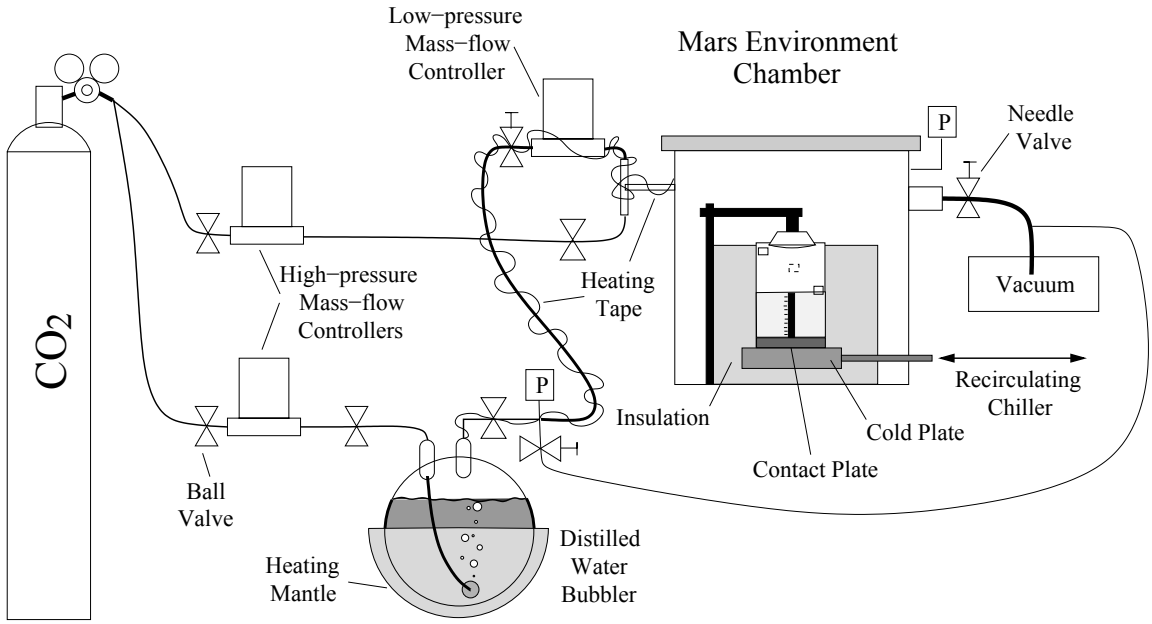

Figure 5.2: Schematic of experimental setup highlighting gas humidification and delivery, and pressure control. The sample container within the environment chamber at right is expanded and annotated in Figure 5.3. The datalogger and electrical interface connections are not shown.

water in locations other than the soil column. The surface of the sample is maintained at 268 K via another independent PID loop controlling a halogen lamp and reflector placed approximately 6 cm above the sample surface. The input for the lamp controller is the surface temperature as measured by the uppermost thermocouple of the sample thermal probe described in the next section.

5.3.2 Sensors

The pressure in the main chamber is monitored using an MKS Baratron 626 capacitance manometer with a full-scale range of 10 torr. The pressure in the bubbler is monitored with an MKS 902-series piezo-transducer, with a full range of 1000 torr.

Water content of the chamber atmosphere is monitored using RH/RTD sensors (Honeywell model HIH-4602-C) which simultaneously report relative humidity (RH) and ambient temperature at the sensor via a platinum resistance temperature device (RTD). The ITS-90 formulation (*Hardy*, 1998) is used to convert the relative humidity into a partial pressure of water. Vapor density is calculated via the ideal gas law using the measured RTD temperature.

Temperature as a function of depth is monitored with a custom temperature probe. The probe consists of 11 T-type thermocouples which protrude at half-centimeter intervals from a perforated plastic tube. The sensing ends of the thermocouples are approximately one half centimeter from the plastic body of the sensor assembly and are held in place with a fin of kapton tape. This arrangement minimizes the effects of vertical heat transport through the sensor body to the thermocouple heads

and allows each thermocouple to be in close equilibrium with the local thermal environment.

The data from an experiment are recorded with a National Instruments Compact DAQ–9172 datalogger. All process variables are monitored throughout an experimental run at approximately three-second intervals. Averaging of these data is performed every minute and the averages are logged. Since all process variables change slowly, this does not compromise the integrity of the dataset.

5.3.3 Sample preparation and method

The porous medium used in all experiments is composed of soda lime glass beads obtained from AGSCO Corporation (mesh size #30–40). The mean particle size is 500 μm, no more than 10% larger than 700 μm and no more than 20% smaller than 400 μm (AGSCO technical data sheet). The density of the glass is 2.5 ± 0.1 g cm^{-3}. The diffusivity of these beads were measured using the techniques of *Hudson et al.* (2007) under 586 Pa CO_2 at 250 K, and was found to be 4.7 ± 0.5 cm^2 s^{-1}. The glass beads' size place them in the sedimentological category of "coarse sand".

The sample caddy is a thin-walled squat plastic cylinder ~7.5 cm in diameter, the base of which is a snugly fit brass contact plate (see Figure 5.3). Oven-dried simulant is poured into the caddy to a depth of 5 cm. The temperature probe is then inserted through the sample and the relative humidity sensor is positioned such that it penetrates the surface of the soil by a few millimeters. The tops and exposed wires of the sensors are wrapped in aluminum foil to reduce heating by the halogen lamp.

The chamber is sealed and evacuated to 600 Pa and maintained at this pressure with input of dry CO_2 for several hours to remove residual water. The recirculating chiller is then activated and the sample is cooled for at least 6 hours until the sample temperature profile reaches steady-state. At all subsequent times the temperature profile is close to linear, but changes in sample thermal conductivity due to ice deposition and heat losses through the caddy walls result in minor deviations following exposure to humid gas. Once thermally equilibrated, the humid CO_2 line is opened and the humidity stabilizes at the desired value.

At the conclusion of the experiment, the chamber is purged and the ice-bearing sample and caddy are extracted to a 260 K freezer. The sample caddy is affixed to a custom extrusion device and the sample is sliced horizontally at half-centimeter intervals. Each layer is removed by scraping and brushing (in the case of poorly consolidated soils) or sawing (in the case of ice-rich soils), and collected in a glass beaker. Samples from each layer are immediately weighed, giving a total mass (ice + simulant), m_t. Beakers of ice-bearing sample are then placed into an oven at 390 K for a minimum of 24 hours. The dried samples are cooled to freezer temperatures in a desiccator. They are weighed again at the same temperature as the ice-bearing samples to obtain the dry simulant mass per layer, m_s.

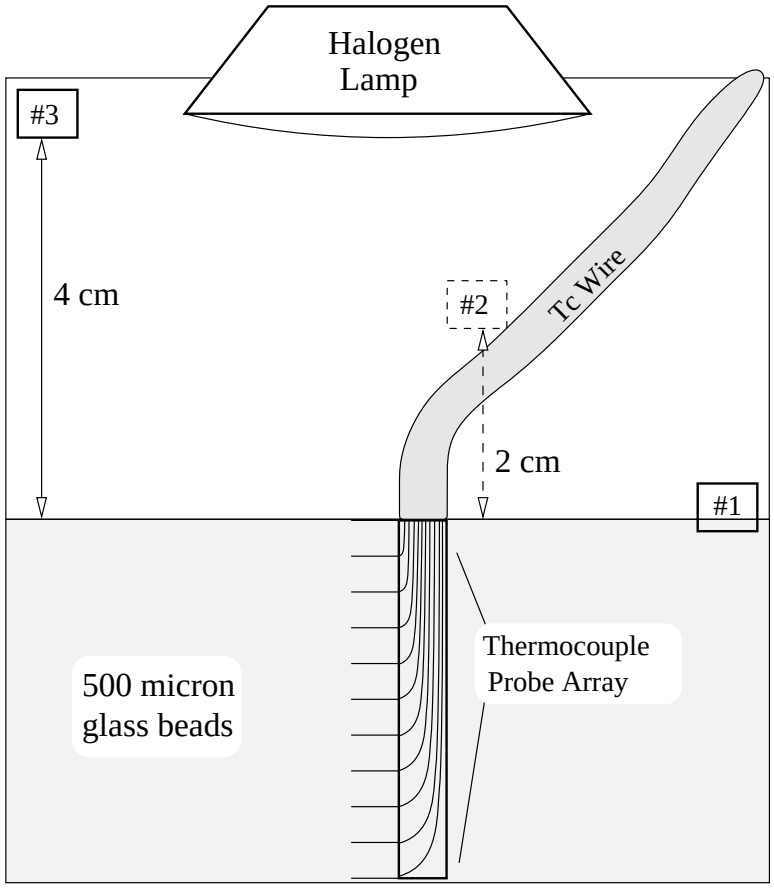

Figure 5.3: Schematic of sample container. Numbered boxes are positions of RH/RTD sensors. Sensor #1 has its sensing face buried ∼2 mm beneath the sample surface. Sensor #1 and Sensor #2 (against the back wall of the cylindrical caddy) are directly illuminated by the lamp. Sensor #3 is not directly illuminated, but is in close proximity to the lamp reflector. Thermocouple leads are wrapped in aluminum foil and cast a shadow over part of the sample surface.

5.3.4 Data analysis

Difference in mass before and after baking is the gravimetric water content. The combined height of all samples measured at the conclusion of the experiments is within ∼1 mm of the pre-experiment values, indicating negligible bulk expansion. For 500 μm glass beads, the bulk density is determined to be $\rho_{\rm bulk} = 1.46 \pm 0.01$ g cm^{-3}. Layer thicknesses are calculated from the measured mass of dry soil as $\delta z = m_s/(\rho_{\rm bulk} A)$, where δz is the thickness of layer z, and A is the area of the sample caddy.

Over the range of temperature encountered in this experiment, the density of bulk ice varies by ∼1%, and it is assumed that all deposited ice has a density of $\rho_{\rm ice} = 918$ kg m^{-3}. The mass of water per layer allows the calculation of ice density relative to free space, $\sigma = m_w/v = (m_t - m_s)/(\delta z A) = \rho_{\rm bulk}(m_t/m_s - 1)$, where m_w and v are the mass of ice and the total volume in a given layer. The maximum possible ice density relative to total sample is $\sigma_0 = \phi_0 \rho_{\rm ice}$, where ϕ_0 is the ice-free porosity and $\rho_{\rm ice}$ is the density of pure ice, and thus the filling fraction is σ/σ_0.

Duration, [hrs]	ρ_1, [g m^{-3}]	Max filling, [%]	z_{ice}, [cm]
0	1.60	0±1	0
6	1.60	11±2	1.1
12	1.60	15±3	0.6
18	1.60	21±2	0.2
24	1.60	29±3	0.1
24	1.60	29±3	0.1
24	1.60	26±3	0
24	1.60	29±3	0
48	1.60	42±3	0
48	1.60	43±3	0
72	1.60	54±4	0
72	1.60	55±4	0
96	1.60	64±5	0
96	1.60	76±4	0
98	1.60	71±9	0
120	1.60	65±4	0
122	1.60	71±5	0
331	1.60	75±5	0
530	1.60	90±4	0
24	0.60	10±2	2.2
24	0.85	13±2	1.8
24	1.10	21±2	0.5
24	1.35	26±3	0.1

Table 5.1: List of experiments. z_{ice} is ice table depth; a value of 0 denotes surface ice.

A control experiment was run to test the degree of ice accumulation during sample analysis. A sample was prepared in the same manner as other samples, but was never exposed to a humid chamber atmosphere. The amount of water collected by the sample during analysis is less than 0.4% filling fraction, negligible compared to all non-zero experiment times.

5.4 Results

Experiment durations, target surface vapor densities and observed ice table depths are given in Table 5.1.

5.4.1 Diffusive ice morphology

The deposition of ice in porous media at conditions below the triple point of water experimentally demonstrates ice-vapor diffusion and deposition in the absence of a liquid phase. Significant deposition occurs at all sample depths, indicating vapor diffusion as the primary mechanism for H_2O transport. Though quasi-liquid films may be present under these conditions in the shallow (T>250 K) regions of the sample (*e.g., Elbaum et al.*, 1993) they would be discontinuous or absent at greater depths with lower temperatures.

Small chips of ice-encrusted beads from several sample depths were examined with an optical microscope in the cold room; Figure 5.4 displays selected images. Figures 5.4 a and b show ice necks connecting individual beads to a larger bulk mass of beads and ice. The necks form annuli around grain contacts, the edges of which are concave toward the contact (see panel b). The shape and location of these necks is consistent with ice growth models based on free-energy arguments (*Hobbs and Mason*, 1964). Panel c shows turbid ice filling the interstices between several beads. Monocrystalline ice should not significantly scatter light and would appear clear; the turbidity implies the presence of crystalline defects or included air. Panel d shows a socket formerly occupied by a bead, revealing the tight association and good thermal contact between ice and the grains of the medium.

Panels e and f reveal bubbles within the ice which are tens of microns across. Spread throughout the sample, such voids could measurably reduce the bulk density of the ice. Though trapped atmospheric gases are common in compressed snowpack ice, their occurrence in diffusively derived ice has not been commented on previously. It thus seems that future landed missions which seek to extract information about ancient climates and atmospheres would be able to find trapped pockets of relic gases in subsurface ice even if that ice were not the result of precipitation.

5.4.2 Ice table morphology

Recent modeling investigations into subsurface ice deposition on Mars have shown that the ice table itself is a sharp boundary between ice-bearing and ice-free soil (*Schorghofer and Aharonson*, 2005). These results differ from earlier models of *Mellon and Jakosky* (1993) which exhibit a more gradual transition spanning several model layers. *Schorghofer and Aharonson* (2005) suggest that the difference may be due to differences in numerical implementation, rather than different physics or underlying assumptions. The experiments reported here exhibit sharp interfaces, the depth and morphology of which are controlled by temperature and atmospheric vapor density. In experiments which develop ice tables beneath the sample surface the mechanical cohesion of the beads exhibits a transition between completely unconsolidated and well-bound over a distance of order one grain diameter.

Because of this sharpness, the ice table shape may be easily seen by brushing away the unbound beads and examining the surface of ice-cemented grains. Figure 5.5 shows one such example: an experiment where some surface ice developed in the colder shadow of the thermocouple wires, but where there remained some warmer, unshadowed beads not yet bound by ice. The top of the RH/RTD sensor is directly illuminated by the lamp and experiences a temperature 5–15 K warmer than the sample surface. This produces a small depression in the ice table which is $\sim$1 mm larger than the sensor diameter. A minor deepening of the ice table exists at the walls of the sample due to heat leakage from the caddy. The ice table is nearly flat in regions not perturbed by shadows,

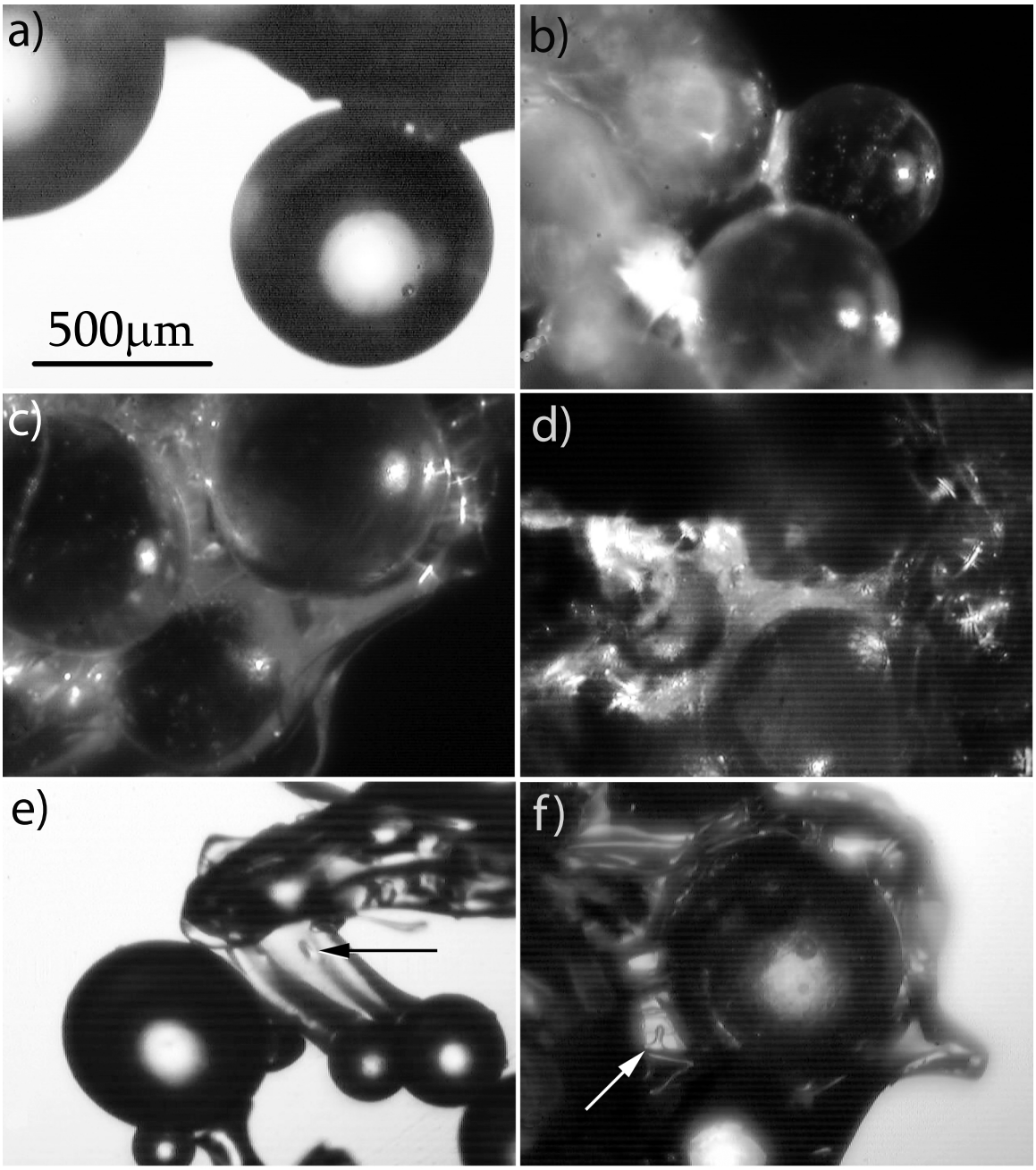

Figure 5.4: Images of the porous medium (500 μm glass beads) after exposure to experimental conditions. Images a, e, and f are back-lit; the scale bar applies to all images. Images a–c are from the 331 hour experiment, d–f are from a 72 hour experiment; all were performed at a nominal vapor density, monitored by sensor #1, of 1.6 g m^{-3}. a–b) Ice necks holding beads in place. Neck shapes are consistent with predictions of ice nucleation and growth based on surface energy. c) Beads embedded in pore-filling ice; the cloudy appearance suggests the presence of air bubbles or other defects. d) Sockets of ice formerly occupied by beads. e–f) Fine necks and pore-filling ice, respectively. Air bubbles trapped within the ice are indicated by arrows.

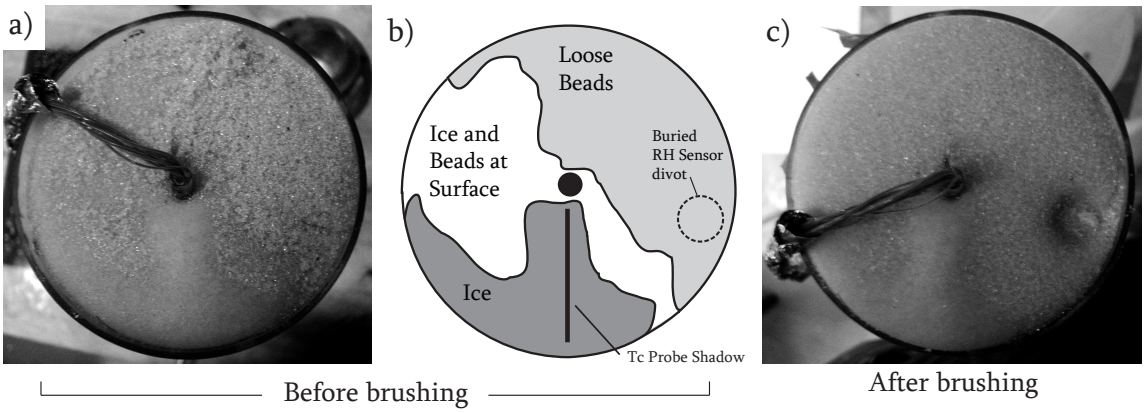

Figure 5.5: The sample surface after 96 hours of exposure to a humid atmosphere. a) The surface as it appeared prior to brushing. b) Schematic indicating a region of free surface ice, an intimate ice and bead mixture, and a region with multiple layers of ice-free beads. The position of the thermocouple wire shadow is indicated. c) The surface after brushing away loose beads, revealing the divot formed around the warm RH/RTD sensor.

edge effects, or the warm sensor, with depth variations less than 1 mm across several cm of surface. Such a uniform depth of the stability boundary indicates a radially uniform temperature profile with isotherms parallel to the surface.

On Mars, patches of darker or brighter dust will experience different radiative equilibrium temperatures for the same amount of insolation. *Sizemore and Mellon* (2006) have examined the consequences of this phenomenon with two- and three-dimensional numerical models. The effects of spatial variations in albedo on the near-surface ice table morphology have been experimentally examined with this facility. A gold-coated disk (albedo ≈1.0), a matte black disk (albedo ≈ 0.1–0.2), and an unaltered, clear disk (control) were placed on the sample surfaces to produce local temperature perturbations. An image of disk placement is in Figure 5.6 a). Samples were chilled and exposed to a humid atmosphere for 48 hours. A T-type thermocouple epoxied to the underside of each disk measured equilibrium temperatures of 263.1 K, 270.8 K, and 268.2 K, for the gold, black, and control disks, respectively. The clear control disk temperature is within 0.1 K of the glass beads (268 K). Following exposure, the disks were removed and the depth to the ice table was measured. A wire mesh placed above each sample defined the positions for ∼1100 individual staggered-grid depth measurements performed with a needle graduated at 1 mm intervals. These measurements were then interpolated to produce the depth maps seen in Figures 5.6 c and d.

To produce the ice table in Figure 5.6 d, the vapor density at the sample surface was set at a nominal value of 1.6 g m^{-3}. As can be seen from both the photograph taken with oblique illumination (Figure 5.6 b and the depth map (5.6 d, the ice table exhibits significant undulations in depth on a scale comparable to the radius of the albedo disks. The depth to the ice table around the rim of the high-albedo disk is the shallowest observed (∼0.3–0.4 cm). In the vicinity of the low-albedo disk,

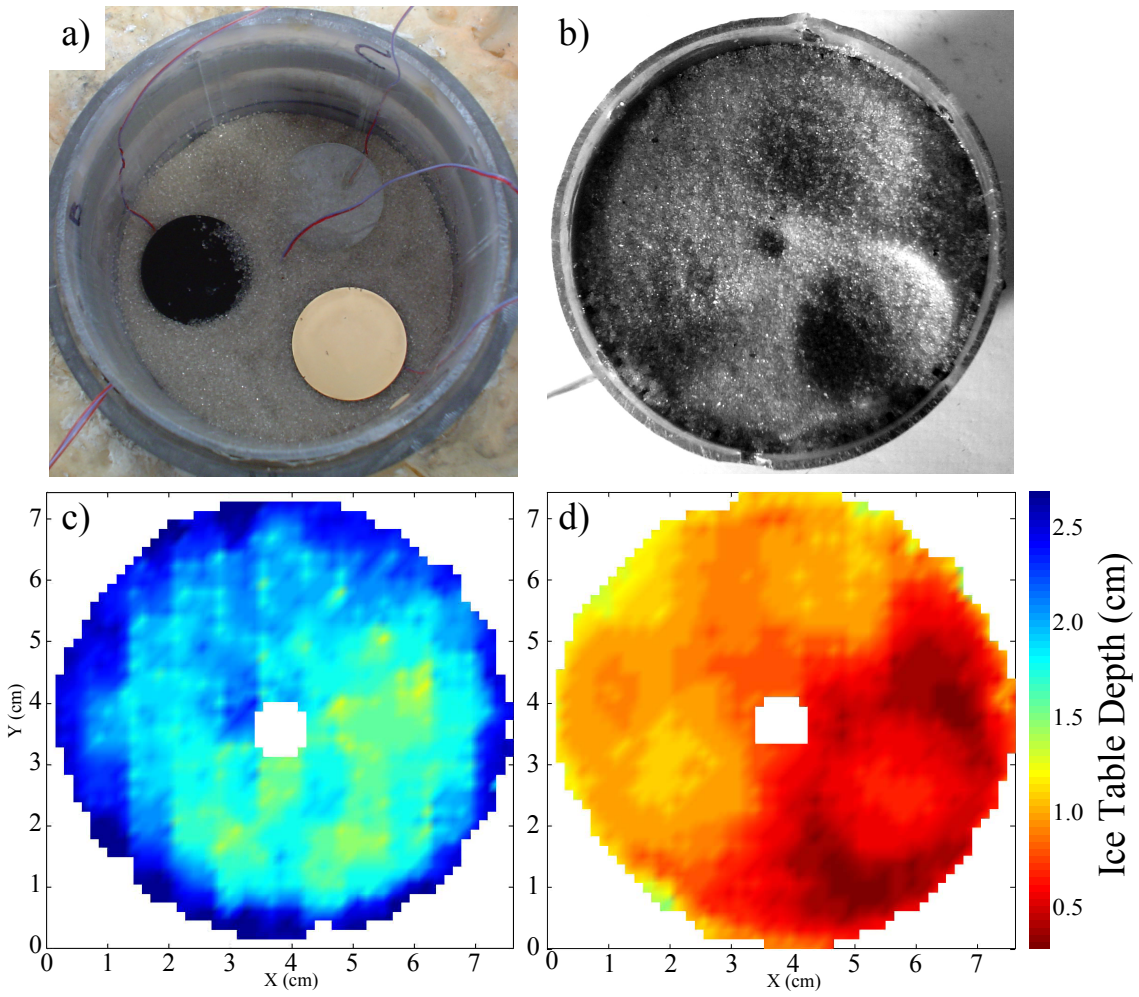

Figure 5.6: Experiments illustrating the effect of surface albedo on ice table development. a) Albedo disk placement on sample surface. b) Ice table for high vapor density case ($\rho_{\text{air}} = 1.6$ g m^{-3}), photographed with oblique illumination from the lower left. c) Ice table depth map for the low vapor density case ($\rho_{\text{air}} = 0.6$ g m^{-3}). d) Ice table depth map for high vapor density case ($\rho_{\text{air}} = 1.6$ g m^{-3}). Both experiments were exposed to a humid atmosphere for 48 hours.

the depth to the ice table is on the order of 1 cm due to isotherm depression by the warmer disk. The clear albedo disk had a smaller effect on the local environment.

An interesting effect of the high-albedo disk is the rim of shallow ice which gives way to a depression beneath the center of the disk. A possible explanation is inhibited vertical diffusion of water vapor due to the impermeable body of the disk, and the curved isotherms beneath it. Vapor moving laterally underneath the disk encounters temperatures where the vapor is saturated (an upwards deflection of the equilibrium ice table), and deposits. Vapor densities in the cold regions under the central portion of the disk are thus small and insufficient to deposit ice.

An experiment with an identical setup and duration but less than half of the atmospheric vapor

density ($\rho_{\rm air}$ = 0.6 g m^{-3}) was performed, and the depth map is shown in Figure 5.6 c. The lower vapor density resulted in a slower upward migration of the ice table. After 48 hours, the mean depth is 2±0.1 cm, compared to 0.8±0.3 cm for the experiment at higher humidity. At lower humidity, the ice table topography is subdued: the effect of the high-albedo disk is still seen over approximately half of the disk's surface, but the central depression effect and the discernible outline of the disk itself are absent. The greater thickness of low thermal conductivity ice-free beads insulates the ice table from the temperature perturbations at the surface. On Mars as in these experiments, the ice-free regolith above the ice table will rapidly attenuate temperature heterogeneities, reducing the sensitivity of ice-table morphology to surface albedo variations as a function of depth.

5.4.3 Ice table depth

To explore the depth of the ice table, several experiments were run for 24 hours with different values of atmospheric vapor density. Figure 5.7 shows the results of eight experiments, four run at the nominal vapor density of 1.6 g m^{-3}, and four at reduced chamber humidities.

The depth of the ice table and the total quantity of ice deposited in a given time depends sensitively on the atmospheric vapor density. The equilibrium ice table depths for the vapor densities 0.6, 0.85, 1.1, 1.35, and 1.6 g m^{-3} under a 13 K cm^{-1} gradient and a surface temperature of 268 K are, respectively, 1.4, 1.1, 0.92, 0.75, and 0.61 cm. Initially, significant ice is deposited several centimeters below the equilibrium depth. Higher vapor densities allow earlier ice deposition at a given level. Once ice has deposited, local temperature gradients in the ice control vapor flux, and the deep ice becomes isolated from the atmospheric vapor content. Experiments with high value of $\rho_{\rm air}$ (1.1–1.6 g m^{-3}) experience early deposition at depth and subsequently evolve at similar rates. Thus, the data for such experiments overlap between the base and ∼3 cm in Figure 5.7. The phenomenology of the early transients in ice deposition is examined further in Section 5.6.4.

5.4.4 Ice profile

The structure of the ice distribution beneath the ice table, in a region which may be termed the cryosphere, is revealed in these experiments as a function of both depth and time and is interpretable in terms of the experimental conditions and durations. The water contents determined from gravimetric analysis reveal profiles of ice content which decrease monotonically below the depth of maximum filling. Low humidity or short-duration experiments give rise to an ice table beneath an ice-free layer, while other conditions (*e.g.*, longer durations, higher vapor densities) produce stable surface ice. Figure 5.8 plots the final ice content results of experiments run for different periods of exposure to an atmosphere with a surface vapor density (reported by sensor #1) of 1.6 g m^{-3}. As described in Section 5.5.2, the actual vapor density driving the flux of water is believed to be

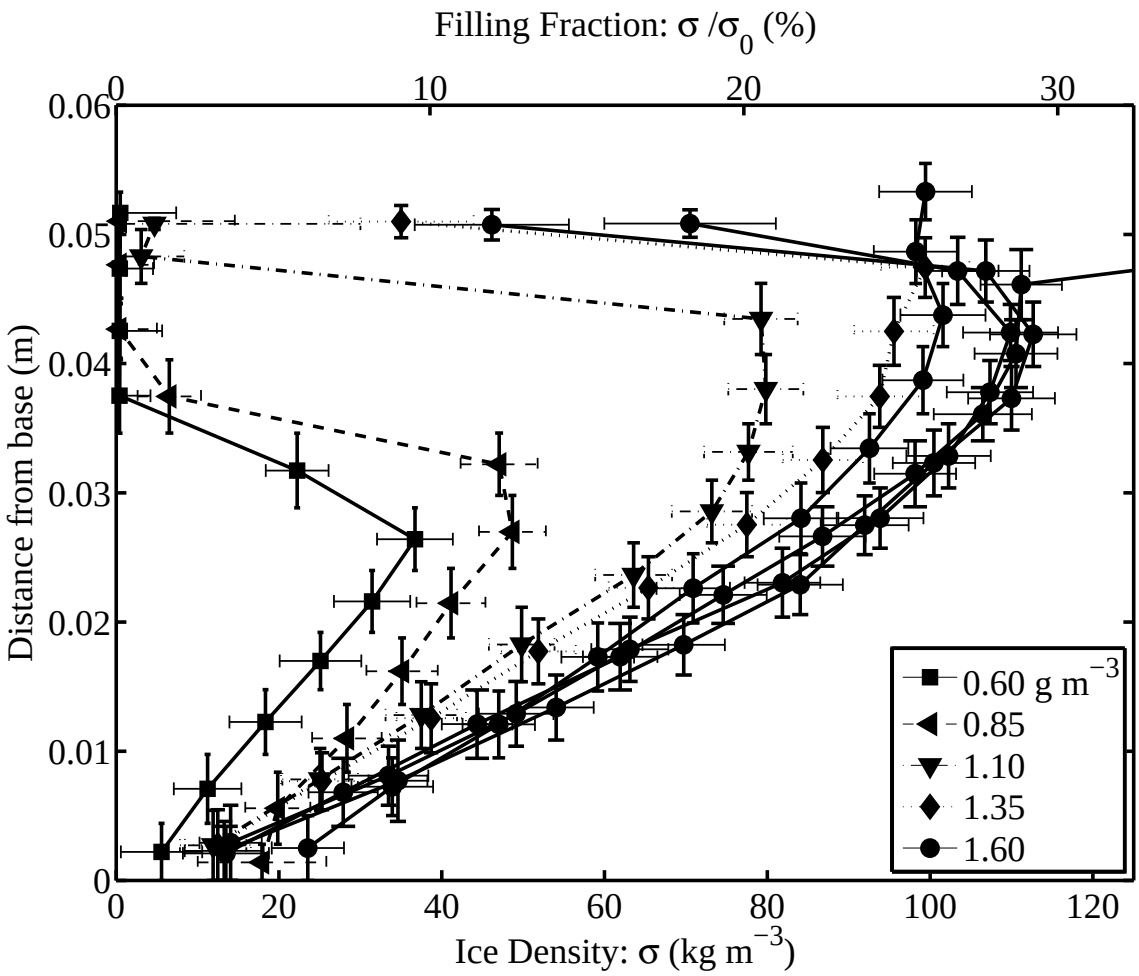

Figure 5.7: Ice content data for experiments run for 24 hours at various vapor densities. Ice contents are reported as density of deposited ice with respect to total volume (σ) and fraction of pore space filled with ice, assuming a constant ice-free porosity of 42%. The maximum density of ice is thus $\phi_0 \rho_{\rm ice} = \sigma_0 = 385.6$ kg m^{-3}

somewhat higher. The maximum filling fraction observed, approximately 90%, was observed at the end of the longest duration experiment.

As revealed in Figure 5.8, the ice contents first increase rapidly, followed by a reduced rate of ice accumulation. The shortest experiments were performed in additive 6-hour increments, the second set's durations were 24 hours apart, and the final long-duration experiments are 110 hours and 199 hours longer than the next shorter runs.

5.4.5 Constriction

In a porous regolith, the free-gas diffusion coefficient is reduced by a factor proportional to the cross-sectional area of the medium. An equivalent diffusivity, D, may be written in a regime which involves both molecule–molecule collisions and collisions with the pore walls to a significant degree.

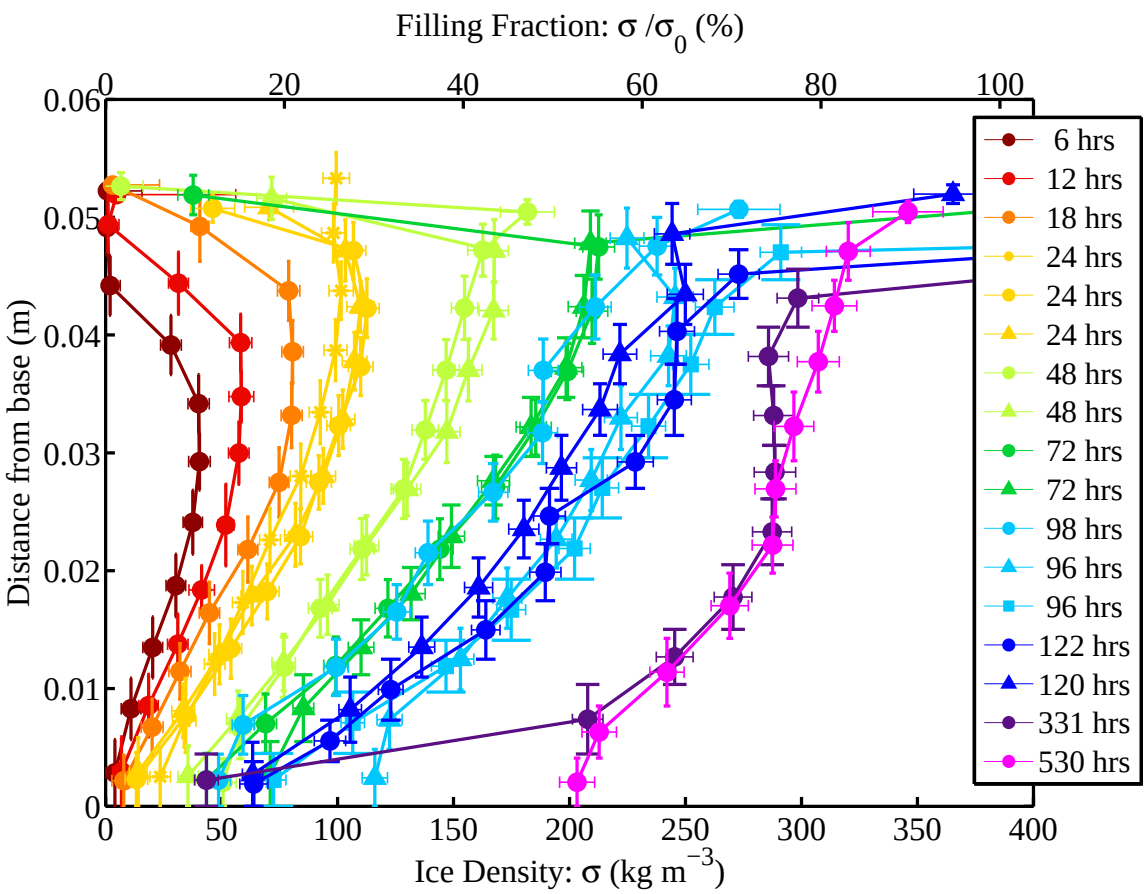

Figure 5.8: Ice content data for experiments run at a nominal surface vapor density of 1.6 g m^{-3} and various durations. After ∼48 hours, free ice deposits at the surface and forces the uppermost point for some samples to have a measured ice content offscale to the right. The colors correspond to duration of exposure to a wet atmosphere, as indicated by the legend. Experiments with similar durations are given the same color, but different symbols.

This is given by the Bosanquet equation,

$$\frac{1}{D} = \frac{1}{D_F} + \frac{1}{D_K}, \tag{5.2}$$

where D_F is the Fickian diffusivity, which dominates when collisions between gas molecules dominate the behavior of the gas movement, and the Knudsen diffusivity D_K which dominates at low pressures when molecules collide more frequently with pore walls than with each other (*Pollard and Present*, 1948). As ice accumulates, the pore space geometry changes, altering the porosity and tortuosity, and increasing the frequency of molecule–wall collisions as the pore size is reduced. D_F and D_K depend upon the pore geometry in potentially different ways. These effects are examined further in Section 5.6.2.

As described in the previous section, the rate of ice growth throughout the column is not uniform due to the non-linear gradient in vapor pressure at depths where ice is present. Initially, ice grows

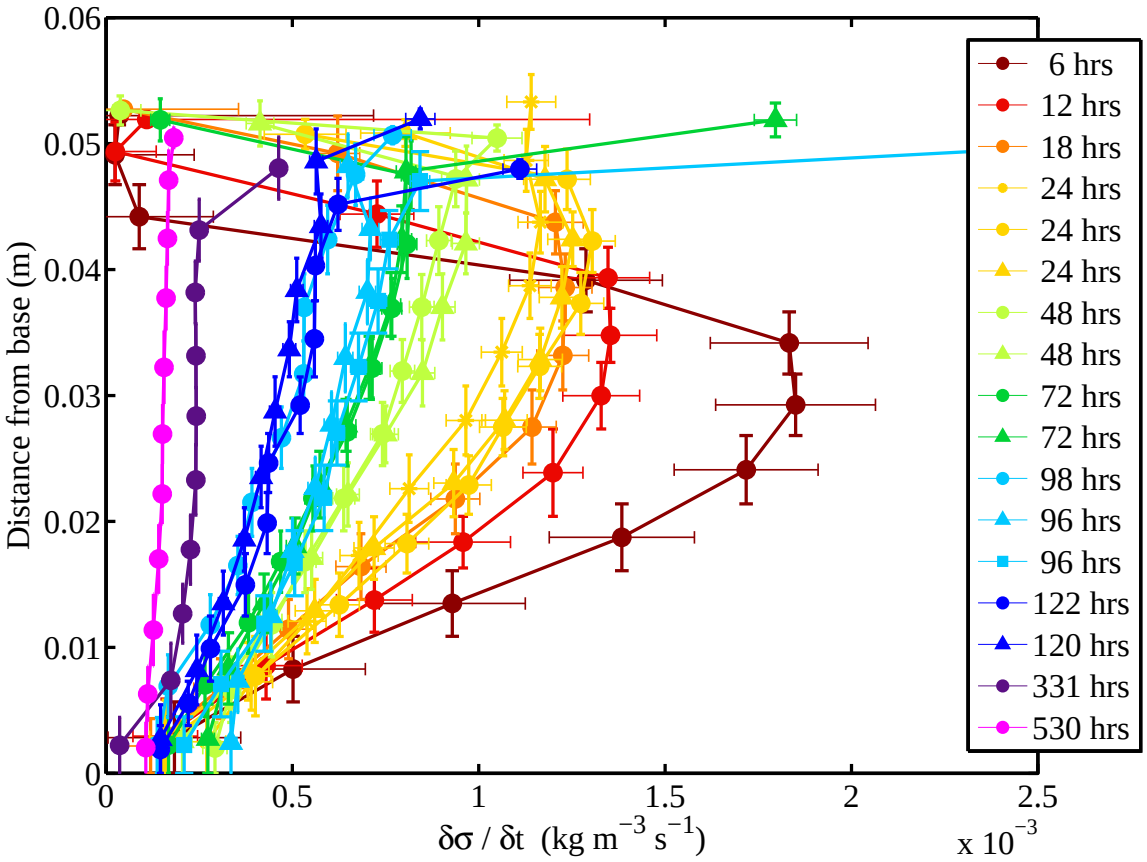

Figure 5.9: The change in ice content for a given depth divided by the time interval for growth. The legend (distinct from Figure 5.8) indicates the end of the time interval (*e.g.,* "6 hours" is 0–6 hours, "48 hours" is 24–48 hours, etc.). The most rapid ice growth occurs during the earliest times of exposure (0–6 hours), and the maximum can be seen to evolve from a depth ∼2.0 cm for 0–6 hours to ∼1.0 cm for 6–12 hours, to the surface for times between 12 and 24 hours. Subsequent to this, the rates are much smaller, are much more uniform across the sample depth, and continue to decrease with time.

most quickly at the top of the ice table where the vapor density gradient is steepest. Beneath the ice table the rate of ice growth also varies with time due to the effect of constriction. This may be seen in the spacing of the contours in Figure 5.8, but is more clearly evident in Figure 5.9, where the difference in ice contents between successively timed experiments are divided by the intervals between those experiments, thus plotting the incremental change in ice content, $\delta\sigma/\delta t$. Similarly timed experiments are differenced from an experiment of significantly shorter (>5 hours) duration.

Figure 5.9 reveals the depth of greatest ice growth in a given time increment. For the first 6 hours (dark red), most ice deposits between 1.5–2.5 cm beneath the surface. In the next longer increment, from 6–12 hours (bright red), the greatest growth is at about 1.0 cm depth. Between 18 hours to 48 hours (orange and yellow), the greatest ice deposition occurs in the uppermost soil layer. At all subsequent times, the ice growth progresses more uniformly with depth, but accumulation rates

decrease as exposure time to a humid atmosphere continues to increase.

5.5 Numerical Model and Experiments

5.5.1 Description of ice-filling model

Vapor transport and phase transitions are calculated with the numerical code described in *Schorghofer and Aharonson* (2005), which is used to model the experiments presented here. Fick's law, local mass conservation, and the ideal gas law lead to

$$\frac{\partial}{\partial t}\left[\left(\phi_0 - \frac{\sigma}{\rho_{\mathrm{ice}}}\right)\frac{p_1}{T} + \frac{R}{18}\sigma\right] = \frac{\partial}{\partial z}\left[D\frac{\partial}{\partial z}\frac{p_1}{T}\right], \tag{5.3}$$

where p_1 is the partial pressure of H_2O. Within the ice-containing region the ice growth can also be obtained from Equations (2.26) and (5.1), but these equations do not directly provide the vapor density in a dry layer or the depth of the ice interface. Hence, the partial differential equation (5.3), which includes these effects, is used.

Equation (5.3) is numerically solved with an explicit forward-difference scheme, with a spatial resolution of 0.5 cm, the spacing of the temperature sensors in the experiment. Models may also be run with temperatures interpolated to a finer grid spacing. Experimentally measured temperature profiles and surface vapor densities are used as input. To remove artificial temperature inflections caused by thermocouple misalignment from exact half-centimeter spacing, the temperature data are fit with a 4th-degree polynomial prior to being used as input. Small time steps are required for numerical stability, and the program subdivides measured temperature profiles, typically available in 1 minute intervals, into smaller time steps of 50–1000 μs by linear interpolation.

5.5.2 Comparison to models and uncertainties

In this section five quantities are considered which impact the agreement of the model with the experimental ice contents. They are: headspace vapor density (ρ_{air}), ice-free diffusion coefficient (D_0), temperature profile, density of deposited ice (ρ_{ice}), and what is here termed the constriction exponent (n).

Experiments performed with three humidity sensors placed as indicated in Figure 5.3 recorded vapor densities consistently 80% higher at sensors #2 and #3 than at sensor #1. Additionally, ice was observed to deposit at the sample surface after ∼48 hours while the vapor density reported by sensor #1 implied an ice table ∼0.6 cm beneath the surface. It is therefore surmised that 1) the atmosphere above the sample in these experiments is not well mixed, and 2) the bulk atmospheric vapor density driving the flux of water vapor is higher than 1.6 g cm^{-3} by almost a factor of 2.

Compensation equations for sensor temperature are provided by the vendor; however the range of validity for those expressions may not extend to low-pressure environments.

This uncertainty in ρ_{air} affects estimates of ice table depth and ice contents in experiments of less than ∼48 hours duration. In Figure 5.10, the final ice content measured for a 24 hour experiment is displayed, along with results of numerical simulations using the model described in Section 5.5.1. All model runs use the subsurface temperature profile as recorded. When vapor densities reported by sensor #1 are used, the model underpredicts ice contents in the upper half of the sample (Figure 5.10, triangular symbols) compared to experimental data (filled circles, solid black curve). When vapor densities are prescribed constant values, models with higher surface vapor densities are seen to produce ice at shallower depths more akin to the experimental profile. The best match between models and experiments for exposure times less than ∼48 hours are with ρ_{air} =2.0–3.2 g m^{-3}, lower values producing the best correspondence with the shortest times. For 48 hour experiments, good agreement between experiments and models is obtained for surface vapor densities of ∼3.2 g m^{-3}. This value is equal to the vapor density of ice at 268 K and 600 Pa, *i.e.*, the conditions maintained at the surface of the sample, and therefore suggests that free surface ice becomes the dominant vapor source.

An important feature of Figure 5.10 is that all model runs, despite differing surface vapor densities, agree beneath the depth where ice is present; the curves merge onto a single line. Flux beneath the ice table is governed by the local vapor pressure, which is controlled by temperature and is independent of the atmospheric vapor density. The important differentiation among models with different surface vapor densities is the time when a particular depth begins to deposit ice. Higher vapor densities advance this point to earlier times at a given depth.

In the rest of this section dealing with model and experiment agreement, the focus is primarily on runs of 48 hours or longer, and the discussion is therefore specific to experimental data and models run with surface vapor densities of 3.2 g m^{-3}. When such models are run, they consistently overpredict the abundance of ice in the sample, indicating that some other factor besides vapor density is acting to reduce ice deposition.

Measurements of D_0 for the 500 μm glass beads have an uncertainty of about 10% (Section 5.3.3). Additional model runs were performed using D_0 = 4.2 cm^2 s^{-1} to determine if reasonably lower values of D_0 would bring closer agreement with experimental results. Such models do exhibit reduced ice contents, but do not bring the model output into good agreement with the data. It is therefore concluded that the major source of variation lies elsewhere and D_0 = 4.7 cm^2 s^{-1} is used for subsequent model analyses.

A ∼1 mm vertical deviation in thermocouple placement results in ∼1 K temperature offset, corresponding to a 10% variation in vapor density at the highest (∼268 K) experiment temperatures. Models run with imposed 1 K shifts to lower temperatures produced insignificant differences in ice

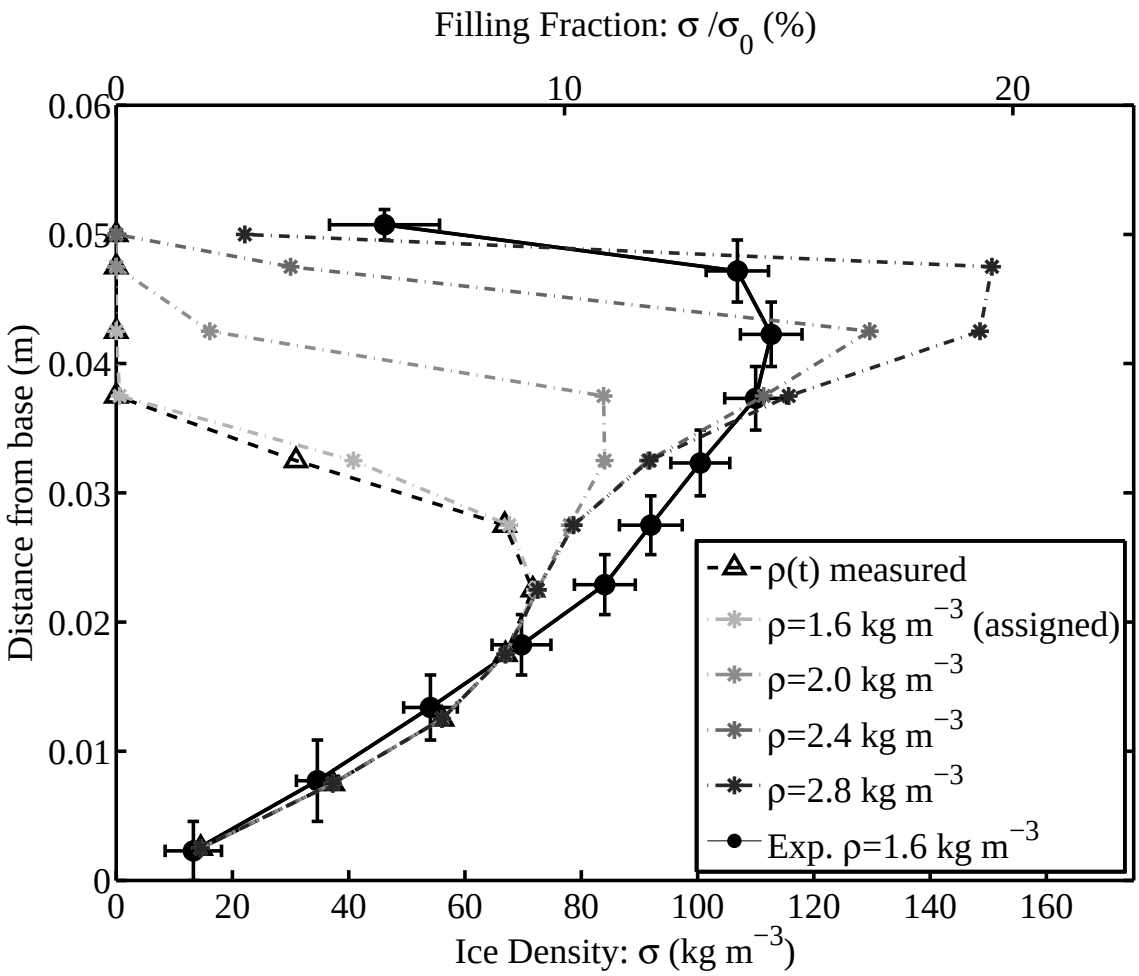

Figure 5.10: Ice content data for a 24-hour exposure experiment at a nominal measured vapor density of 1.6 g m^{-3} (black circles, solid line), compared to model simulations (broken lines) using experimental temperature data interpolated to 2x resolution. One model was run with surface vapor densities as measured (triangles) and several were run with assigned values of ρ (asterisks). Notice that the models agree below the depth where ice has accumulated, indicating gradient control by the saturation vapor pressure.

abundances compared to unshifted temperature data.

The maximum observed filling fraction is less than 100%, suggesting the possibility that the deposited ice is less dense than pure ice. This is consistent with micrograph images (see Figure 5.4) which show encapsulated bubbles and turbid ice. If the numerical model is modified such that the density of deposited ice is lower, the results can be made to match more closely with the experimental data. Figure 5.11 shows such results for four selected datasets and their attendant model runs using ice densities of 918 and 734 kg m^{-3}, the latter being equivalent to 80% maximum filling. Such a reduced density improves the model fit, but filling fractions up to 90% are observed in the longest experiment. In the simplest case it can be assumed that all deposited ice has the same density, which should be at least the maximum observed in any experiment, suggesting that

a density of 734 kg m^{-3} is too low. It is possible that the density of deposited ice varies depending on local geometric effects, temperature, and time of deposition. The density of the deposited ice is not measured directly and thus cannot constrain ice density as a function of time. Given this uncertainty and the observation of 90% filling (implied ice density ∼826 kg m^{-3}), another possibility is considered: non-linear constriction.

The model results presented thus far have used a linear relation between diffusivity and filling fraction, as used by *Mellon and Jakosky* (1993), to account for constriction. In this schema, the porosity at time t is

$$\phi(t) = \phi_0(1 - \frac{\sigma(t)}{\phi_0 \rho_{\text{ice}}}). \tag{5.4}$$

The ice-free diffusion coefficient $D_0 = D(\phi_0)$ is thereby modified by a factor of ϕ/ϕ_0. The constriction model of *Mellon and Jakosky* (1993) subsumes all variation in pore geometry into the value of the porosity, ϕ, and leaves the tortuosity term unaltered. This was justified due to a lack of experimental or theoretical data on the effects of constriction on tortuosity.

It is found, however, that agreement between the experimental data and the ice contents predicted by the models can be improved if the density is maintained at ∼918 kg m^{-3}, but the constriction factor is modified by an exponent, n:

$$D = D_0 \left(1 - \frac{\sigma}{\sigma_0}\right)^n. \tag{5.5}$$

The reduction of porosity (understood as the available area through which vapor can pass) due to deposited ice is linear in σ, hence the base model used here and that of *Mellon and Jakosky* (1993) assume $n = 1$. It can be seen in Figure 5.11 that models with $n = 1$ match the data well for filling fractions of ∼40% or less, but that they overpredict the amount of ice deposited for longer times with higher filling fractions. A model run for the 330 hour experiment, wherein filling fractions are >70%, which uses $n = 2$ and $\rho_{\text{ice}} = 918$ kg m^{-3} is plotted in Figure 5.11 as a red dashed curve and is seen to be in close agreement with the experimentally measured ice contents. The degree of agreement between this model and the experimental data is comparable to that between the data and the model with $n = 1$ and 80% ice density, but this scenario is not favored because observed densities reach at least 90%. Changes other than reduction of porosity, *e.g.,* the shortening of molecular hop distances as ice reduces the available volume, add additional constriction effects which cause a non-linear dependence of D on σ when filling fractions are large. In the model parameterization, these effects are captured in n, as described in Section 5.6.2.

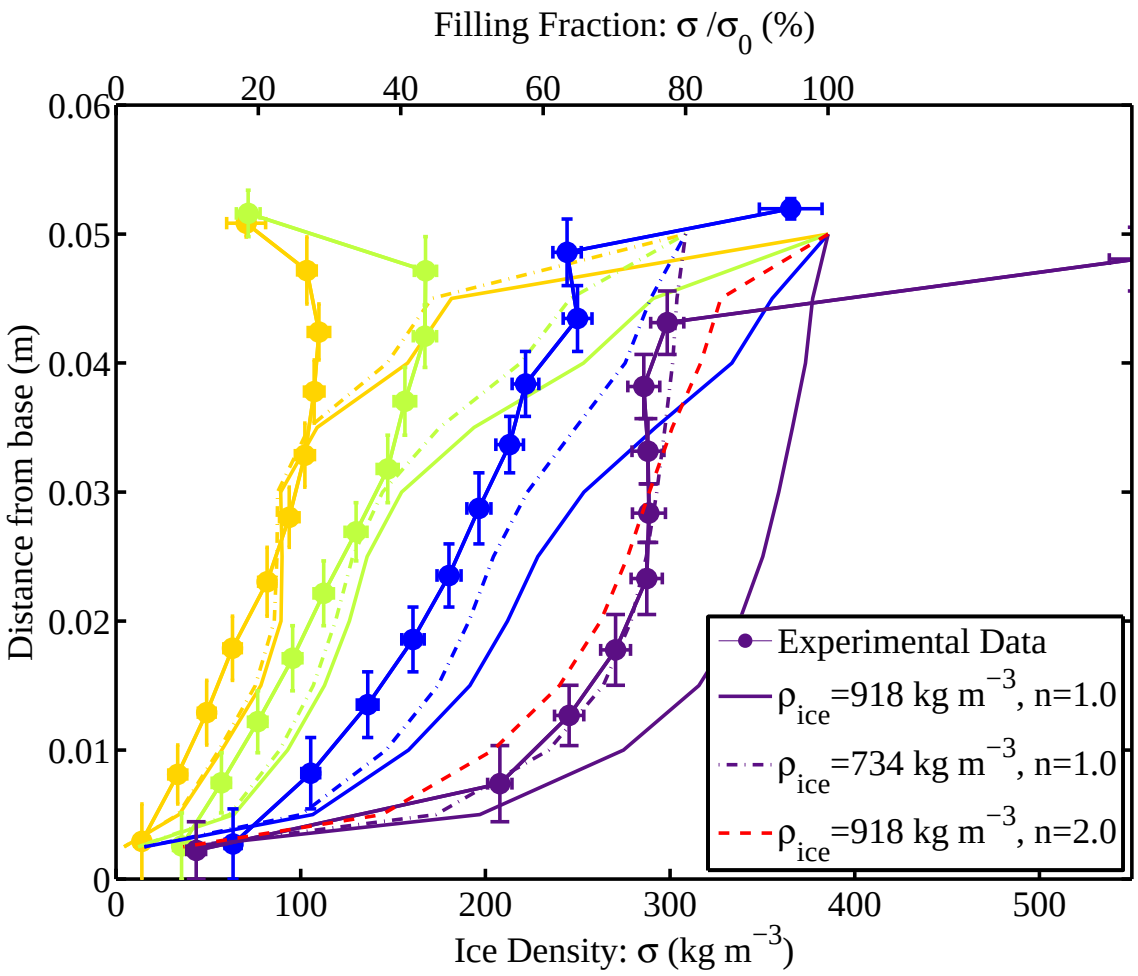

Figure 5.11: Experimental data and model outputs for 24, 48, 120, and 330 hour experiments. Experimental data are filled circles with error bars. Model results vary as the maximum density of deposited ice is changed, and the best agreement for the experiments with high filling fractions appears to be with $\rho_{\text{ice}} = 734$ kg m^{-3}, or 80% the density of pure ice. For times shorter than ~48 hours, models which assume diffusivity is linearly proportional to filling fraction agree with the experimental data. A single dashed line (in red) indicates the model output for the 330 hour experiment if 100% ice density is assumed, and diffusivity varies as the square of the filling fraction (*i.e.,* constriction exponent equals 2).

5.5.3 Time-varying diffusion coefficients

The diffusivity as a function of time can be extracted from the available experimental data by making the simplifying assumption that variations of D with depth are slow. The right hand side of Equation (2.26) may then be used to estimate the diffusion coefficient as a function of ice density. The relation used is:

$$\frac{\sigma(t+\delta t)-\sigma(t)}{\delta t} = D(t+\frac{\delta t}{2})\frac{1}{\delta t}\int_t^{t+\delta t}\frac{\partial^2\rho_1}{\partial z^2}dt', \tag{5.6}$$

where δt indicates the time interval separating successive experiments. The accumulated quantity of ice in an interval, $\delta\sigma/\delta t$, divided by average values of the density divergence in the same interval

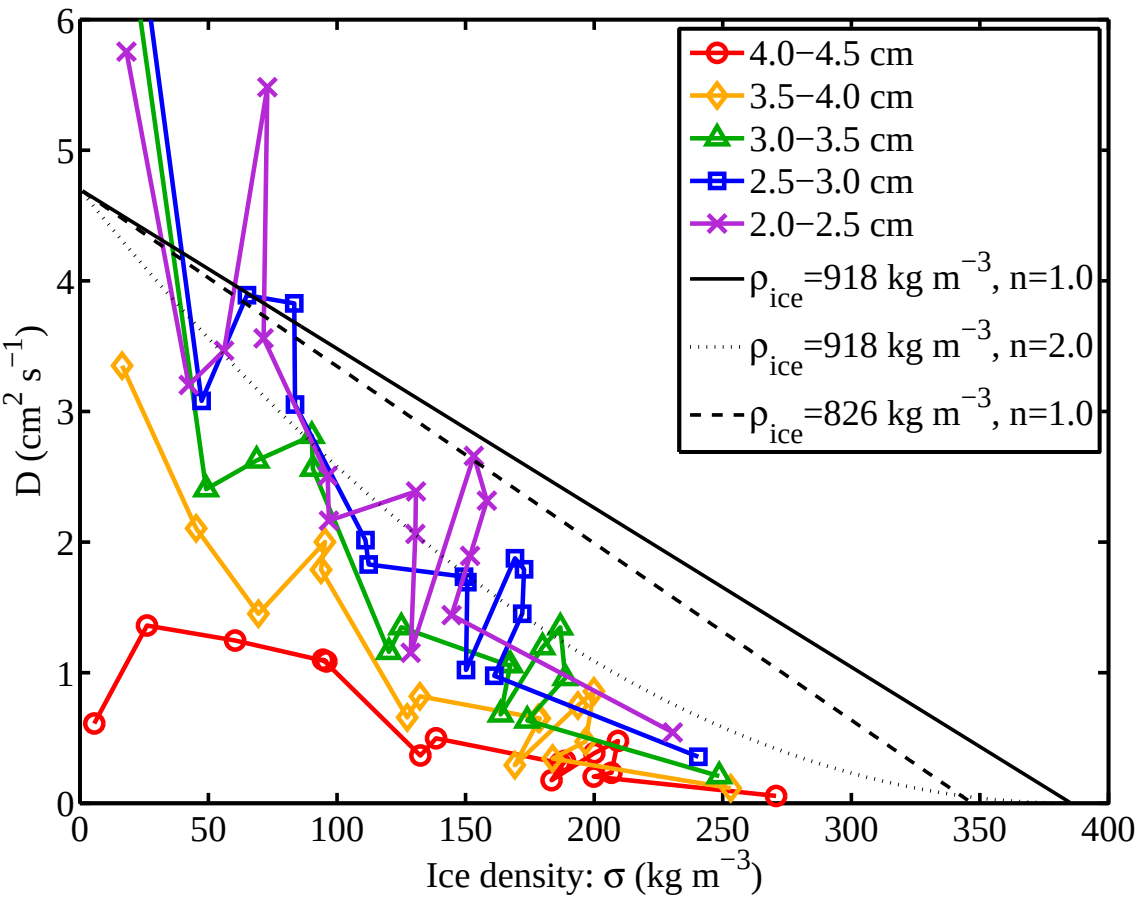

Figure 5.12: Plot of the diffusion coefficient evaluated using the technique described in Section 5.5.3 versus ice content for 5 deep levels in the sample column. Overplotted are expected variations in D with σ using $\rho_{\rm ice} = 918$ kg m^{-3} for $n = 1$ (solid) and $n = 2$ (dotted). The trend in the diffusion coefficient exhibits a concave-upwards slope which is consistent with n greater than unity. If the density of deposited ice were 90% of pure ice density, and $n = 1$, the diffusion coefficient would follow the dashed line.

gives a proxy for D, which may be plotted versus the average ice content over δt at a particular depth. Figure 5.12 thus displays the change in diffusivity due to constriction in the deepest layers where the changes in ice content are easiest to observe.

Systematic differences among experiments result in a considerable scatter in Figure 5.12, but an overall trend to lower values of D can be discerned. The trends are consistent with the expected variation of D with σ for a constriction exponent greater than unity ($n = 1$ and 2 are plotted as solid and dotted lines, respectively). If n is constrained to be equal to unity, but the maximum ice density relative to free space is allowed to be less than 386 kg m^{-3}, then the linear trend (dashed line) would reach a smaller maximum value. But filling fractions of 90% imply a σ of at least 347 kg m^{-3}. The trend of D with σ using this lower density and $n = 1$ does not match the data as well as the data with a higher constriction exponent, suggesting that $D(\sigma)$ depends on σ and is non-linear for high

filling fractions.

The reduced deposition rate as a function of time exhibited by these data is consistent with the constriction phenomenon. The close agreement between the reduced rate of ice accumulation in models and experimental data improves confidence that the model employing non-linear adjustment of D with σ more closely captures the physics of the ice deposition process. Both effects of reduced ice density and non-linear constriction may be important in controlling the evolution of ice at high filling fractions obtained for long exposures to ice-growth conditions.

5.5.4 Long-duration behavior

The longest experiment was run for 530 hours of exposure to humid gas. The rate of change between the 330 and 530 hour experiments is small, indicating significant constriction in the shallow layers and concurrent reduction of ice deposition rates at greater depths. The numerical model has been run for 6000 hours of experiment time using a static, linear temperature profile of the same magnitude as used in the experiments. The other parameters are a constriction exponent of $n = 2$, an ice density of 918 kg m^{-3}, the total pressure of 600 Pa, and surface densities of 1.6 and 3.2 g m^{-3}.

Figure 5.13 plots the cumulative ice content as a function of time for the two model runs (broken lines), column-integrated ice contents for the experiments (filled symbols), and the local column ice density for the most ice-rich layer in each experiment, scaled by a factor of 10 (open symbols). The column integrated ice contents are computed over the depth of the ice-bearing sample. Both models are seen to converge asymptotically to the maximum theoretical ice content, σ_0/Z, with the difference being $< 5\%$ after $\sim$5000 hours. The experimental data agrees well with the model using the higher vapor density, particularly for times greater than 24 hours, corresponding to surface ice at 268 K, rather than the atmosphere, being the dominant vapor source.

The experimental data are consistent with the asymptotic approach of the ice content to total filling. Further experiments which achieve high filling fractions may improve understanding of the ice deposition process, potentially revealing important phenomena that only affect ice deposition when constriction effects are large.

5.6 Discussion

5.6.1 Theoretical uncertainties in vapor transport

The governing equation for the diffusive transport of water vapor (denoted by subscript 1) in CO_2 (denoted by subscript 2) is given by (*Landau and Lifshitz*, 1987)

$$J_1 = -\rho_0 \left[\mathcal{D}_{12} \frac{\partial}{\partial z} \frac{\rho_1}{\rho_0} + \frac{\mathcal{D}_T}{T} \frac{\partial T}{\partial z} \right], \tag{5.7}$$

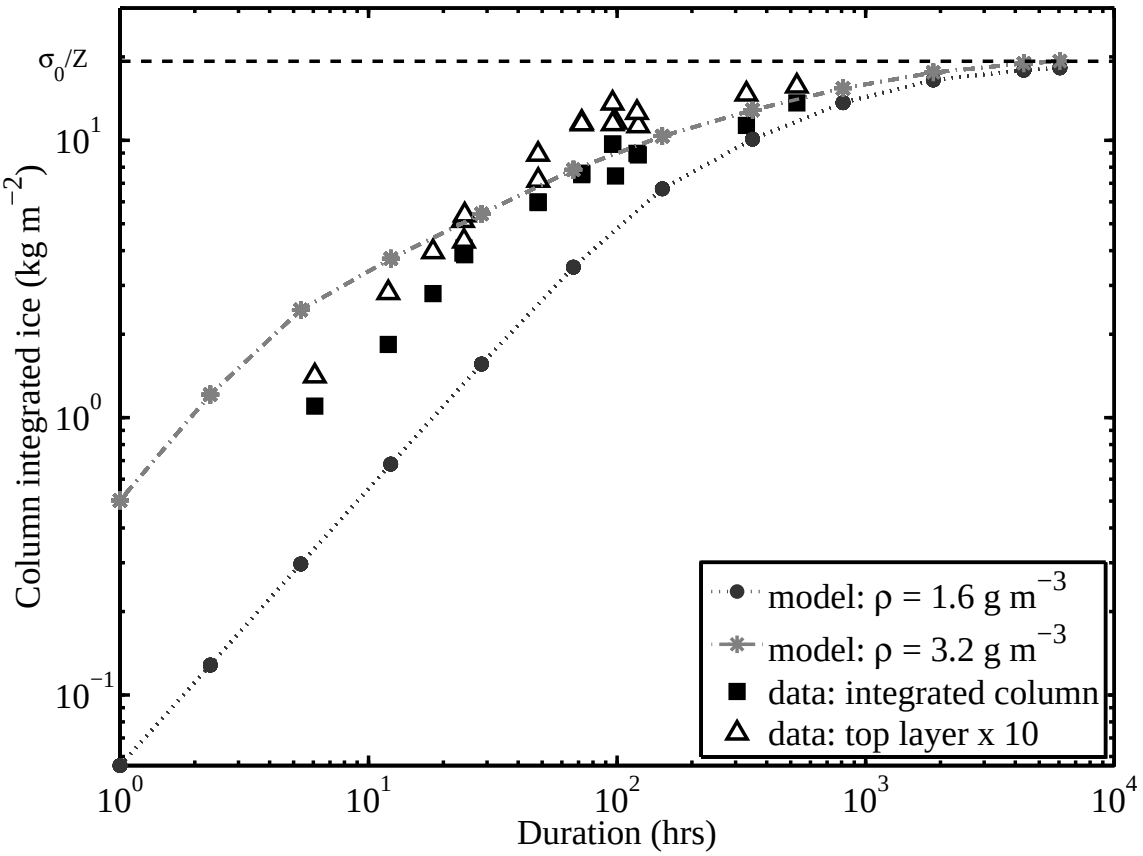

Figure 5.13: Column-integrated ice abundances for experiments and two long-duration models (parameters given in text). Solid symbols are integrated column densities, open symbols represent ice contents in the uppermost ice-bearing layer (*i.e.*, the most ice-rich layer) scaled by a factor of 10. Model runs with vapor densities of 3.2 g cm^{-3} match total ice abundances well after 24 hours, supporting the conclusion that the driving vapor density is that of the surface ice at 268 K. Maximum column density for ice in a 42% porosity medium would be $\sigma_0/Z = 19.3$ kg m^{-2}.

where J_1 is the diffusive mass flux of gas 1, ρ_0 is the total mass density, $\rho_0 = \rho_1 + \rho_2$, $\mathcal{D}_{12}$ the mutual diffusion coefficient in free-gas, $\mathcal{D}_T$ the coefficient for "thermodiffusion", and T the temperature. The contribution of barodiffusion to the vapor flux is neglected.

In *Hudson et al.* (2007) a review of the thermal diffusion effect is presented and is shown to be a negligible contributor to the vapor flux in the experiments described therein. Here, the issue is revisited for the high thermal gradients in the present experimental setup. The concentration-dependent thermal diffusion factor α_T is at most $\alpha_T \approx 0.8$ for H_2O–CO_2, using the conservative elastic sphere model (*Chapman and Cowling*, 1970). By definition $\mathcal{D}_T/\mathcal{D}_{12} = \alpha_T(n_1/n_0)(n_2/n_0)$, where n indicates number densities. At low concentration, $\mathcal{D}_T/\mathcal{D}_{12} \approx \alpha_T(\rho_1/\rho_0)(\mu_2/\mu_1)$, where μ_1 and μ_2 are the masses of H_2O and CO_2 molecules, respectively.

In equilibrium, the total H_2O flux vanishes, rendering the ratio of thermodiffusion flux to concentration-driven flux as an inappropriate measure. Instead, an estimate of the change in ice

table depth δz due to thermodiffusion in this laboratory setup is determined by

$$-\rho_0 \mathcal{D}_T \frac{1}{T}\frac{\partial T}{\partial z} = \frac{\partial J_1}{\partial z}\delta z. \tag{5.8}$$

The total diffusive flux J_1 is approximately, $-D_{12}\partial\rho_1/\partial z$, and thus

$$\rho_1 \alpha_T \frac{\mu_2}{\mu_1}\frac{1}{T}\frac{\partial T}{\partial z} = \frac{\partial^2 \rho_1}{\partial z^2}\delta z. \tag{5.9}$$

From equation (5.1) and $H/(RT) \approx 23 \gg 1$, an approximate expression for $\partial^2\rho_1/\partial z^2$ is obtained and used in equation (5.9) to give,

$$\alpha_T \frac{\mu_2}{\mu_1} \approx \delta z \left(\frac{H}{RT}\right)^2 \frac{1}{T}\frac{\partial T}{\partial z}. \tag{5.10}$$

Hence, $\delta z \lesssim 8 \times 10^{-4}$ m, which is negligible compared with the relevant length scales.

The contribution of advection or bulk flow to the vapor transport is also small. The sample container has an impermeable bottom boundary, such that bulk motion can only be caused by the displacement of gas from the growing ice volume, surely negligible, and the contribution of the H_2O flux to the overall motion. The latter should be on the order of p_1/p_0; the maximum p_1 is reached at the ice table, where $p_{sv}(268\text{ K}) = 397$ Pa, while $p_0 = 600$ Pa. Figure 5.1 demonstrates that rapid ice growth only occurs when the equilibrium vapor pressure of H_2O is not much smaller than the total pressure.

By eliminating the advective velocity from equations for the total flux of interdiffusing species, it is found that the inward flux is larger than what is obtained from diffusion alone by a factor of $\rho_0/(\rho_0 - \rho_1)$ (*Landau and Lifshitz*, 1987; *Hudson et al.*, 2007). This expression is not applicable for Knudsen diffusion, but qualitatively indicates that advection increases the flux in these experiments. For model runs greater than 48 hours, the excess ice relative to observations using a linear dependence of D on filling fraction, *i.e.,* $n = 1$, can therefore not be explained by an unaccounted advective contribution.

5.6.2 Constriction physics

In equation (5.5), an exponent, n, is introduced to modify the change in diffusion coefficient as a function of filling fraction. The changing geometry of the pore space during ice deposition results in a non-linear dependence of D on σ at high filling fractions. A cause of this phenomenon arises from reduced pore space volume, which results in a greater frequency of molecule–wall collisions for a given pressure. The effect of mean free path and molecular hop length on D can be seen in the following derivation.

The free-gas diffusivity may be approximately written as

$$D_{12} = \frac{1}{3}\bar{\nu}_1 \lambda, \tag{5.11}$$

where $\bar{\nu}_1$ is the mean thermal speed of water molecules and λ is the mean free path. The Fickian diffusion coefficient in a porous medium may be written as

$$D_F = \frac{\phi}{\tau} D_{12}, \tag{5.12}$$

and the Knudsen diffusion coefficient may be written as

$$D_K = \frac{1}{3}\bar{\nu}_1 l \frac{\phi}{\tau}, \tag{5.13}$$

where l is a measure of characteristic hop length, and any prefactor is subsumed into the relation between l and pore size. This treatment is similar to the treatment of *Evans et al.* (1961), who derive a Knudsen diffusion expression which is also proportional to the obstruction factor, ϕ/τ. Since l is proportional to available pore size,

$$l = l_0 \phi / \phi_0, \tag{5.14}$$

where l_0 is for the dry porous medium. Equations (5.2), (5.11), (5.12), (5.13), and (5.14) lead to

$$D = \frac{\phi}{\tau}\frac{\bar{\nu}_1}{3}\left(\frac{1}{\lambda} + \frac{1}{l}\right)^{-1}. \tag{5.15}$$

Hence, changes in D with ice content can be attributed to three contributions: porosity ϕ, tortuosity τ, and restriction in hop length l. If τ were constant with time, then D varies proportionally with ϕ when $\lambda \ll l$, and it varies as ϕ^2 for $\lambda \gg l$.

The diffusivity therefore changes from linear in σ to a stronger dependence as deposition progresses. At high filling fractions, the l term in equation (5.15) dominates over the λ term, the porosity term is small, and the tortuosity will become large as diffusive paths are closed off. Figure 5.11 shows that models with low filling fractions agree well with experimental data if the relationship between D and σ is linear, *i.e.,* the constriction exponent n equals 1, while models for long-term experiments with high filling fraction overpredict the ice abundance with $n = 1$. Equation (5.15) implies that the functional relationship between D and σ changes with σ, and a real system would not be described by a constant constriction exponent, as was employed in the model (Section 5.5.3). Further study of the constriction phenomenon may reveal the appropriate prefactors and dependencies to model this transition.

5.6.3 Initial ice deposition

The preferential deposition at grain contact points, as revealed by the micrographs in Figure 5.4, could first fill the smallest pore spaces and narrowest gaps between grains. Most of the flux in a medium of distributed pore sizes is carried in the largest pores (*Clifford and Hillel*, 1983, 1986), and this initial deposition should not greatly alter the effective diffusion coefficient. But this small amount of ice may still affect the availability of pathways to conduct vapor, changing the tortuosity of the medium.

Another consequence of ice deposition is a change in bulk thermal conductivity (*Paige*, 1992). The thermal conductivity of ice-free 500 μm glass beads used in these experiments is 0.18 W m^{-1} K^{-1} (*Ham and Benson*, 2004). This value is higher than the values of bulk thermal conductivity for particulate material used by *Mellon and Jakosky* (1995) (0.02 W m^{-1} K^{-1}). Ice, on the other hand, has a bulk thermal conductivity of $\sim$2.2 W m^{-1} K^{-1}. The addition of ice at grain contact points greatly increases the conductivity of the sample through increased area of heat conduction and the high thermal connectivity of the added material. The effect of included ice on the bulk conductivity of an ice-bearing soil was represented in *Mellon et al.* (1997) by the action of two parallel conductors where the contribution of ice in the intergrain space was proportional to the square root of the filling fraction, $(\sigma/\sigma_0)^{1/2}$ in the notation used here. This model exhibits a rapid increase in thermal conductivity for small filling fractions. The effect of the earliest deposited ice is significant with respect to its effect on the thermal properties of the regolith.

5.6.4 Ice growth physics and phenomenology

An initially dry soil subjected instantaneously to a moist atmosphere will experience a rise in vapor density at all depths until saturation is reached, or an unsaturated gradient is established between the surface and the saturation depth (shown schematically in Figure 5.14 as point B). Initially, point B is the top of the ice table, and the density gradient between this depth and the atmosphere must be linear if no ice is deposited in this region.

The nonlinearity of the vapor density gradient (exponential temperature dependence) results in the greatest quantity of ice being deposited at the top of the transient ice table. The gradients of the vapor density in the ice-bearing and ice-free regions are equal at the interface, and initially the fluxes are as well. But constriction reduces the diffusion coefficient and flux through an ice-bearing layer while leaving the vapor density gradient unaffected. Conservation of mass then requires that the flux in the ice-free region also be reduced. Since in this region the flux depends only on the vapor density at the surface and the depth to the ice table, the interface must move upwards, from point B toward point C.

As the interface becomes shallower, the gradient of vapor density through the ice-free region is

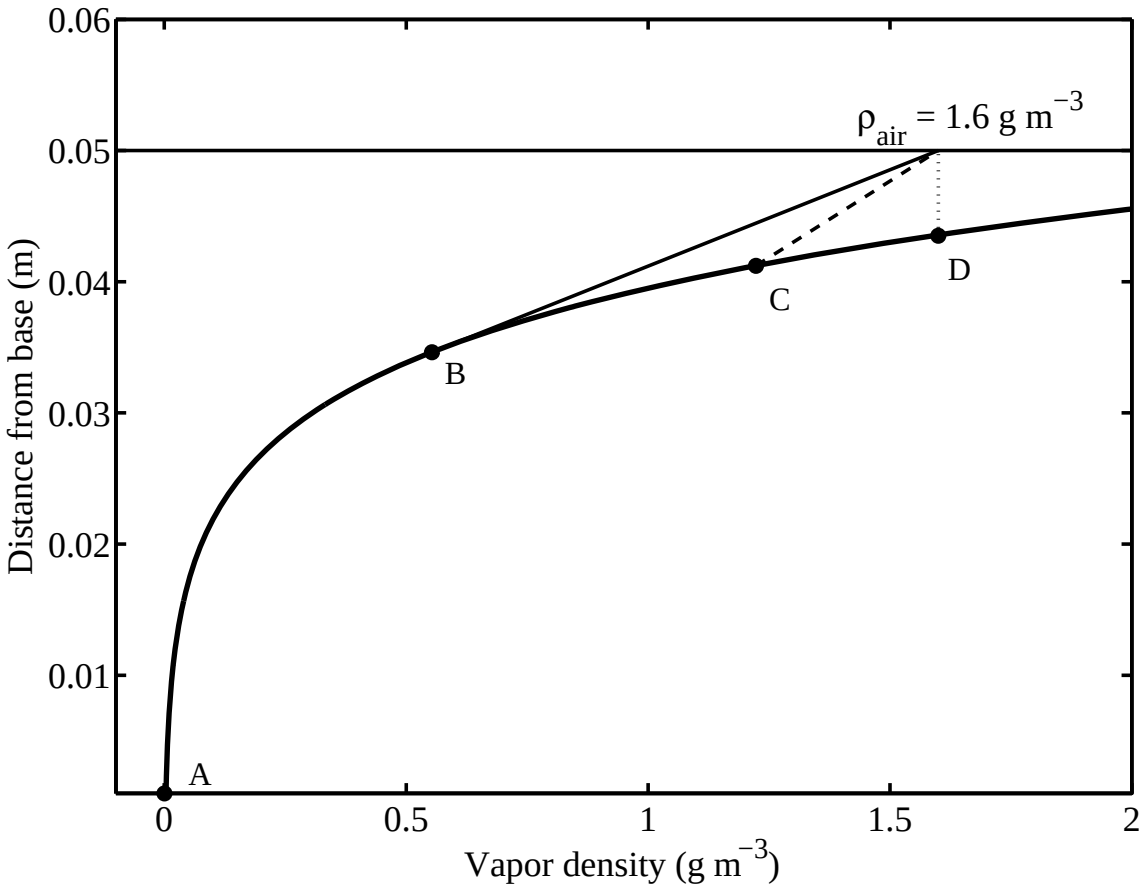

Figure 5.14: The steady-state vapor density for a sample with a 13 K cm^{-1} temperature gradient. For levels where ice is present, the vapor density is set by the saturation vapor pressure of ice (thick curved line). For levels with no ice present, the gradient is linear (or approximately so) between the saturation line of the uppermost ice and the atmospheric vapor density, which is here set at 1.6 g m^{-3}.

diminished, thus ultimately reducing the flux to the ice table and the rate of ice deposition. Since small changes in depth correspond to large changes in vapor density gradients in steep regions of the saturation curve, the rate of ice table migration slows. The difference in rates of ice growth between deep and shallow depths decreases with time, and the ice-content profile becomes progressively more uniform. This occurs despite the higher gradients at shallow depths because greater ice contents restrict vapor flux.

At all times, the ice beneath the ice table interface continues to evolve down-gradient. Water vapor surrounded above and below by ice feels only the local vapor gradient due to temperature; it is independent of the atmospheric density. If the atmospheric water content were to drop sharply, the ice table would begin to recede from the top down. Existing subsurface ice would continue to migrate deeper until all ice above it was removed and it was able to feel the effect of the vapor density gradient (now reversed in sign) in the ice-free region above.

If the atmospheric vapor density remains high, the ice table will evolve toward its equilibrium at point D. At equilibrium, the gradient in the ice-free region and the inward flux must be zero. But since ice beneath the ice table is continuously redistributing down gradient, there must remain a positive net flux into the subsurface. Thus the ice table interface must be beneath the equilibrium depth so long as the porous medium is unsaturated down to some zero-flux boundary. Substantial constriction permits only small fluxes, allowing the ice table to be close to the equilibrium position when filling fractions are high. If the climate on Mars has been stable enough to permit substantial filling, differences between equilibrium predictions of ice table depth (*e.g., Mellon et al.* (2004); *Schorghofer and Aharonson* (2005)) and observed depths (within the accuracy achievable by spacecraft such as Mars Odyssey and the Phoenix Lander) are unlikely to be large.

Where the conditions have been favorable to ice growth for long times, the filling fraction in the layers of the regolith immediately beneath the ice table may approach saturation. But since there is a non-zero flux to some depth, the shallow ice must remain porous to accommodate this transport. In situations with very high filling fractions, where pore spaces are no longer continuous, downward flux may persist through the mechanism of counterdiffusion of water molecules and lattice defects or vacancies.

In a stable environment, complete choking of the regolith column, meaning zero flux to deeper depths, will not occur until all available pore spaces are filled. The volume which is available for filling will depend on the depth of the zero-flux boundary. This may either be some layer in the regolith with zero diffusivity or the inflection depth of the mean annual vapor density gradient, as determined by the conductivity of the regolith, the local temperature environment, and the geothermal gradient.

5.6.5 Voluminous pore ice on Mars

Two mechanisms by which significant volumes of ice can be emplaced in the shallow subsurface of Mars are 1) precipitation and subsequent burial and 2) inward diffusion of atmospherically derived vapor. The former process requires climate conditions significantly different from those currently observed, while the latter may have operated frequently in the past in addition to being active today.

Most unconsolidated sandy terrestrial soils have porosities between 30–50% (*Taylor*, 1977), though finer particulates can give rise to porosities up to 60% (*Baver*, 1940). Even including constriction, near-complete filling of such void fractions can occur at present-day conditions in $\sim 10^5$ years, resulting in ice contents approximately equal to the ice-free porosities. Climate changes which destabilize subsurface ice may reset shallow ice contents to zero periodically, preventing the depths accessible by remote sensing from attaining complete filling.

The Gamma Ray Spectrometer on board Mars Odyssey measured mid- to high-latitude hydrogen abundances equivalent to up to 70% ice by volume (*Prettyman et al.*, 2004). Ice contents of this magnitude would require precipitation and burial, the subsurface growth of pure ice lenses, or

unusually high initial porosities which may be filled by diffusion. The presence of polygonal terrain on Mars shows that a mechanism capable of moving soil grains has been active in these regions. Liquid water films, an important component of ice-wedge formation on Earth (*Konrad and Morgenstern*, 1980; *Konrad and Duquennoi*, 1993; *Dash et al.*, 1995; *Wettlaufer*, 1999), are not favored on Mars at present. Thermal contraction cracking (*Mellon et al.*, 1997) may play a dominant role in the dynamics of presently forming polygons (*Mellon et al.*, 1997). No evidence of heaving, lensing, or grain-segregation is observed in this static-environment experimental setup, but this is not surprising given the absence of a thermal wave oscillation. It should also be noted that microscopic effects of grain movement accumulate over long times, and cracking due to the stress of thermal contraction require distances on the order of a polygon diameter (10s to 100s of meters) (*Mangold*, 2005), much greater than the times and length-scales characteristic of these experiments.

Fisher (2005) suggests that thermal cracking of solid (perhaps interstitial) ice due to seasonal temperature variations may serve to keep deep regolith more open to vapor transport despite constrictive flux reduction in shallow layers. Cracks could penetrate into an otherwise ice-saturated soil, opening up further volume for subsurface deposition. Ice wedges on Earth form through the trapping of seasonal meltwater in the thermal cracks. The absence of a liquid phase on present-day Mars would tend to favor sand-wedge formation. But vapor propagation through the space opened by the crack would be enhanced over porous medium diffusion, and material at the base of the crack is shielded from direct insolation and will therefore remain cold relative to the surface. Ice wedges on Mars may therefore arise from vapor diffusion processes. If the combined volume of the vertically penetrating ice veins arising from such cracks is large, they could contribute to high observed ice contents.

5.6.6 Phoenix Mars lander

The Phoenix Mars Lander will land in the north polar region of Mars where equilibrium models and neutron spectrometer data from the Mars Odyssey spacecraft predict the presence of subsurface ice within centimeters of the surface (*Boynton et al.*, 2006; *Arvidson et al.*, 2008; *Mellon et al.*, 2008). The lander is equipped with a robotic arm which will be able to trench on the order of half a meter into relatively unconsolidated surface regolith; excavation down to the ice table is one of the primary mission goals (*Arvidson et al.*, 2008). In doing so, Phoenix will be able to provide a number of ground truths regarding the behavior of subsurface ice on Mars.

The robotic arm has limited mechanical strength and leverage and may be unable to penetrate deeply through soil with a high ice content, or through pure ice if it is not highly porous. Despite this limitation, the Phoenix arm may be able to sense an abrupt change in mechanical strength of the regolith which would indicate a sharp ice table as predicted theoretically and as has been seen in these experiments. Using the rasping tool at the scoop, Phoenix will attempt to remove some

surface layers of the shallow ice table. Photographic analysis of these raspings and the divots made in the ice table, as well as planned delivery of icy regolith to various on-deck instruments, may constrain the soil-to-ice mixing ratio. This could illuminate whether this ice was diffusively derived, as would be suggested by a low to moderate ice-to-soil ratio, or was emplaced by precipitation and subsequent burial, consistent with a high ratio.

If the ice-bearing regolith has a sufficiently low mechanical strength that it may be penetrated by the robotic arm, it may be possible to create a cross-section of the regolith column revealing the ice table interface. The morphology of the ice table could be correlated with the original surface albedo and rock distribution. Though it is not equipped with a brush to remove unconsolidated debris, a number of such profiles, as from a widening trench, may allow a coarse three-dimensional map of the ice table to be developed.

Low mechanical strength of the ice-bearing soil layers would be indicative of filling fractions less than 100%. Though not equipped with means of directly determining water content, Phoenix instruments such as the Thermal and Evolved Gas Analyzer (TEGA) and the Thermal and Electrical Conductivity Probe (TECP) may be able to constrain this quantity. Incomplete filling would be indicative of a non-equilibrium state which is continuing to evolve over time, constraining the history of the temperature and atmospheric water content at the landing site. Combined data sets from measurements of soil thermal conductivity and optical microscope images of the regolith particles will help constrain other soil properties, such as diffusivity, which are necessary inputs to understanding the history of subsurface ice.

5.7 Summary

A Mars environment chamber has been used to demonstrate the diffusive filling of regolith pore spaces from atmospherically derived water vapor in the absence of a bulk liquid phase. This allows the first examination of bulk ice deposition via vapor diffusion at low pressures in the laboratory. This process is studied at three scales.

At the scale of individual soil grains, optical micrographs have revealed preferential deposition at grain contact points, forming ice necks in close association with regolith particles which should significantly affect the thermal conductivity. Much of the deposited ice is turbid, suggesting the presence of grain boundaries, vacancies, or trapped gases within the ice which would reduce its bulk density. Bubbles on the order of 10–20 μm across have been observed trapped in the ice, suggesting that ice on Mars deposited through vapor diffusion may be a candidate for the extraction of trapped atmospheric gases.

At the scale of the ice table, measurements of the transition depth have revealed the sharpness and shape of the contact. The transition between well-cemented and completely unconsolidated

grains is on the order of a single grain diameter (∼500 μm). The morphology of the interface is sensitive to the local temperature field and is affected by surface irregularities such as heat pipes (*e.g.*, a warm probe head or a rock) and albedo variations (*e.g.*, coated disks or dust patches), and the magnitude of these perturbations decays with depth. The ice table follows temperature isotherms, which parallel the surface unless perturbations arising from, for example, albedo differences, deflect the temperature field.

Finally, at the deeper scale of the "cryosphere", *i.e.,* the ice beneath the dry interface, the quantity and distribution of ice as a function of depth and time has been revealed through gravimetric water content analysis. A series of experiments and numerical models of differing atmospheric vapor densities illustrate the sensitivity of ice table growth rate to the humidity of the atmosphere, and the insensitivity of ice at depths beneath the ice table to this same quantity. The evolution of the cryospheric ice beneath the ice table depends only on the local temperature gradient.

The deposition of ice significantly reduces subsequent deposition rates via a process of pore-space constriction. Numerical models of the experimental conditions which incorporate constriction capture the major effects of that process with a parameterized modification of the diffusion coefficient proportional to filling fraction. Although some observed differences between experiments and models may involve a lower density of deposited ice, observations of 90% filling after 530 hours show that the minimum density is at least this much. At intermediate filling, a stronger obstruction than linear in filling fraction is observed. The simultaneous reduction of available porosity and of molecular hop length (*i.e.,* the increasing frequency of collisions with pore walls) as ice is deposited results in an expected dependence of D proportional to the square of the filling fraction, consistent with measurements when the filling fracton is high. The tortuosity may also change at moderate to high filling fractions, further increasing the sensitivity of D to σ. Further investigation is needed to describe the constriction at high filling fraction.

The numerical model is used to examine long-term growth effects under simulated temperature and humidity conditions. The effect of constriction asymptotically diminishes the vapor flux beneath the ice table and similarly retards the ice deposition rate.

The complete filling of the regolith with atmospheric vapor on obliquity-scale times will be inhibited by reduced rates of ice deposition due to constriction, but complete choking will not occur unless the pore volume is completely saturated with ice. Lack of complete filling in a regolith column implies a nonequilibrium condition such that the quantity and distribution of subsurface ice is continually evolving. These studies will inform observations of subsurface ice by Phoenix and subsequent spacecraft addressing similar regions.

Chapter 6

Modeling of Subsurface Ice Growth

6.1 Chapter Summary

A numerical model is developed and applied to the problem of ice growth in the cryosphere beneath the ice table interface. The accumulation of subsurface ice as a function of depth, the dynamics and rate of ice growth, and the effects of deposited ice on the surface and subsurface thermal structure are considered. Climate oscillations over the past 5 million years have repeatedly deposited and removed ice in mid- to high-latitude regoliths, but the past 300 kyr have been relatively quiescent and generally favorable to pore ice accumulation in these regions. The model considers the effects of several parameters on ice growth rate including: ice-free porosity, magnitude of constriction arising from a changing pore-space geometry, thickness of an ice-free surface layer, and the presence of a massive ice sheet below some depth. The different constriction parameterizations and ice-free porosities are found to have only moderate effects on the total quantity of ice deposited and the shape of the ice content profile. Deep ice layers significantly perturb the subsurface temperature field and result in increased ice accumulation at all depths if the massive ice sheet is within 10 m of the surface. Near surface ice-free layers have the greatest influence of the effects considered; a change in surface layer thickness from 2 cm to 5 cm can decrease the subsurface ice content accumulated in 300 kyr by nearly 50%. The environmental parameters chosen for the model match the known properties of the Phoenix Scout Mission landing site. The lowland bright terrain to which the spacecraft is targeted is predicted to harbor an ice-rich subsurface layer within 2–6 cm of the surface. Given this range of ice-free surface, the model indicates that the maximum amount of ice accumulated at the ice table in 300 kyr will be between 70–92% of complete filling, decreasing by not more than 15% at 0.5 m depth in the absense of a buried ice sheet. The true accumulated quantity in the upper layers is likely less than predicted, given that ice-loss events of moderate extent are likely to have occured in the last 300 kyr.

6.2 Influences on Cryosphere Ice Evolution

6.2.1 Atmospheric independence

The non-linear dependence of vapor pressure on temperature allows high temperatures to control the shape of the time-averaged vapor density profile in a regolith subjected to a depth-decaying periodic thermal wave. In an ice-bearing porous medium this gives rise to a down-directed mean-annual vapor density gradient. Vapor moving within the pore spaces follows this gradient irrespective of the gradient between the atmosphere and the ice table.

Upon an increase in subsurface temperature or a drop in atmospheric humidity, the ice table at the top of the cryosphere will become unstable and will retreat deeper into the subsurface by providing a flux of vapor to the atmosphere. The upward directed gradient from the ice table is set by the vapor density difference between the ice table and the atmosphere (*Mellon and Jakosky*, 1993; *Mellon et al.*, 2004; *Schorghofer and Aharonson*, 2005). The downward gradient from the ice table, however, depends only on the subsurface temperature profile, since pore vapor surrounded by ice experiences vapor concentrations and concentration gradients dependent only on the vapor pressure (*i.e.,* temperature) of the local ice. Thus, even as the ice table interface retreats, deeper ice, insulated from the desiccating gradient to the atmosphere, will continue to migrate down the mean annual vapor density gradient. This allows the evolution of ice beneath the ice table to be determined using only subsurface temperatures and not atmospheric water content. It is important, however, to include the thermal effects of ice-free layers near the surface, which attenuate the temperature wave before it reaches the depth of ice stability.

Within the pore spaces themselves, the vapor pressure of water in the pore gas will be in equilibrium with the surrounding ice. In a pore space of order 1 mm, a free-gas diffusion coefficient of $\sim$30 cm^2 s^{-1} (*Wallace and Sagan*, 1979) will permit equilibration between pore ice and the gas within the pore on a timescale of $<$ 1 second, much faster than diurnal temperature and vapor pressure changes. In most diffusion-dominated pore spaces, the pore radius will tend to be smaller than 1 mm. Bulk flow of less humid gas over the ice may also strip the boundary layer away and increase the time to equilibration. Yet the speed of the "wind" within the regolith due to thermal expansion and contraction of air masses rarely exceeds 1 cm per sol, much slower than the rate of diffusive flux (see Section 2.6.1). Thus, the partial pressure of water in pore spaces will remain saturated with respect to the local ice as long as the temperature fluctuations are not overly rapid (*i.e.,* shorter than diurnal variations).

6.2.2 Icy soil thermal conductivity

The thermal conductivity of the bulk regolith material depends on the amount of ice present. This analysis adopts a series addition of interstice and grain conduction after *Mellon et al.* (1997). Here,

k_w is the conductivity through the solid regolith grains and k_i is the conductivity of the interstice, which may be filled with either gas or ice. The bulk conductivity, k, is thus expressed as

$$k = \frac{k_w k_i}{(1-\phi_0)k_i + \phi_0 k_w}. \tag{6.1}$$

The ice-free porosity, ϕ_0, is assumed to be homogeneous and isotropic on length scales larger than several tens of grains. The parallel conductivity through the interstice, with contributions from gas and solid ice, is

$$k_i = (1-f_c)k_{i0} + f_c k_{\rm ice}, \tag{6.2}$$

where k_{i0} is the ice-free interstitial conductivity. The fraction of the cross-sectional area through which heat conduction occurs, f_c, was modeled by *Mellon et al.* (1997) and found to be related to the square root of the filling fraction, $f_c = (\sigma/\sigma_0)^{1/2}$; to be largely independent of grain shape; and to be completely independent of grain size at these scales. An effective grain conductivity for basaltic regolith particles of $k_w = 3.0$ W m^{-1} K^{-1}, as used by *Mellon et al.* (1997), is adopted here. Using this formulation, k is thus a rational function of the form $(A+Bf_c)/(C+Df_c)$, where A, B, C, and D are constants for a particular temperature. Thus, The thermal conductivity when the filling fraction is zero is written as $k(f_c(0)) = k_0$.

Presley and Christensen (1997) found that at atmospheric pressures appropriate for Mars, the bulk thermal conductivity in particulate media depends weakly on the absolute pressure, $k \propto p^{2/3}$, and also varies as the particle diameter as $k \propto d^{1/2}$. At 8 mbar, the range of thermal conductivities under simulated Mars conditions was found to vary from 0.011 to 0.11 W m^{-1} K^{-1} over a particle size range of 11–900 μm. Sand-sized grains composed of basaltic material were found to have $k \simeq 0.06$ W m^{-1} K^{-1}. These experimental values are similar to those used by *Mellon and Jakosky* (1995) for a general particulate regolith (0.02 W m^{-1} K^{-1}). Ice, on the other hand, has a bulk thermal conductivity of $\sim$2.2 W m^{-1} K^{-1} at 273 K, but as high as 3.6 W m^{-1} K^{-1} at 180 K. The conductivity of ice is given by the expression $k_{\rm ice} = 488.19/T + 0.4685$ W m^{-1} K^{-1}, which is valid in the temperature ranges of interest (*Hobbs*, 1974).

The addition of ice at grain contact points greatly increases the conductivity of the sample through increased thermal contact and conduction area attributable to preferential ice depositon as annuli at grain contact points (Chapter 5 and *Hobbs*, 1974). The parallel conductor model appropriately exhibits a rapid increase in thermal conductivity for small filling fractions. For low ice-free bulk thermal conductivities ($k_0 \simeq 0.01$ W m^{-1} K^{-1}), the value of k reaches 50% of its ice-saturated value at 10% filling. Higher ice-free values of $k_0 \simeq 1.0$ W m^{-1} K^{-1} may reach this point at only 1.5% filling. In either case, the earliest deposited ice has a significant effect on the thermal properties of the regolith.

The above scheme describing the variation in bulk thermal conductivity with ice content derives

from theoretical considerations. Data is lacking which can be used to constrain this model insofar as the data reflect changing thermal properties due to vapor-deposited interstitial ice. Investigations are currently in progress at the Mars Simulation and Ice Laboratory at Caltech to measure the dependence of k on filling fraction for a variety of materials.

6.2.3 Evolving pore geometries

6.2.3.1 *Constriction*

Three effects arising from pore ice deposition change the diffusion coefficient of the medium and thus the rate of further ice growth. First, the cross-sectional area of the pores reduces in proportion to the quantity of ice deposited. The expression

$$\phi = \phi_0 \left(1 - \frac{\sigma}{\sigma_0}\right), \tag{6.3}$$

captures the reduction of ϕ as a function of filling fraction, where ϕ_0 is the ice-free porosity and $\sigma_0 = \rho_{\rm ice}\phi_0$ represents the maximum ice content relative to free space. This parameterization was used by *Mellon and Jakosky* (1995) in modeling shallow subsurface ice growth. In Chapter 5, laboratory ice growth experiments indicated a stronger effect than that given by equation (6.3) alone. This led to the introduction of a second factor of diffusion reduction arising from a transition between Fickian and Knudsen diffusion as the pore geometry changes.

Initially, pores on the order of several tens of microns will be in the transition regime under typical Mars pressures; the mean free path of gas molecules at ∼600 Pa being within a factor of 10 of the pore diameter. The deposition of ice reduces the pore size and pushes the porous medium further toward Knudsen diffusion. In that regime, when molecule collisions with pore walls dominate the transport, one defines a chord (*i.e.,* an individual molecular "hop") as a straight line segment terminated at both ends by a pore wall. As Knudsen diffusion comes to dominate, the chord-length distribution of the pore space, l, rather than the mean free path, constrains the possible molecular trajectories. In Chapter 5, an analogous treatment to that of *Evans et al.* (1961), writes l as in equation (5.14). In this manner, the chord length is proportional to its ice-free value, l_0, and also to the porosity reduction. If the Knudsen diffusion coefficient is written as in equation (5.13), such that it depends on l and the obstruction factor ϕ/τ, as does the Fickian expression (equation (2.3)), then the combined effective diffusion coefficient (using the Bosanquet interpolation formula, equation (2.15)), can be written

$$\frac{1}{D} = \frac{1}{D_{F,0}v} + \frac{1}{D_{K,0}v^2}, \tag{6.4}$$

where $v = (1 - \sigma/\sigma_0)$ is the void fraction and $D_{F,0}$ and $D_{K,0}$ represent the ice-free values of the Fickian and Knudsen diffusion coefficients, wherein l_0 and ϕ_0 substitute for l and ϕ in equations (5.12)

and (5.13). As the filling fraction increases, v becomes smaller and the second term in equation (6.4) dominates over the first if $D_{K,0}$ is comparable in magnitude to $D_{F,0}$.

Since porosity changes with filling fraction, it is reasonable to assume that tortuosity changes as well; this being a third effect contributing to constriction. *Mellon and Jakosky* (1993) subsume all pore geometry variation into a changing ϕ; however, while ϕ changes linearly in filling fraction, τ has a different behavior. As the constricting medium approaches the limit of disconnected pores, molecules will be forced to take convoluted paths as more direct avenues are closed. Once the pore volume is no longer continuous, the tortuosity will be infinite and the gas-phase diffusivity will be zero, although empty pore volume may remain.

A variety of possible pore shape and interconnection models exist; few studies exist on which to base a robust physical relationship between tortuosity and filling fraction. The expression

$$\tau = \tau_0 \left(1 - \frac{\sigma}{\sigma_0}\right)^{-1}, \tag{6.5}$$

where τ_0 is the ice-free tortuosity, represents one simple model. Though pore spaces in a real porous medium will likely become disconnected before the filling fraction reaches σ_0, equation (6.5) has the proper values of $\tau = \tau_0$ and $\tau = \infty$ at the limits of ice-free ($\sigma = 0$) and ice-saturated ($\sigma = \sigma_0$) pore space. As appropriate for some models of pore constriction (*Zalc et al.*, 2004), equation (6.5) changes slowly at low filling fractions, rapidly increasing as complete filling is approached. Since tortuosity enters the obstruction factor of both Fickian and Knudsen diffusion coefficients, adding this expression for tortuosity into the calculations raises the exponent of v by one in both denominators of equation (6.4).

If at time $t = t_0$ the pore spaces are ice free, the Bosanquet expression is just equation (6.4) with v equal unity. At time $t > t_0$ after some ice has deposited, the ratio of equation (6.4) to the ice-free value, D_{t_0}, expresses the reduction in D as a function of $\sigma(t)$. Consider first the case where the tortuosity is independent of filling fraction (*i.e.,* τ=τ_0 for all t). If $D_{K,0} \gg D_{F,0}$, the second term in equation (6.4) is negligible and D_t/D_{t_0} will be linear in σ, giving a 50% reduction in the diffusion coefficient for 50% filling. If instead $D_{K,0} \approx D_{F,0}$, 50% filling will reduce the diffusion coefficient to less than 30% of its ice-free value, and a filling fraction of 90% would exhibit a diffusion coefficient one hundredth as large as D_{t_0}. Considering the case where tortuosity varies as the expression in equation (6.5), there is no linear dependence of D on σ. For $D_{K,0} \gg D_{F,0}$, 50% filling results in a 75% reduction over D_{t_0}, while with $D_{K,0} \approx D_{F,0}$, 50% filling gives $D_t/D_{t_0} = 14\%$.

6.2.3.2 *Choking*

Constriction restricts the flux passing into a given depth, but the reduction of pore space does not affect the saturated state of pore-space gas. An imposed barrier of low-diffusivity material, such as a

soil-free cavity in the subsurface or the top of the ice table (and its attendant phase transition), will impose discontinuities in the diffusion coefficient. But within a homogeneous, ice-bearing regolith beneath the ice table, the diffusion coefficient will change slowly as a function of position. If $\partial D/\partial z$ is indeed small, D may be taken out of the derivative in the right-hand side of equation (2.26), leaving the growth of ice at any depth in an ice-bearing region dependent on the value of the local diffusion coefficient and not its gradient. Hence, in a region with slowly and smoothly changing physical properties, ice growth at any depth is independent of the magnitude of constriction in surrounding layers. Complete filling at some depth (*i.e.,* choking) does not prevent the continued migration and redistribution of ice within unsaturated pore spaces.

These constriction effects are most strongly experienced by the shallowest stable ice, since stronger vapor density gradients experienced at the ice table relative to deeper ice produce a faster rate of ice deposition. It has been suggested (*Clifford*, 1993; *Mellon and Jakosky*, 1995) that ice deposited from vapor may completely choke off transport through these ice-rich layers. Such a condition will obtain with full saturation, when the regolith is ice-filled and no more pore spaces are available for vapor migration. Though a gradient in partial pressure still exists, the vapor flux through such a filled medium must be zero everywhere. However, an unsaturated pore space further down the mean vapor density gradient will provide a sink for the down-directed flux. If an ice-filled layer, perhaps deposited by precipitation, is introduced into the regolith column, the downward flux will erode the bottom of this layer, potentially opening up paths between the unsaturated subsurface and the atmosphere.

6.2.4 Combined effects

For a sufficiently small depth interval containing no discontinuities, the temperature gradient may be considered linear and the diffusion coefficient will be independent of depth to first order. Hence, for a constant diffusion coefficient, equation (2.26) can be written

$$\frac{\partial \sigma}{\partial t} = D\frac{18}{RT}\frac{\partial^2 p_1}{\partial z^2} \approx D\frac{18 p_1 H}{R^2 T^4}\left(\frac{H}{RT} - 2\right)^2 \left(\frac{\partial T}{\partial z}\right)^2, \tag{6.6}$$

where p_1 is the partial pressure of water vapor. The approximation above holds true for a linear temperature gradient. For a given thermal flux, the thermal gradient ($\partial T/\partial z$) is inversely proportional to thermal conductivity, k. If the instantaneous rate of ice growth in a regolith at the time deposition begins is $\partial\sigma/\partial t|_{t_0}$, and the growth rate after some time t is $\partial\sigma/\partial t|_t$, then the ratio of ice growth rates for a given vapor density gradient may be written as

$$\frac{\frac{\partial\sigma}{\partial t}\big|_t}{\frac{\partial\sigma}{\partial t}\big|_{t_0}} = \frac{D_t}{D_{t_0}}\frac{k_{t_0}^2}{k_t^2}, \tag{6.7}$$

where the identical vapor density gradients have canceled. This relationship permits comparison of relative ice deposition rates if both D_t and k_t are known functions of σ, such as were given in Sections 6.2.2 and 6.2.3.

Using the relations developed above for thermal conductivity and diffusion coefficient as functions of ice content, the reduction in deposition rate at time t relative to the initial deposition rate is shown in Figure 6.1, where $k_{t_0} = 0.05$ W m^{-1} K^{-1} and $D_{t_0} = 4.0$ cm^2 s^{-1}. This figure illustrates the extreme variation in ice growth rates which result from the initial deposition as ice enhances the conductivity of an unconsolidated medium. The solid black line and solid gray line have identical constriction parameterizations, but the gray line takes $k_t = k_{t_0}$ for all t.

The rapidly increasing thermal conductivity reduces both the thermal gradients and the ice growth rate. The thermal structure of the porous medium dominates the ice growth behavior at filling fractions below ∼25% if the thermal conductivity is allowed to vary with ice content. By approximately 1% filling fraction, the ice growth rate has been reduced by two orders of magnitude. Another order of magnitude reduction occurs by 13% filling. The reduction of D_t relative to D_{t_0} is linear in v at higher filling fractions, and the slopes of the lines in log-log space (1, 2, and 3) represent the exponent of this factor. Though thermal conductivity continues to change, it does not alter the slopes of the lines beyond about 25% filling because σ appears to the 1/2 power in both numerator and denominator of the expression for k.

6.3 Numerical Model

The growth rate of ice in pore spaces is given by equation (2.26). This equation is repeated here for ease of referral:

$$\frac{\partial \sigma}{\partial t} = -\frac{\partial J_1}{\partial z} = \frac{\partial}{\partial z}\left(D\frac{\partial \rho_1}{\partial z}\right). \tag{6.8}$$

The model uses the expressions for constriction and thermal conductivity developed in Sections 6.2.2 and 6.2.3 to determine subsurface ice growth on 100 kyr timescales. The solution of equation (6.8) may be computed efficiently because it requires only knowledge of D and temperature as functions of depth at any time. The diffusion coefficient and its gradients depend on temperature and the current filling fraction, and vapor density depends on temperature alone.

Subsurface temperatures are computable using an unconditionally stable implicit scheme. Temperature fluctuations can give rise to large variations in vapor density, particularly at the boundary between ice-bearing and ice-free soils, where the latter can experience unsaturated levels of ρ_1. The large vapor density gradients which can exist across this boundary are normally handled through explicit solution of the differential equations (as in equation (5.3)). But within the ice-bearing region, this complication may be removed if the assumption of pore-gas vapor saturation obtains at all times. The thermal diffusivity of the regolith is on the order of 10^{-8} m^2 s^{-1}, approximately

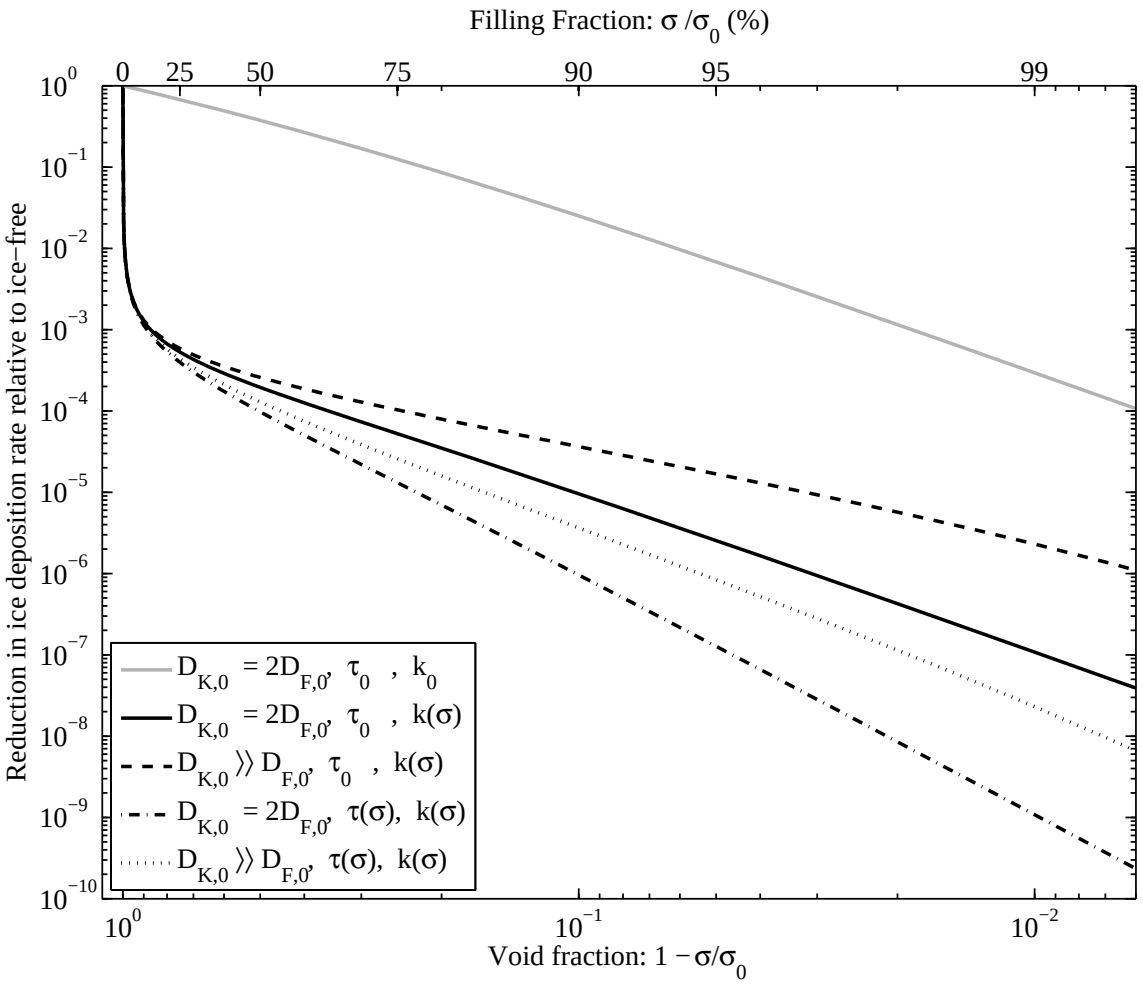

Figure 6.1: The reduction in ice deposition rate relative to the instantaneous initial deposition rate caused by constriction and thermal conductivity changes, given a constant vapor-density profile. For all curves shown, the ice-free thermal conductivity is 0.05 W m^{-1} K^{-1}. Solid lines indicate cases where tortuosity is constant with filling fraction and $D_{K,0} \approx D_{F,0}$, with $D_{F,0} = 6.0$ cm^2 s^{-1} and $D_{K,0} = 12.0$ cm^2 s^{-1}. The solid gray line excludes the effect of changing thermal conductivity. The slope of the solid lines is 2, reflecting the exponent on the dominant term in equation (6.4). The dot-dashed curve incorporates a changing tortuosity with σ and has a slope of 3. By setting $D_{K,0} =$ 1000 cm^2 s^{-1}, the second term in the expression for the effective diffusion coefficient is negligible, resulting in a model of constriction that depends on only one factor of v as in equation (6.3); this is illustrated with the dashed line (with a slope of unity).

four orders of magnitude smaller than the concentration diffusivity. Thus, the timescale for the propagation of vapor density differences is fast enough compared to the speed of the thermal wave that a timestep on the order of 10^3–10^4 seconds may be taken without violating the assumption of a vapor-saturated pore-gas. If there are no discontinuities in the diffusion coefficient within the domain of ice deposition (*i.e.,* no abrupt jumps in temperature or ice content), the growth behavior will be numerically stable with time steps on the order of several thousand seconds.

The model consists of three numerical layers. The top 0.3 m of the numerical grid resolves the

diurnal temperature wave at ∼0.9 cm intervals. This spatial resolution, coupled with the model's sub-sol timestep, provides accurate determination of surface thermal emission, which is strongly non-linear in temperature. A second grid, more coarsely spaced at ∼12.5 cm intervals, extends from the base of the diurnal region to 15 m, encompassing multiple annual skin depths. The skin depth of an ice-saturated regolith extends farther than an ice-free regolith by a factor of $\sqrt{k_1/k_0}$, where k_1 and k_0 are the bulk thermal conductivities of ice-rich and ice-free regoliths, respectively. This factor is of order 2.5 for basaltic particles with $k_0 = 0.05$ and $k_1 = 2.5$ W m^{-1} K^{-1}. The model region resolving the annual thermal wave extends to approximately ten times the skin depth of a dry regolith, and therefore encompasses ∼4–5 skin depths if the pore spaces are ice filled. Beneath this domain, a logarithmically spaced region of 50 points extends to 500 m to resolve obliquity-scale thermal oscillations.

To properly compute heat fluxes at a given location during a particular epoch, the model uses the long-term orbital element solutions for Mars computed by *Laskar et al.* (2004). These solutions provide obliquity, eccentricity, and longitude of perihelion for up to 20 Myr into Mars' past. The model computes fluxes at the surface at least ten times per sol for a given epoch, latitude, and surface albedo; timesteps may be up to 5 times smaller in cases where required by subsurface thermal properties. The surface flux includes direct and diffuse radiation using the schema of *Aharonson and Schorghofer* (2006) which assumes a diffuse IR component equal to 2% of noon insolation (*Kieffer*, 1976). The model neglects scattered radiation from atmospheric dust.

The mean annual solar insolation for the model was checked against analytical solutions given in *Ward* (1974) for polar, equatorial, and intermediate latitudes. Surface fluxes are passed to an implicit Crank-Nicolson thermal conduction scheme which propagates the temperature wave through the subsurface given thermal properties as modified by the presence of ice. If surface temperatures fall below 145 K, CO_2 deposits at the surface. The surface temperature remains fixed at the CO_2 frostpoint until the mass of accumulated CO_2 again reaches zero.

The effective bulk thermal conductivity in ice-free material, k_0, is the sum of contributions from conduction through the void space gas, conduction within the solid particles and ice, and thermal radiation between the particles. This latter contribution is usually negligible for temperatures less than 300 K. The model uses the scheme of Section 6.2.2 to compute thermal conductivity as a function of filling fraction.

The vapor pressure within the regolith is set at all points by the temperature of the ice. In cases where an ice-free surface layer is imposed, vapor densities and growth rates in this region are zero and equation (6.8) is computed for depths beneath the imposed cryosphere boundary. Similarly, an imposed ice-saturated regolith extending beneath some depth does not change with time and represents a no-flux boundary.

The diffusive properties of the ice-free regolith are assumed to be homogeneous. The diffusivities

are adjusted for every gridpoint and timestep based on temperature dependence of the Fickian ($D \propto T^{3/2}$) and Knudsen ($D \propto T^{1/2}$) regimes, as appropriate. Atmospheric pressures are assumed constant, so the P^{-1} dependence of Fickian diffusion does not play a role. The effective diffusion coefficient when the filling fraction is non-zero is computed using equation (6.4). Unless otherwise stated, the models assume an ice-free porosity of 40%.

One investigation below focuses on the relative strengths of the contributing constriction effects. By setting the ice-free Fickian and Knudsen diffusion coefficients to $D_{F,0} = 6.0$ cm^2 s^{-1} and $D_{K,0} = 12.0$ cm^2 s^{-1}, respectively, the effects of the changing pore geometry indicated by the results of Chapter 5 are employed and the effective diffusion coefficient of the ice-free medium is 4.0 cm^2 s^{-1}. This method incorporates both changing porosity and the transition to greater Knudsen diffusion contributions as the pore space constricts. To employ a constriction model equivalent to that of *Mellon and Jakosky* (1993), wherein only the porosity changes with filling fraction, the ice-free Fickian coefficient is set to $D_{F,0} = 4.0$ cm^2 s^{-1} and the ice-free Knudsen diffusion coefficient is given the unphysically large value of $D_{K,0} = 1000$ cm^2 s^{-1}. This ensures that the contribution of the Fickian term always dominates and allows the constriction parameterization to be selected at run-time given appropriate choices of ice-free diffusion coefficients. The constriction models may also include either a constant or changing tortuosity, via the relation in equation (6.5). These choices therefore bracket the range of effects attributable to the choice of constriction model. See Section 6.3.2 for a discussion of appropriate ranges for diffusion coefficients.

Having thus obtained the vapor density and the effective diffusion coefficient at all depths for a particular time, equation (6.8) gives the quantity of ice deposited in a single timestep. As a check on the model computation of ice growth rates, the accumulation of ice in early growth stages (before the diffusion coefficient was significantly altered by constriction) was compared to values computed from equation (6.8) using the diffusivity and values for the mean annual vapor density gradients computed for a perpetually ice-free regolith. The model results when ice is permitted to deposit agree well with this benchmark, with minor over-accumulation in the simple calculation being attributable to a static diffusion coefficient.

6.3.1 Model assumptions

The sub-second timesteps required to explicitly solve the vapor diffusion equation preclude running such models as those in Chapter 5 for thousands or millions of model years. Focusing on ice contents beneath the stability depth and one key assumption permits the model to be simplified and thus executed more efficiently. First, gas in close contact with ice is assumed to be saturated at all times. Gas in an ice-bearing pore equilibrates with that ice; the partial pressure of water vapor equals the vapor pressure of the ice, which in turn depends only on its temperature. This assumption is valid in circumstances where temperatures change slowly and bulk motion of the gas is negligible

(see Section 6.2.1). As discussed in Section 6.3, the concentration diffusivity is three to four orders of magnitude larger than the thermal diffusivity, allowing changes in vapor density to maintain a saturated pore space gas if the temperature fluctuations are of diurnal frequency or slower. A consequence of this assumption is that ice beneath the ice table is insulated from the vapor content of the atmosphere as discussed in Section 6.2.1.

For locations where these assumptions are valid, such as the evolution of ice perpetually beneath the ice table, they give rise to several advantages. For example, gradients which drive vapor flux within the ice-bearing regolith are independent of the atmospheric humidity, a poorly constrained quantity over long timescales. The gradients instead depend only on subsurface temperature, which is used to compute vapor densities via the Clausius-Clayperon equation and the ideal gas law. Temperature can be tracked with time-efficient implicit schemes given the surface thermal flux balance and subsurface thermal properties.

The regions of interest for the model presented here are latitudes where subsurface ice is currently stable, and depths where surface thermal fluctuations overwhelm the geothermal gradient and give rise to an inward mean-annual vapor flux. These models therefore do not include any geothermal heat flux and incorporate no subsurface vapor source; all ice which accumulates is ultimately derived from the atmosphere.

6.3.2 Model parameters: Phoenix landing site

Parameters for this model are chosen to be appropriate to the site selected for the Phoenix Mars lander; Table 6.1 summarizes these choices. The landing ellipse for Phoenix is centered on lowland bright terrain of the Scandia formation at 68.16 degrees North latitude, 233.35 degrees East longitude. The scientific rationale for selection of this region includes the presence of a near surface ice table. A variety of techniques including the gamma ray and neutron spectroscopy, ice stability theory, and TES and THEMIS seasonal temperature and thermal inertia maps indicate an ice rich layer beneath between 2–6 cm of ice-free soil (1–9 cm, including uncertainties) (*Mellon et al.*, 2008). The spectrometry calculations assume a dry soil density of 1600 kg m^{-3}. This depth allows the possibility that both the ice table and a region of ice-free soil will be within reach of Phoenix's robot arm. The thermal inertia for ice free soil in this region is expected to be $\sim$250 J m^{-2} K^{-1} $s^{-1/2}$ (*Putzig et al.*, 2005; *Putzig et al.*, 2006). The bulk thermal conductivity chosen to represent dry particulate basaltic regolith (0.05 W m^{-1} K^1) falls close to the value of 0.06 given by *Presley and Christensen* (1997) for medium-sand-sized particles. This is slightly higher than the value of 0.02 W m^{-1} K^1 used by *Mellon and Jakosky* (1993). The albedo of the landing site region is approximately 0.28 (*Paige et al.*, 1994; *Putzig et al.*, 2006). The range of atmospheric pressure experienced at the landing site region ranges from 700–1100 Pa (*Tamppari et al.*, 2008), and a constant value in the middle of this range, 900 Pa, is chosen for use in the model.

The porosity of the ice-free soil at this site is unknown, so a mid-range value of 40%, typical of medium-sand-sized material, is chosen. Variation of porosity over a wide range of 20–70% is shown to have a minor effect on the ice density profiles which develop. The ice-free diffusivity is also a poorly constrained quantity for Mars surface materials. Previous work described in Chapter 2 and the investigations of Chapters 3 and 4 suggest that a value in the range of 2–6 $cm^2\ s^{-1}$ is appropriate. An effective diffusivity of 4.0 $cm^2\ s^{-1}$ is obtained using 6.0 and 12.0 $cm^2\ s^{-1}$ as values for the ice-free Fickian and Knudsen diffusivities. The individual ice-free diffusion coefficients are also within a plausible range and are similar to the results obtained in Section 3.5.1.2, where these two quantities were determined for 50–80 μm glass beads.

Parameter	Value	Reference
Latitude	68°	*Arvidson et al.* (2008)
Albedo	0.28	*Paige et al.* (1994); *Putzig et al.* (2006)
Pressure	900 Pa	*Tamppari et al.* (2008)
k_0	0.05 W m^{-1} K^1	*Presley and Christensen* (1997)
Thermal inertia	250 J m^{-2} K^{-1} $s^{-1/2}$	*Putzig et al.* (2006); *Mellon et al.* (2008)
Regolith bulk density	1600 kg m^{-3}	*Boynton et al.* (2002); *Feldman et al.* (2002)
Ice-free diffusivity	4 $cm^2\ s^{-1}$	*Hudson et al.* (2007); *Hudson and Aharonson* (2008)
Ice table depth	2–6 cm (1–100 cm)	*Mellon et al.* (2008)
Ice-free porosity	40% (20–70%)	*Hudson et al.* (2007) and references therein[1]

Table 6.1: Model parameters; chosen for similarity to Phoenix landing site. Values in parentheses represent the range of values examined in various model runs. [1] No data on soil porosities at the Phoenix landing site are currently available; the range and nominal value given is based on laboratory simulants and terrestrial sand-sized soils.

Both ice-free soil at the surface and a massive sheet of ice-cemented soil at some depth will perturb the thermal profile, thereby affecting the rate of ice growth in unsaturated pore spaces. The history of subsurface ice over 5 million years of recent Mars history was examined in *Schorghofer* (2007). It was shown that numerous retreat events would have depleted a initial massive ice sheet deposited during earlier epochs via precipitation. The retreat of the ice sheet, which was assumed to include some quantity of soil particles, resulted in the formation of a porous lag deposit. This deposit would, during favorable epochs, experience interstitial ice deposition via diffusive processes. For a climate which favors ice loss to remove mass from the ice table, it would first need to remove all of the pore ice in the above regolith.

Three retreat events of sufficient strength and duration to do so have occurred between 600–300 ky ago; however, the quiescent obliquity history of the past 300 ky have not been conducive to ice loss events of comparable magnitude. The models discussed below begin 300,000 years ago, after the last substantial ice-loss event.

The initial conditions for all models include some depth of ice-free regolith. The depth to the shallowest stable ice, the ice table, is manually set for each model run. To illuminate the effect of a massive subsurface ice sheet, some models are run with pore-filling ice which extends from some

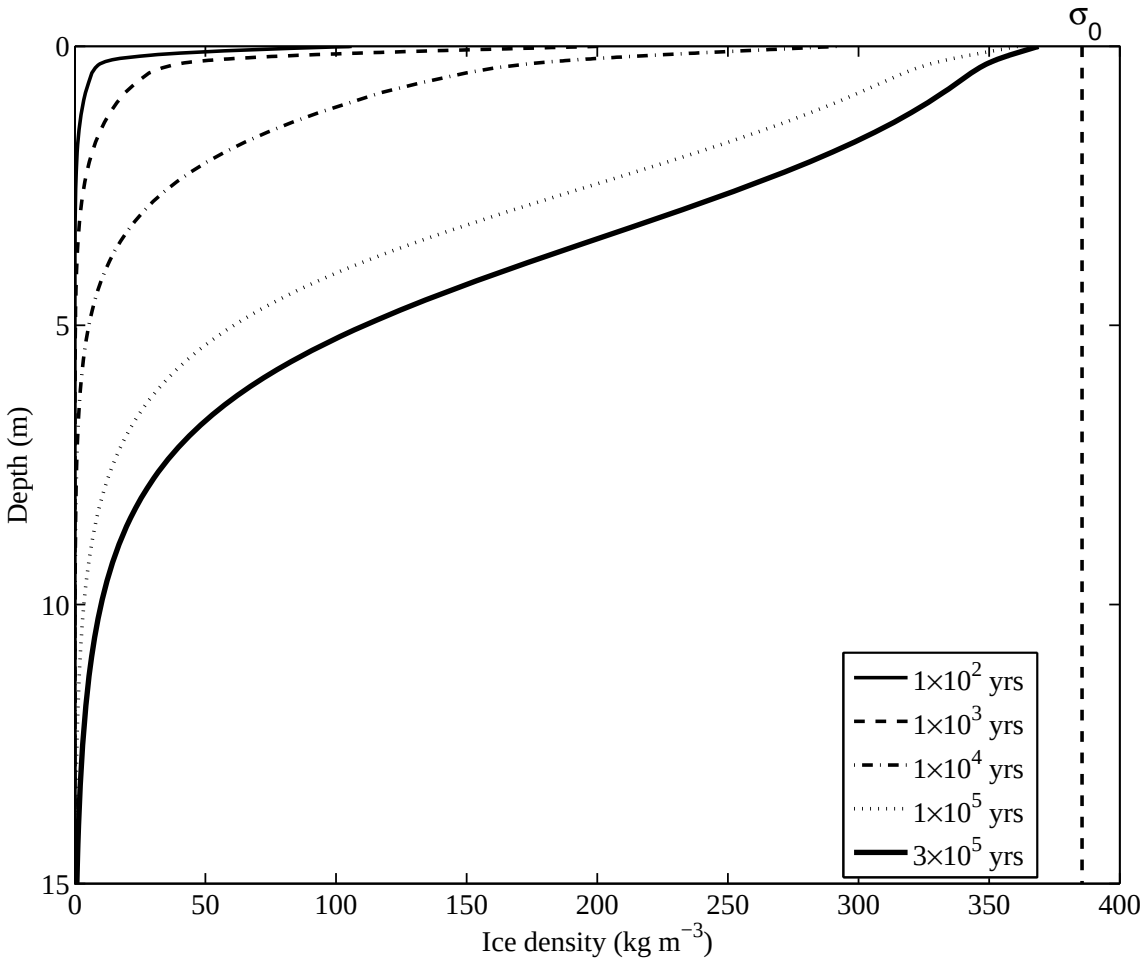

Figure 6.2: Logarithmically spaced time intervals of modeled pore-ice growth from 10 to 100,000 years; the final model profile at 300,000 years is also shown. The constriction model uses $D_{F,0} = 6.0$ and $D_{K,0} = 12.0$ (in cm^2 s^{-1}) and a constant τ. High temperature gradients in shallow depths give rise to high filling fractions in short time intervals, creating a sharp bend in the early profiles. Increasing thermal conductivity of shallow layers as ice deposits results in higher gradients and growth rates at depth, thereby smoothing the profiles with time.

shallow depth down to the bottom of the model domain. These models do not simulate minor ice-loss events which may have penetrated to depths shallower than the massive ice sheet in the last 300 ky, but instead assume conditions favorable to ice deposition below the ice table depth for the entire time interval. Therefore, these results represent an upper bound on the quantity of ice, deposited since 300 kya, which may exist in the subsurface.

6.4 Results

A profile of ice content as a function of depth at logarithmically spaced time intervals is given in Figure 6.2. These profiles are for a single model begun with an initially ice-free regolith and allowed

to evolve for the most recent 300,000 years of Mars' orbital history; ice stability was assumed for all depths. The model uses a constriction parameterization wherein the ice-free Knudsen diffusion coefficient is comparable to the Fickian diffusion coefficient ($D_{F,0} = 6.0$ cm^2 s^{-1} and $D_{K,0} = 12.0$ cm^2 s^{-1}), and τ does not vary with filling fraction.

This figure shows that ice growth is most rapid in the shallowest layers, with the surface reaching 27% filling in 100 years and 52% filling in 10,000 years. This rapid growth arises from the high thermal gradients, producing in turn high vapor density gradients, permitting the rapid deposition of ice. The deposition rate is reduced as the effect of constriction becomes stronger. In the first 100,000 years of growth, the surface layer accumulates enough ice to fill 94% of the available pore space. In the last 200,000 years, however, the ice content of the surface layer grows by only 2%, reaching 96% filling, despite the obliquity exhibiting a similar amplitude over the entire modeled time interval.

As ice accumulates in the shallow subsurface, the thermal conductivity of ice-bearing layers increases. This has two effects: First, the gradients in the shallowest layers are reduced, further contributing, along with constriction, to the reduction in shallow ice growth rate. Second, greater quantities of heat are conducted to depth, permitting larger gradients there and enhancing ice deposition. These effects smooth out the ice content profile, which initially exhibits a sharp bend at approximately 0.2 m depth for times less than 1,000 years. If conditions favorable to ice deposition persist, the profile will continue to accumulate ice, with all depths approaching the maximum possible filing, σ_0. The base of the cryosphere is indistinct as ice content reduces slowly toward zero with increasing depth. Though not shown here, the annual thermal wave will be overwhelmed by the geothermal gradient at approximately 10–20 m and this may affect the profile at these depths.

6.4.1 Constriction effect on ice growth

The ice contents following 300,000 years of accumulation for various constriction models are presented in Figure 6.3a. The diffusion parameters are chosen such that at zero ice content, the effective diffusion coefficients of the models are the same: for a case where the ice-free Fickian and Knudsen diffusion coefficients are comparable in magnitude, $D_{F,0} = 6.0$, $D_{K,0} = 12.0$. When $D_{K,0} \gg D_{F,0}$, then $D_{F,0} = 4.0$ and $D_{K,0} = 1000$ (vaules are in cm^2 s^{-1}). Ice stability is assumed at all depths.

Overall, there is only a moderate difference between the models following 300 kyr of accumulation as displayed in Figure 6.3a. Initially, the ice growth rates of all models are comparable since the initial ice-free diffusion coefficients are identical. Only after some significant quantity of ice deposits do the differences in constriction parameterization come to dominate the further evolution. For example, in Figure 6.3a, the strongest and weakest constriction models bracked the intermediate cases for depths where the accumulation has become greater than ∼25–40% (*e.g.,* for depths shallower than ∼4 m). The weakest parameterization uses a constant τ and $D_{K,0} \gg D_{F,0}$, such that constriction

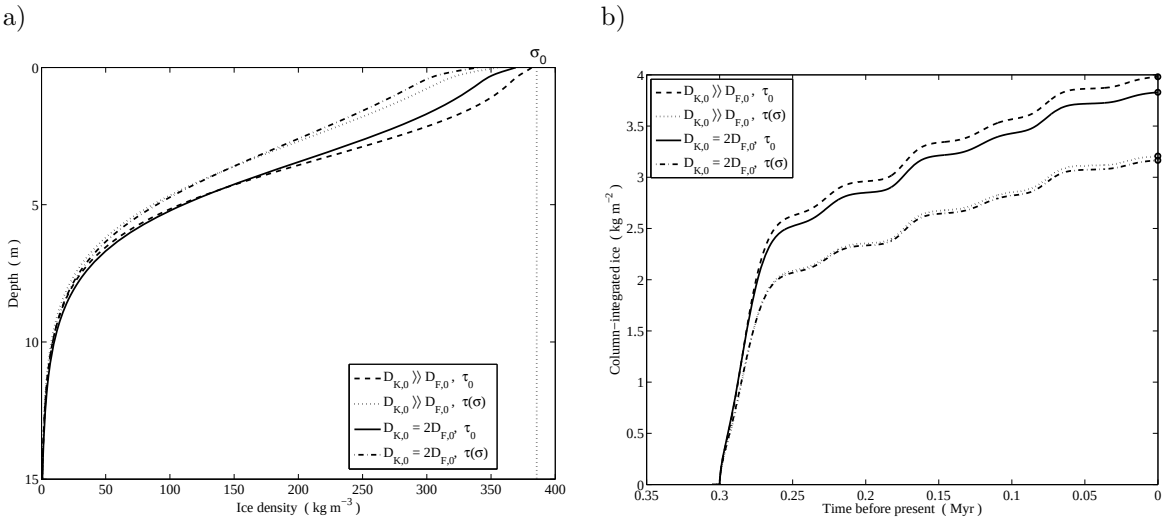

Figure 6.3: These plots compare a) ice content profiles as a function of depth and b) column-integrated ice contents as a function of time for models incorporating various parameterizations of constriction. Plot a) shows the final ice contents following 300,000 years of ice growth. The ice-free diffusion coefficients when $D_{K,0} \gg D_{F,0}$ are (in cm^2 s^{-1}): $D_{F,0} = 4.0$, $D_{K,0} = 1000$; otherwise $D_{F,0} = 6.0$, and $D_{K,0} = 12.0$. A constant tortuosity is indicated by τ_0, while $\tau(\sigma)$ denotes tortuosity varying according to equation (6.5). The weakest (dashed line) and strongest (dash-dotted line) constriction models bracket the others following sufficient profile evolution for differences in constriction to become apparent. The weakest constriction model reaches within 1% of complete filling at the surface in 300 kyr. In b) the total quantity of ice accumulated differs by less than 50% between the strongest and weakest constriction models at 300 kyr, and that most of the difference among models arises from different parameterizations of τ. All models presented here assume ice stability at all depths.

is entirely due to changes in ϕ (as in equation (6.3)). Such a model reaches 99.0% pore filling at the surface in 300,000 years. In contrast, the surface filling fraction for the strongest constriction model, incorporating a variable τ and $D_{K,0} \approx D_{F,0}$, attains only 88.1% in the same interval.

Figure 6.3b compares the column-integrated ice contents for various constriction models as a function of time. The ice content below ∼15 m is approximately zero, so these column-integrated values essentially trace only the evolution in the upper 15 m of the regolith. All exhibit a rapid increase in ice content early in the deposition phase due to high temperatures and the resulting high vapor density gradients at the surface. After approximately 20,000 years, the accumulation rates decrease sharply and the models diverge as the weaker constriction parameterizations permit more ice to deposit. After ice growth has progressed for 300,000 years, the column integrated ice contents differ by at most 50%. Yet most of this difference is due to the choice in τ parameterization. If one particular model for tortuosity is selected, the difference between column ice contents for $D_{K,0} \approx D_{F,0}$ versus $D_{K,0} \gg D_{F,0}$ is less than 5%.

Figure 6.4 contains the same model data as Figure 6.3, but displays the difference in ice content relative to a comparison case for two particular depths. The comparison case is chosen to be the

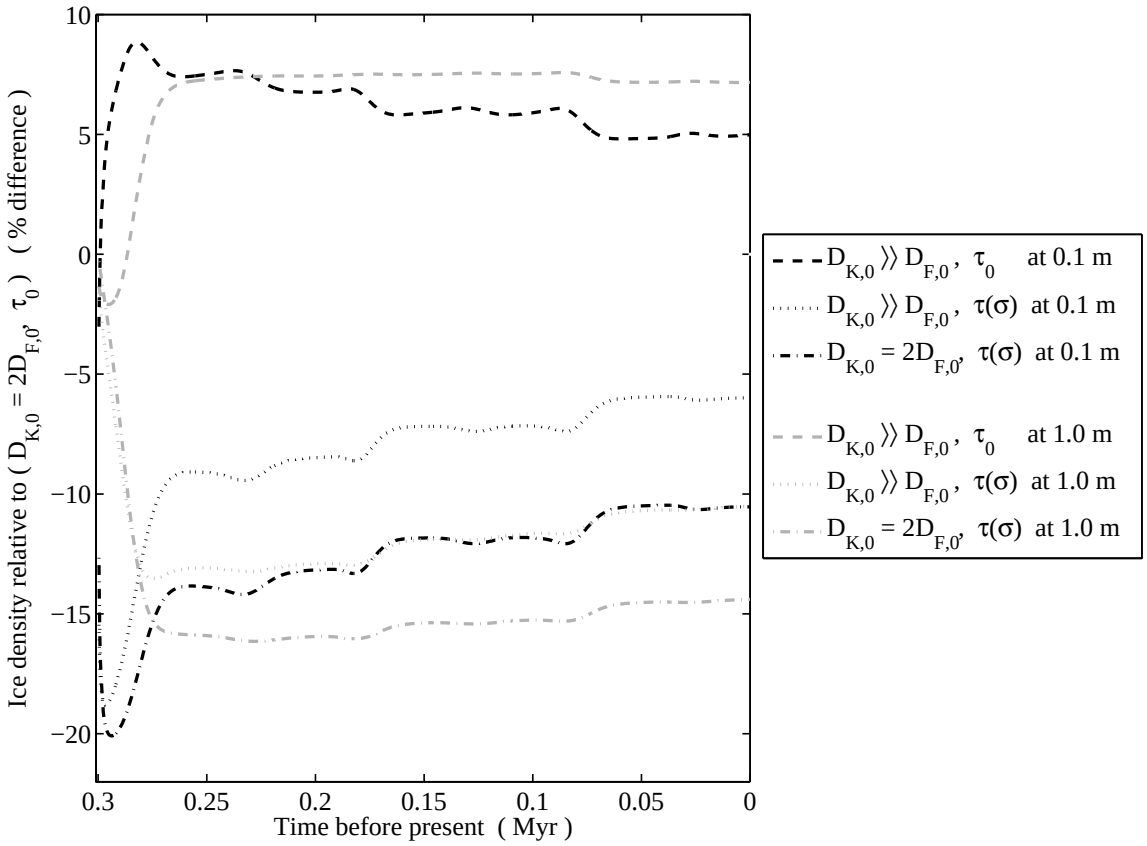

Figure 6.4: This figure plots, as a function of time, the difference in ice content between the constriction model that employs both constant tortuosity and $D_{K,0} = 2D_{F,0}$, and the other three models presented. The black lines represent the difference at 0.1 m depth; the gray lines 1.0 m. The models with constant τ (dashed lines) accumulate more ice than the comparison model at these depths and exhibit between 5–10% more ice for most of the modeled time interval. Variable τ models accumulate less ice than the comparison model, differing by as much as 20%. The maximum differences (at early times) are more exaggerated for shallower depths where accumulation can occur the fastest; for the same reason, these depths also converge toward zero difference faster than deeper levels. The slow approach of all models to the comparison case reflects the long times requried to reach the ultimate end-state of a completely filled regolith.

model incorporating constant tortuosity, $D_{K,0} = 12.0$ cm^2 s^{-1}, and $D_{F,0} = 6.0$ cm^2 s^{-1} (*i.e.,* the solid lines in Figure 6.3). Black lines in Figure 6.4 show relative ice contents at 0.1 m and gray lines show relative contents at 1.0 m. After long times, all regolith depths approach 100% filling and the difference between cases will become zero.

The constriction model that is weaker than the comparison case, *i.e.,* the one which incorporates only changes in ϕ to account for reduced diffusion coefficients, exhibits an overall higher ice content than the comparison model at a given time. The initial divergence at shallow depths is fast, occuring within the first 20,000 years, and is followed by a slow convergence toward the comparison case. Models which incorporate a changing τ are more strongly constricted than the comparison case and exhibit negative relative ice contents. The higher constriction experienced by these models results in

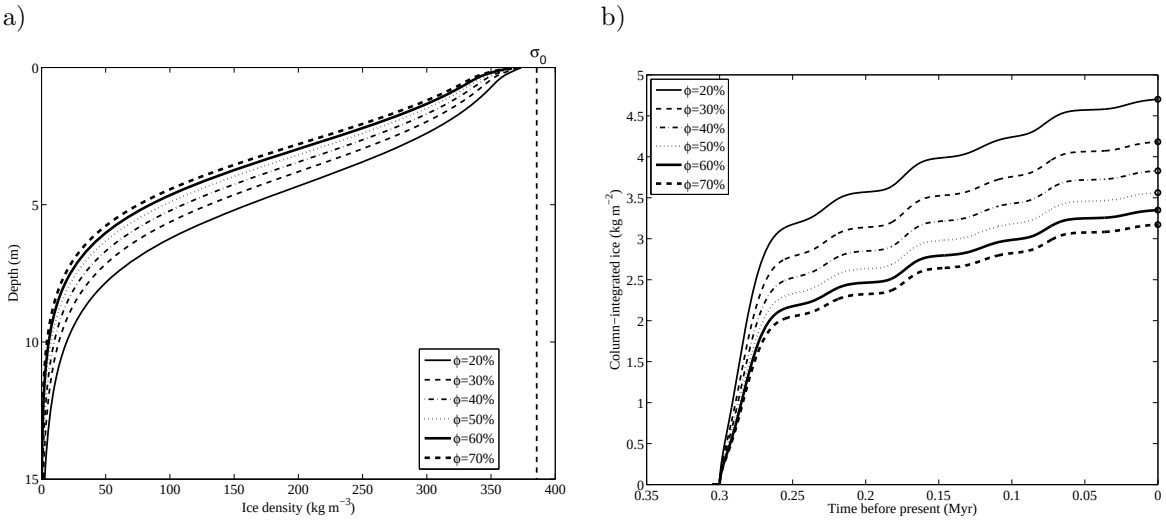

Figure 6.5: Models with identical constriction parameterizations are run with different ice-free porosities assuming ice stability at all depths. The value of τ is constant and $D_{F,0}$ and $D_{K,0}$ are 6.0 and 12.0 cm^2 s^{-1}, respectively. The divergence among these models is of the same order as that arising from different constriction models (compare Figure 6.3). Surface ice contents are only ∼6% different between 20% and 70% porosity cases. The variation in column ice contents seen in b) is less than 40% after 300,000 years of ice accumulation.

their slower convergence back to the comparison case compared to the weaker constriction models. Also, the stronger constriction models diverge more sharply from the comparison case than the weaker model, exhibiting a maximum relative density difference of 20% versus 10%.

High thermal gradients in the shallow subsurface produce the fastest growth rates. This explains the divergence from and re-convergence to the comparison case being most rapid for near-surface soils. The deeper soils generally exhibit a subdued trend compared to shallower soils, lacking the large early divergence peak and experiencing slower convergence to the filled state.

6.4.2 Porosity

Figure 6.5 displays the model outputs using a range of values of ice-free porosity from 20–70%. The constriction parameterization for all these models employs constant τ, $D_{F,0}$ = 6.0 cm^2 s^{-1} and $D_{K,0}$ = 12.0 cm^2 s^{-1}; ice stability is assumed for all depths. The differences among the ice content profiles in Figure 6.5a is smaller in magnitude than that seen among the constriction models in Figure 6.3. The range in ice contents for near-surface layers after 300 kyr are 86–91% of total filling. Comparing column-integrated ice contents among models with different porosities (Figure 6.5b exhibits differences of at most 40% following 300,000 years of ice accumulation. This degree of variation is similar in magnitude to that arising from various constriction models.

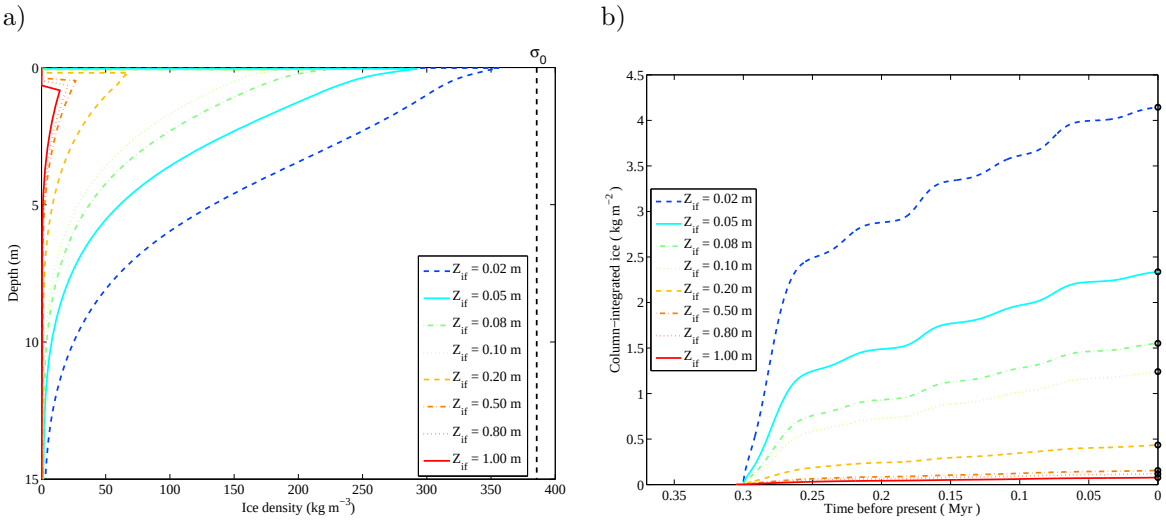

Figure 6.6: These figures show the results of models run with identical constriction parameterizations ($D_{F,0} = 6.0$ cm^2 s^{-1}, $D_{K,0} = 12.0$ cm^2 s^{-1}, constant τ), but different thicknesses of ice-free surface layers ($Z_{\rm if}$). In cases where ice grows near the surface, the high temperature fluctuations give rise to greater quantities of deposited ice. This ice, in turn, conducts surface heat to depth with greater efficiency than dry regolith, resulting in increased gradients at depth and a more ice-rich column than more insulated cases. The depth of the shallowest ice affects the quantity of subsurface ice growth much more strongly than the effect arising from different constriction parameterizations.

6.4.3 Ice-free layer

For this and all subsequent models, unless otherwise indicated, the constriction parameterization used employs $D_{F,0} = 6.0$ cm^2 s^{-1}, $D_{K,0} = 12.0$ cm^2 s^{-1}, and constant $\tau = \tau_0$.

Figure 6.6 displays the ice content profiles and column-integrated ice contents for 9 models run with different thicknesses of perpetually ice-free surface layers. The range of ice-free layer thicknesses, $Z_{\rm if} = 0.01$–1.0 m, reflects the range of ice-table stability depths experienced by mid- to high-latitude regions on Mars under the present climate (*Mellon et al.*, 2004).

Ice accumulation is greatly subdued by small increases in ice-free layer thickness. At a depth of 1 m, the model employing $Z_{\rm if} = 1$ cm accumulates more than 10 times as much ice as the model where $Z_{\rm if} = 1$ m. The difference in column-integrated ice content is even larger, being approximately two orders of magnitude between the cases with 1 cm and 1 m ice tables.

6.4.4 Deep ice

If conditions favorable to precipitation existed prior to ∼5 million years ago, a massive ice sheet may still exist below some depth at high latitudes (*Schorghofer*, 2007). The effect of this ice will be to impose perturbations on the subsurface temperature field and to present a shallow no-flux boundary to diffusive transport. In the model discused here, such a massive ice sheet is represented by pore ice with a 100% filling fraction, the difference in thermal conductivity between pure ice and ice-filled

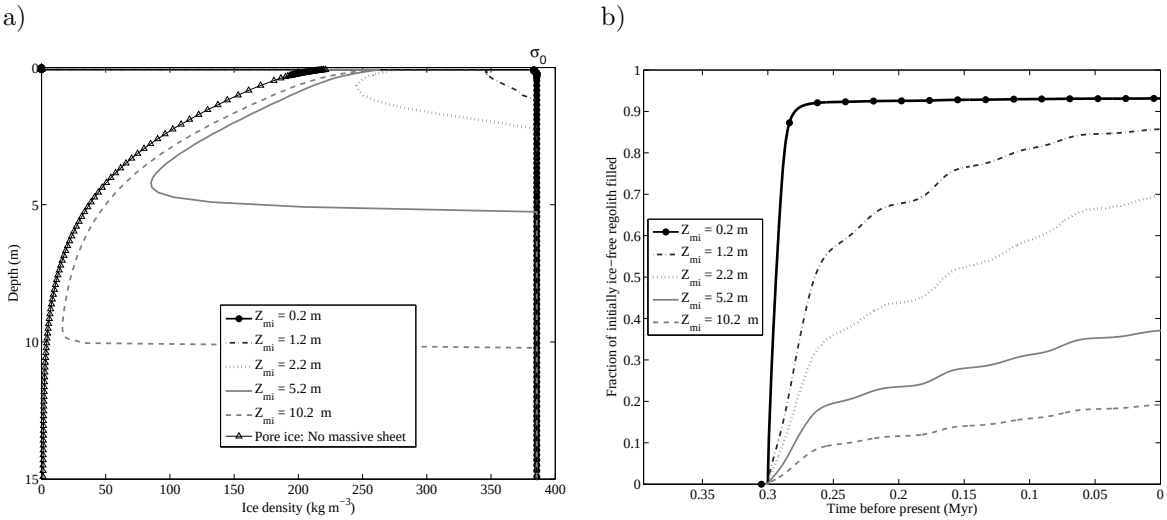

Figure 6.7: Models with identical constriction parameterizations ($D_{F,0}$ = 6.0 cm^2 s^{-1}, $D_{K,0}$ = 12.0 cm^2 s^{-1}, constant τ) are run with initial massive ice sheets extending for various depths ($Z_{\rm mi}$) to the bottom of the model domain. Each model is run with an 8 cm ice free surface layer. Rather than column-integrated ice contents, panel b) plots the fraction of initially available pore space that has filled as a function of time. Shallow regoliths fill more quickly than deeper regoliths, both due to smaller available volumes and higher thermal (and therefore vapor density) gradients.

regolith being only ∼10%.

Figure 6.7 presents plots of the ice contents for a series of models run with pore-filling massive ice sheets extending from some depth ($Z_{\rm mi}$) to the base of the model domain. Each model has an ice-free regolith layer 8 cm thick above the ice-stability depth. Panel a shows the ice content profiles for each model with a deep ice layer. For comparison, a model from Figure 6.3 with the same constriction parameters (solid black line in that figure) and without any initial pore ice is also shown (solid line with triangular gridpoints).

In Figure 6.7b, rather than column-integrated ice contents which would be skewed by the presence of the initial pore-filling ice, the curves represent the fraction of initially available regolith pore space which has become filled as a function of time. The model designated $Z_{\rm mi}$ = 0.2 m, has a massive ice sheet extending from 0.2–500 m, and an ice-free layer between the surface and 8 cm. This small initially ice-free volume fills rapidly, approaching within 1% of total filling by 60,000 years. Constriction is strong when ice contents are so high, and even though this model does not incorporate a changing tortuosity, the effects of porosity reduction and increased Knudsen diffusion reduce the ice accumulation rate to almost zero.

To explicitly examine the variation in ice content at particular depths as a function of $Z_{\rm mi}$, Figure 6.8 plots the difference in ice content ($\delta\sigma$), relative to a model with no massive ice sheet (the solid black curve in Figure 6.3 a), for depths of 0.1 and 1.0 m. The gray lines, which plot variation at 1.0 m depth, are not plotted for $Z_{\rm mi}$ = 0.2 and 0.8 meters. At all times and depths, the models

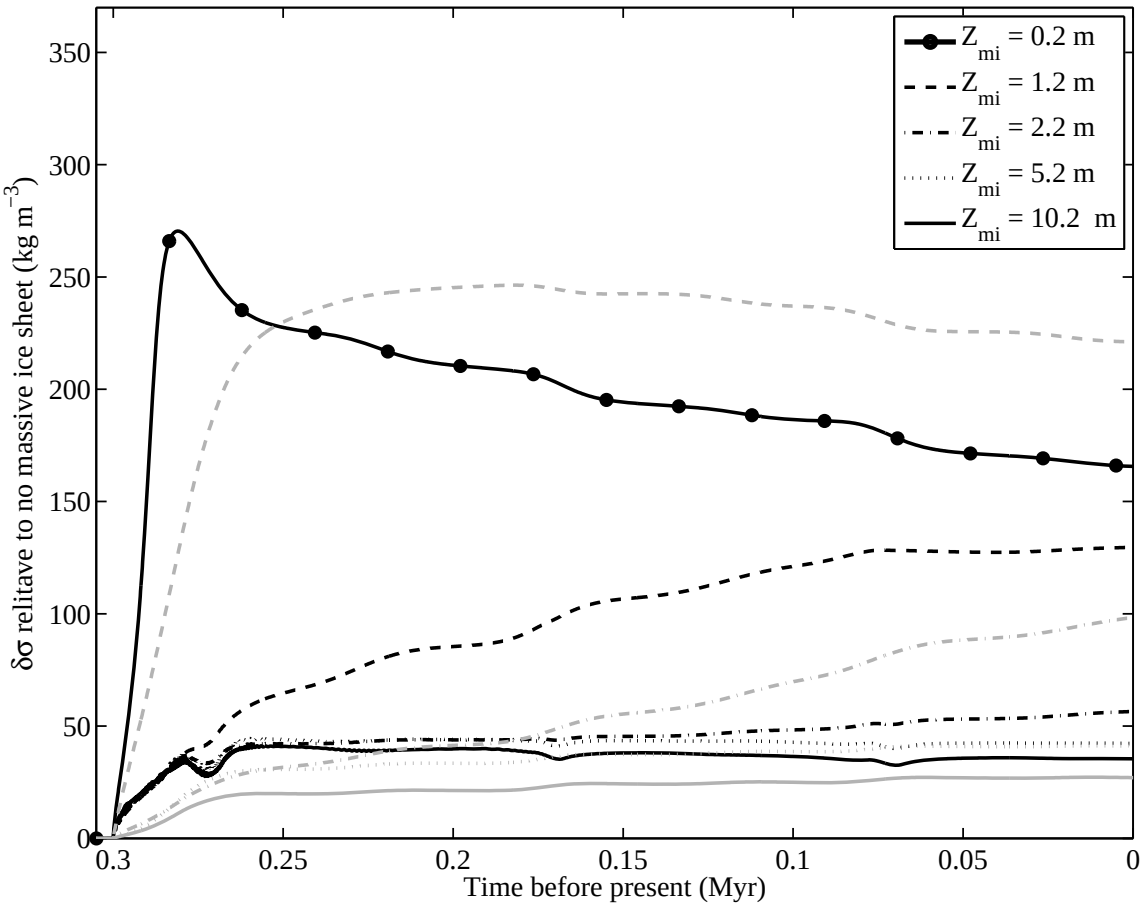

Figure 6.8: The same data as in Figure 6.7, plotted as the quantity of ice accumulated at various depths (black for 0.1 m, gray for 1.0 m) relative to a model with no massive ice sheet (*i.e.,* the solid black line in Figures 6.3 a) and 6.7 a). The cases where $Z_{\mathrm{mi}} = 0.2$ and 0.8 m are not plotted for 1.0 m depth (gray).

exhibit an increased ice content relative to a model with no ice sheet. The ice sheet significantly increases the heat capacity of the regolith and so reduces the temperature fluctuations at the base of the ice accumulation region. This compresses the thermal gradients in this region, resulting in higher driving forces for ice accumulation at all depths.

The deviation is minor for depths which are both far from the ice table and the massive ice sheet. An interesting effect is the enhanced deposition at the base of the accumulation region close to the massive ice sheet. This effect is seen as the change in direction of ice content profiles in Figure 6.7a, where they smoothly approach 100% filling near their respective massive ice sheets. For example, the grey dash-dotted line represents accumulation at 1.0 m depth for a case where a massive ice sheet exists below 1.2 m. At such proximity to the ice table, significantly more ice accumulates relative to the case without a massive ice sheet. This is despite the initial profiles having a sharp jump from ice-free to ice-full at these depths.

The two effects of altered temperature profiles and no-flux boundaries result in an enhanced deposition of ice at all depths when a massive ice sheet is present, compared to porous soil exhibiting no such massive ice. Presumably, the same effect would occur if the massive sheet were replaced by solid rock, since the rock would also exhibit higher thermal conductivity and prevent the flux of vapor. The magnitude of the effect, however, may be different due to the difference in heat capacity of rock versus ice.

6.5 Discussion

The model code in Chapter 5 explicitly solves the complete diffusion equation and requires several days of computer time to simulate ice deposition over a one-week interval. The innovative technique used in this chapter requires that gradients in vapor density arising from temperature variations propagate fast enough relative to the model timestep that pore-gas saturation is maintained. This requires that the model examine only regions where ice is present; it therefore does not include the ice table and does not compute equilibrium ice table depths. This modeling scheme is more than seven orders of magnitude faster than that employing equation (5.7), permitting the accumulation of subsurface ice to be tracked for many obliquity cycles with similar computational expense to the models of Chapter 5.

In the foregoing model results, the effect of a number of parameters on subsurface ice content were examined. By far the most influential of these, both with respect to the quantity of near-surface ice and to the total amount of ice accumulated in the regolith column, is the thickness of the ice-free layer at the surface. The low thermal inertia of the dry regolith layers rapidly attenuates the extreme diurnal temperature fluctuations, thus the maximum temperatures and temperature gradients experienced by deeper ice tables are significantly reduced relative to shallower ice. The vapor density gradients driving ice deposition are likewise lower.

For the Phoenix landing site, where the ice table is predicted to be within 2–6 cm of the surface, models here indicate that 300 kyr would allow between 70% (for $Z_{\mathrm{if}} = 6$ cm) and 92% (for $Z_{\mathrm{if}} = 2$ cm) of the pore spaces at the top of the ice table to become filled. Figure 6.9 shows these ice contents in the upper 0.5 m of the regolith as predicted by the model for values of Z_{if} between 2 and 10 cm. If the depth to ice stability is more than $\sim$2 cm, conditions at the Phonenix landing site will not have produced a completely ice-filled regolith since a major ice-loss event 300 kya. As the depth to the ice table increases, the total quantity of ice deposited in a given time interval is reduced.

The ice-free layer thicknesses assigned in the models do not change over the 300 kyr interval considered. However, Mars' climate during this time, though perhaps more stable than in periods with higher amplitude obliquity oscillations, has doubtless experienced some fluctuation in mean annual atmospheric water content, shifting the equilibrium ice table position. Ice loss events which

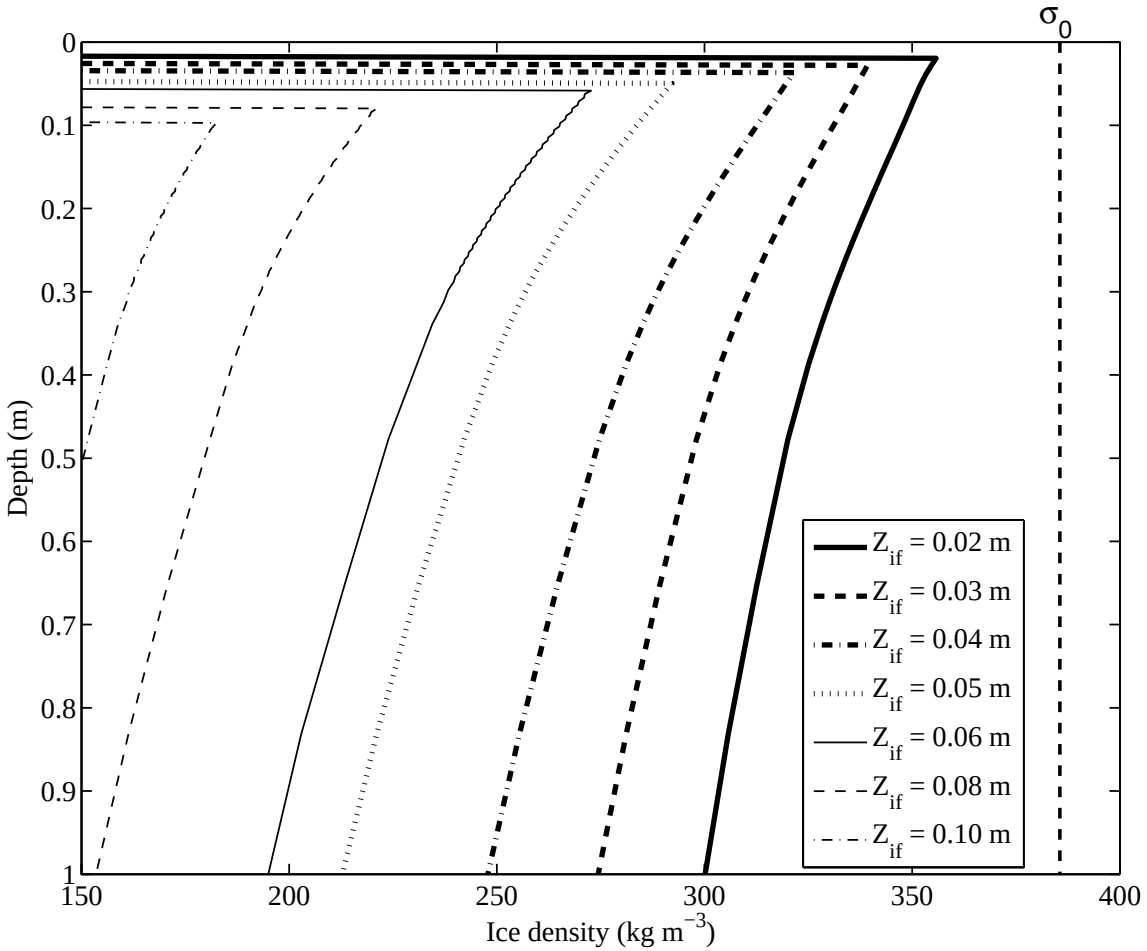

Figure 6.9: This figure presents ice content profiles of near-surface layers as in Figure 6.6 a), with additional values of $Z_{\rm if}$ shown. In cases where ice grows near the surface, the high temperature fluctuations give rise to greater quantities of deposited ice. This ice, in turn, conducts heat to depth with greater efficiency than dry regolith, resulting in a more ice-rich column than in cases where ice deposits only at deeper levels. A change of $Z_{\rm if}$ from 2.0 to 6.0 cm results in a decrease in filling fraction at the ice table from 92% to 70%. The depth of the shallowest ice affects the quantity of subsurface ice growth much more strongly than the effect arising from different constriction parameterizations.

have desiccated the porous regolith down to some depth will partially reset the ice accumulation in shallow layers. Ice which remains below the lowest depth of penetration of the ice table will affect subsequent accumulation through both its effect on the thermal structure of the regolith and the lower diffusion coefficient in the ice-bearing region.

As revealed in Figure 6.7a, and in Figure 6.8, the presence of a massive ice sheet results, for all depths and time intervals, in ice contents being greater than those accumulated when no ice sheet is present. When an ice-saturated sheet exists, the ice content at a depths near the sheet are significantly enhanced over the initially ice-free regolith. This effect arises from the no-flux condition

imposed by the massive ice sheet. Vapor is unable to move through the ice sheet and cannot move against the mean annual vapor density gradient. The local vapor density is thus increased above the saturation point and ice deposits against the ice sheet. Ice profiles developed in initially ice-free pore spaces in the presence of a massive ice sheet therefore exhibit a local minimum in ice content at some depth, rather than a monotonic decrease to the ice sheet boundary. Such inflections may be observable in high-resolution subsurface ice measurement techniques such as coring.

The ice-age dynamics model of *Schorghofer* (2007) predicts that a massive ice sheet which initially extended to the surface 5 million years ago would have been forced to retreat by periods of climate conducive to ice loss. The amount by which the ice sheet is predicted to have retreated would give rise to an approximately 40-cm-thick porous lag if the initial ice sheet contained ∼15% regolith material. If the depth to the present-day massive ice sheet were close to this value, and conditions had been favorible to subsurface ice growth beneath 8 cm for the last 300 kyr, then the regolith would be almost completely ice-filled and the current ice profile would fall between the dash-dotted line of Figure 6.7a and a condition of nearly complete filling at all depths.

Besides massive ice sheet depth and ice-free surface layer thickness, the other effects considered were seen to have minor effects on the ice content profiles. If the pore geometry were changed in such a way as to retain the ice-free diffusion coefficient at 4.0 cm^2 s^{-1}, but ice free porosity were varied between 20 and 70%, at most a 40% change in column-integrated ice content would result. A real material, however, would exhibit simultaneous changes in ϕ, $D_{F,0}$, and $D_{K,0}$. Such combined effects are not explored here.

Constriction was also observed to have a comparatively minor effect on ice content profiles. The various models employed result in an approximately 50% difference in total accumulated ice content in 300 kyr, but only a 10% difference in pore filling at the surface. This is a small variation compared to changing the ice-free layer thickness by ∼1 m, which results in two orders of magnitude difference in column integrated ice. The small differences in surface ice content among various constriction models, though easily measurable in a laboratory, may be difficult to detect *in situ*. Between the models with the strongest and the weakest constriction parameterizations, there is no more than a ∼20% difference in ice content which could be observed. It is therefore unlikely that investigations by the Phoenix lander will discriminate among the constriction models presented here; further theoretical and laboratory investigations will be necessary to make an informed choice of constriction model.

At any given site of ice accumulation and long-term stability, both the models included here and those of previous investigations (*Mellon and Jakosky*, 1995; *Schorghofer and Aharonson*, 2005) indicate that the site of greatest ice accumulation will be the local equilibrium depth. Future investigations which probe subsurface ice contents, either via indirect sensing techniques such as ground-penetrating radar or directly through drilling and coring activities, will likely encounter the

highest water contents at the ice table. The pore ice concentration will be reduced with increasing depth, though the change may be only 10–15% over distances on the order of 0.5 m (see Figure 6.9). A smaller degree of reduction in ice content with depth would be expected if the ice had been accumulating for longer than 300 kyr and thus had been able to approach total filling over a significant depth range. Such a distribution would indicate that climate changes inducing ice loss have not been of sufficient magnitude or duration to penetrate and reset the ice contents over these depths.

Figure 6.10 shows the difference in mean annual surface temperatures resulting for various distributions of subsurface ice. An ice-filled regolith (excepting an 8 cm ice-free surface layer) exhibits a 10 K temperature difference relative to a completely ice-free soil. Intermediate distributions of subsurface ice will modulate the mean annual surface temperatures between these extremes. If ice exists only deep within the regolith (*i.e.,* below several annual skin depths), its effect on the surface temperature will be small, as exhibited by the closeness ($\sim$1 K difference) of the pore-ice-free case (light solid black line) and the case with no accumulated pore ice, but $Z_{\rm mi} = 10$ m (heavy grey dashed line). Shallow pore ice more effectively changes the mean temperatures experienced at the surface. If $Z_{\rm mi} = 10$ m but pore ice deposits in the shallow depths below 8 cm, the mean annual surface temperature is $\sim$6 K higher than the case with no pore ice.

The Phoenix lander is incapable of excavating more than approximately 0.5 m into the regolith, and may be limited to even shallower depths if the ice table is shallow and has a high cohesive strength. Ground-penetrating radars on orbiting spacecraft do not currently have the resolution to discern ice distributions within the upper 10-15 m of the surface. Observations of mean annual temperatures and comparisons between these observations and models are the only presently available means to determine at what depth a shallow massive ice sheet may exist at high latitudes. The accuracy of subsurface and surface temperature models will be improved by Phoenix's measurements of regolith thermal properties with the Thermal and Electrical Conductivity Probe (TECP). Combined with Phoenix's measurements of ice table depth and (possibly) ice content in the shallow ice-bearing layers, mean annual surface temperature observations will constrain the depth range of a massive or pore-filling subsurface ice sheet. If ground-truth thermal properties from the Phoenix site are adjusted for locale-specific thermal inertias and albedos, then limits on massive ice sheet depths in other high-latitude regions may be assessed.

The Phoenix lander's robot arm will excavate into the surface regolith and deliver samples to the spacecraft deck for analysis. The stereoscopic imager, robotic arm camera, and the microscopy suite on MECA (Microscopy, Electrochemistry, and Conductivity Analyzer) cover a resolution range extending below 1 micron. Measurements of regolith particle sizes and shapes will help constrain the expected diffusion coefficient of the surface regolith. The cohesive strength of the regolith will also reveal, via observations of required digging power and the appearance of any coherent surface crusts, whether the effects of cementing agents such as salts may have acted to reduce the diffusivity,

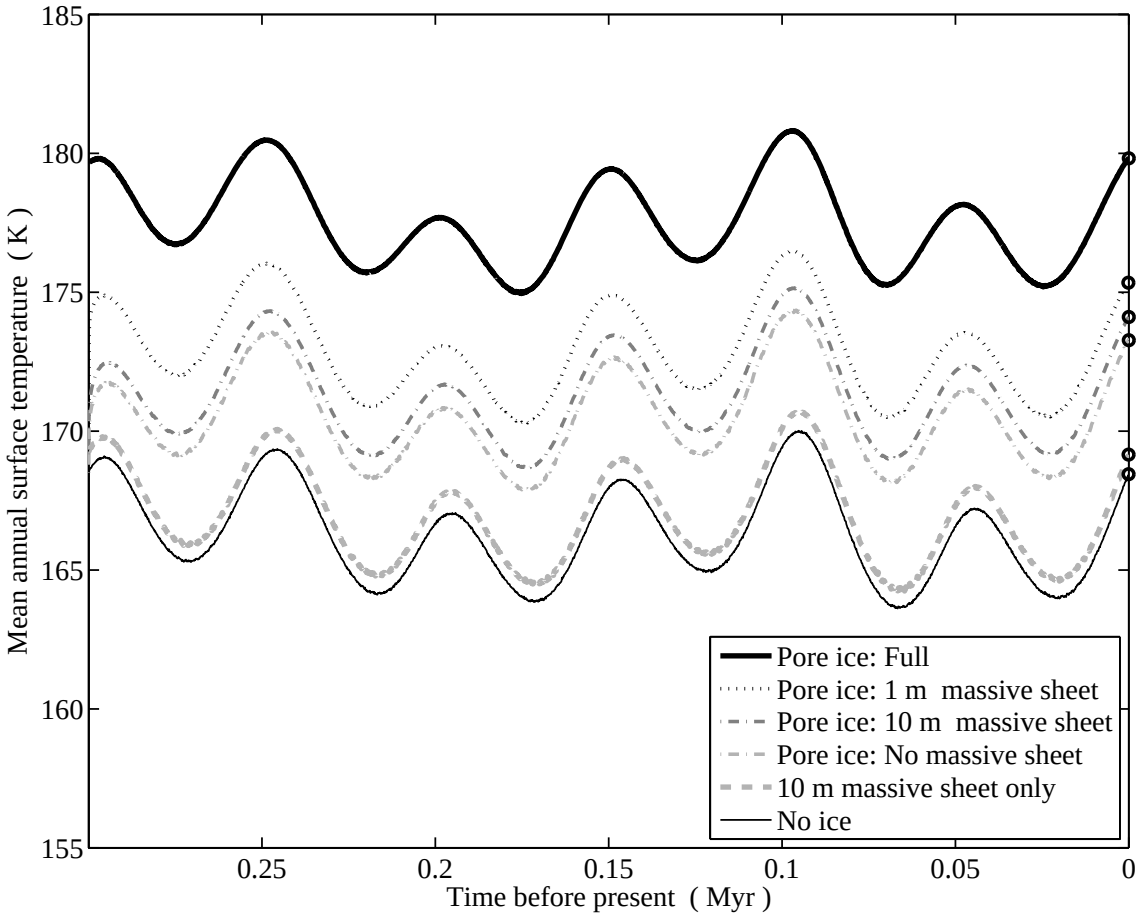

Figure 6.10: Mean annual surface temperatures differ depending on the subsurface ice content. The possible range is bracketed by an ice-free and ice-filled (excepting an 8-cm-thick ice-free surface layer) regolith. The difference between these extremes is 10 K, representing the range within which annual surface temperature deviations may fall. Also shown between these extremes are: two cases wherein pore ice deposits beneath a dry layer of 8 cm thickness (dash-dotted lines), one of which contains a massive sheet of pore-filling ice below 10 m (darker gray); and a third intermediate case with a massive ice sheet below 10 m, but no shallow pore ice (gray dashed line). The two cases which deposit pore ice exhibit an approximately 1 K difference in mean annual temperature. The case with a deep massive ice sheet but no pore ice is also about 1 K warmer than the case with no pore ice at all. These differences may permit the presence and depth of a massive ice sheet to be determined from seasonal temperature observations obtained from orbiting instruments.

as seen in Chapeter 4. At some shallow depth, Phoenix is expected to encounter ice-cemented soil. The depth of this ice table will represent ground-truth, to be compared to the various observations and models used to predict ice table depth. These measurements will be combined with estimates of the regolith diffusion coefficient to evaluate the proximity of the ice table to its equilibrium depth and the resulting implications for climate at the Phoenix site and throughout Mars' north polar region.

It is not known if the robot arm on Phoenix will be able to penetrate an ice-cemented soil, even

if the filling fraction is significantly less than 100%. The predictions of these and other models (*Schorghofer*, 2007; *Mellon et al.*, 2008) are that the region of the subsurface accessible to Phoenix will exhibit pore-filling, rather than pure ice. Given the instruments available, precise determinations of the filling fraction of these soils will be difficult. Raspings from the surface of the ice table, observed either through microscopy or a sublimating tailings pile, may constrain the relative fractions of ice and soil in the near-surface cryosphere. These model investigations suggest that at the depth of the ice table, the filling fraction will be between ∼70–90%. If a smaller filling fraction is observed, this would indicate an ice loss event more recent than 300 kya. The timing of such an event may be constrained by the observed ice contents and present ice table depth. Conversely, ice contents observed to be greater than ∼70–90% would be a strong indicator of a massive ice sheet within 0.5 m of the surface.

High latitude regions exhibit some shallow equilibrium ice table depth at all obliquities between 15 and 45 degrees (*Mellon and Jakosky*, 1993; *Feldman et al.*, 2005). Ice in these regions below a certain depth may survive periodic ice loss events. When the climate switches from a state that favors accumulation to one that favors loss, the ice table will retreat. Though ice at all depths may be unstable with respect to the atmosphere, its vapor pressure will still be set by the local temperature. If the assumption of saturated pore gas remains valid, ice beneath the ice table will continue to migrate downward even as the ice table descends. Low diffusivity of the overlying regolith, low subsurface temperatures in high-latitude regions, or high atmospheric vapor content may induce a relatively low rate of ice loss from the ice table. If the rate of ice table retreat is not sufficient to remove all subsurface ice by the time the climate again becomes favorable to ice preservation or growth, then deep subsurface ice may survive many cycles of climate change.

The deep ice carries information about past climate conditions through its abundance and depth distribution. The maximum depth of loss from a particular event may be recorded as an abrupt jump in the subsurface ice content, since the ice table interface will remain sharp as it retreats during a loss event. When accumulation is again favored, ice will grow throughout the region below the new equilibrium depth. Though the saturated vapor density of the pore space is independent of the filling fraction, the ice accumulation rate is modulated by the gradient in the diffusion coefficient, which will be steep across such an interface. Over time, the formerly sharp interface at the previous ice table depth will be softened as the relatively ice-poor regolith accumulates ice faster than the ice-rich region that has a more constricted diffusivity. Such local maxima in ice content profiles encode the history of local temperature and humidity environments and may be interpretable with models incorporating ice-loss events.

At depths between 10–15 m, the model indicates only minor accumulation of ice in 300 kyr if the initial state is ice-free. If protected from removal events by the overlying ice-rich pore spaces, the accumulation will continue unperturbed at these depths. Such deep ice may grow to fill a

substantial fraction of the pore space over long times. If these depths remain in diffusive contact with the atmosphere, isotopic climate tracers from epochs many obliquity cycles before the present may become trapped as the growing ice isolates pore spaces and produces bubbles.

The last decade has seen the theoretical and numerical prediction of ground ice on Mars, its detection from orbit, and immiment sampling expected from the Phoenix Lander. Equilibrium models have progressed dramatically; understanding the dynamics of subsurface ice position, loss, and exchange is ongoing. Experimental investigations and *in situ*observations continue to expand and enhance the understanding of these important processes in the Mars water cycle.

Notation

a_w	water activity
c	mass concentration of water vapor = ρ_1/ρ_0
$\bar{c}$	average c across sample
D	concentration diffusion coefficient for porous medium
D	concentration diffusion coefficient for ice-free porous medium
D_F	Fickian diffusion coefficient
$D_{F,0}$	Fickian diffusion coefficient in ice-free medium
D_K	Knudsen diffusion coefficient
$D_{K,0}$	Knudsen diffusion coefficient in ice-free medium
D'	uncorrected ("raw") diffusion coefficient
$\mathcal{D}_{11}$	coefficient of self-diffusion in free-gas
$\mathcal{D}_{12}$	concentration diffusion coefficient in free-gas
$\mathcal{D}_T$	thermodiffusion coefficient in free-gas
$\mathcal{D}_p$	barodiffusion coefficient in free-gas
d	particle diameter
$\bar{d}$	mean particle diameter
dT_{ice}	error in measured ice temperature
f_c	square root of filling fraction: $\sqrt{\sigma/\sigma_0}$
J_1	mass flux of water vapor
J_2	mass flux of carrier gas
J_{Adv}	advective component of J_1
J_{Diff}	diffusive component of J_1
K_0	Knudsen regime structural parameter
k_B	Boltzmann constant
k	Bulk thermal conductivity
k_i	Interstitial thermal conductivity
k_{i0}	Thermal conductivity of ice-free interstice
k_{ice}	Thermal conductivity of ice
k_0	Ice-free bulk thermal conductivity
k_w	Regolith grain thermal conductivity
k	Boltzmann constant
k_p	barodiffusion ratio
k_T	thermodiffusion ratio

l	molecular hop length
$\langle l_p \rangle$	first moment of pore size distribution
$\langle l_p^2 \rangle$	second moment of pore size distribution
L	dry regolith lag thickness or porous medium length
L_e	pore path length
M_1	molar weight of water
M_2	molar weight of carrier gas
M_c	mass of coarse component in mixture
M_f	mass of fine component in mixture
M_T	total mass of mixture
m_1	molecular mass of water
m_2	molecular mass of carrier gas
n	constriction exponent
n_0	total number density in gas phase, $n_0 = n_1 + n_2$
n_1	number density of water vapor
n_2	number density of carrier gas
n_d	number density of particles in dusty gas model
$p(l)$	pore size distribution
p_0	total pressure, $p_0 = p_1 + p_2$
p_1	partial pressure of water
p_2	partial pressure of carrier gas
p_{ref}	reference pressure
$p_{\mathrm{sv}}^{\mathrm{liq}}$	saturation vapor pressure over liquid water
$p_{\mathrm{sv}}^{\mathrm{ice}}$	saturation vapor pressure over ice
R	universal gas constant or correlation coefficient
RH	relative humidity
r	pore or particle radius
$\bar{r}$	average radius
T	temperature
T_{ice}	temperature of ice surface
T_{air}	temperature of chamber air measured at hygrometer
t	time
V_1	molecular volume of water
V_2	molecular volume of carrier gas
v	void fraction: 1-σ/σ_0
w	vertical velocity of gas
X_f	mass fraction of dust
Z	thickness of ice added or removed
Z_0	initial ice table depth
z	depth
z_{corr}	correction term

α	density of adsorbed phase
$\Delta\rho_1$	water vapor density difference
Δz	sample thickness
κ	intrinsic permeability of a porous medium
λ_1	mean free path of water vapor
μ	dynamic viscosity
$\bar{\nu}_1$	mean velocity of water vapor
$\pi\sigma_{12}^2$	scattering cross section
ρ_0	total mass density, $\rho_0 = \rho_1 + \rho_2$
ρ_1	density of water vapor
$\rho_{1\mathrm{A}}$	density of water vapor at ice surface
$\rho_{1\mathrm{B}}$	density of water vapor at lower sample surface
$\rho_{1\mathrm{C}}$	density of water vapor at upper sample surface
$\rho_{1\mathrm{D}}$	density of water vapor at hygrometer
ρ_2	density of carrier gas
ρ_{ice}	density of ice
$\rho_{c,\mathrm{bulk}}$	density of bulk coarse particles
$\rho_{c,\mathrm{true}}$	density of individual coarse particles
$\rho_{f,\mathrm{bulk}}$	density of bulk fines
$\rho_{f,\mathrm{true}}$	density of individual fines particles
σ	ice density relative to free space
σ_1	molecular radius of water
σ_2	molecular radius of carrier gas
τ	tortuosity factor
ϕ	porosity
ϕ_{mix}	porosity of mixture
Ω_{12}	collision integral

Appendix A

Diffusion Experiment Data

This appendix contains experimental conditions, sample types, measured data, and calculated quantities for the diffusive ice-loss experiments presented in Chapeters 3 and 4.

The quantities tabulated are:

Date	month/day, date of experiment
Δ_z	cm, thickness of sample
p_0	pascal, total pressure of experimental chamber
T_{ice}	K, temperature of ice surface
T_{air}	K, temperature of air at relative humidity sensor
RH	percent, relative humidity measured above sample
J_1	mg m^{-2} s^{-1}, flux of water vapor
$\bar{c}$	unitless, vapor density ratio ρ_1/ρ_0
$\Delta\rho_1$	g m^{-3}, vapor density difference across sample
D	cm^2 s^{-1}, corrected diffusion coefficient
$D/\mathcal{D}_{12}$	unitless, obstruction factor
ϕ	percent, calculated porosity of sample
τ	unitless, calculated tortuosity of sample
X_f	percent, mass fraction of fine materials relative to total mass
Salt Content	percent, weight percent of epsomite in salt crust

50–80 μm Glass Beads @ 260 K

Conditions	Date	Δz cm	p_0 Pa	T_{ice} K	T_{air} K	RH %	J_1 mg m^{-2}s^{-1}	$\bar{c}$	$\Delta\rho_1$ g m^{-3}	D cm^{2}s^{-1}	$D/\mathcal{D}_{12}$
	Nov 28	1.03	612	256.9	260.8	20.56	27.25	0.072	0.88	5.02±0.66	0.20±0.03
	Dec 05	1.05	611	256.7	261.2	11.13	20.44	0.065	1.02	3.27±0.41	0.13±0.02
	Dec 08	0.99	634	256.6	260.8	15.57	19.71	0.064	0.94	3.31±0.41	0.13±0.02
	Dec 15	1.06	584	256.3	260.2	13.06	26.00	0.066	0.96	4.47±0.53	0.17±0.03
	Dec 15	0.93	584	256.7	260.3	12.35	29.83	0.068	1.01	4.47±0.54	0.17±0.03
	Feb 06	1.02	630	254.5	260.1	19.65	22.51	0.056	0.68	5.31±0.73	0.22±0.03
	Dec 16	2.10	596	257.4	260.8	12.92	20.60	0.072	1.07	5.15±0.52	0.20±0.02
	Dec 16	1.92	596	256.7	260.8	7.38	22.63	0.063	1.09	5.21±0.51	0.20±0.02
	Dec 17	2.10	598	257.5	260.9	7.93	19.19	0.069	1.17	4.41±0.42	0.17±0.02
	Dec 17	1.92	598	257.1	260.9	13.35	22.12	0.070	1.02	5.41±0.56	0.21±0.03
	Feb 07	1.87	598	256.5	260.7	15.29	17.77	0.068	0.94	4.64±0.50	0.18±0.02
	Feb 07	1.85	598	256.2	260.5	16.57	20.05	0.067	0.88	5.54±0.62	0.21±0.03
	Feb 14	2.08	594	257.1	261.1	14.98	17.46	0.072	0.99	4.69±0.50	0.18±0.02
	Feb 14	2.15	594	256.7	261.0	17.74	19.62	0.072	0.90	5.95±0.66	0.23±0.03
	Feb 17	1.74	592	256.6	260.5	18.05	20.14	0.071	0.90	5.17±0.59	0.20±0.03
263 K	Feb 17	1.71	592	256.1	260.3	19.48	20.86	0.069	0.83	5.75±0.68	0.22±0.03
CO_2	Sep 16	4.76	571	259.1	262.0	10.63	12.71	0.088	1.30	5.24±0.46[a]	0.19±0.04
	Sep 22	4.95	586	259.2	262.1	13.83	11.11	0.090	1.25	4.93±0.45[a]	0.18±0.03
	Dec 18	4.94	595	259.3	261.5	5.18	12.71	0.082	1.44	4.87±0.40	0.18±0.02
	Dec 18	4.97	595	259.5	261.5	4.55	9.57	0.082	1.47	3.61±0.29	0.14±0.02
	Jan 09	5.04	603	259.6	261.5	4.72	9.75	0.082	1.49	3.68±0.30	0.14±0.02
	Jan 09	5.14	603	259.8	261.4	5.52	10.21	0.084	1.50	3.90±0.32	0.15±0.02
	Feb 08	4.95	594	259.0	261.4	7.34	12.30	0.081	1.36	5.01±0.42	0.19±0.02
	Feb 08	4.91	594	258.9	261.2	5.48	10.36	0.078	1.38	4.13±0.34	0.16±0.02
	Dec 09	10.13	616	260.5	261.6	6.07	7.37	0.089	1.58	4.98±0.39	0.20±0.03
	Dec 09	10.11	616	260.3	262.7	3.84	6.09	0.086	1.59	4.10±0.32	0.16±0.02
	Dec 20	9.98	575	260.3	261.6	3.17	7.10	0.093	1.62	4.64±0.35	0.17±0.02
	Dec 20	9.97	575	260.3	261.5	3.51	6.38	0.094	1.61	4.17±0.32	0.15±0.02
	Feb 10	9.90	580	260.0	261.6	6.67	5.98	0.092	1.50	4.17±0.33	0.15±0.02
	Feb 10	9.69	580	259.9	261.5	7.87	8.95	0.092	1.48	6.22±0.50	0.23±0.03
	Feb 18	9.84	583	260.0	261.5	8.20	7.07	0.092	1.48	4.99±0.41	0.19±0.02
	Apr 13	9.87	589	259.8	261.5	8.43	6.03	0.089	1.44	4.37±0.36	0.16±0.02
	Apr 13	9.79	588	259.8	261.3	7.95	7.74	0.087	1.45	5.54±0.45	0.21±0.02
	Apr 03	2.08	592	248.4	248.4	22.40	8.19	0.029	0.44	3.87±0.59	0.21±0.03
253 K[b]	Mar 22	5.02	572	249.5	251.1	10.45	3.83	0.031	0.55	3.49±0.16	0.15±0.02
CO_2	Mar 27	4.96	585	249.7	251.3	11.10	5.69	0.031	0.56	5.04±0.30	0.23±0.02
	Mar 29	4.96	602	249.5	251.2	13.87	5.03	0.031	0.53	5.73±0.31	0.22±0.02
	Mar 31	4.96	610	249.8	251.3	14.75	5.11	0.031	0.53	4.75±0.27	0.22±0.02
	Jan 04	0.94	625	256.1	259.8	14.57	31.55	0.061	0.92	5.57±0.88	0.22±0.03
263 K	Jan 04	0.92	625	256.6	259.9	11.21	33.33	0.062	1.02	5.24±0.76	0.21±0.03
N_2	Jan 06	10.01	637	260.1	261.5	3.73	8.59	0.082	1.57	5.84±0.18	0.23±0.02
	Jan 06	9.85	637	260.0	261.5	5.38	7.13	0.083	1.54	4.89±0.14	0.19±0.02

Table A.1: Experimental conditions, data, and corrected diffusion coefficients for 50–80 μm glass beads at ∼600 Pa. Data taken in 2005–2006

[a] Experiments on Sep 16 and 22 carried out in a plastic vacuum chamber built in-house.
[b] z_{corr} not calculated for 253 K experiments; uncorrected diffusion coefficients, D', reported.

Glass Beads at Variable Pressures @ 260 K

Date	Δz cm	p_0 Pa	T_{ice} K	T_{air} K	RH %	J_1 mg m^{-2}s^{-1}	$\bar{c}$	$\Delta\rho_1$ g m^{-3}	D' cm^{2}s^{-1}	$D'/\mathcal{D}_{12}$
Mar 31	4.79	294	257.6	260.8	11.64	13.14	0.178	1.22	5.61±0.50	0.11±0.01
600 Pa data are reported in the table on page 157										
Feb 21	4.95	1173	260.2	261.8	7.41	7.24	0.041	1.52	2.37±0.19	0.18±0.02
Feb 21	4.92	1173	260.1	261.7	7.44	7.88	0.041	1.51	2.58±0.21	0.19±0.02
Mar 29	4.86	2917	260.8	261.5	13.58	3.46	0.018	1.49	1.13±0.10	0.21±0.02
Mar 14	4.98	5875	261.3	261.6	5.99	1.25	0.008	1.71	0.37±0.03	0.14±0.01
Mar 14	4.94	5875	261.2	261.4	4.87	3.88	0.008	1.73	1.11±0.09	0.42±0.04
Mar 16	4.98	5880	261.0	261.5	5.05	1.41	0.008	1.68	0.42±0.03	0.16±0.02
Mar 16	4.94	5880	261.1	261.4	6.71	2.89	0.008	1.68	0.85±0.07	0.33±0.03
Mar 27	4.96	5899	261.3	261.7	12.50	1.80	0.009	1.59	0.56±0.05	0.21±0.02
Mar 27	4.82	5899	261.3	261.6	13.08	1.78	0.009	1.58	0.54±0.05	0.20±0.02

Table A.2: Experimental conditions and diffusion coefficients for 5 cm samples of 50–80 μm beads at 263 K and various pressures. A correction term was not determined for pressures other than 600 Pa; the values reported are therefore raw values D'. These data are plotted in Figure 3.8 along with non-linear fit parameters for $D_F(p_0)$ and D_K. Data taken in 2006.

Additional Experiments @ 260 K

Sample	Date	Δz cm	p_0 Pa	T_{ice} K	T_{air} K	RH %	J_1 mg m^{-2}s^{-1}	$\bar{c}$	$\Delta\rho_1$ g m^{-3}	D' cm^{2}s^{-1}	$D/\mathcal{D}_{12}$
Frit 4	Feb 13	0.63	582	255.0	259.0	27.47	26.92	0.068	0.63	2.71±0.55	0.10±0.02
Frit 5	Feb 13	0.57	582	255.0	259.0	28.37	27.40	0.068	0.62	2.53±0.55	0.10±0.02
Frits 1 & 4	Feb 03	1.28	594	257.9	260.3	16.56	23.25	0.078	1.08	2.75±0.33	0.10±0.01
	Feb 23	1.28	588	256.0	260.2	19.15	21.10	0.069	0.83	3.26±0.42	0.12±0.02
	Feb 24	1.28	586	256.9	260.1	20.05	18.37	0.075	0.91	2.57±0.21	0.10±0.01
	Feb 28	1.28	584	256.8	259.9	21.09	21.34	0.075	0.89	3.07±0.33	0.12±0.02
	Mar 01	1.28	542	256.5	260.8	11.04	21.54	0.072	1.00	2.75±0.40	0.10±0.01
Frits 5 & 8	Feb 03	1.20	594	257.4	260.1	18.83	19.63	0.076	0.98	2.39±0.31	0.09±0.01
	Feb 23	1.20	588	256.8	260.0	22.93	22.73	0.076	0.86	3.17±0.43	0.12±0.02
	Feb 24	1.20	586	256.6	260.2	19.45	22.67	0.072	0.88	3.08±0.41	0.12±0.02
	Feb 28	1.20	584	256.3	259.8	22.74	22.12	0.073	0.82	3.25±0.44	0.12±0.02
	Mar 01	1.20	542	256.0	260.9	9.94	23.89	0.068	0.97	2.95±0.36	0.10±0.02
Frits 1–4	Jan 28	2.52	610	258.5	261.0	7.39	14.18	0.074	1.30	2.74±0.25	0.11±0.01
	Jan 29[a]	2.52	609	259.0	261.0	5.80	13.96	0.077	1.39	2.52±0.22	0.10±0.01
Frits 5–8	Jan 28	2.46	610	258.7	260.9	3.67	15.26	0.072	1.38	2.71±0.24	0.11±0.01
	Jan 29	2.46	609	258.8	260.9	7.28	15.58	0.077	1.34	2.85±0.26	0.11±0.01
	Feb 15	2.46	630	258.7	261.1	15.99	14.82	0.079	1.17	3.12±0.31	0.13±0.02
Frits 1–8	Mar 20	5.07	589	259.8	261.5	10.12	7.79	0.091	1.41	2.80±0.24	0.11±0.01
	Mar 21	5.07	589	259.8	261.6	10.01	7.98	0.091	1.42	2.85±0.24	0.11±0.01
JSC Mars-1	Apr 03	2.03	595	254.6	260.8	18.99	23.97	0.061	0.68	7.18±0.90	0.27±0.04
	Mar 22	5.05	594	257.9	261.2	13.55	11.58	0.077	1.11	5.29±0.49	0.20±0.02
	Mar 22	5.08	594	257.6	261.1	11.40	13.12	0.073	1.11	5.98±0.54	0.23±0.03
	Apr 03	10.11	608	259.0	261.4	7.98	6.29	0.079	1.34	4.73±0.39	0.18±0.02
1-3 μm loose	Oct 24	0.98	503	257.7	260.8	10.47	22.60	0.087	1.15	1.93±0.26	0.06±0.01
	Apr 17	2.09	584	255.8	260.7	17.91	17.45	0.067	0.81	4.50±0.52	0.17±0.02
	Apr 17	2.00	584	255.1	260.5	15.25	20.15	0.061	0.80	5.07±0.57	0.19±0.03
1-3 μm packed	Nov 02	0.95	547	260.3	261.3	10.53	12.10	0.105	1.48	0.77±0.10	0.027±0.005
	Nov 04	0.96	540	260.7	262.3	5.59	12.24	0.107	1.62	0.73±0.09	0.025±0.005
	Apr 25	1.04	604	261.2	259.2	11.93	8.69	0.101	1.63	0.55±0.07	0.022±0.003
	Apr 25	1.11	604	261.1	258.2	9.51	8.96	0.099	1.64	0.60±0.07	0.024±0.003
	Sep 14	2.07	625	261.4	262.7	6.98	1.65	0.099	1.70	0.20±0.02	0.008±0.001
	Apr 21	2.21	591	260.1	261.5	8.38	4.08	0.091	1.48	0.61±0.06	0.023±0.003
	Apr 21	2.20	591	259.8	261.3	7.45	9.29	0.088	1.46	1.40±0.13	0.053±0.006

Table A.3: Experimental data and diffusion coefficients for various simulants measured under 600 Pa CO_2. Correction terms were either near zero (frits) or not determined due to insufficient data. Raw diffusion coefficients D' are reported. Data taken in 2005–2006.

[a]Experiment on Jan 29 with frits 1–4 was run upside-down to check for gravity-dependent effects.

50–80 μm Glass Beads @ 250 K

Date	Δz, cm	p_0, Pa	T_{ice}, K	T_{air}, K	RH, %	J_1, mg m^{-2} s^{-1}	$\Delta\rho_1$, g m^{-3}	D, cm^2 s^{-1}	$D/\mathcal{D}_{12}$	ϕ, %	τ
26 Sep	1.09	599	247.8	250.0	32.25	10.75	0.32	3.54±0.66	0.14±0.03	42.7	3.0
26 Sep	0.99	599	247.6	251.0	36.00	10.87	0.26	3.96±0.87	0.16±0.04	41.7	2.6
30 Oct	0.88	610	247.4	249.8	37.65	10.99	0.27	3.50±0.79	0.15±0.03	42.9	2.9
30 Oct	0.89	610	247.5	250.8	30.59	11.82	0.30	3.42±0.72	0.14±0.03	43.4	3.1
3 Apr	1.93	613	248.5	250.4	24.68	7.60	0.40	3.62±0.49	0.15±0.02	48.1	2.9
18 Sep	2.08	592	248.4	251.1	21.80	8.19	0.41	4.14±0.54	0.16±0.02	42.0	2.8
18 Sep	1.83	595	248.5	250.4	27.36	7.97	0.38	3.74±0.54	0.15±0.02	49.6	3.1
9 Nov	2.08	595	248.7	251.5	21.49	8.11	0.42	4.01±0.52	0.16±0.02	42.3	2.8
20 Sep	4.95	599	249.6	250.5	14.17	4.21	0.53	3.87±0.38	0.16±0.02	45.0	2.9
20 Sep	4.91	599	249.4	251.5	14.14	4.03	0.52	3.82±0.38	0.15±0.02	44.8	2.9
6 Oct	5.03	593	249.4	251.7	12.25	4.00	0.53	3.81±0.37	0.15±0.02	44.2	2.9
10 Oct	4.95	591	249.2	251.5	11.12	4.06	0.53	3.80±0.37	0.15±0.02	43.4	2.9
16 Oct	4.95	600	249.5	250.4	15.52	3.66	0.53	3.43±0.34	0.14±0.02	42.6	3.0
16 Oct	4.83	600	249.4	251.5	13.57	3.98	0.52	3.66±0.36	0.15±0.02	46.8	3.1
25 Oct	4.91	603	249.6	250.4	16.13	3.65	0.52	3.43±0.34	0.14±0.02	45.9	3.3
25 Oct	4.82	603	249.4	251.5	13.43	3.90	0.52	3.58±0.36	0.25±0.02	46.2	3.2
29 Oct	9.87	599	250.2	250.6	8.95	2.25	0.61	3.63±0.32	0.15±0.02	43.7	3.0
29 Oct	9.72	599	250.0	251.6	7.15	2.31	0.61	3.69±0.32	0.15±0.02	44.4	2.9
3 Nov	9.71	610	250.2	250.6	9.86	2.30	0.60	3.71±0.33	0.15±0.02	44.7	2.9
3 Nov	9.83	610	249.9	251.7	7.69	2.24	0.60	3.68±0.32	0.15±0.02	45.0	3.0

Table A.4: Experimental conditions, data, and corrected diffusion coefficients for 50–80 μm glass beads. Data taken in 2006.

Epsomite Salt Crusts @ 250 K

Salt Content % Epsomite	Date	Δz, cm	p_0, Pa	T_{ice}, K	T_{air}, K	RH, %	J_1, mg m^{-2} s^{-1}	$\Delta\rho_1$, g m^{-3}	D, cm^2 s^{-1}	$D/\mathcal{D}_{12}$
18.4 %	29 Jan	1.47	596	250.5	251.1	12.21	1.902	0.60	0.47±0.05	0.02±0.00
	16 Jul	1.00	586	247.3	249.0	15.71	2.200	0.41	0.53±0.06	0.02±0.00
	16 Jul	1.00	586	247.0	247.9	12.86	2.943	0.43	0.69±0.07	0.03±0.00
14.2 %	10 Oct	0.88	591	249.6	250.3	16.35	5.440	0.52	0.91±0.14	0.04±0.01
9.7 %	6 Oct	1.96	593	249.7	250.5	18.20	5.511	0.51	2.10±0.23	0.08±0.01
	12 Feb	1.25	586	249.0	251.6	20.20	7.075	0.44	1.99±0.27	0.08±0.01
	17 Feb	1.10	586	248.5	250.2	27.74	6.863	0.38	1.97±0.30	0.08±0.01
	20 Feb	1.10	586	248.7	250.3	31.29	6.293	0.37	1.87±0.30	0.07±0.01
4.9 %	27 Nov	1.00	613	248.3	250.4	25.60	8.070	0.38	2.11±0.33	0.08±0.01
	27 Nov	1.00	613	248.4	251.5	24.97	8.771	0.37	2.34±0.37	0.10±0.02
	30 Apr	1.00	586	245.8	248.9	31.87	7.340	0.25	2.92±0.51	0.12±0.02
	7 May	1.10	586	245.3	248.5	40.27	8.685	0.19	5.04±1.04	0.20±0.04
2.0 %	22 Nov	1.00	624	249.4	250.8	19.85	6.428	0.48	1.33±0.19	0.06±0.01
	22 Nov	1.00	624	249.1	251.9	21.74	5.855	0.44	1.34±0.20	0.06±0.01
	1 Dec	1.00	590	248.1	250.1	27.56	8.570	0.37	2.34±0.37	0.09±0.02
	1 Dec	1.00	590	248.0	251.1	24.90	9.183	0.37	2.52±0.40	0.10±0.02
1.0 %	14 Dec	1.00	581	250.6	250.2	29.06	9.682	0.50	1.92±0.29	0.08±0.01
	14 Dec	1.00	581	247.8	251.2	26.80	9.660	0.34	2.88±0.47	0.11±0.02
	19 Dec	1.00	586	247.9	250.1	30.75	11.21	0.33	3.36±0.56	0.13±0.02
	19 Dec	1.00	586	247.3	251.2	27.54	9.871	0.31	3.20±0.54	0.13±0.02
	16 Apr	1.00	583	246.3	249.0	28.11	6.435	0.29	2.20±0.26	0.09±0.02
	16 Apr	1.00	583	246.1	247.9	22.77	6.743	0.33	2.04±0.31	0.08±0.01
	20 Apr	1.00	586	246.1	248.9	30.56	7.213	0.27	2.66±0.45	0.11±0.02
	20 Apr	1.00	586	246.0	247.8	26.45	7.936	0.31	2.59±0.41	0.11±0.02
	7 May	0.45	586	245.2	247.3	39.49	10.79	0.21	2.29±0.63	0.09±0.03

Table A.5: Experimental conditions, data, and corrected diffusion coefficients for salt crusts. Data taken in 2006–2007.

Mixtures of Glass Beads with JSC Mars-1 @ 250 K

X_f %	Date	Δz, cm	p_0, Pa	T_{ice}, K	T_{air}, K	RH, %	J_1, mg m^{-2} s^{-1}	$\Delta\rho_1$, g m^{-3}	D, cm^2 s^{-1}	$D/\mathcal{D}_{12}$	ϕ	τ
43.1	22 Dec	4.68	591	250.2	251.9	7.344	1.932	0.61	1.48±0.13	0.06±0.01	57.8	9.8
	10 Jan	4.84	596	250.7	252.5	7.557	1.357	0.64	1.03±0.09	0.04±0.00	53.3	12.9
	19 Jan	5.03	586	250.5	252.2	7.480	1.783	0.63	1.43±0.13	0.06±0.01	57.3	10.2
27.4	24 Jan	5.01	596	250.2	252.2	9.471	2.809	0.60	2.36±0.22	0.09±0.01	52.3	5.5
	6 Feb	4.96	596	250.2	252.0	10.75	2.750	0.58	2.34±0.27	0.09±0.01	48.6	5.2
	13 Apr	4.95	586	247.6	248.3	11.34	2.293	0.46	2.47±0.23	0.10±0.01	53.3	5.4
15.9	24 Jan	4.93	596	249.9	251.1	12.13	3.606	0.56	3.17±0.30	0.13±0.01	47.8	3.7
	6 Feb	4.94	596	249.2	250.9	13.70	3.573	0.51	3.46±0.34	0.14±0.02	47.3	3.4
	26 Mar	5.11	586	247.4	249.3	12.63	2.714	0.43	3.13±0.30	0.13±0.01	47.6	3.8
	13 Apr	5.02	586	249.6	250.5	11.09	3.354	0.56	3.07±0.28	0.12±0.01	50.1	4.1
11.4	19 Mar	5.16	586	249.9	250.9	9.852	2.934	0.58	2.60±0.24	0.10±0.01	50.9	4.9
	10 Apr	5.09	586	247.6	248.2	11.71	2.515	0.46	2.80±0.26	0.11±0.01	51.4	4.5
7.06	22 Dec	4.75	591	249.7	250.8	10.98	3.530	0.56	2.99±0.28	0.12±0.01	46.0	3.8
	10 Jan	4.87	595	250.2	251.4	11.66	3.336	0.58	2.79±0.26	0.11±0.01	49.5	4.4
	19 Jan	4.97	586	250.0	251.1	11.19	3.334	0.57	2.88±0.27	0.11±0.01	46.3	4.0
	26 Mar	5.16	586	249.4	251.6	12.07	3.140	0.53	3.05±0.29	0.12±0.01	52.7	4.4
3.29	19 Mar	5.14	586	249.6	251.9	12.91	3.726	0.53	3.59±0.35	0.14±0.02	45.7	3.2
	10 Apr	5.10	586	247.3	249.3	13.56	3.095	0.42	3.73±0.37	0.15±0.02	46.6	3.1

Table A.6: Experimental conditions, data, and diffusion coefficients for 50–80 μm sand and JSC Mars-1 dust mixtures. Data taken in 2006–2007.

Mixtures of Glass Beads and 1–3 μm dust @ 250 K

X_f %	Date	Δz, cm	p_0, Pa	$T_{\rm ice}$, K	$T_{\rm air}$, K	RH, %	J_1, mg m^{-2} s^{-1}	$\Delta\rho_1$, g m^{-3}	D, cm^2 s^{-1}	$D/\mathcal{D}_{12}$	ϕ	τ
39.8	7 Jun	4.62	586	247.0	249.1	13.53	3.057	0.41	3.42±0.15	0.14±0.01	74.2	5.4
	11 Jun	5.00	586	247.0	249.1	15.13	3.221	0.40	4.00±0.16	0.16±0.01	74.6	4.6
	11 Jun	5.00	586	247.0	249.1	14.66	3.171	0.40	3.92±0.17	0.16±0.01	74.6	4.7
24.9	9 May	4.95	586	247.0	249.1	13.87	2.923	0.41	3.51±0.17	0.14±0.01	65.0	4.6
	16 May	4.96	586	247.0	249.1	13.93	2.941	0.41	3.54±0.16	0.14±0.01	63.9	4.5
	1 Jun	5.32	586	247.2	249.4	14.03	3.105	0.41	3.98±0.30	0.16±0.02	66.1	4.1
14.2	9 May	5.05	586	247.2	248.0	12.68	2.553	0.43	2.98±0.15	0.12±0.01	60.0	5.0
	5 Jun	5.34	586	247.0	249.1	13.87	2.941	0.41	3.84±0.17	0.15±0.01	59.3	3.8
10.1	14 May	5.05	586	247.1	249.1	13.79	2.770	0.41	3.38±0.16	0.14±0.01	54.7	4.0
	19 May	5.00	586	247.1	249.1	14.10	2.993	0.41	3.62±0.19	0.15±0.01	57.5	4.0
	22 May	5.14	586	247.0	249.1	13.81	3.174	0.43	3.95±0.17	0.16±0.01	58.1	3.7
	1 Jun	5.20	586	247.3	248.3	13.80	3.069	0.42	3.71±0.22	0.15±0.01	58.1	3.9
6.19	14 May	5.00	586	247.1	248.0	13.51	2.457	0.42	2.90±0.14	0.12±0.01	56.9	4.9
	19 May	4.97	586	247.1	248.0	13.87	3.083	0.42	3.62±0.20	0.15±0.01	53.9	3.7
	5 Jun	5.12	586	247.0	248.0	14.28	2.939	0.42	3.62±0.17	0.15±0.01	54.3	3.7
2.82	16 May	5.12	586	247.0	248.0	13.82	3.050	0.42	3.72±0.17	0.15±0.01	54.3	3.6
	22 May	5.10	586	247.0	248.0	13.90	2.518	0.42	3.06±0.15	0.12±0.01	53.8	4.4
	7 Jun	5.50	586	247.0	248.1	13.96	3.098	0.42	4.06±0.18	0.16±0.01	55.1	3.4

Table A.7: Experimental conditions, data, and diffusion coefficients for 50–80 μm sand and 1–3 μm dust mixtures. Data taken in 2007.

Pure Dusts: JSC Mars-1 and 1–3 μm Dust @ 250 K

Sample %	Date	Δz, cm	p_0, Pa	$T_{\rm ice}$, K	$T_{\rm air}$, K	RH, %	J_1, mg m^{-2} s^{-1}	$\Delta\rho_1$, g m^{-3}	D, cm^2 s^{-1}	$D/\mathcal{D}_{12}$	ϕ	τ
JSC Mars-1:	2 Feb	4.98	586	250.5	251.3	9.78	0.891	0.61	0.72±0.08	0.03±0.00	72.5	25
Loose	26 Feb	5.06	586	250.0	250.7	8.25	2.338	0.60	1.98±0.08	0.08±0.01	78.8	10
	16 Jun	4.92	586	247.4	249.1	9.86	1.594	0.45	1.72±0.08	0.07±0.01	75.2	11
JSC Mars-1:	26 Feb	2.28	586	250.1	251.8	7.34	1.192	0.61	0.45±0.03	0.02±0.00	62.9	36
Packed	25 Jun	3.42	586	247.6	249.2	9.75	1.147	0.47	1.04±0.05	0.04±0.00	85.8	21
1–3 μm dust:	17 Oct[a]	1.03	600	248.4	249.4	74.48	5.964	0.10	6.04±4.36	0.25±0.18	85.8	3.5
Loose	11 Jun	4.48	586	246.7	248.0	17.28	3.895	0.38	4.54±0.20	0.18±0.01	66.8	3.6
	11 Jun	4.48	586	246.8	248.0	16.15	3.963	0.39	4.51±0.21	0.18±0.01	91.3	5.0
	16 Jun	5.13	586	246.8	248.1	15.85	4.106	0.40	5.31±0.26	0.21±0.02	91.5	4.3
1–3 μm dust:	19 Oct	1.02	550	249.2	249.8	60.39	4.177	0.22	1.94±0.68	0.07±0.03	83.1	11
Packed	21 Oct	1.91	550	249.4	249.9	27.02	1.770	0.44	0.76±0.12	0.03±0.00	78.0	27
	25 Jun	3.49	586	247.3	248.1	12.62	2.705	0.44	2.16±0.09	0.09±0.01	90.8	10

Table A.8: Experimental conditions, data, and diffusion coefficients for crushed JSC Mars-1 and 1–3 μm dusts. Data taken in 2005–2007.

[a]Data not used in analyses.

Bibliography

Abrahamson, J., and J. Marshall (2002), Permanent electric dipoles on gas-suspended particles and the production of filamentary aggregates, *Journal of Electrostatics*, *55*, 43–63.

Aharonson, O., and N. Schorghofer (2006), Subsurface ice on Mars with rough topography, *Journal of Geophysical Research*, *111*(E11007), doi:10.1029/2005JE002636.

Allen, C., R. Morris, D. Lindstrom, M. Lindstrom, and J. Lockwood (1997), JSC Mars-1: Martian regolith simulant, *Abstracts of Papers Submitted to the Lunar and Planetary Science Conference*, *282*(1797).

Allen, C., K. Jager, R. Morris, D. Lindstrom, M. Lindstrom, and J. Lockwood (1998), Martian soil simulant available for scientific, educational study, *EOS Transactions*, *79*(34).

Anderson, P. (1995), Mechanism for the behavior of hydroactive materials used in humidity sensors, *Journal of Atmospheric and Oceanic Technology*, *12*, 662–667.

Arvidson, R. E., J. L. Gooding, and H. J. Moore (1989), The martian surface as imaged, sampled, and analyzed by the Viking landers, *Reviews of Geophysics*, *27*, 39–60.

Arvidson, R. E., D. Adams, G. Bonfiglio, P. Christensen, et al. (2008), Mars exploration program 2007 Phoenix landing site selection and characteristics, *Journal of Geophysical Research*, (submitted).

Baker, V. R. (1982), *The Channels of Mars*, 204 p. pp., University of Texas Press, Austin, TX.

Baker, V. R. (2001), Water and the martian landscape, *Nature*, *412*, 228–236.

Baker, V. R., M. H. Carr, V. C. Gulick, C. R. Williams, and M. S. Marley (1992), Channels and valley networks, in *Mars*, edited by H. Kieffer, B. Jakosky, C. Snyder, and M. Matthews, Space Science Series, pp. 493–522, University of Arizona Press.

Banin, A., B. C. Clark, and H. Wänke (1992), Surface chemistry and mineralogy, in *Mars*, edited by H. Kieffer, B. Jakosky, C. Snyder, and M. Matthews, Space Science Series, pp. 594–625, University of Arizona Press.

Baver, L. D. (1940), *Soil Physics*, chap. V. Soil Structure, pp. 160–167, John Wiley & Sons, Inc., London.

Bockheim, J. G. (2002), Landform and soil development in the McMurdo Dry valleys, Antarctica: A regional synthesis, *Arctic, Antarctic, and Alpine Research*, *34*, 308–317, doi:10.2307/1552489.

Bose, N., and B. Chakraborty (1955–56), Diffusion coefficients of vapours into pure gases and their mixtures, *Trans. Indian Inst. Chem Eng.*, *8*, 67.

Boynton, W., et al. (2002), Distribution of hydrogen in the near-surface of Mars: Evidence for subsurface ice deposits, *Science*, *297*(5578), 81–85.

Boynton, W. V., D. M. Janes, M. J. Finch, and R. M. S. Wiliams (2006), Simultaneous determination of dry-layer thickness and sub-surface ice content in the polar regions of Mars: Implications for the Phoenix landing site selection, in *37th Annual Lunar and Planetary Science Conference*, 2736, Lunar and Planetary Institute.

Bryson, K., V. Chevrier, and D. W. Sears (2007), An Experimental Study of the Behavior of Ice Under a Basalt Regolith and Implications for the Martian Diurnal Water Cycle, the Formation of Liquid, and the Presence of Ice at Low Latitudes on Mars, in *AAS/Division for Planetary Sciences Meeting Abstracts*, *AAS/Division for Planetary Sciences Meeting Abstracts*, vol. 39, pp. #17.07–+.

Cabrol, N., J. Farmer, E. Grin, L. Richter, L. Soderblom, R.Li, K. Herkenhoff, G. Landis, and R. Arvidson (2006), Aqueous processis at Gusev crater inferred from physical properties of rocks and soils along the Spirit traverse, *Journal of Geophysical Research*, *111*(E02S20), doi:10.1029/2005JE002490.

Cabrol, N. A., C. P. McKay, E. A. Grin, et al. (2007), Signatures of habitats and life in Earth's high-altitude lakes: Clues to Noachian aqueous environments on Mars, in *The Geology of Mars*, edited by M. G. Chapman, pp. 349–370, Cambridge University Press.

Carr, M. H. (1981), *The surface of Mars*, New Haven : Yale University Press.

Carr, M. H. (1996), *Water on Mars*, New York: Oxford University Press.

Chamberlain, M. A., and W. V. Boynton (2007), Response of Martian ground ice to orbit-induced climate change, *Journal of Geophysical Research*, *112*(E11), 6009–+, doi:10.1029/2006JE002801.

Chapman, S., and T. G. Cowling (1970), *The mathematical theory of non-uniform gases. An account of the kinetic theory of viscosity, thermal conduction and diffusion in gases, (3rd ed.)*, Cambridge: University Press.

Chevrier, V., and P. Mathé (2007), Mineralogy and evolution of the surface of Mars: A review, *Planetary and Space Science*, *55*, 289–314.

Chittenden, J., V. Chevrier, D. W. Sears, L. A. Roe, K. Bryson, L. Billingsly, and J. Hanley (2006), Insights into Interactions of Water Ice with Regolith under Simulated Martian Conditions, in *Bulletin of the American Astronomical Society*, *Bulletin of the American Astronomical Society*, vol. 38, pp. 603–+.

Christensen, P. (1986), Regional dust deposits on Mars—physical properties, age, and history, *Journal of Geophysical Research*, *91*(B3), 3533.

Christensen, P. R., J. L. Bandfield, R. N. Clark, et al. (2000), Detection of crystalline hematite mineralization on Mars by the Thermal Emission Spectrometer: Evidence for near-surface water, *Journal of Geophysical Research*, *105*(E4), 9623–9642, doi:10.1029/1999JE001093.

Clark, B., and D. van Hart (1981), The salts of Mars, *Icarus*, *45*, 370–378, doi:10.1016/0019-1035(81)90041-5.

Clark, B. C., A. K. Baird, H. J. Rose Jr., P. Toulmin, R. P. Christensen, W. C. Kelliher, A. J. Castro, C. D. Rowe, et al. (1977), The Viking X-ray fluorescence experiment: Analytical methods and early results, *Journal of Geophysical Research*, *82*, 4577–4594.

Clifford, S., and D. Hillel (1986), Knudsen diffusion: The effect of small pore size and low gas pressure on gaseous transport in soil, *Soil Science*, *141*(4), 289.

Clifford, S. M. (1993), A model for the hydrologic and climatic behavior of water on Mars, *Journal of Geophysical Research*, *98*(E6), 10,973–11,016.

Clifford, S. M., and D. Hillel (1983), The stability of ground ice in the equatorial region of Mars, *Journal of Geophysical Research*, *88*(B3), 2456–2474.

Clow, G. (1987), Generation of liquid water on Mars through melting of a dusty snowpack, *Icarus*, *72*, 95–127.

Cooper, C., and J. Mustard (2002), Spectroscopy of loose and cemented sulfate-bearing soils: Implications for duricrust on Mars, *Icarus*, *158*(1), 42–55.

Crider, W. (1956), The use of diffusion coefficients in the measurement of vapor pressure, *Journal of the American Chemical Society*, *78*, 924–925.

Cunningham, R., and R. Williams (1980), *Diffusion in Gases and Porous Media*, New York: Plenum Press.

Currie, J. (1960), Gaseous diffusion in porous media, part I: Dry granular materials, *British Journal of Applied Physics*, *11*, 318–324.

Cutts, J. A., and B. H. Lewis (1982), Models of climate cycles recorded in Martian polar layered deposits, *Icarus*, *50*, 216–244, doi:10.1016/0019-1035(82)90124-5.

Dash, J., H. Fu, and J. Wettlaufer (1995), The premelting of ice and its environmental consequences, *Rep. Prog. Phys.*, *58*, 115–167.

deWiest, R. J. M. (1969), *Flow Through Porous Media*, Academic Press.

Doran, P., C. McKay, G. Clow, G. Dana, A. Fountain, T. Nylen, and W. Lyons (2002), Valley floor climate observations from the McMurdo dry valleys, Antarctica, 1986–2000, *Journal of Geophysical Research*, *107*(D24), doi:10.1029/2001JD002045.

Elbaum, M., S. G. Lipson, and J. G. Dash (1993), Optical study of surface melting on ice, *Journal of Crystal Growth*, *129*, 491–505, doi:10.1016/0022-0248(93)90483-D.

Epstein, N. (1989), On tortuosity and the tortuosity factor in flow and diffusion through porous media, *Chemical Engineering Science*, *44*(3), 777–779.

Evans, R., G. M. Watson, and E. A. Mason (1961), Gaseous diffusion in porous media at uniform pressure, *Journal of Chemical Physics*, *35*(6), 2076–2083.

Fanale, F., and W. Cannon (1971), Adsorption on Martian regolith, *Nature*, *230*(5295), 502.

Fanale, F., and W. Cannon (1974), Exchange of adsorbed H_2O and CO_2 between the regolith and atmosphere of Mars caused by changes in surface insolation, *Journal of Geophysical Research*, *79*(24), 3397–3402.

Fanale, F. P., J. R. Salvail, A. P. Zent, and S. E. Postawko (1986), Global distribution and migration of subsurface ice on Mars, *Icarus*, *67*, 1–18.

Farmer, C. (1976), Liquid water on Mars, *Icarus*, *28*, 279–289.

Farmer, C., and P. Doms (1979), Global seasonal variation of water vapor on Mars and the implications for permafrost, *Journal of Geophysical Research*, *84*(B6), 2881–2888.

Feldman, W., et al. (2002), Global distribution of neutrons from Mars: Results from Mars Odyssey, *Science*, *297*(5578), 75–78.

Feldman, W., et al. (2003), The global distribution of near-surface hydrogen on Mars, in *Proc. Sixth Intern. Conf. Mars*, no. 3218.

Feldman, W. C., J. W. Head, S. Maurice, T. H. Prettyman, R. C. Elphic, H. O. Funsten, D. J. Lawrence, R. L. Tokar, and D. T. Vaniman (2004a), Recharge mechanism of near-equatorial hydrogen on Mars: Atmospheric redistribution or sub-surface aquifer, *Geophysical Research Letters*, *31*, 18,701–+, doi:10.1029/2004GL020661.

Feldman, W. C., et al. (2004b), Global distribution of near-surface hydrogen on Mars, *Journal of Geophysical Research*, *109*(E18), 9006–+, doi:10.1029/2003JE002160.

Feldman, W. C., et al. (2005), Topographic control of hydrogen deposits at low latitudes to midlatitudes of Mars, *Journal of Geophysical Research*, *110*(E9), 11,009–+, doi:10.1029/2005JE002452.

Ferris, J., J. Dohm, V. Baker, and T. Maddock (2002), Dark slope streaks on Mars: Are aqueous processes involved?, *Geophysical Research Letters*, *29*(10), 10.1029/2002GL014,936.

Fisher, D. A. (2005), A process to make massive ice in the martian regolith using long-term diffusion and thermal cracking, *Icarus*, *179*, 387–397, doi:10.1016/j.icarus.2005.07.024.

Flasar, F., and R. Goody (1976), Diurnal behavior of water on Mars, *Planetary and Space Science*, *24*(2), 161–181.

Forget, F., et al. (1999), Improved general circulation models of the martian atmosphere from the surface to above 80 km, *Journal of Geophysical Research*, *104*, 24,155–24,176.

Freeze, R. A., and J. A. Cheng (1979), *Groundwater*, Prentice Hall.

Gille, W., D. Enke, and F. Janowski (2001), Stereological macropore analysis of a controlled pore glass by use of small-angle scattering, *Journal of Porous Materials*, *8*, 179–191.

Gille, W., D. Enke, and F. Janowski (2002), Pore size distribution and chord length distribution of porous VYCOR glass (PVG), *Journal of Porous Materials*, *9*, 221–230.

Gilliland, E., R. Baddour, G. Perkinson, and K. J. Sladek (1974), Diffusion on surfaces. 1. Effect of concentration on the diffusivity of physically adsorbed gases, *Ind. Eng. Chem. Fundam.*, *13*(2), 95–100.

Gilmore, M. S., M. D. Merrill, and R. Castano (2004), Effect of Mars analogue dust deposition on the automated detection of calcite in visible/near-infrared spectra, *Icarus*, *172*(2), 641–646.

Greeley, R., R. Leach, B. White, J. Iversen, and J. Pollack (1980), Threshold windspeeds for sand on Mars, *Geophysical Research Letters*, *172*(2), 121–124.

Greeley, R., N. Lancaster, S. Lee, and P. Thomas (1992), Martian aeolian processes, sediments, and features, in *Mars*, edited by H. Kieffer, B. Jakosky, C. Snyder, and M. Matthews, Space Science Series, pp. 730–765, University of Arizona Press.

Greeley, R., G. Wilson, R. Coquilla, B. White, and R. Haberle (2000), Windblown dust on Mars: Laboratory simulations of flux as a function of surface roughness, *Planetary and Space Science*, *48*, 1349–1355.

Grew, K., and T. Ibbs (1952), *Thermal Diffusion in Gases*, Cambridge: Cambridge Univeristy Press.

Gross, F. B., S. B. Grek, C. I. Calle, and R. U. Lee (2001), JSC Mars-1 martian regolith simulant particle charging experiments in a low pressure environment, *Journal of Electrostatics*, *53*(4), 257–266.

Guglielmo, G. (1882), Sulla determinazione del coefficiente di diffusione del vapor acqueo per nell'aria, nell'idrogeno e nell'acido carbonico, *Annal. Phys. Chem., Beibl.*, *6*, 475–477.

Haberle, R., J. Murphy, and J. Schaeffer (2003), Orbital change experiments with a Mars general circulation model, *Icarus*, *161*, 66–89.

Ham, J. M., and E. J. Benson (2004), On the construction and calibration of dual-probe heat capacity sensors, *Soil Science Society of America Journal*, *68*, 1185–1190.

Hardy, B. (1998), ITS-90 formulations for vapor pressure, frostpoint, temperature dewpoint temperature, and enhancement factors in the range -100 to +100c, in *Third International Symposium on Humidity & Moisture (Proceedings)*, edited by B. Hardy, National Physical Laboratory, London: National Physical Laboratory.

Hare, D., and C. Sorensen (1987), The densty of supercooled water. II: Bulk samples cooled to the homogeneous nucleation limit, *Journal of Chemical Physics*, *87*(2), 4840–4845.

Head, J. W., J. F. Mustard, M. A. Kreslavsky, R. E. Milliken, and D. R. Marchant (2003), Recent ice ages on Mars, *Nature*, *426*, 797–802.

Head, J. W., et al. (2005), Tropical to mid-latitude snow and ice accumulation, flow and glaciation on Mars, *Nature*, *434*, 346–351, doi:10.1038/nature03359.

Hecht, M. (2002), Metastability of liquid water on Mars, *Icarus*, *156*, 373–386.

Herkenhoff, K. E., S. W. Squyres, R. Arvidson, D. S. Bass, J. F. Bell III, P. Bertelsen, N. A. Cabrol, et al. (2004), Textures of the soils and rocks at Gusev Crater from Spirit's Microscopic Imager, *Science*, *305*(824), doi:10.1126/science.3050824.

Hindmarsh, R., F. Van der Wateren, and A. Verbers (1998), Sublimation of ice through sediment in Beacon Valley, Antarctica, *Geografiska Annaler*, *80A*(3-4), 209–219.

Hippenmeyer, B. (1949), Die Diffusion von Wasserdampf in Wasserstoff, Stickstoff und deren Gemischen, *Z. Angew. Phys.*, *1*, 549.

Hobbs, P. V. (1974), *Ice Physics*, New York: Oxford Universiy Press.

Hobbs, P. V., and B. J. Mason (1964), The sintering and adhesion of ice, *Philosophical Magazine*, *9*(98), 181–197, doi: 10.1080/14786436408229184.

Holman, J. (1997), *Heat Transfer*, 8th ed., New York: McGraw Hill.

Hoogschagen, J. (1955), Diffusion in porous catalysts and adsorbents, *Industrial and Engineering Chemistry*, *47*(5), 906–912.

Hudson, T., and O. Aharonson (2008), Diffusion barriers at Mars surface conditions: Salt crusts, particle size mixtures, and dust, *Journal of Geophysical Research*, (submitted).

Hudson, T., O. Aharonson, N. Schorghofer, C. Farmer, M. Hecht, and N. Bridges (2007), Water vapor diffusion in Mars subsurface environments, *Journal of Geophysical Research*, *112*(E05016), doi:10.1029/2006JE002815.

Hudson, T., O. Aharonson, and N. Schorghofer (2008), Laboratory simulations of diffusive implacement of ground ice on Mars, *Journal of Geophysical Research*, (submitted).

Ingersoll, A. P. (1970), Mars: Occurrence of liquid water, *Science*, *168*, 972–973.

Jakoksy, B., and P. Christensen (1986), Global duricrust on Mars: Analysis of remote-sensing data, *Journal of Geophysical Research*, *91*(B3), 3547.

Jakosky, B. (1983), The role of seasonal reservoirs in the Mars water cycle. 1. Sesonal exchange of water with the regolith, *Icarus*, *55*(1), 1–18.

Jakosky, B. (1985), The seasonal water cycle on Mars, *Space Science Reviews*, *41*, 131–200.

Jakosky, B., A. Zent, and R. Zurek (1997), The Mars water cycle: Determining the role of exchange with the regolith, *Icarus*, *130*, 87.

Jakosky, B. M., M. T. Mellon, E. S. Varnes, W. C. Feldman, W. V. Boynton, and R. M. Haberle (2005), Mars low-latitude neutron distribution: Possible remnant near-surface water ice and a mechanism for its recent emplacement, *Icarus*, *175*, 58–67, doi:10.1016/j.icarus.2004.11.014.

Jakosky, D. M., and R. M. Haberle (1992), The seasonal behavior of water on Mars, in *Mars*, edited by H. Kieffer, B. Jakosky, C. Snyder, and M. Matthews, Space Science Series, pp. 969–1016, University of Arizona Press.

Jerolmack, D. J., D. Mohrig, J. P. Grotzinger, D. A. Fike, and W. A. Watters (2006), Spatial grain size sorting in eolian ripples and estimation of wind conditions on planetary surfaces: Application to Meridiani Planum, Mars, *Journal of Geophysical Research*, *111*(E12S02), doi:10.1029/2005JE002544.

Kahn, R., T. Martin, R. Zurek, and S. Lee (1992), The martian dust cycle, in *Mars*, edited by H. Kieffer, B. Jakosky, C. Snyder, and M. Matthews, Space Science Series, pp. 1017–1053, University of Arizona Press, Tucson.

Kennard, E. (1938), *Kinetic Theory of Gasses*, New York: McGraw-Hill.

Kieffer, H., J. Chase, E. Miner, G. Munch, and G. Neugebauer (1973), Preliminary report on infrared radiometric measurements from Mariner 9 spacecraft, *Journal of Geophysical Research*, *78*, 4291–4312.

Kieffer, H. H. (1976), Soil surface temperatures at the Viking landing sites, *Science*, *194*, 1344–1346.

Komatsu, G., and V. R. Baker (2007), Formation of valleys and cataclysmic flood channels on Earth and Mars, in *The Geology of Mars*, edited by M. G. Chapman, pp. 297–321, Cambridge University Press.

Konrad, J.-M., and C. Duquennoi (1993), A model of water transport and ice lensing in freezing soils, *Water Resources Research*, *29*(9), 3109–3124.

Konrad, J.-M., and N. R. Morgenstern (1980), The segregation potential of a freezing soil, *Canadian Geotechnical Journal*, *18*, 482–491.

Koop, T. (2002), The water activity of aqueous solutions in equilibrium with ice, *Bulletin of the Chemical Society of Japan*, *75*(12), 2587–2588, doi:10.1246/bcsj.75.2587.

Krasnopolsky, V., J. Maillard, and T. Owen (2004), Detection of methane in the martian atmosphere: Evidence for life?, *Icarus*, *172*(2), 537–547, doi:10.1016/j.icarus.2004.07.004.

Landau, L., and E. Lifshitz (1987), *Fluid Mechanics*, Pergamon Press, Oxford.

Landis, G., et al. (2004), Transient liquid water as a mechanism for induration of soil crusts on Mars, in *35th Annual Lunar and Planetary Science Conference*, 1197.

Laskar, J., B. Levrard, and J. F. Mustard (2002), Orbital forcing of the martian polar layered deposits, *Nature*, *419*, 375–377.

Laskar, J., M. Gastineau, F. Joutel, B. Levrard, P. Robutel, and A. Correia (2004), A New Astronomical Solution for the Long Term Evolution of the Insolation Quantities of Mars, in *Lunar and Planetary Institute Conference Abstracts*, *Lunar and Planetary Institute Conference Abstracts*, vol. 35, edited by S. Mackwell and E. Stansbery, pp. 1600–+, http://www.imcce.fr/fr/presentation/equipes/ASD/insola/mars/mars.html.

Leighton, R., and B. Murray (1966), Behavior of carbon dioxide and other volatiles on Mars, *Science*, *153*, 136.

Levitz, P. (1993), Knudsen diffusion and excitation transfer in random porous media, *Journal of Physical Chemistry*, *97*, 3813–3818.

Levrard, B., F. Forget, J. Laskar, and F. Montmessin (2005), A GCM recent history of northern martian polar layered deposits: Contribution from past equatorial ice reservoirs, in *36th Annual Lunar and Planetary Science Conference*, edited by S. Mackwell and E. Stansberry, pp. 1783–1784.

Lide, D. (Ed.) (2003), *CRC Handbook of Chemistry and Physics*, 84th ed., CRC Press.

Litvak, M. L., et al. (2006), Comparison between polar regions of Mars from HEND/Odyssey data, *Icarus*, *180*, 23–37.

Malin, M., and K. Edgett (2000), Evidence for recent groundwater seepage and surface runoff on Mars, *Science*, *288*, 2330–2335.

Mangold, N. (2005), High latitude patterned grounds on Mars: Classification, distribution, and climatic control, *Icarus*, *174*, 336–359, doi:10.1016/j.icarus.2004.07.030.

Marrero, T., and E. Mason (1972), Gaseous diffusion coefficients, *J. Phys. Chem. Ref. Data*, *1*(1), 3–118.

Mason, E., and A. Malinauskas (1983), *Gas Transport in Porous Media: The Dusty-Gas Model*, *Chemical Engineering Monographs*, vol. 17, Amsterdam: Elsevier.

Masson, P., M. H. Carr, F. Costard, et al. (2001), Geomorphologic evidence for liquid water, in *Chronology and Evolution of Mars*, edited by R. Kallenbach, J. Giess, and W. K. Hartmann, pp. 333–364, Dordrecht: Kluwer Academic.

McKay, C. P., R. L. Mancinelli, C. R. Stoker, and R. A. Wharton, Jr. (1992), The possibility of life on Mars during a water-rich past, in *Mars*, edited by H. Kieffer, B. Jakosky, C. Snyder, and M. Matthews, Space Science Series, chap. 34, pp. 1234–1248, University of Arizona Press.

McKay, C. P., M. T. Mellon, and E. I. Friedmann (1998), Soil temperatures and stability of ice-cemented ground in the McMurdo Dry Valleys, Antarctica, *Antarctic Science*, *10*(1), 31–38.

Mellon, M., and B. Jakosky (1993), Geographic variations in the thermal and diffusive stability of ground ice on Mars, *Journal of Geophysical Research*, *98*(E2), 3345–3364.

Mellon, M., and B. Jakosky (1995), The distribution and behavior of Martian ground ice during past and present epochs, *Journal of Geophysical Research*, *100*(E6), 11,781–11,799.

Mellon, M., B. Jakosky, and S. Postawko (1997), The persistence of equatorial ground ice on Mars, *Journal of Geophysical Research*, *102*(E8), 19,357–19,369.

Mellon, M., W. Feldman, and T. Prettyman (2004), The presence and stability of ground ice in the southern hemisphere of Mars, *Icarus*, *169*(2), 324–340, doi:10.1016/j.icarus.2003.10.022.

Mellon, M. T., and R. J. Phillips (2001), Recent gullies on Mars and the source of liquid water, *Journal of Geophysical Research*, *106*(10), 23,165–23,180, doi:10.1029/2000JE001424.

Mellon, M. T., B. M. Jakosky, H. H. Kieffer, and P. R. Christensen (2000), High-resolution thermal inertia mapping from the Mars Global Surveyor Thermal Emission Spectrometer, *Icarus*, *148*(2), 437–455.

Mellon, M. T., W. V. Boynton, W. C. Feldman, R. E. Arvidson, et al. (2008), A pre-landing assessment of the ice-table depth and ground-ice characteristics in martian permafrost at the Phoenix landing site, *Journal of Geophysical Research*, (submitted).

Merrison, J., J. Jensen, K. Kinch, R. Mugford, and P. Nørnberg (2004), The electrical properties of Mars analogue dust, *Planetary and Space Science*, *52*, 279–290, doi:10.1016/j.pss.2003.11.003.

Mischna, M. A., and M. I. Richardson (2005), A reanalysis of water abundances in the Martian atmosphere at high obliquity, *Geophysical Research Letters*, *32*(L03201), doi:10.1029/2004GL021865.

Moore, H. (1987), Physical properties of the surface materials at the Viking landing sites on Mars, *U.S. Geol. Surv. Prof. Paper*, *222*(1389).

Moore, H. J. (1992), Estimates of some physical/mechanical properties of Martian rocks and soillike materials, *Open-File Report 91-568*, Menlo Park, CA: U.S. Geological Survey.

Moore, H. J., C. R. Spitzer, K. Z. Bradford, P. M. Cates, R. E. Hutton, and R. W.Shorthill (1979), Sample fields of the Viking landers, physical properties, and aeolian processes, *Journal of Geophysical Research*, *84*, 8365–8384.

Murray, B. C., L. A. Soderblom, J. A. Cutts, R. P. Sharp, D. J. Milton, and R. B. Leighton (1972), Geological Framework of the South Polar Region of Mars (A 4. 4), *Icarus*, *17*, 328–+.

Murray, J. B., et al. (2005), Evidence from the Mars express high resolution stereo camera for a frozen sea close to Mars' equator, *Nature*, *434*, 352–356.

Nagata, I., and T. Hasegawa (1970), Gaseous diffusion coefficients, *Journal of Chemical Engineering of Japan*, *3*(2), 143–145.

Nelson, E. (1956), The measurement of vapour diffusivities in coal-gas and some common gases, *Journal of Applied Chemistry*, *6*, 286.

Neufeld, P., A. Janzen, and R. Aziz (1972), Empirical equations to calculate 16 of the transport collision integrals $\Omega(l,s)^*$ for the Lenndard-Jones (12-6) potential, *Journal of Chemical Physics*, *57*, 1100, doi:10.1063/1.1678363.

O'Connell, J., M. Gillespie, W. Krostek, and J. Prausnitz (1969), Diffusivities of water in nonpolar gases, *Journal of Physical Chemistry*, *73*, 2000.

Paige, D. (1992), The thermal stability of near-surface ground ice on Mars, *Nature*, *356*(6364), 43–45.

Paige, D. A., J. E. Bachman, and K. D. Keegan (1994), Thermal and albedo mapping of the polar regions of Mars using Viking thermal mapper observations: 1. North polar region, *Journal of Geophysical Research*, *99*, 25,959–25,991.

Papendick, R., and J. Runkles (1965), Transient-state oxygen difusion in soil: I. The case when rate of oxygen consumption is constant, *Soil Science*, *100*, 251–261.

Picardi, G., J. Plaut, D. Biccari, O. Bombaci, D. Calabrese, M. Cartacci, et al. (2005), Radar soundings of the subsurface of Mars, *Science*, *310*(5756), 1925–1928, doi:10.1126/science.1122165.

Plaut, J. J., G. Picardi, A. Safaeinili, A. B. Ivanov, S. M. Milkovich, A. Cicchetti, et al. (2007), Subsurface radar sounding of the South Polar Layered Deposits of Mars, *Science*, *316*(5821), 92–95, doi:10.1126/science1139672.

Pollard, W., and R. Present (1948), On gaseous self-diffuson in long capillary tubes, *Physical Review*, *73*, 762–774.

Presley, M., and P. Christiensen (1989), The distribution and origin of duricrusts on Mars, in *20th Annual Lunar and Planetary Science Conference*, pp. 868–869.

Presley, M. A., and P. R. Christensen (1997), Thermal conductivity measurements of particulate materials: 2. Results, *Journal of Geophysical Research*, *102*(E3), 6551–6566.

Prettyman, T. H., et al. (2004), Composition and structure of the Martian surface at high southern latitudes from neutron spectroscopy, *Journal of Geophysical Research*, *109*, E05,001, doi:10.1029/2003JE002139.

Putzig, N. E., M. T. Mellon, K. A. Kretke, and R. E. Arvidson (2005), Global thermal inertia and surface properties of Mars from the MGS mapping mission, *Icarus*, *173*(2), 325–341.

Putzig, N. E., M. T. Mellon, M. P. Golombek, and R. E. Arvidson (2006), Thermophysical Properties of the Phoenix Mars Landing Site Study Regions, in *37th Annual Lunar and Planetary Science Conference*, *Lunar and Planetary Institute Conference Abstracts*, vol. 37, edited by S. Mackwell and E. Stansbery, pp. 2426–+.

Reid, R., J. Prausnitz, and B. Poling (1987), *The Properties of Gases and Liquids*, 4th ed., New York: McGraw-Hill.

Richardson, M. I., and R. J. Wilson (2002), Investigation of the nature and stability of the Martian seasonal water cycle with a general circulation model, *Journal of Geophysical Research*, *107*(E5), doi:10.1029/2001JE001536,.

Rossbacher, L. A., and S. Judson (1981), Ground ice on Mars—Inventory, distribution, and resulting landforms, *Icarus*, *45*, 39–59.

Rossie, K. (1953), Die Diffusion von Wasserdampf in Luft bei Temperaturen bis 300°c, *Forsch. Gebiete Ingenieur.*, *19A*, 49.

Ruff, S. W., and P. R. Christensen (2002), Bright and dark regions on Mars: Particle size and mineralogical characteristics based on Thermal Emission Spectrometer data, *Journal of Geophysical Research*, *107*(E12), doi:10.1029/2001JE001580.

Schorghofer, N. (2005), A physical mechanism for long-term survival of ground ice in Beacon Valley, Antarctica, *Geophysical Research Letters*, *32*(L19503), doi:10.1029/2005GL023881.

Schorghofer, N. (2007), Dynamics of ice ages on Mars, *Nature*, *449*, 192–194, doi:10.1038/nature06082.

Schorghofer, N., and O. Aharonson (2005), Stability and exchange of subsurface ice on Mars, *Journal of Geophysical Research*, *110*(E05003), doi:10.1029/2004JE002350.

Schorghofer, N., O. Aharonson, and S. Khatiwala (2002), Slope streaks on Mars: Correlations with surface properties and the potential role of water, *Geophysical Research Letters*, *29*(23), 41–1, doi:10.1029/2002GL015889.

Schwertz, F., and J. Brow (1951), Diffusivity of water vapor in some common gases, *Journal of Chemical Physics*, *19*(5), 640–646.

Sharp, R. P., and M. C. Malin (1975), Channels on Mars, *Geological Society of America Bulletin*, *86*, 593–609.

Sizemore, H. G., and M. T. Mellon (2006), Effects of soil heterogeneity on martian ground-ice stability and orbital estimates of ice table depth, *Icarus*, *185*, 358–269.

Sizemore, H. G., and M. T. Mellon (2007), Laboratory measurements of tortuosity and permeability in Mars analog soils, in *35th Annual Lunar and Planetary Science Conference*, 3055.

Skorov, Y. V., W. J. Markiewicz, A. T. Basilevsky, and H. U. Keller (2001), Stability of water ice under a porous nonvolatile layer: Implications to the south polar layered deposits of Mars, *Planetary and Space Science*, *49*, 59–63.

Smith, M. (2002), The annual cycle of water vapor on Mars as observed by the Thermal Emission Spectrometer, *Journal of Geophysical Research*, *107*(E11), 5115.

Smoluchowski, R. (1968), Mars: Retention of ice, *Science*, *159*, 1348–1350.

Soderblom, L. A., and D. B. Wenner (1978), Possible fossil H_2O liquid-ice interfaces in martian crust, *Icarus*, *34*, 622–637, doi:10.1016/0019-1035(78)90050-7.

Squyres, S. W. (1984), The history of water on Mars, *Annual Reviews in Earth and Planetary Science*, *12*, 83–106.

Squyres, S. W., and A. H. Knoll (2005), Sedimentary rocks at Meridiani Planum: Origin, diagenesis, and implications for life on Mars, *Earth and Planetary Science Letters*, *240*, 1–10, doi:10.1016/j.epsl.2005.09.038.

Squyres, S. W., S. M. Clifford, R. O. Kuzmin, J. R. Zimbelman, and F. M. Costard (1992), Ice in the martian regolith, in *Mars*, edited by H. Kieffer, B. Jakosky, C. Snyder, and M. Matthews, Space Science Series, pp. 523–556, University of Arizona Press.

Squyres, S. W., et al. (2004a), The Opportunity Rover's Athena Science Investigation at Meridiani Planum, Mars, *Science*, *306*, 1698–1703, doi:10.1126/science.1106171.

Squyres, S. W., et al. (2004b), In Situ Evidence for an Ancient Aqueous Environment at Meridiani Planum, Mars, *Science*, *306*, 1709–1714, doi:10.1126/science.1104559.

Sugden, D., D. Marchant, N. Potter, R. Souchez, G. Denton, C. Swisher, and J. Tison (1995), Preservation of Miocene glacier ice in East Antarctica, *Nature*, *376*(6539), 412–414.

Sullivan, R., et al. (2005), Aeolian processes at the Mars Exploration Rover Meridiani Planum landing site, *Nature*, *436*, 58–61, doi:10.1038/nature03641.

Tamppari, L. K., J. Barnes, E. Bonfiglio, B. Cantor, et al. (2008), The atmospheric environment expected for the Phoenix landed season and location, *Journal of Geophysical Research*, (submitted).

Taylor, J. C. M. (1977), Sandstones as reservoir rocks, in *Developments in petroleum geology—1*, edited by G. D. Hobson, chap. 5, pp. 147–196, London: Applied Science Publishers LTD.

Toon, O. B., J. B. Pollack, W. Ward, J. A. Burns, and K. Bilski (1980), The astronomical theory of climatic change on Mars, *Icarus*, *44*, 552–607.

Trautz, M., and W. Müller (1935a), Die Reibung, Wärmeleitung und Diffusion in Gasmischungen XXXIII. Die Korrektion der Bisher mit der Verdampfungsmethode gemessenen Diffusionskonstanten, *Annalen der Physik*, *414*(4), 333–352.

Trautz, M., and W. Müller (1935b), Die Reibung, Wärmeleitung und Diffusion in Gasmischungen XXXIV. Neue Messungen von Diffusionskonstanten und abschliessende Zusammenfaßung über Gas-Diffusionskonstanten, *Annalen der Physik*, *414*(4), 353–374.

Vaniman, D., D. Bish, S. Chipewa, C. Fialips, J. Carrey, and W. Feldman (2004), Magnesium sulfate salts and the history of water on Mars, *Nature*, *431*, 663–665.

Wallace, D., and C. Sagan (1979), Evaporation of ice in planetary atmospheres: Ice-covered rivers on Mars, *Icarus*, *39*, 385–400.

Wang, A., J. Bell, and R. Li (2007), Salty soils at Gusev crater as revealed by Mars Exploration Rover Spirit, in *38th Annual Lunar and Planetary Science Conference*, 1196.

Wang, A., et al. (2006), Sulfate deposition in subsurface regolith in Gusev crater, Mars, *Journal of Geophysical Research*, *111*(E02S17), doi:10.1029/2005JE002513.

Ward, W. R. (1974), Climate variations on Mars 1. Astronomical theory of insolation, *Journal of Geophysical Research*, *79*(24), 3375–3386.

Washburn, E., et al. (Eds.) (2003), *International Critical Tables of Numerical Data, Physics, Chemistry and Technology*, first electronic ed., Norwich, New York: Knovel.

Weiss, B., Y. Yung, and K. Nealson (2000), Atmospheric energy for subsurface life on Mars?, *Proc. Nat. Acad. Sci. USA*, *972*(4), 1395–1399.

Weitz, C. M., et al. (2006), Soil grain analyses at Meridiani Planum, Mars, *Journal of Geophysical Research*, *111*(E10), 12–+, doi:10.1029/2005JE002541.

Wettlaufer, J. S. (1999), Ice surfaces: macroscopic effects of microscopic structure, *Philosophical Transactions of the Royal Society of London, A*, *357*, 3403–3425.

Winkelmann, A. (1884a), I. ueber die Diffusion von Gasen und Dämpfen, *Annalen der Physik*, *258*(5), 1–31.

Winkelmann, A. (1884b), Ii. ueber die Diffusion von Gasen und Dämpfen, *Annalen der Physik*, *258*(6), 152–161.

Winkelmann, A. (1889), Ueber den Einfluss der Temperatur auf die Verdampfung und auf die Diffusion von Dämpfen, *Annalen der Physik und Chemie*, *272*(1), 93–114.

Yen, A., R. Gellert, et al. (2005), An integrated view of the chemistry and mineralogy of martian soils, *Nature*, *436*, 49–54.

Yen, A. S., R. V. Morris, R. Gellert, B. C. Clark, D. W. Ming, G. Klingelhöfer, T. J. McCoy, M. E. Schmidt, and Athena Science Team (2007), Composition and Formation of the "Paso Robles" Class Soils at Gusev Crater, in *Lunar and Planetary Institute Conference Abstracts*, *Lunar and Planetary Institute Conference Abstracts*, vol. 38, pp. 2030–+.

Yu, B., J. Li, Z. Li, and M. Zou (2003), Permeabilities of unsaturated fractal porous media, *International Journal of Multiphase Flow*, *29*, 1625–1642, doi:10.1016/S0301-9322(03)00140-X.

Zalc, J. M., S. C. Reyes, and E. Iglesia (2004), The effects of diffusion mechanism and void structure on transport rates and tortuosity factors in complex porous structures, *Chemical Engineering Science*, *59*, 2947–2960, doi:10.1016/j.ces.2004.04.028.

Zent, A., and R. Quinn (1995), Simultaneous adsorption of CO_2 and H_2O under Mars-like conditions and appliation to the evolution of the martian climate, *Journal of Geophysical Research*, *100*(E3), 5341–5349.

Zent, A., and R. Quinn (1997), Measurement of H_2O adsorption under Mars-like conditions: Effects of adsorbent heterogeneity, *Journal of Geophysical Research*, *102*(E4), 9085–9095.

Zent, A., F. Fanale, J. Salvail, and S. Postawko (1986), Distribution and state of H_2O in the high-latitude shallow subsurface of Mars, *Icarus*, *67*, 19–36.

Zent, A. P., R. M. Haberle, H. C. Houben, and B. M. Jakosky (1993), A coupled subsurface-boundary layer model of water on Mars, *Journal of Geophysical Research*, *98*, 3319–3337.

Zuber, M. T., R. J. Phillips, J. C. Andrews-Hanna, S. W. Asmar, A. S. Konopliv, F. G. Lemoine, J. J. Plaut, and S. E. Smrekar (2007), Density of mars' south polar layered deposits, *Science*, *317*, 1718–1719, doi:10.1126/science.1146995.